Effective Field Theory Interpretation of ATLAS Top Quark Measurements

by

Sebastian Andreas Merkt

Diplom-Physiker, Karlsruhe Institute of Technology, 2012

Submitted to the Graduate Faculty of

the Kenneth P. Dietrich School of Arts and Sciences in partial fulfillment

of the requirements for the degree of

Doctor of Philosophy

University of Pittsburgh

2019

UNIVERSITY OF PITTSBURGH

DIETRICH SCHOOL OF ARTS AND SCIENCES

This dissertation was presented

by

Sebastian Andreas Merkt

It was defended on

November 15th 2019

and approved by

Dr. James Mueller, University of Pittsburgh

Dr. Joseph Boudreau, University of Pittsburgh

Dr. Brian Batell, University of Pittsburgh

Dr. Andrew Zentner, University of Pittsburgh

Dr. Manfred Paulini, Carnegie Mellon University

Dissertation Director: Dr. James Mueller, University of Pittsburgh

Effective Field Theory Interpretation of ATLAS Top Quark Measurements

Sebastian Andreas Merkt, PhD

University of Pittsburgh, 2019

In the first part of this dissertation, the combination of ATLAS top quark measurements to constrain dimension-six operator coefficients is presented. Top quark measurements provide a powerful tool to constrain the electroweak interaction of top quarks. Many models of physics Beyond the Standard Model (BSM) predict deviations of top quark interactions from the Standard Model. The Standard Model Effective Theory (SMEFT) provides a framework to parameterize BSM effects in a model independent way. Combining top quark measurements allows to constrain several Wilson coefficients of the dimension-six SMEFT operators at once. Specifically, the combination of the $\sqrt{s} = 8$ TeV t-channel single top cross section, the W helicity fractions and the single top decay distributions is studied. This allows to constrain a set of five Wilson coefficients, four of which generate modifications to the Wtb interaction vertex and one four-quark interaction. Systematic uncertainties are correlated between the measurements and these correlations are calculated and included in the combination. Limits are set simultaneously on all Wilson coefficients as well as individually. All limits are in accordance with Standard Model predictions.

In the second part, the new ATLAS 3D event display VP1-Light is presented. VP1-Light is a lightweight, standalone version of the general purpose 3D event display VP1. VP1 is tightly integrated into the ATLAS experiment's software framework, making the use of VP1 rather restrictive. With VP1-Light these restrictions have been eliminated giving ATLAS physics analysis users an easy to use event display.

Table of Contents

List of Tables

List of Figures

1.0 Introduction

The Standard Model of particle physics was established in the 1960's and was since confirmed by numerous experiments. Among the most important discoveries were the electroweak gauge bosons in 1983 and the recent discovery of a heavy scalar boson at the LHC, that looks much like the Higgs boson, predicted by the Standard Model. All these features provide reason to measure every aspect of the Standard Model to highest precision. On the other hand, the Standard Model can not provide answers to all phenomena found in the universe. Some of these, like the presence of dark matter, the matter-antimatter asymmetry or the existence of neutrino masses can not be explained by the Standard Model and thus needs an extended or modified theory. This gives reason to not only measure the Standard Model in full precision, but also to search for effects of new physics that may provide answers to these unsolved questions. in this work, an analysis is presented, that constrains the effects of physics beyond the Standard Model in terms of effective couplings. Constraining these couplings is possible by fitting the couplings to a combination of different top quark measurements conducted by ATLAS. Each measurement has its own advantages and is able to constrain different regions of the parameter space of the effective couplings. This combination will be the first part of this work.

In the second part, the new standalone event display of the ATLAS collaboration, VP1-Light is presented. VP1-Light is a lightweight version of the event display VP1, which served the experiment for many years as one of the primary event displays to generate graphics of the ATLAS detector and collision events, but also as a tool for development and debugging. However, VP1 is tightly integrated into the experiments software framework and can therefore not be used on personal computer. VP1-

Light does not have this constraint and it is possible to run VP1-Light on personal computers running macOS or Linux.

This work is organized as follows. In Chapter 1, an introduction to the physics concepts is given. The Standard Model of particle physics is reviewed and the concept of Effective Field Theories is introduced. An overview of the physics of the top quark is also given. Further, some technical details required for this combination are given. This includes some basics of statistics and Monte Carlo Generation. In Chapter 2, the combination of the ATLAS top quark measurements is given in full detail. Finally, in Chapter 3, the new standalone event display of ATLAS, VP1-Light is presented.

1.1 The Standard Model Of Particle Physics

The Standard Model (SM) of elementary particle physics describes three of the four known interactions of the universe, namely the strong interaction, the weak interaction, and the electromagnetic interaction. Furthermore it describes the interaction of these with the fermions that form the known matter. The gauge group of the SM is

$$\mathrm{SU(3)_C} \times \mathrm{SU(2)_L} \times \mathrm{U(1)_Y} \rightarrow \mathrm{SU(3)_C} \times \mathrm{U(1)_{em}}, \tag{1.1}$$

where $\mathrm{SU(3)_C}$ is the gauge group of the strong interaction or Quantum Chromodynamics (QCD), $\mathrm{SU(2)_L}$ the gauge group of the weak interaction and $\mathrm{U(1)_Y}$ the hypercharge gauge group. Each interaction has its corresponding gauge bosons and coupling constant g, which are independent parameters in the SM. The $\mathrm{SU(3)_C}$ group has 8 gauge fields $G^{\mu a}$, $a = 1, \cdots, 8$ called gluons, the $\mathrm{SU(2)_L}$ group has three gauge

fields $W^{\mu a}$, $a = 1, 2, 3$ and the $\mathrm{U(1)_Y}$ group has one gauge field B^{μ}. The Lagrangian density or Lagrangian of the Standard Model is given in short notation by

$$\begin{aligned}\mathcal{L}_{\mathrm{SM}} = &-\frac{1}{4}B_{\mu\nu}B^{\mu\nu} - \frac{1}{4}W^{I}_{\mu\nu}W^{I\mu\nu} - \frac{1}{4}G^{A}_{\mu\nu}G^{A\mu\nu} \\ &+ \left(D_{\mu}\varphi\right)^{\dagger}\left(D_{\mu}\varphi\right) - V\left(\varphi\right) \\ &+ i\left(\bar{L}\not{D}L + \bar{e}_R\not{D}e_R + \bar{q}\not{D}q + \bar{u}_R\not{D}u_R + \bar{d}_R\not{D}d_R\right) \\ &- \left(\bar{L}\Gamma_e e_R\varphi + \bar{q}\Gamma_u u_R\widetilde{\varphi} + \bar{q}\Gamma_d d_R\varphi + \mathrm{h.c.}\right). \end{aligned} \tag{1.2}$$

The first row holds the kinetic terms of the gauge fields. The second row corresponds to the Higgs sector. It contains the kinetic term of the Higgs field φ, its interaction with the SU(2) gauge fields and the Higgs potential. The Higgs potential, given by

$$V\left(\varphi\right) = -\mu^2\varphi^{\dagger}\varphi + \frac{1}{2}\lambda\left(\varphi^{\dagger}\varphi\right)^2, \tag{1.3}$$

contains the self-interaction terms of the Higgs field. The coefficients μ and λ need to be determined experimentally. The covariant derivative applied to the Higgs field is given by

$$D_{\mu}\varphi = \left(\partial_{\mu} - ig'YB_{\mu} - ig\frac{\tau^I}{2}W^{I}_{\mu}\right)\varphi. \tag{1.4}$$

The third row contains the kinetic terms of the fermions and their interactions with the gauge bosons. The physical fermion fields after spontaneous symmetry braking are grouped according to their transformation properties under $\mathrm{SU(2)}_L$ into doublets and singlets

$$L_i = \begin{pmatrix} e_{Li} \\ \nu_{Li} \end{pmatrix}, \qquad e_{Ri}, \tag{1.5}$$

$$q_i = \begin{pmatrix} u_{Li} \\ d_{Li} \end{pmatrix}, \qquad u_{iR}, d_{Ri}, \tag{1.6}$$

where L and q are the left-handed doublets of leptons and quarks, respectively. e_R, u_R and d_R are the right-handed charged leptons and the up and down type quarks, respectively. The generation index i denotes the three generations of leptons

$$e_1 = e \text{ (electron)}, \qquad e_2 = \mu \text{ (muon)}, \qquad e_3 = \tau \text{ (tau)}, \tag{1.7}$$

and quarks

$$u_1 = u \text{ (up)}, \qquad u_2 = c \text{ (charm)}, \qquad u_3 = t \text{ (top)}, \tag{1.8}$$

$$d_1 = d \text{ (down)}, \qquad d_2 = s \text{ (strange)}, \qquad d_3 = b \text{ (bottom)}. \tag{1.9}$$

A right-handed neutrino does not exist in the Standard Model, since would be a singlet under all three gauge groups. The covariant derivative for the leptons and quarks is given by

$$D_\mu L = \left(\partial_\mu - ig' Y B_\mu - ig\frac{\tau^I}{2} W_\mu^I\right) L \tag{1.10}$$

$$D_\mu q = \left(\partial_\mu - ig' Y B_\mu - ig\frac{\tau^I}{2} W_\mu^I - ig_s\frac{\lambda^A}{2} G_\mu^A\right) q. \tag{1.11}$$

Through the covariant derivative, the fermions get their interaction terms with the gauge fields. The gluon field G_μ^A only couples to the color carrying quarks. The last row of Eq. 1.2 holds the Yukawa interactions between the Higgs field and the fermions. It also provides masses to the fermions through the Higgs mechanism [3, 4, 5]. The Yukawa couplings Γ are matrices in generation space of the fermion and $\widetilde{\varphi} = i\tau^2\varphi^*$.

The Standard Model gauge group of Eq. 1.1 is spontaneously broken via the Higgs mechanism to

$$SU(3)_{\mathrm{C}} \times U(1)_{\mathrm{em}}, \tag{1.12}$$

Name (Symbol)	Electric Charge	Weak Isospin	Mass
Electron neutrino (ν_e)	0	$\frac{1}{2}$	< 1.1 eV[1]
Muon neutrino (ν_μ)	0	$\frac{1}{2}$	< 1.1 eV
Tau neutrino (ν_τ)	0	$\frac{1}{2}$	< 1.1 eV
Electron (e)	-1	$-\frac{1}{2}$	0.511 MeV
Muon (μ)	-1	$-\frac{1}{2}$	105.66 MeV
Tau (τ)	-1	$-\frac{1}{2}$	1776.86 MeV
Up (u)	$+\frac{2}{3}$	$\frac{1}{2}$	2.16 MeV
Charm (c)	$+\frac{2}{3}$	$\frac{1}{2}$	1.27 GeV
Top (t)	$+\frac{2}{3}$	$\frac{1}{2}$	173.29 GeV
Down (d)	$-\frac{1}{3}$	$-\frac{1}{2}$	4.67 MeV
Strange (s)	$-\frac{1}{3}$	$-\frac{1}{2}$	93 MeV
Bottom (b)	$-\frac{1}{3}$	$-\frac{1}{2}$	4.18 GeV

Table 1: The fermions of the Standard Model are divided into leptons and quarks. They are shown here with their electric charge, weak isospin and mass. All masses taken from Ref. [2] unless otherwise stated.

where $\mathrm{U}(1)_{\mathrm{em}}$ is the electromagnetic gauge group. In the Higgs mechanism, an additional $\mathrm{SU}(2)_L$ invariant doublet is introduced, which acquires a non-vanishing vacuum

expectation value. The Higgs doublet is given by

$$\varphi(x) = \begin{pmatrix} \varphi^+ \\ \varphi^0 \end{pmatrix} \quad \rightarrow \quad \varphi(x) = \begin{pmatrix} 0 \\ \frac{1}{\sqrt{2}}[v + h(x)] \end{pmatrix} \tag{1.13}$$

where v is the vacuum expectation value and h is the physical Higgs field. The Higgs-doublet field $\varphi(x)$ is given in its general form on the left side of Eq. 1.13 and in the unitary gauge on the right side. In the unitary gauge, the unphysical degrees of freedom have been eliminated. The vacuum expectation value is the minimum of the Higgs potential in Eq. 1.3. Its value, given by

$$|\varphi| = \frac{v}{\sqrt{2}}, \tag{1.14}$$

$$v = \left(\sqrt{2}G_F\right)^{-\frac{1}{2}} \approx 246.2 \text{ GeV}, \tag{1.15}$$

can not be predicted by the Standard Model, but it can be expressed in terms of the well measured Fermi constant [6]. The mass of the Higgs boson is likewise not predicted by the Standard Model. It was discovered in 2012 by the ATLAS [7] and CMS [8] experiments and subsequently its mass was measured to $m_h = 125.09 \pm 0.24$ GeV [9]. Plugging in the Higgs field in unitary gauge into the Higgs part of the Standard Model Lagrangian in Eq. 1.2, the term involving the covariant derivative of the Higgs field provides both interactions of the Higgs and the gauge bosons and mass terms for the gauge boson. The physical, charged gauge bosons can now be written as

$$W_\mu^\pm = \frac{1}{\sqrt{2}} \left(W_\mu^1 \mp W_\mu^2\right), \tag{1.16}$$

and the neutral gauge bosons are

$$\begin{pmatrix} A_\mu \\ Z_\mu \end{pmatrix} = \begin{pmatrix} \cos\theta_W & -\sin\theta_W \\ \sin\theta_W & \cos\theta_W \end{pmatrix} \begin{pmatrix} B_\mu \\ W_\mu^3 \end{pmatrix}, \tag{1.17}$$

where the sine and cosine of the Weinberg angle θ_W are given by a ratio of the weak and hypercharge coupling constants as

$$\sin\theta_W = \frac{g'}{\sqrt{g^2+g'^2}},$$
$$\cos\theta_W = \frac{g}{\sqrt{g^2+g'^2}} \tag{1.18}$$
$$e = g\sin\theta_W = g'\cos\theta_W = \sqrt{4\pi\alpha}. \tag{1.19}$$

The last equation relates the Weinberg angle to the electric charge and the electromagnetic coupling constant. The charges of the $\mathrm{SU(2)_L} \times \mathrm{U(1)_Y}$ are related to the charge of the $\mathrm{U(1)_{em}}$ group through the Gell-MannNishijima formula

$$Q = I_3 + Y, \tag{1.20}$$

where Q is the generator of the electric charge. The masses of the gauge bosons are then given by

$$m_W = \frac{gv}{2}, \qquad m_Z = \frac{v}{2}\sqrt{g^2+g'^2}, \qquad m_A = 0. \tag{1.21}$$

Table 2 lists the bosons of the Standard Model including their electric charge, spin and mass. The masses of the fermions are generated via Yukawa couplings in the last row of the Standard Model Lagrangian in Eq. 1.2. Diagonalizing the matrices Γ creates mass terms for the fermions. However, this diagonalization involves a rotation of the fermions from their flavor eigenstates to their mass eigenstates. Writing the interaction terms of the fermions with the gauge bosons in terms of the mass eigenstates introduces the matrices from the diagonalization to the interaction terms. In

Name (Symbol)	Electric Charge	Spin	Mass [2]
Photon (A)	0	1	0
W boson ($W^{\pm}$)	± 1	1	80.4 GeV
Z Boson (Z)	0	1	91.2 GeV
Gluon (g)	0	1	0
Higgs (h)	0	0	125.1 GeV

Table 2: The bosons of the Standard Model are the electroweak gauge bosons (γ, W, Z), the gauge boson of the strong interaction (g) and the Higgs boson (h) listed with their electric charge, spin and mass.

most cases they drop out, however, there is one remaining matrix in the interaction term between the W boson and the quarks. This interaction term can be written as

$$\mathcal{L}_{\text{gauge}} \supset \frac{g}{\sqrt{2}} \sum_{i,j=1}^{3} \bar{d}_{Li} \gamma^{\mu} V_{ij} u_{Lj} W_{\mu}^{-} + \text{h.c.}, \tag{1.22}$$

where the unitary matrix V is the Cabibbo-Kobayashi-Maskawa (CKM) matrix [10]. The first consequence of the CKM matrix is that its off-diagonal elements induce flavor changing currents. Flavor refers to the different types of quarks in Eq. 1.9. Further, the CKM matrix is a complex matrix and in general $V_{ij} \neq (V_{ij})^{\dagger}$. Therefore, a process that is proportional to V_{ij} differs from its conjugate process. This leads to CP-violation in the Standard Model.

1.1.1 QCD At Hadron Colliders

In a Quantum Field Theory like the Standard Model, higher order corrections in the perturbation series introduce divergences. To remove these divergences, the theory has to be renormalized. However, renormalization introduces a scale dependence of physical quantities such as masses and couplings. The scale is referred to as the renormalization scale μ_R. In theory, this scale dependence drops out when calculating observables such as cross sections or decay rates. However, in practice this might not always be the case. As an example, the dependency of strong coupling constant $\alpha_s = \frac{g_s^2}{4\pi}$ on the renormalization scale is given by

$$\alpha_s\left(\mu_R^2\right) = \frac{\alpha_s\left(\mu^2\right)}{1 + \frac{(33-2n_f)}{12\pi}\alpha_s\left(\mu^2\right)\ln\frac{\mu_R^2}{\mu^2}}, \tag{1.23}$$

where is the μ_R is the renormalization scale and $\alpha_s\left(\mu^2\right)$ is the coupling constant at a known scale μ. A common choice for μ is the Z boson mass, $\mu = m_Z$, where $\alpha_s\left(m_Z^2\right) \approx 0.1181$. The scale at which the strong interaction becomes non-perturbative, that is $\alpha_s\left(\Lambda_{QCD}^2\right) = 1$, is called the QCD scale and $\Lambda_{QCD} \approx 200$ MeV.

In proton collisions at high energies the proton can not be described simply by its valence quarks $p = (uud)$. Instead, a more detailed description in terms of all partons occurring in a proton has to be used. In the parton description of the proton, the proton consists of a sea of strongly interacting particles. Since the proton's quantum numbers are still given by the valence quarks, the contribution of the quantum numbers of the quarks and gluons in the sea has to vanish. As a consequence, sea-quarks always come in quark-anti-quark pairs. When two protons collide, the hard interaction is then described by the collision of two partons, rather

than the protons themselves. The cross section of a collision process between two protons p into some final state X can then be written as

$$\sigma_{IJ}\left(pp \to X\right) = \sum_{i\in I, j\in J} \int \mathrm{d}x_i \mathrm{d}x_j f_{i/I}\left(x_i, \mu_F^2\right) f_{j/J}\left(x_j, \mu_F^2\right) \sigma\left(ij \to X\right), \tag{1.24}$$

where i, j are the two parton coming from proton I, J, respectively. The parton distribution functions (PDF) $f_{i/I}\left(x_i, \mu_F^2\right)$ and $f_{j/J}\left(x_j, \mu_F^2\right)$ give the probability of finding parton i, j in proton I, J, with momentum fractions x_i and x_j. The momentum fraction x_i is the fraction of the total momentum of the proton carried by parton i. The factorization scale μ_F is the scale that separates the perturbative QCD interaction that are part of the hard interaction cross section from the non-perturbative QCD interactions, such as soft gluon radiation, that are part of the PDF. Figure 1 shows the PDF of the protons for two different energy scales. It gives a measure of the probability of finding a parton with momentum fraction x in the proton. At low proton energies, the valence quarks carry most of the momentum, while the contribution of the gluons and sea quarks becomes more and more important with increasing energy. The hard scattering process of the partons is given by $\sigma\left(ij \to X\right)$. The hard scattering process is calculated perturbatively at the renormalization μ_R as an expansion in α_s as

$$\sigma_{ij}\left(\mu_R\right) = \sigma_{\mathrm{LO}} + \alpha_s\left(\mu_R^2\right)\sigma_{\mathrm{NLO}} + \alpha_s^2\left(\mu_R^2\right)\sigma_{\mathrm{NNLO}} + \mathcal{O}\left(\alpha_s^3\right), \tag{1.25}$$

where σ_{LO} is the Leading-Order (LO), σ_{NLO} is the Next-to-Leading-Order (NLO), and σ_{NNLO} is the Next-to-Next-to-Leading-Order (NNLO) cross section, and so on.

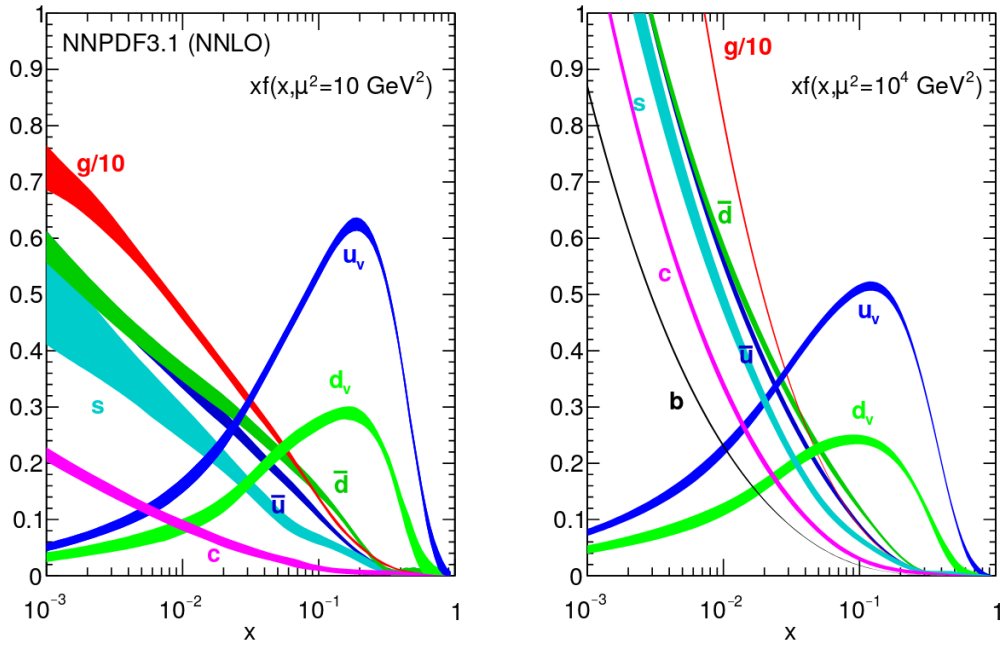

Figure 1: The proton's parton distribution function for different energy scales $\mu_F^2 =$ 10 GeV^2 (left) and $\mu_F^2 = 10^4$ GeV^2 as given by the NNPDF3.1 NNLO PDF sets [11].

1.2 Effective Field Theory

The approach of effective theories has been used in physics for a long time, be it the multi-pole expansion in electrodynamics, planetary motion or the spectrum of the hydrogen atom. All these examples have one thing in common. They connect different sizes, length, or energy scales. In the multi-pole expansion one is not interested in the details of a charge distribution if the region of interest is located at a large distance from that charge distribution. Similarly, for the planetary motion

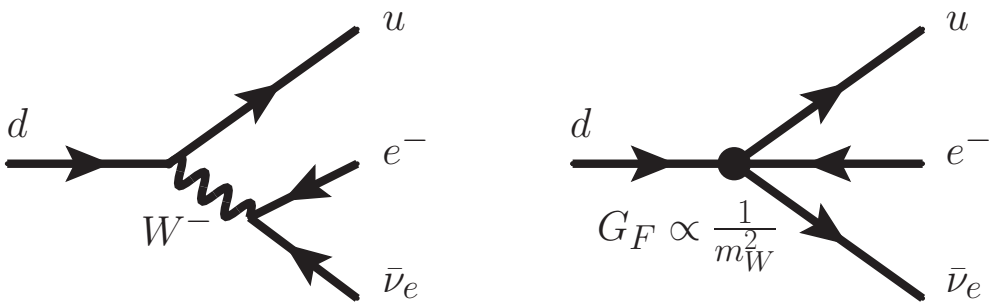

Figure 2: In the Fermi interaction, an up quark in a proton is converted into a down quark, a positron and a neutrino. On the left, the full model shows the decay through the mediation of a W boson. On the right, the effective conversion is shown as a four-fermion point interaction.

the size of the planets is of no interest, and when calculating the spectrum of the hydrogen atom one is usually not concerned about the nucleus consisting of quarks.

In a quantum field theory, large scale differences decouple such that the physics at a high energy scale does not affect the physics at a low scale. More precisely, the large scale effects are suppressed by powers of the ratio of the scales in the problem. This leads to an Effective Field Theory (EFT) that can be parameterized in terms of the symmetries and degrees of freedom of the low scale. One such example is the Fermi theory of beta decay [12], which explains the decay of a neutron through the transition of a down quark within the neutron into an up quark, an electron and an electron anti-neutrino. It is described in the Standard Model (full theory) by the mediation of a W boson. Therefore, the high scale of this problem is the W boson mass. The momentum transfer in the transition through the W boson is however

much lower than the W boson mass. At this low scale, the beta decay can be described by a four-fermion contact interaction. Figure 2 shows the transition of the up quark into a down quark, an electron and an electron anti-neutrino. On the left side, the transition is mediated by a W boson. On the right side, the transition is described by a contact interaction, where the coupling constant G_F is proportional to the inverse of the W boson mass squared. The W boson, the heavy degree at the high scale has been integrated out. Matching the two diagrams one gets an expression of the Fermi constant

$$G_F = \frac{\sqrt{2}g^2}{8m_W^2}, \tag{1.26}$$

where g is the weak coupling constant and m_W is the W boson mass.

In an EFT that is a power expansion in terms of the high energy scale Λ, each order in the expansion is suppressed by more powers of that scale and therefore contributes less and less to the low energy phenomena. This expansion contains in principle to an infinite number of terms. However, in practice only a few terms need to be considered and the number of terms depends on the required accuracy of the problem. In the example of the beta decay, the Fermi contact interaction is only the first term in such a series. The interaction is formally calculated by integrating out the W boson, that is by performing the path integral over those degrees of freedom. In practice, integrating out is usually done using the Feynman diagram methods instead of path integrals. In the Feynman diagram method, an interaction is calculated in both, the full and the effective theory and the coupling terms are then matched onto each other. This approach is also known as the top-down approach in which the full theory is known and an effective theory is constructed by integrating out the heavy degrees.

In the bottom-up approach, a known theory is assumed to be an effective theory of some unknown theory. The most prominent example of the is the Standard Model Effective Theory (SMEFT). In the SMEFT, the Standard Model is treated as an EFT of an unknown theory Beyond the Standard Model (BSM) at a higher scale, where the scale of the Standard Model is characterized by the electroweak scale given by the vacuum expectation value v. Even though the BSM theory is not know, its effects can still be parameterized by higher dimension operators in the power expansion. Therefore, the effective SM Lagrangian can be written as an expansion

$$\mathcal{L}_{\text{eff}} = \mathcal{L}_{\text{SM}}^{(4)} + \frac{1}{\Lambda}\sum_i c_i^{(5)}\mathcal{O}_i^{(5)} + \frac{1}{\Lambda^2}\sum_i c_i^{(6)}\mathcal{O}_i^{(6)} + \mathcal{O}\left(\frac{1}{\Lambda^3}\right), \tag{1.27}$$

with expansion parameter Λ, the energy scale of the BSM physics. The c_i are the Wilson coefficients [13] or EFT coefficients of the operators $\mathcal{O}_i$ which contain all the degrees of freedom at the scale Λ. The scale Λ is the cut-off scale at which the power expansion breaks down and the BSM theory can not be explained described by the effective theory anymore. At this scale the heavy degrees of freedom can be produced on-shell and need to be taken into account. The number in parentheses is the mass or energy dimension of the respective operators. The operators consist of SM fields and respect all the SM symmetries. At dimension 5 there only exists one possible operator, called the Weinberg operator [14] given by

$$c_{i,j}^{(5)}\mathcal{O}_{i,j}^{(5)} = c_{i,j}^{(5)}\left(\widetilde{\varphi}^\dagger L_i\right)^T C\left(\widetilde{\varphi}^\dagger L_j\right), \tag{1.28}$$

where C is the charge conjugation operator, $\widetilde{\varphi} = i\tau^2\varphi^*$, where φ is the Higgs doublet and τ^2 is the second Pauli matrix. i, j are the generation indices of the leptons. Since there are two charged leptons in the Weinberg operator, it violates lepton number

by $\Delta L = 2$. After spontaneous symmetry breaking and in the unitary gauge the Weinberg operator becomes

$$\frac{c_{i,j}^{(5)}}{\Lambda^2}\mathcal{O}_{i,j}^{(5)} \propto \frac{c_{i,j}^{(5)}}{\Lambda^2} v^2 \bar{\nu_{Li}^c} \nu_{Lj}, \tag{1.29}$$

giving a Majorana mass to the neutrinos through the mass matrix

$$M_{i,j} \propto c_{i,j}^{(5)} \frac{v^2}{\Lambda^2}. \tag{1.30}$$

For Wilson coefficients of order one and neutrino masses of less than about 1 eV this implies a mass scale of $\mathcal{O}\left(10^{14}\right)$, which is well out of reach for the LHC.

At dimension 6, there is a significant amount of operators the can be constructed from the Standard Model degrees of freedom [15]. However, many of the possible operators are redundant and can be removed from the basis by using the equations of motion of the fields or Fierz identities. A complete, non-redundant basis has been found [16] which consists of 59 independent operators, not counting flavor indices and hermitian conjugates.

To study the interactions of top quarks only a subset of these operators, involving at least one top quark, is needed. Ref. [17] gives a detailed overview of the SMEFT top quark sector, listing all dimension-six operators that couple to at least one top quark. However, not all of these operators contribute to the processes studied in this analysis. In particular, there are six contributing dimension-six operators. Four of

these contribute directly to the Wtb vertex which governs both the single top quark production and decay. The general form of these operators is given by

$$\begin{aligned}
\mathcal{O}_{\varphi q}^{3(ij)} &= \left(\varphi^\dagger i \overleftrightarrow{D}_\mu^I \varphi\right) \left(\bar{q}_i \, \gamma^\mu \tau^I q_j\right), \\
\mathcal{O}_{\varphi ud}^{(ij)} &= \left(\widetilde{\varphi}^\dagger i D_\mu \varphi\right) \left(\bar{u}_i \, \gamma^\mu d_j\right), \\
\mathcal{O}_{uW}^{(ij)} &= \left(\bar{q}_i \, \sigma^{\mu\nu} \tau^I u_j\right) \tilde{\varphi} \, W_{\mu\nu}^I, \\
\mathcal{O}_{dW}^{(ij)} &= \left(\bar{q}_i \, \sigma^{\mu\nu} \tau^I d_j\right) \varphi \, W_{\mu\nu}^I.
\end{aligned} \tag{1.31}$$

The operators that contribute specifically to top quark physics are given by Eq. 1.31 by setting $i = 3$, $j = 3$ to select the operators that involve third generation quarks. Then, writing Eq. 1.31 in the physical basis, each of these operators contribute to the Wtb Lagrangian as by

$$\begin{aligned}
\mathcal{O}_{\varphi q}^{3} &\supset -\frac{gv^2}{\sqrt{2}} \bar{b}_L \gamma^\mu t_L W_\mu^-, \\
\mathcal{O}_{\varphi tb} &\supset \left[\frac{gv^2}{2\sqrt{2}} \bar{b}_R \gamma^\mu t_R W_\mu^-\right]^\dagger, \\
\mathcal{O}_{tW} &\supset 2v \bar{b}_L i\sigma^{\mu\nu} q_\nu t_R W_\mu^-, \\
\mathcal{O}_{bW} &\supset \left[2v \bar{b}_R i\sigma^{\mu\nu} q_\nu t_L W_\mu^-\right]^\dagger.
\end{aligned} \tag{1.32}$$

Note, that the flavor indices have been dropped. Each of the operators contributes to the Wtb vertex with a different Lorentz structure. $\mathcal{O}_{\varphi Q}^{(3)}$ has a Lorentz structure similar to the SM in Eq. 1.22 and therefore modifies the left-handed vector coupling present in the SM. $\mathcal{O}_{\varphi tb}$ induces a right-handed vector coupling and $\mathcal{O}_{bW}$ and $\mathcal{O}_{tW}$ contribute as left-handed and right-handed tensor couplings, respectively. Furthermore, $\mathcal{O}_{\varphi tb}$, $\mathcal{O}_{bW}$, and $\mathcal{O}_{tW}$ are non-Hermitian operators and therefore their Wilson coefficients are complex. A non-vanishing imaginary part can then lead to CP violation.

It is customary to write the general for of the Lagrangian describing the Wtb interaction in terms of the so called anomalous couplings as [18, 19]

$$\mathcal{L}_{Wtb} = -\frac{g}{\sqrt{2}}\bar{b}\,\gamma^{\mu}\left(V_L P_L + V_R P_R\right) t\, W_{\mu}^{-} - \frac{g}{\sqrt{2}}\bar{b}\,\frac{i\sigma^{\mu\nu}q_{\nu}}{m_W}\left(g_L P_L + g_R P_R\right) t\, W_{\mu}^{-} + \text{h.c.}, \tag{1.33}$$

where $P_{L/R}$ is the left- and right handed projection operator, m_W is the mass of the W and g is the weak couplings constant. The anomalous couplings V_L, V_R, g_L, and g_R are then each proportional to one dimension-six Wilson coefficient

$$\begin{aligned} V_L &= V_{tb} + \frac{v^2}{\Lambda^2}c_{\varphi q}^{(3)}, & g_L &= -\sqrt{2}\frac{v^2}{\Lambda^2}c_{bW}^{*}, \\ V_R &= \frac{1}{2}\frac{v^2}{\Lambda^2}c_{\varphi tb}^{*}, & g_R &= -\sqrt{2}\frac{v^2}{\Lambda^2}c_{tW}. \end{aligned} \tag{1.34}$$

There is a relative minus sign between the definitions in Ref. [18, 19] and Eq. 1.34 in the coefficients g_L and g_R. This sign difference arises from different conventions for the covariant derivative. In Eq. 1.32 the covariant derivative is defined with a minus sign as shown in Eq. 1.4 where in Ref. [18, 19] the sign of the B_μ and W_μ terms is a plus sign. This sign difference can be absorbed by a field redefinition

$$\begin{aligned} B_\mu &\to -B_\mu, \\ W_\mu &\to -W_\mu, \end{aligned} \tag{1.35}$$

leaving the operators $\mathcal{O}_{\varphi q}^{3}$ and $\mathcal{O}_{\varphi tb}$ unchanged. However, the operators $\mathcal{O}_{tW}$ and $\mathcal{O}_{bW}$ contain an explicit $W_{\mu\nu}^{I}$ in their definition. Therefore, Eq. 1.35 introduces a relative minus sign for these two operators.

The remaining two operators contributing to the top quark physics studied in this analysis are two four-quark operators. These operators are given by, assuming minimal flavor violation (MFV),

$$\begin{aligned}\mathcal{O}_{qq}^{1(ijkl)} &= \left(\bar{q}_i \gamma_\mu q_j\right)\left(\bar{q}_k \gamma^\mu q_l\right), \\ \mathcal{O}_{qq}^{3(ijkl)} &= \left(\bar{q}_i \gamma_\mu \tau^a q_j\right)\left(\bar{q}_k \gamma^\mu \tau^a q_l\right).\end{aligned} \tag{1.36}$$

Minimal flavor violation (MFV) assumes a unit CKM matrix and only non-vanishing Yukawa couplings for the top and bottom quarks so that $\Gamma_u = \mathrm{diag}\,(0, 0, y_t)$ and $\Gamma_d = \mathrm{diag}\,(0, 0, y_b)$ and the third generation of quarks does not mix with the first two generations. The four-quark operators can be rewritten as

$$\begin{aligned}c_{Qq}^{3,1} &= c_{qq}^{3(ii33)} + \frac{1}{6}\left(c_{qq}^{1(i33i)} - c_{qq}^{3(i33i)}\right) \\ c_{Qq}^{3,8} &= c_{qq}^{1(i33i)} - c_{qq}^{3(i33i)},\end{aligned} \tag{1.37}$$

where the first one is an SU(2) triplet and color singlet and the second one is an SU(2) triplet and color octet. From these two, only the color singlet interferes with the Standard Model amplitude, while the color octet contributes at $\mathcal{O}\left(\Lambda^{-4}\right)$. Therefore, it is assumed that the color singlet operator dominates and this analysis restricts the study to the operator $c_{Qq}^{3,1}$.

1.3 The Top Quark

The existence of the top quark was first proposed by Kobayashi and Maskawa in 1973 [10] to explain the CP violation in the decay of K mesons. 22 years later, in 1995, the top quark was discovered by the CDF [20] and DØ [21] experiments at the Tevatron collider at Fermilab, the only collider with a sufficiently high center-of-mass energy to produce top quarks. With a pole mass of $m_t = 173.29 \pm 0.95$ GeV it is the heaviest particle in the Standard Model. This mass corresponds to the current LHC combination shown in Figure 3. It is a combination of top mass measurements from the ATLAS and CMS experiments for different channels at different center-of-mass energies. Since the discovery and especially since the start-up of the LHC, top quark interactions have been an active field of research. Having a a very short lifetime of approximately 3×10^{-25} s [23], the top quark does not hadronize before it decays, since the hadronization time scale is much larger, $\mathcal{O}\,(10^{-23}s)$. This makes the top quark the only quark in the Standard Model that can be studied almost as a free quark. Due to the short lifetime, the decay products of the top quark also retain the information of the top quarks polarization. This makes the study of single top quarks especially interesting, since the top quarks are produced predominantly left-handed through electroweak interaction. Precise measurements of these interactions may then reveal new forms of interactions. The following sections give a review of the different production mechanism of top quarks at the LHC are discussed. Further, the top quark decay and related observables are discussed.

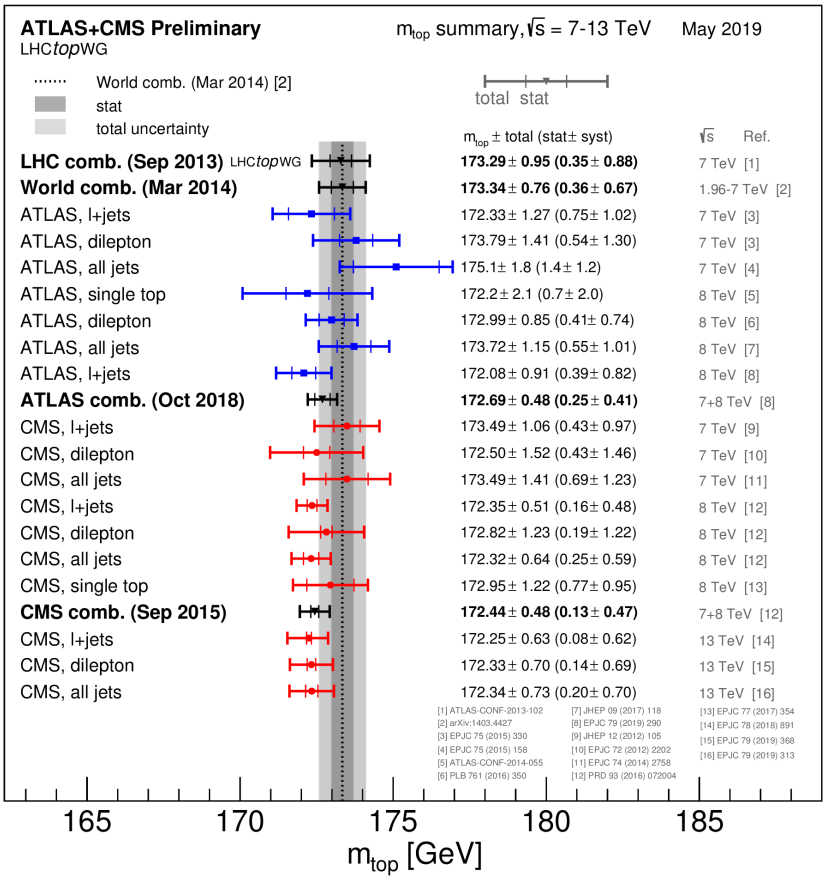

Figure 3: Comparison of ATLAS and CMS top mass measurements taken from Ref. [22].

1.3.1 Top Quark Production

At the LHC, the production of top quarks are produced through two different mechanisms. Top quark pairs are predominantly produced through the strong interaction and single top quarks are produced through electroweak processes. The single

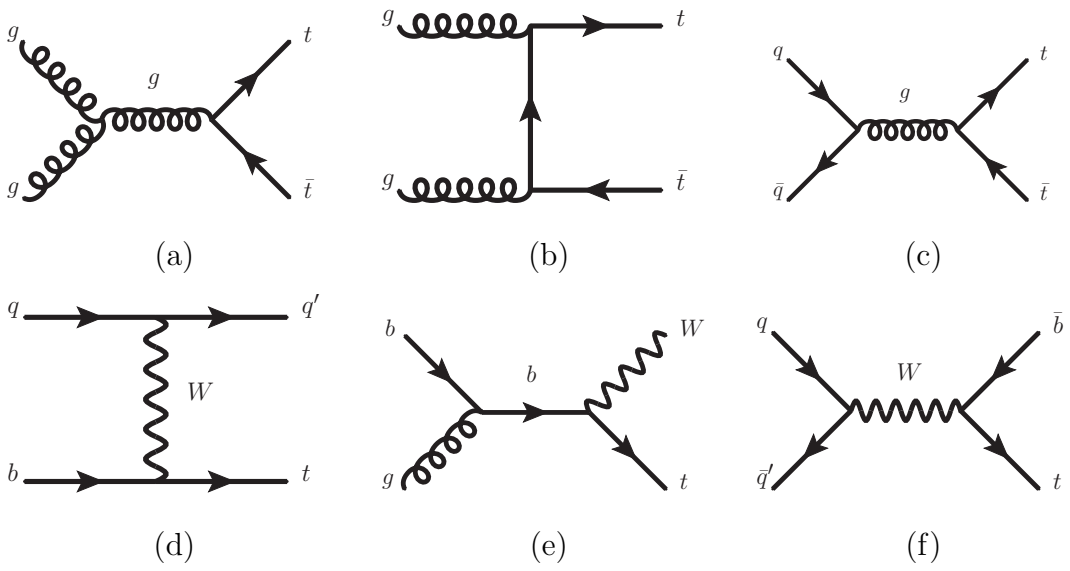

Figure 4: Leading order Feynman diagrams of top pair production through gluon fusion (a), (b) and quark-anti-quark annihilation (c). Single top quark production through the t-channel process (d), s-channel process (e) and production in association with a W boson (f).

top productions is again divided into three different types. The top quark can be produced in a t-channel W boson scattering process, an s-channel Drell-Yan process and in association with a W boson. All processes are shown in Figure 4. The top row shows the top pair production processes and the bottom row shows the single top production processes. Top pairs can be produced either through gluon fusion (a), (b) or quark-anti-quark annihilation (c). Diagram (c) exists in principle also with an intermediary photon or Z boson. However, their contribution to the cross section is very small compared to the QCD process involving gluons. The single top

production processes are ranked according to the size of the cross section, t-channel (d), associated production with a W boson (e), and s-channel (f). To illustrate the relative size of the cross sections, Tables 3–6 shows the cross sections of all processes for different center-of-mass energy. Both theoretical predictions[1] and experimental results by ATLAS and CMS are shown. Both top pair production and t-channel single top production were measured at ATLAS and CMS at $\sqrt{s}$ = 7,8,13 TeV. Evidence was found for the single top production in association with a W boson at $\sqrt{s}$ = 7 TeV and it was subsequently measured at $\sqrt{s}$ = 8, 13 TeV. For the s-channel single top production, evidence was first found at $\sqrt{s}$ = 8 TeV at both ATLAS and CMS. This analysis focuses on the t-channel single top quark production, which is the dominating single top process at the LHC. In the t-channel process, a bottom quark and a light quark or anti-quark interact through the exchange of a t-channel W boson, to produce a top quark and a light quark or anti-quark. The t-channel process is shown in Figure 5 in the 5 flavor-scheme (a) corresponding to the $2 \to 2$ process $pp \to tj$ and in the 4 flavor-scheme (b) corresponding to the $2 \to 3$ process $pp \to t\bar{b}j$. In the 5 flavor scheme, the mass of the bottom quark is assumed to be negligible compared the the energy scale of the process. The bottom quark is therefore taken to be massless and there is a non-zero probability of finding a bottom quark in the proton. The light quark q in Figure 5 (a) can be either of $q = u, c, \bar{d}, \bar{s}$ for top quark production and $q = d, s, \bar{u}, \bar{c}$ for top anti-quark production. Since the abundance of u valence quarks is twice the abundance of down valence quarks, the top quark cross section is approximately a factor of two larger than the top anti-quark production. In the 4 flavor scheme, the bottom quark mass is taken to be non-zero.

[1] Theory values calculated with a top quark mass of m_t = 172.5 GeV using Top++ [24] for $t\bar{t}$ cross section and the HatHor v2.1 tool [25] for the single top cross sections.

Experiment/Theory[1]	$\sqrt{s}$ (TeV)	σ (pb)	
Theory	$t\bar{t}$	7	$177.31^{+11.48}_{-11.57}$
Theory	$t\bar{t}$	8	$252.89^{+15.31}_{-16.27}$
Theory	$t\bar{t}$	13	$831.76^{+46.45}_{-50.85}$
ATLAS	$t\bar{t}$	7	182.9 ± 7.15 [26]
ATLAS	$t\bar{t}$	8	242.9 ± 8.76 [26]
ATLAS	$t\bar{t}$	13	818 ± 36 [27]
CMS	$t\bar{t}$	7	174.5 ± 6.1 [28]
CMS	$t\bar{t}$	8	245.6 ± 9.0 [28]
CMS	$t\bar{t}$	13	803 ± 32 [29]

Table 3: Predicted and measured values of the top quark pair production cross sections.

In this case, the bottom quark comes from a gluon splitting into a $b\bar{b}$ pair, as seen in (b) of Figure 5. A similar diagram in the 4 flavor-scheme where the gluon splits into a $t\bar{t}$ pair also contributes, although with a much smaller cross section. In principle, there is also a remaining $\bar{b}$ quark in the 5 flavor scheme. However, the $\bar{b}$ quark is not part of the hard process. Instead, the $\bar{b}$ is part of the initial state radiation process and is taken care of by the PDF set of the proton. This also means, that the $\bar{b}$ has a small transverse momentum and goes undetected along the direction of the beam pipe.

The t-channel single top production proceeds through the Wtb vertex and there-

Experiment/Theory[1]	Process	$\sqrt{s}$ (TeV)	σ (pb)
Theory	t-chan	7	$63.89^{+2.91}_{-2.52}$
Theory	t-chan	8	$84.69^{+3.44}_{-1.91}$
Theory	t-chan	13	$216.99^{+9.04}_{-7.71}$
ATLAS	t-chan	7	68 ± 8 [30]
ATLAS	t-chan	8	89.6 ± 6.7 [31]
ATLAS	t-chan	13	247 ± 46 [32]
CMS	t-chan	7	67.2 ± 6.1 [33]
CMS	t-chan	8	83.6 ± 7.7 [34]
CMS	t-chan	13	219 ± 36 [35]

Table 4: Predicted and measured values of the combined top quark and anti-quark t-channel cross section.

fore the top quarks in this production mechanism are highly polarized. This is due to the $V-A$ structure of the Wtb interaction in Eq. 1.22, which restricts couplings of the W boson to left-handed top quarks. The polarization of the top quark in t-channel production is usually defined through the direction of the spectator quark momentum $\vec{p}_s$, that is the $\hat{z}$-direction of the polarization is

$$\hat{z} = \frac{\vec{p}_s}{|\vec{p}_s|}. \tag{1.38}$$

When referring to the top quark polarization, the polarization in the $\hat{z}$-direction $P = P_z$ is meant, unless otherwise stated. The Standard Model NNLO prediction of

Experiment/Theory[1]	Process	$\sqrt{s}$ (TeV)	σ (pb)
Theory	Wt	8	$22.37^{+1.52}_{-1.52}$
Theory	Wt	13	$71.7^{+3.85}_{-3.85}$
ATLAS	Wt	8	23.0 ± 3.8 [36]
ATLAS	Wt	13	94 ± 27 [37]
CMS	Wt	8	23.4 ± 5.4 [38]
CMS	Wt	13	63.1 ± 6.97 [39]

Table 5: Predicted and measured values of the combined top quark and anti-quark Wt cross section.

Experiment/Theory[1]	Process	$\sqrt{s}$ (TeV)	σ (pb)
Theory	s-chan	8	$5.24^{+0.22}_{-0.20}$
ATLAS	s-chan	8	4.8 ± 1.7 [40]
CMS	s-chan	8	13.4 ± 7.3 [41]

Table 6: Predicted s-channel cross section and results of searches for s-channel single top production by ATLAS and CMS.

the polarization is $P \approx 0.91$ [42]. Experimentally, the top quark polarization can be accessed by measuring the angular distribution of the analyzer in a top quark decay,

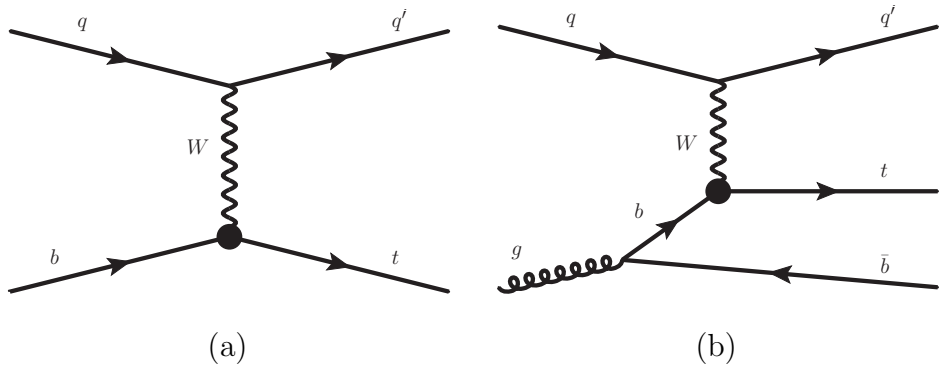

Figure 5: Single top quark production in the 5 flavor scheme (a) and in the 4 flavor scheme (b). The black dot represents the Wtb vertex with possible contributions from EFT operators, see Section 1.2.

e.g. the lepton coming from the W boson decay. Then, the top quark polarization can be determined from

$$\frac{1}{\Gamma}\frac{d\Gamma}{d\cos\theta_X} = \frac{1}{2}\left(1 + P\alpha_X \cos\theta_X\right), \tag{1.39}$$

where θ_X is the angle between the momentum of the decay product $X = \ell^+$, ν_ℓ, q, $\bar{q}'$, W^+, b in the top quark rest frame and the top spin direction. Since the top quark is predominantly left-handed, its spin points in the opposite direction of its momentum, which corresponds to the direction of the spectator quark momentum, or the $\hat{z}$-direction. Here, q and q' denote up and down type quarks from the W boson decay. α_X is the spin analysing power of the decay product X, where $-1 \leq \alpha_X \leq 1$, e.g. $\alpha_{\ell^+} \approx \alpha_{\bar{q}'} \approx 1$ and $\alpha_q \approx -0.32$ at leading order. The product of the spin analysing power and the polarization was measured at ATLAS at a center-of-mass energy of $\sqrt{s} = 8$ TeV in the lepton channel to be $\alpha_l P = 0.97 \pm 0.12$ [43].

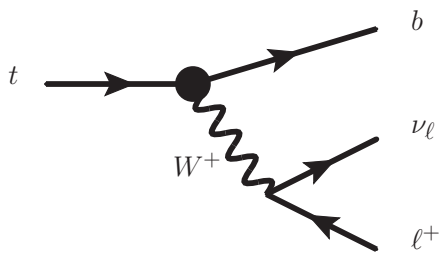

Figure 6: Semi-leptonic decay of a top quark into a bottom quark and a W boson, where the W boson subsequently decays into a charged lepton and a neutrino. The black dot represents the Wtb vertex with possible contributions from EFT operators, see Section 1.2.

1.3.2 Top Quark Decay

The decay of the top quark proceeds through the electroweak interaction vertex given in Eq. 1.22 and shown in Figure 6 including also the leptonic decay of the W boson. Since the CKM matrix element $V_{tb} \approx 1 \gg V_{ts}, V_{td}$, top quarks decay predominantly into a W boson and a bottom quark.

1.3.2.1 W Boson Helicity The W boson coming from the decay of a top quark is produced on-shell. An on-shell W has three distinct polarization states, two transverse and one longitudinal. These polarization states can be measured in terms of the helicity fractions F_0, F_L and F_R, where F_0 is the fraction of longitudinal and F_L and F_R are the fractions of left- and right-handed W bosons, respectively. In the W boson rest frame, a differential cross section can be written down in terms of the W

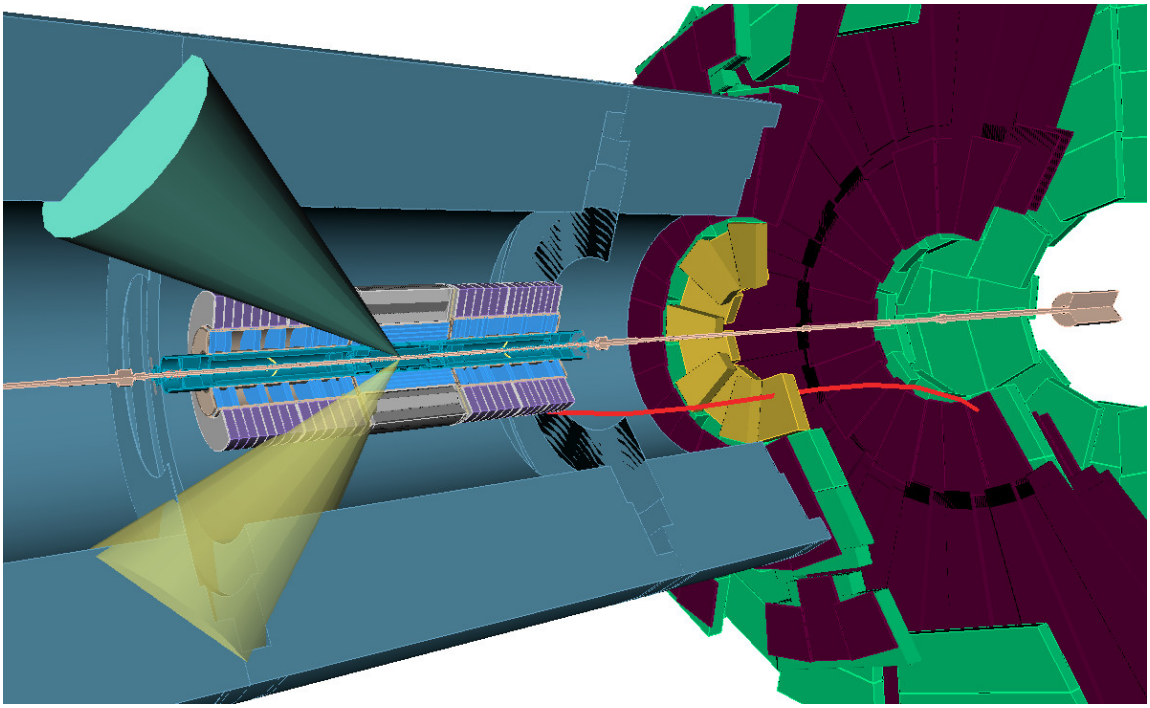

Figure 7: Event display of a t-channel single top event. The top quark decays into a b-quark and a W boson. The b-quark initializes a b-jet which is shown as a blue cone. The W boson then decays into a muon, shown as a curved red line and a neutrino (not shown). The yellow cone represents the jet initiated by the spectator quark from the single top quark production. Also shown are parts of the ATLAS detector, discussed in Section 1.4.2.

helicity fractions as [44]

$$\frac{1}{\sigma}\frac{d\sigma}{d\cos\theta^*} = \frac{3}{4}\left(1-\cos^2\theta^*\right)F_0 + \frac{3}{8}\left(1-\cos\theta^*\right)^2 F_L + \frac{3}{8}\left(1+\cos\theta^*\right)^2 F_R. \qquad (1.40)$$

Here, θ^* is the angle between the reversed direction of b-quark momentum and the lepton momentum in the W rest frame. In the Standard Model the W helicity fractions are given at leading order for $m_b = 0$ by [45, 46]

$$F_0 = \frac{|V_{tb}|^2}{|V_{tb}|^2 + 2x_W^2 |V_{tb}|^2}, \tag{1.41}$$

$$F_L = \frac{2x_W^2 |V_{tb}|^2}{|V_{tb}|^2 + 2x_W^2 |V_{tb}|^2}, \tag{1.42}$$

$$F_R = 0. \tag{1.43}$$

For $V_{tb} \approx 1$ and $x_W = \frac{m_W}{m_t}$ this gives

$$F_0 = 0.7, \tag{1.44}$$

$$F_L = 0.3, \tag{1.45}$$

$$F_R = 0. \tag{1.46}$$

1.3.2.2 Top Quark Decay Distributions The previous section discussed the W helicity fraction which are described through the angular distribution of the b-quark coming from the top decay and the charged lepton coming from the W decay. It is possible to describe the decay of the top quark in a more general form. Eq. 1.40 of the W helicity fractions parameterizes the decay through a single angle between b-quark and lepton. In a similar way, the semi-leptonic decay of the top quark as depicted in Figure 6, can be written down in a more generalized, triple differential decay rate as [47, 48]

$$\frac{1}{N} \frac{d^3 N}{d(\cos\theta)\, d\Omega^*} = \sum_{k=0}^{2} \sum_{l=0}^{2} \sum_{m=-l}^{l} a_{k,l,m} M_{k,l}^{m} (\theta, \theta^*, \phi^*), \tag{1.47}$$

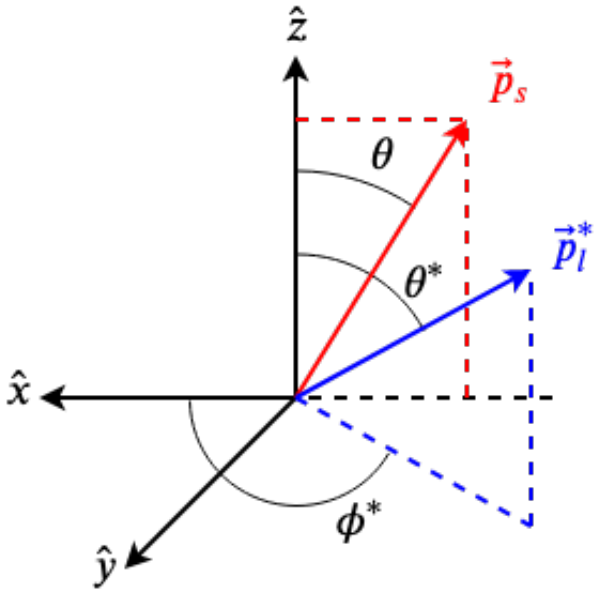

Figure 8: Coordinate system used in the single top decay distribution measurement. θ measures the angle between the direction of the W boson, given by $\hat{z}$, and the spectator quark momentum $\vec{p}_s$. The angle θ^* and ϕ^* measure the polar and azimuthal angle of the charged lepton momentum $\vec{p}_l^{\,*}$ and the W boson. See text for more details.

where the M-functions are given by a product of spherical harmonics

$$M_{k,l}^{m}\left(\theta,\theta^{*},\phi^{*}\right)=\sqrt{2\pi}Y_{k}^{m}\left(\theta,0\right)Y_{l}^{m}\left(\theta^{*},\phi^{*}\right), \tag{1.48}$$

and $a_{k,l,m}$ are the angular expansion coefficients. There are 9 non-zero angular coefficients $a_{k,l,m}$ plus one constant normalization factor. The angles of the M-functions are defined through the right-handed coordinate system shown in Figure 8. θ is the

angle between the direction of the W boson indicated by $\hat{z} = \vec{q}/|\vec{q}|$ and the spectator quark $\vec{p}_s$ in the top quark rest frame. The spectator quark is the light quark q' that is produced along the top quark in on the left side of Figure 5. These two vectors, $\hat{z}$ and $\vec{p}_s$ define the $\hat{x} - \hat{z}$ plane of the coordinate system and the remaining $\hat{y}$ axis is perpendicular to that. The angles θ^* and ϕ^* are the azimuthal and polar angle between the direction of the W momentum and the momentum of the charged lepton $\vec{p}_l^*$, respectively.

The additional information from the angles θ and ϕ^* allows to not just measure the helicity of the W boson, but instead the four decay amplitudes A_{λ_W,λ_b} given through the helicities of both the W boson λ_W and the b-quark λ_b. These decay amplitudes correspond to a top quark decaying into

- a longitudinal W plus a left-handed b-quark $|W_0 b_L\rangle$, given by $A_{0,-\frac{1}{2}}$,
- a longitudinal W plus a right-handed b-quark $|W_0 b_R\rangle$, given by $A_{0,\frac{1}{2}}$,
- a left-handed W plus a left-handed b-quark $|W_L b_L\rangle$, given by $A_{-1,-\frac{1}{2}}$,
- a right-handed W plus a right-handed b-quark $|W_R b_R\rangle$, given by $A_{1,\frac{1}{2}}$.

From these decay amplitudes, generalized helicity fractions and phases can be constructed. There are three fractions given by

$$f_1 = \frac{\left|A_{1,\frac{1}{2}}\right|^2 + \left|A_{-1,-\frac{1}{2}}\right|^2}{\left|A_{1,\frac{1}{2}}\right|^2 + \left|A_{-1,-\frac{1}{2}}\right|^2 + \left|A_{0,\frac{1}{2}}\right|^2 + \left|A_{0,-\frac{1}{2}}\right|^2}, \tag{1.49}$$

$$f_1^+ = \frac{\left|A_{1,\frac{1}{2}}\right|^2}{\left|A_{1,\frac{1}{2}}\right|^2 + \left|A_{-1,-\frac{1}{2}}\right|^2}, \tag{1.50}$$

$$f_0^+ = \frac{\left|A_{0,\frac{1}{2}}\right|^2}{\left|A_{0,\frac{1}{2}}\right|^2 + \left|A_{0,-\frac{1}{2}}\right|^2}, \tag{1.51}$$

where f_1 is the fraction decays containing transverse W bosons, f_1^+ is the fraction of events containing right-handed W bosons and f_0^+ is the fraction of events that contain longitudinal W bosons together with right-handed b-quarks. The two relative phases are

$$\delta_+ = \arg\left(A_{1,\frac{1}{2}} A^*_{0,\frac{1}{2}}\right), \tag{1.52}$$

$$\delta_- = \arg\left(A_{-1,-\frac{1}{2}} A^*_{0,-\frac{1}{2}}\right), \tag{1.53}$$

where δ_+ is the relative phases between the amplitudes of top quarks decaying into right-handed W bosons and longitudinal W bosons, together with a right-handed b-quark. The phase δ_- is the phase between the amplitudes of top quarks decaying into left-handed W bosons and longitudinal W bosons, together with a left-handed b-quark. The generalized fractions f_1 and f_1^+ are related to the W helicity fractions in Eq. 1.43. The W helicity fraction

$$\begin{aligned} F_L &= f_1\left(1 - f_1^+\right), \\ F_R &= f_1 f_1^+, \\ F_0 &= 1 - f_1, \end{aligned} \tag{1.54}$$

such that $f_1 = F_L + F_R$. With these fractions and phases, the angular coefficients $a_{k,l,m}$ can be written in terms of the helicity amplitudes as

$$\begin{aligned} a_{0,0,0} &= \frac{1}{\sqrt{8\pi}}, \\ a_{0,1,0} &= \sqrt{\frac{3}{8\pi}} f_1 \left(f_1^+ - \frac{1}{2}\right), \\ a_{0,2,0} &= \frac{1}{\sqrt{40\pi}} \left(\frac{3}{2} f_1 - 1\right), \end{aligned} \tag{1.55}$$

$$
\begin{aligned}
a_{1,0,0} &= +P\frac{1}{\sqrt{24\pi}}\left(f_1\left(2f_1^+-1\right)+\left(1-f_1\right)\left(1-2f_0^+\right)\right),\\
a_{1,1,0} &= +P\frac{1}{\sqrt{32\pi}}f_1,\\
a_{1,2,0} &= +P\frac{1}{\sqrt{480\pi}}\left(f_1\left(2f_1^+-1\right)-2\left(1-f_1\right)\left(1-2f_0^+\right)\right),\\
a_{1,1,1} &= a^*_{1,1,-1}\\
&= -P\frac{1}{\sqrt{16\pi}}\sqrt{f_1\left(1-f_1\right)}\left\{\sqrt{f_1^+f_0^+}e^{i\delta_+}+\sqrt{\left(1-f_1^+\right)\left(1-f_0^+\right)}e^{-i\delta_-}\right\},\\
a_{1,2,1} &= a^*_{1,2,-1}\\
&= -P\frac{1}{\sqrt{80\pi}}\sqrt{f_1\left(1-f_1\right)}\left\{\sqrt{f_1^+f_0^+}e^{i\delta_+}-\sqrt{\left(1-f_1^+\right)\left(1-f_0^+\right)}e^{-i\delta_-}\right\}. \quad (1.56)
\end{aligned}
$$

Expressions of the generalized helicity fractions and phases in terms of the EFT coefficients can be found in Appendix B.

1.4 The LHC And The ATLAS Experiment

1.4.1 The Large Hadron Collider

The Large Hadron Collider is the largest, most energetic particle collider build to date. The LHC concept started in 1984 and after 25 years of planning and construction the first proton - proton collisions occurred on the 20. November 2009 at a beam energy of 450 GeV. It then exceeded the previous record of 0.98 TeV per beam held by Fermi National Accelerator Laboratorys Tevatron collider 10 days later with an energy of 1.18 TeV per beam. Subsequently, the collision energy was increased to $\sqrt{s} = 7$ TeV during the first part and $\sqrt{s} = 8$ TeV during the second part of Run-1 (2010 - 2013). In its latest configuration during Run-2 (2015 - 2018)

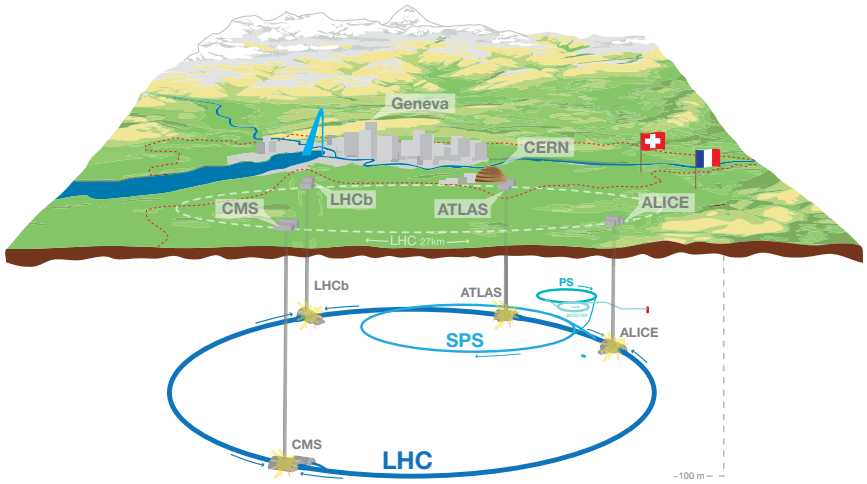

Figure 9: Schematic overview of the LHC located near Geneva, Switzerland, approximately 100 m underground. The four main experiments, ATLAS, CMS, LHCb and ALICE, and their location at the LHC are also shown. Graphic taken from [49].

the LHC had a center-of-mass energy of $\sqrt{s} = 13$ TeV with an expected increase to its maximum design center-of-mass energy of $\sqrt{s} = 14$ TeV during Run-3 stating in 2021. The LHC measures approximately 27 km in circumference and it is located 100 m underground the Swiss - French border near Geneva, as seen in Figure 9. The four main experiments at the LHC are the ATLAS (A Large Toroidal LHC ApparatuS)

experiment at Point 1 [50], CMS (Compact Muon Solenoid) at Point 5 [51], LHCb (LHC beauty) at Point 8 [52], and ALICE (A Large Ion Collider Experiment) at Point 2 [53]. Both ATLAS and CMS are general purpose experiments, LHCb is a flavor physics experiment specialized in measuring properties of b flavored hadrons and CP violation. ALICE is a dedicated heavy ion detector, designed to measure the physics of strongly interacting matter.

The LHC is a collider with the ability to run either proton - proton (pp), heavy ion (HI) lead - lead collisions, or a combination of proton - lead. For the protons or heavy ions to reach their final collision energy, they pass through several pre-acceleration steps. Initially, the protons are separated from hydrogen atoms, then accelerated in the linear accelerator LINAC-2 to an energy of 50 MeV. Next, the Proton Synchrotron Booster (PSB) accelerates the protons to an energy of 1.4 GeV. After that, the protons enter the Proton Synchrotron (PS) where they reach an energy of 25 GeV. Then, they are transferred to the Super Proton Synchrotron (SPS), where they are further accelerated to an energy of 450 GeV. Finally, they are injected into the LHC where they reach their final energy of 6.5 TeV. Figure 10 schematically shows the steps of this acceleration process. Once the protons have reached their collision energy in the LHC, they circulate in two counter-rotating beams. The beams cross at four points along the ring at the sites of the four experiments. To keep the beams on their circular track, superconducting dipole magnets cooled to a temperature of 1.9 K are placed along the beam pipe and quadrupole magnets are used to focus the beams.

To measure the performance of the LHC the interaction rate is used. The interaction rate, that is the number of events per time, is given by

$$\frac{\mathrm{d}N}{\mathrm{d}t} = \sigma \mathcal{L}_{ins}, \tag{1.57}$$

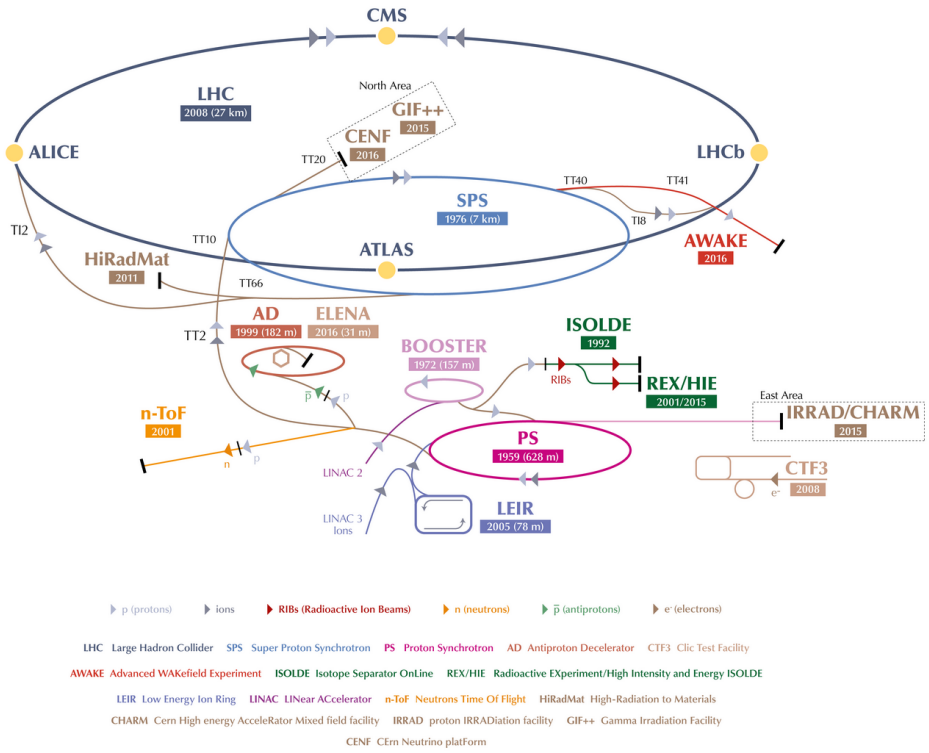

Figure 10: Schematics of the acceleration process used to boost the protons to their final energy. The LHC is the last setup in this acceleration process where the proton reach their collision energy of 6.5 TeV. Graphic taken from [54].

where σ is the cross section of a given process and $\mathcal{L}_{ins}$ is the instantaneous luminosity, a measure of the number of collisions per cm^2 per second, which depends only on accelerator parameters. The integrated luminosity gives a measure on the total number of events that occurred and therefore the amount of data taken. This quantity is useful since it can be used to calculate the cross section of a given process

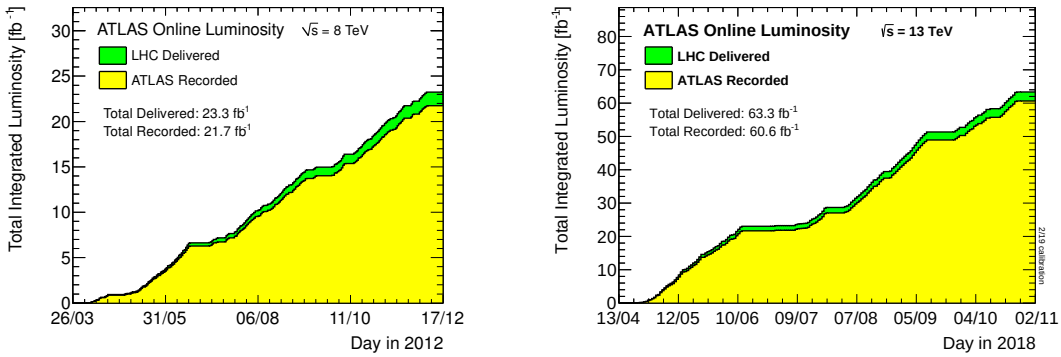

(a) (b)

Figure 11: Integrated luminosity during 2012 at $\sqrt{s} = 8$ TeV (a) and during 2018 at $\sqrt{s} = 13$ TeV (b) during stable proton - proton collisions. Courtesy of ATLAS.

by counting the number of events of that process

$$\sigma = \frac{N}{L}, \tag{1.58}$$

where $L = \int \mathcal{L}_{ins} \mathrm{d}t$ is the integrated luminosity. During the $\sqrt{s} = 8$ TeV Run-1 the luminosity delivered by the LHC was 23.3 fb^{-1} of which 21.7 fb^{-1} was recorded by ATLAS, see Figure 1.58. Due to upgrades of the LHC, both the luminosity delivered by the LHC and the luminosity recorded by ATLAS increased significantly during Run-2.

1.4.2 The ATLAS Detector

The ATLAS detector is one of the two large general purpose experiments at the LHC. It has a diameter of about 25 m and a length of 46 m, weighting 7,000 tons.

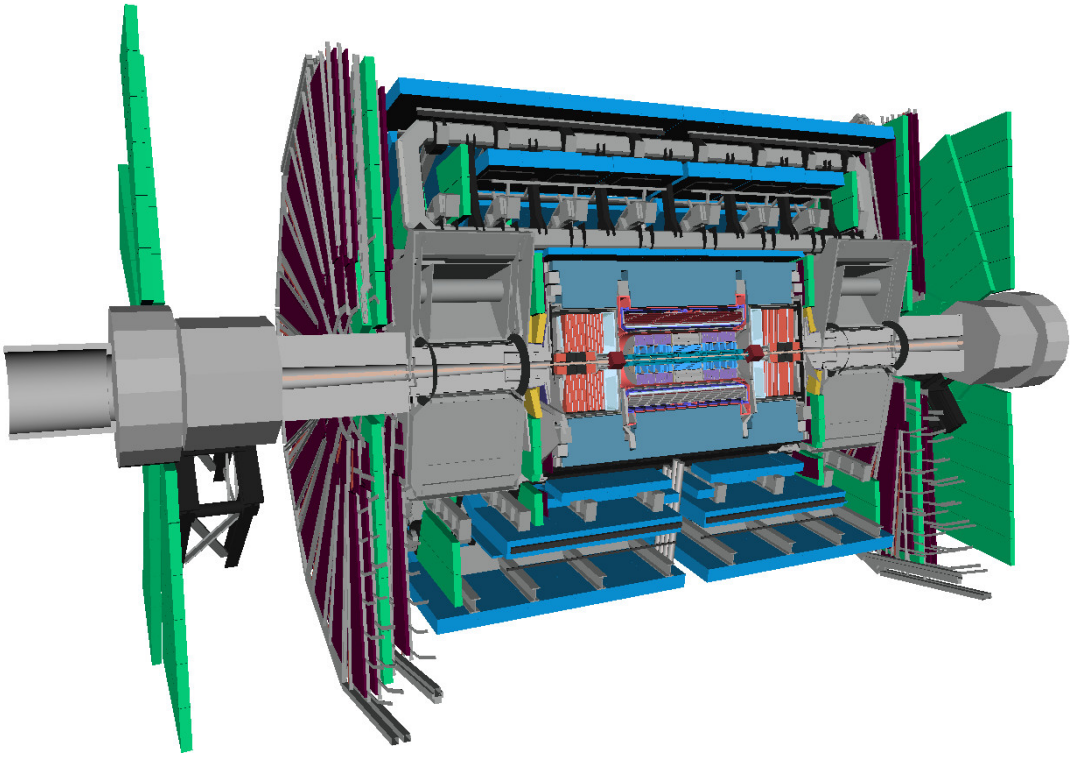

Figure 12: VP1-Light displaying the full ATLAS detector with a ϕ-sector cut-out to reveal the various sub-detector systems.

The detector itself is divided into three main sub-detector systems: Inner Detector (ID), Calorimeters, and Muon Spectrometer (MS). In addition, there are two types of magnet systems, a superconducting solenoid magnet surrounding the Inner Detector and a system of toroid magnets integrated into the Muon Spectrometer. Both magnet systems generate a magnetic field needed for tracking of charged particles. The sub-detector systems are arranged in cylindrical layers around the center of the detector and endcaps cover the region along the beam pipe. With this setup, the ATLAS

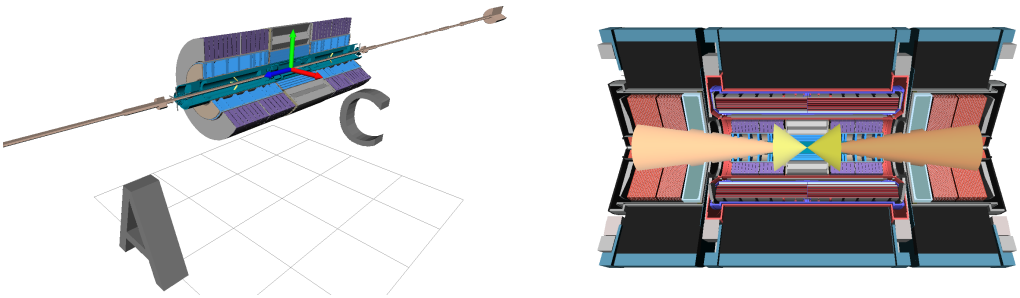

(a) (b)

Figure 13: The ATLAS coordinate system (a) as described in Section 1.4.2.1, where the x-axis is displayed in red, the y-axis in green and the z-axis in blue. The letters A and C refer to the two sides of the detector towards the positive and negative z-directions. In (b), a view of the η cones at $|\eta| = 1$ (yellow) and $|\eta| = 2.5$ (orange) is shown.

detector is near hermetic which means that almost all the energy of the collision is absorbed within the detector.

This section shows several images displaying parts of the ATLAS detector. These images were created using the new VP1-Light event display covered in Section 3.

1.4.2.1 The ATLAS Coordinate System In ATLAS, a right-handed coordinate system is defined as follows. The center of the coordinate system is located at the interaction point (IP) at the center of the detector. From there, the positive x-axis points towards the center of the LHC ring, the positive y-axis points upwards to the surface and the z-axis points along the beam pipe. The coordinate system is

shown in Figure 13 (a) along with the beam pipe and the Inner Detector. In the plane perpendicular to the beam pipe a polar coordinate system (r, ϕ) is used, where r measures the radial distance from the beam pipe and ϕ is the angle measured from the x-axis. The direction perpendicular to (r, ϕ) is given by the polar angle θ, defined from the positive z-axis. In practice, the pseudorapidity η is used instead of the polar angle θ. The pseudorapidity is defined by

$$\eta = -\log\left(\tan\frac{\theta}{2}\right). \tag{1.59}$$

In Figure 13 (b) two η cones are shown at $|\eta| = 1$ and $|\eta| = 2.5$ along with the Inner Detector and calorimeters. In the limit of massless particles, the pseudorapidity is invariant under Lorentz boosts in the direction of the beam axis. Since in a hadronic collider the momenta of the initial partons is unknown, total momentum conservation can not be applied. However, momentum in the direction transverse to the beam pipe is conserved. Therefore, instead of the total momentum p of a particle or physics object, the transverse component of the momentum p_T is used for its description.

1.4.2.2 The Inner Detector The inner detector (ID) is located around the beam pipe nearest to the interaction point. The main function of the inner detector is to locate the primary and secondary interaction vertices and the tracking of the charged particles in the magnetic field of the superconducting solenoid. Particle tracks are reconstructed from hits in the detector material of the ID. From the curvature of the track, particle properties such as direction, momentum and charge can be determined. Locations in the interaction region of the detector where multiple tracks intersect indicated the locations of primary and secondary vertices. The primary vertex represents the point of the initial interaction between the constituents of the protons. Secondary vertices are vertices that are displaces from the primary

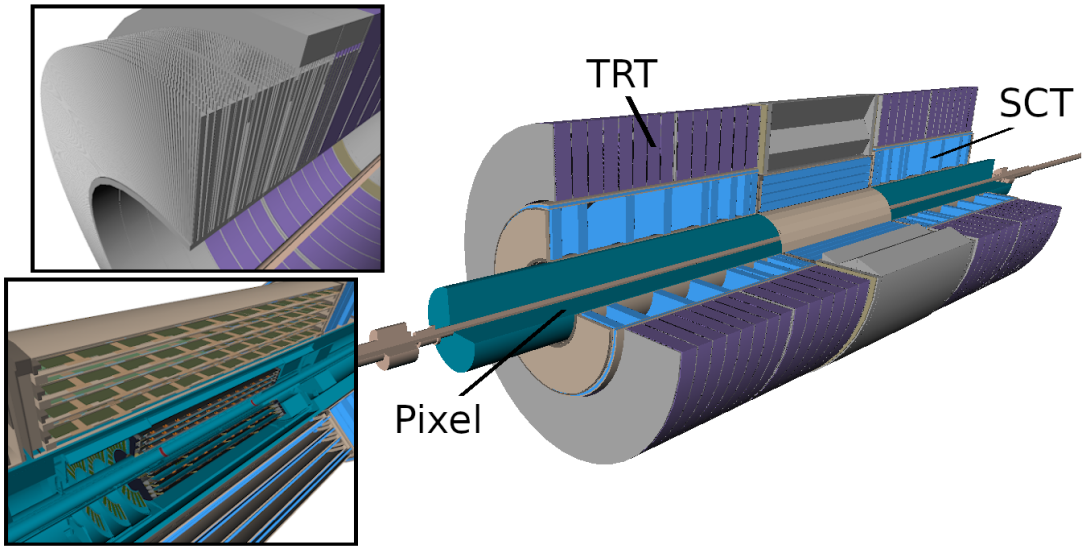

Figure 14: VP1-Light displaying the Inner Detector. The left image shows the Inner detector with a ϕ-sector cut-out which reveals details of the sub-detector systems. On the top left is a detailed view of the TRT which shows a close-up of the straw tubes. On the bottom left is a view of the Pixel (turquoise) and SCT (gray/blue)), where the silicon sensors are displayed in dark green.

vertex. They indicate the location of the decay of short-lived particles such as B hadrons. B hadrons are hadrons that consist of a b-quark. These are important for the identification of jets initiated by b-quarks, which is essential for top quark physics at the LHC. The innermost layer of the ID is the Pixel Detector which consists of 80 million silicon pixels for a very precise measurement of of the tracks close to the interaction point. The next layer is the Semiconductor Tracker (SCT), a silicon microstrip tracker. Similar to the Pixel Detector, it is made out of silicon modules. However, unlike the Pixel Detector, the modules are large silicon strips to cover a

wider region in the radial direction. The outermost layer of the ID is the Transition Radiation Tracker (TRT). The TRT consists of 50,000 straw tubes, each with a gold-plated tungsten wire at the center. Different kinds of gases between the straw tubes act as a transition radiation detector that allows to differentiate between different charged particles, such as electrons and pions. Figure 14 shows the ID including detailed views of the Pixel and SCT's silicon sensors and the TRT's straw tubes.

1.4.2.3 The Calorimeters The calorimeters are designed to measure the energy of the particles in the detector. Ideally, the total energy of the particles is deposited in the calorimeter. The calorimeters are constructed in layers of absorbing and active media. The absorbing medium is a high density material that initiates the showering of the incoming particles and the active medium measures the deposited energy through sampling. Besides the energy, the calorimeters are also able to measure the direction, that is the polar angle in the plane perpendicular to the beam axis and the pseudorapidity, of a particle shower. In ATLAS, two calorimeters are present, an electromagnetic calorimeter to measure the energy of electrons and photons, and a hadronic calorimeter to measure the energy of hadrons such as pions and kaons. Both calorimeters combined cover a pseudorapidity range of $|\eta| < 4.9$. The Liquid Argon (LAr) calorimeter is the electromagnetic calorimeter located radially just outside of the solenoid magnet. It uses liquid argon cooled down to a temperature of $-183°$C as an active material and layers of lead as the passive material. The barrel and end-caps of the LAr electromagnetic calorimeters cover a pseudorapidity range of $|\eta| < 3.2$. In addition, the remaining pseudorapidity range is covered by copper/LAr and tungsten/LAr modules acting as electromagnetic and hadronic calorimeters, respectively. Figure 15 (a) shows a cut-out view of the LAr calorimeter where the layers of absorber/liquid argon can be seen in both the central and the forward region. The Tile

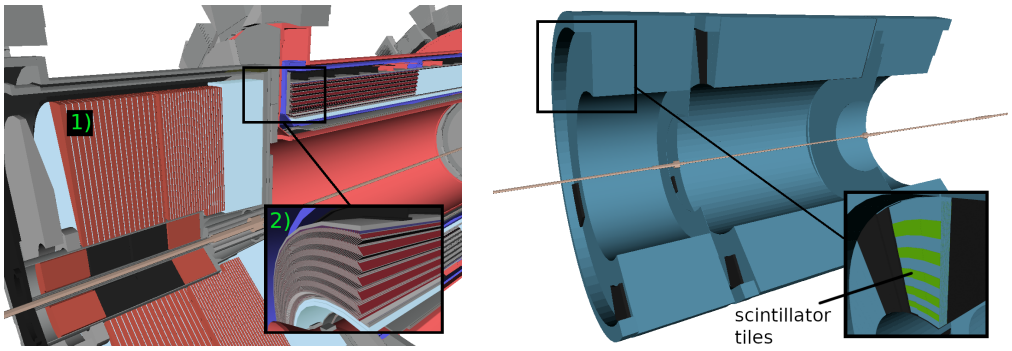

(a) (b)

Figure 15: VP1-Light displaying the calorimeters. Shown on the left (a) is a close-up of the LAr calorimeter. Part 1) on the left side of the image shows the end-cap region acting as both electromagnetic and hadronic calorimeter. The red discs shown are copper absorbers of the hadronic calorimeter and the light blue disks represent the liquid argon filled space. In the detailed view of 2) the barrel region is shown, where a close-up of the accordion-shaped lead absorbers can be seen. The right image (b) shows the tile calorimeter. A detailed close up shows the scintillator tiles (green).

Hadronic Calorimeter (TileCal) uses plastic scintillator tiles to measure the energy of the hadronic particles and steel absorbers to initiate showering. It is segmented into three barrel structures covering a pseudorapidity range of $|\eta| < 1.7$. The end-cap region is covered by a copper/LAr hadronic calorimeter. Figure 15 (b) shows the tile calorimeter including a detailed view of the scintillator tiles.

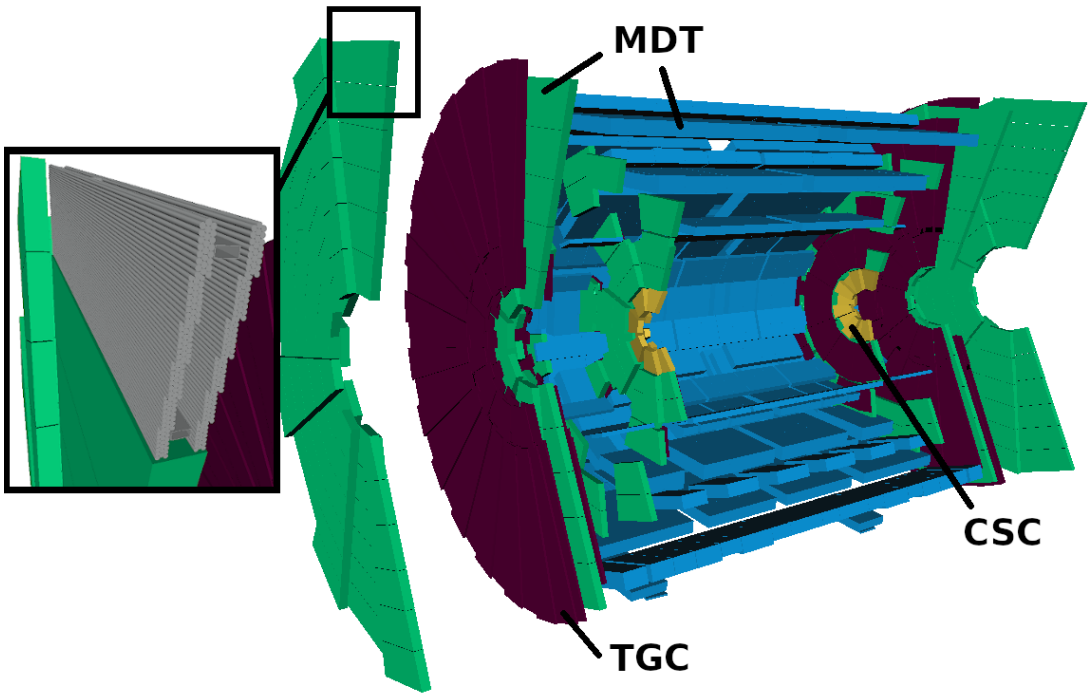

Figure 16: VP1-Light displaying the Muon System with a ϕ-sector cut-out. Also shown in the black box is a detailed view of one of the end-cap MDT's (green/blue) which consists of an arrangement of drift tubes (shown as gray cylinders). The remaining parts of the Muon System are the CSC (yellow) and TGC (purple).

1.4.2.4 The Muon Spectrometer Muons usually pass the Inner Detector and the calorimeters without interacting with the detector itself. Therefore, a large Muon Spectrometer (MS) is installed outside of the calorimeters. From the center axis of the detector, the MS ranges from a radius of 4.25 m to a radius 11 m. The MS is constructed from four different detection systems, Thin Gap Chambers (TGC),

Resistive Plate Chambers (RPC), Monitored Drift Tubes (MDT), and Cathode Strip Chambers (CSC). Three layers of MDT's measure the curves of muon tracks in a pseudorapidity range of $|\eta| < 2.7$ by measuring the distance of the track to the wire at the center of the tubes. The CSC's precisely measure the coordinates at the ends of the detector in a pseudorapidity range of $2.0 < |\eta| < 2.7$ Due to the high background in this region the CSC are designed to operate at a high event rate. The muon trigger system consists of the TGC and the RPC which also act as a second coordinate measurement in a non-bending direction at the ends of detector and in the central region, respectively. The RPC's cover a pseudorapidity range of $|\eta| < 1.5$ and are arranged in layers with the MDT's and CSC's. The TGC's cover the endcap region with a pseudorapidity range of $1.05 < |\eta| < 2.7$. Figure 16 shows both the barrel and end-cap region of the MS. A detailed view of MDT's drift tubes is also shown.

1.4.2.5 The Magnet System The magnets bend the tracks of charged particles and allow the measurement of the momentum. For the momentum measurement in the inner detector, a 5.3 m long and 2.4 m diameter superconducting solenoid magnet surrounds the ID, providing a magnetic field of 2 T parallel to the beam axis. Liquid helium is used to cool the solenoid to an operating temperature of 4.5 K. The muon spectrometer includes a system of superconducting air-core toroid magnet with 8 separate coils in the barrel region (shown in Figure 17) and 2 end-caps with 8 coils each for the precision measurement of the muon tracks. The barrel toroids cover a pseudorapidity range of $|\eta| < 1.4$ and the end-caps cover a range of $1.6 < |\eta| < 2.7$. The field integral of the toroids ranges between 2.0 Tm and 6.0 Tm throughout the detector. With a length of 25.3 m and an outer diameter of 20.1 m it is one of the larges systems within the ATLAS detector. Since the magnetic field is produced by a

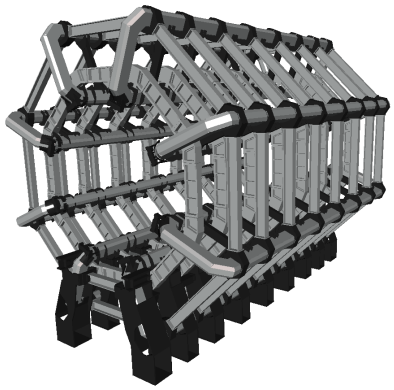

Figure 17: VP1-Light displaying the eight superconducting toroid magnets in the barrel region.

combination of barrel and end-cap toroids, the resulting magnetic field is non-uniform and therefore a detailed modelling is required for precise momentum measurement of the muons.

1.4.2.6 The Trigger And Data Acquisition The trigger system of the ATLAS detector reduces the rate at which events are selected for storage on disk. Due to limitations in the electronics and storage capabilities only a fraction of the events occurring in the ATLAS detector can be permanently stored. The trigger system reduces the number of events in two stages.

The first stage is the Level-1 (L1) hardware trigger build from custom electronics and directly build into the hardware of the detector. The L1 trigger uses a subset of the information from the calorimeters and triggers of the muon spectrometer to identify events with predefined signatures for further processing. L1 also identifies

regions of interest (RoI) that will be further investigated in the second stage. This reduces the 40 MHz bunch crossing rate to about 100 kHz.

In the second stage, the High-Level Trigger (HLT), a software based trigger operated on a large farm of CPU's. The HLT performs a more detailed analysis of the events that passed the L1 trigger, by examining the whole event for specified sub-detectors, such as calorimeters, tracker or MS and by focusing on a RoI of that event. Information on the RoI are passed down by the L1 trigger. This allows to categorize an event based on further details, such as identifying it as having a b-tagged jet. All of this results in a reduction of the event rate from about 100 kHz to about 1 kHz. In the second step of the HLT, the event filter further reduces the rate to about 200 Hz based on the fully reconstructed events. All events that passed the trigger systems are then written to permanent storage.

2.0 Combination Of ATLAS Top Quark Measurements

2.1 Introduction And Motivation

Constraining the size of possible BSM interactions by constraining the coefficients of the dimension 6 operators discussed in Section 1.2 is an important milestone on the way of understanding the physics beyond the Standard Model. In ATLAS, many precision measurements are able to measure the interactions of top quarks in such detail, that makes it possible to look for deviations from the expected Standard Model behaviour.

Combinations of measurements in order to get a better hold on the BSM parameters haven been carried out for a long time. However, most of these combinations neglect the possibility that the measurements that are combined can be correlated and these correlations have the potential to change the limits obtained for the BSM parameters. In this analysis, a combination of top quark measurement is performed, where the correlations of systematic uncertainties between the measurements is taken into account in a systematic way, by utilizing the full detail of each measurement. The measurements combined in this analysis are the single top decay distributions, that measure a set of generalized helicity fractions and phases, the W helicity fraction that measure the fractions transversely and longitudinally polarized W bosons in top quark decays and the $\sqrt{s} = 8$ TeV t-channel fiducial top quark and anti-quark cross section.

This chapter is organized as follows. First, an introduction to the basics of statistics needed to combine the measurements is given in Section 2.2. Then, a short review of Monte Carlo simulations is given in Section 2.3. In Section 2.4, the mea-

surements are reviewed and then in Section 2.5, the relevant EFT coefficients used in the fit are discussed. At that point, previous results are discussed in Section 2.6. In Sections 2.7 and 2.8 the parameterization of the cross section in terms of the EFT coefficients and the calculation of these parameters is described. Section 2.9 gives a detailed explanation of the uncertainties of the measurements and how the correlations between the measurements are evaluated. In Section 2.10 discusses the dependency of the observables of the single top decay distribution measurement on the EFT parameters and how this dependency was included in the fit. Finally, in Section 2.11 the results of the combined fit are discussed and Section 2.12 gives the conclusion.

2.2 Statistical Background And The EFT*fitter* Tool

Bayes Theorem

For a given set of measured quantities $\boldsymbol{x}$ and a set of parameters $\boldsymbol{\theta}$ the posterior probability distribution of the parameters given the measured quantities is given by Bayes Theorem [55]

$$p\left(\boldsymbol{\theta}\middle|\,\boldsymbol{x}\right) = \frac{p\left(\boldsymbol{x}\middle|\,\boldsymbol{\theta}\right) p\left(\boldsymbol{\theta}\right)}{p\left(\boldsymbol{x}\right)}, \tag{2.1}$$

where $\boldsymbol{\theta}$ is a set of parameters to be determined and $\boldsymbol{x}$ is a set of measured quantities, or the data. Then $p\left(\boldsymbol{\theta}\middle|\,\boldsymbol{x}\right)$ is the posterior probability distribution, that is the probability of the parameters given the data. $p\left(\boldsymbol{x}\middle|\,\boldsymbol{\theta}\right)$ is the probability of the data given a set of parameters, also called the Likelihood of $\boldsymbol{\theta}$. The evidence $p\left(\boldsymbol{x}\right)$ is a normalization factor

$$p\left(\boldsymbol{x}\right) = \int \mathrm{d}\boldsymbol{\theta} p\left(\boldsymbol{x}\middle|\,\boldsymbol{\theta}\right) p\left(\boldsymbol{\theta}\right). \tag{2.2}$$

The prior $p(\boldsymbol{\theta})$ is the probability of the parameters $\boldsymbol{\theta}$ and has to be estimated. It describes ones prior knowledge of the distribution of the parameters. For an unbiased analysis, a constant or uniform prior $p(\boldsymbol{\theta}) = 1$ is chosen.

Maximum Likelihood and the Method of Least Squares

Given the Likelihood $L(\boldsymbol{\theta}) = p(\boldsymbol{x}\,|\boldsymbol{\theta}\,)$ for a set of measured quantities $\boldsymbol{x}$ and a set of parameters $\boldsymbol{\theta} = (\theta_1, \ldots \theta_N)$, the maximum Likelihood is defined such that

$$\frac{\partial \ln L}{\partial \theta_i} = 0 \qquad i = 1, \ldots, N. \tag{2.3}$$

The set of parameters that fulfills this equation is called the maximum Likelihood estimator. Here, the logarithm is used since it simplifies working with the Likelihood and the same parameters $\boldsymbol{\theta}$ that maximize L also maximize $\ln L$. For a set of N uncorrelated, normally distributed measurements y_i at known points x_i with variance σ_i^2 and mean $\mu(x_i\,|\theta\,)$ the method of Likelihood is related to the method of least squares by

$$\chi^2(\boldsymbol{\theta}) = -2\ln L(\boldsymbol{\theta}) + \text{const.} = \sum_{i=1}^{N} \frac{(y_i - \mu(x_i;\boldsymbol{\theta}))^2}{\sigma_i^2}. \tag{2.4}$$

Then, maximizing the Likelihood is equivalent to minimizing the chi-square function χ^2. If the measurements y_i are correlated, then Eq. 2.4 becomes

$$\chi^2(\boldsymbol{\theta}) = (\boldsymbol{y} - \boldsymbol{\mu}(\boldsymbol{\theta}))^T \boldsymbol{V}^{-1} (\boldsymbol{y} - \boldsymbol{\mu}(\boldsymbol{\theta})), \tag{2.5}$$

where $\boldsymbol{V}_{ij} = \text{cov}[y_i, y_j]$ is the covariance matrix of the measurements $\boldsymbol{y}$ and the vector $\boldsymbol{\mu}(\boldsymbol{\theta})$ contains the predicted values. The specific set of parameters $\boldsymbol{\theta}$ that minimizes χ^2 are called the least-squares estimators. The minimum of the χ^2 gives a measure of agreement between the measurements and the fit.

Combining Measurements in EFT*fitter*

Constraining a set of parameters can often be done by combining a set of measurements and finding the posterior probability distribution of the parameters. The EFT*fitter* tool has been developed to combine a set of measurements and constrain the effects of EFT operator coefficients.

The set of N measurements $\boldsymbol{x}$ can be any direct observable, such as cross sections, decay rates or angular distributions. The set of n observables $\boldsymbol{y}(\boldsymbol{\theta})$ corresponding to these measurements can be described analytically in terms of the EFT coefficients. Then the χ^2 function in Eq. 2.5 can be written as

$$\chi^2(\boldsymbol{\theta}) = \sum_{i=1}^{n}\sum_{j=1}^{n} \left(\boldsymbol{x} - \boldsymbol{U}\cdot\boldsymbol{y}(\boldsymbol{\theta})\right)_i^T \boldsymbol{V}_{ij}^{-1} \left(\boldsymbol{x} - \boldsymbol{U}\cdot\boldsymbol{y}(\boldsymbol{\theta})\right)_j , \tag{2.6}$$

where $\boldsymbol{U}$ is an $n \times N$ matrix with non-zero elements only for entries where measurement x_i corresponds to observable y_i. In the Bayesian treatment, Eq. 2.6 can be combined with Eq. 2.4 and Eq. 2.1 to calculate the posterior probability distribution.

Marginalization

The Likelihood fit is performed in the full parameter space of the EFT coefficients. To obtain results in the form of 2-dimensional regions or 1-dimensional limits it is necessary to reduce the dimensionality. This is achieved by marginalizing over the remaining dimensions of the parameter space. For this, the parameters that one is not interested in can be treated as nuisance parameters and integrated out

$$p(\boldsymbol{\theta}'|\,\boldsymbol{x}) = \int \mathrm{d}\boldsymbol{\nu}\, p(\boldsymbol{\theta}', \boldsymbol{\nu}|\,\boldsymbol{x}) , \tag{2.7}$$

where $\boldsymbol{\theta}'$ is the subset of parameters of interest and $\boldsymbol{\nu}$ are the nuisance parameters that are integrated out. This allows to calculate one or two dimensional distributions that correspond to allowed regions of parameters. It also allows the treatment of other parameters of the problem. E.g. the single top decay distribution discussed in Section 1.3.2.2 are written in terms of the EFT coefficients and the polarization P. When constraining the EFT coefficients, the polarization can be treated as a nuisance parameter and integrated out.

2.3 Monte Carlo Event Generation

This section gives a short review of the Monte Carlo (MC) simulation of collision events. The event generation consists of several steps, that are briefly discussed here.

In the first step, the two partons participating in the hard collision process are selected according to the proton's PDF and the physical process. This is shown in Figure 18 in purple. The three lines connected to the proton represent the valence quarks, where the red lines are the partons taking part in the hard scattering process and the purple lines are the proton remnants. The red line is not necessarily a valence quark, but could also be a sea quark or gluon, depending on the process.

In the second step, the hard interaction is calculated. This is shown in Figure 18 in red. Event generators performing this task are referred to as Matrix Element (ME) generators. Some examples of ME generators are MadGraph [56, 57], Powheg [58, 59] or Protos, where the first ones are general purpose ME generators and the last one is specifically for the generation of top quark events including the effects of anomalous couplings. The hard process is calculated perturbatively using matrix elements derived from Feynman rules. The integrals are computed using Monte

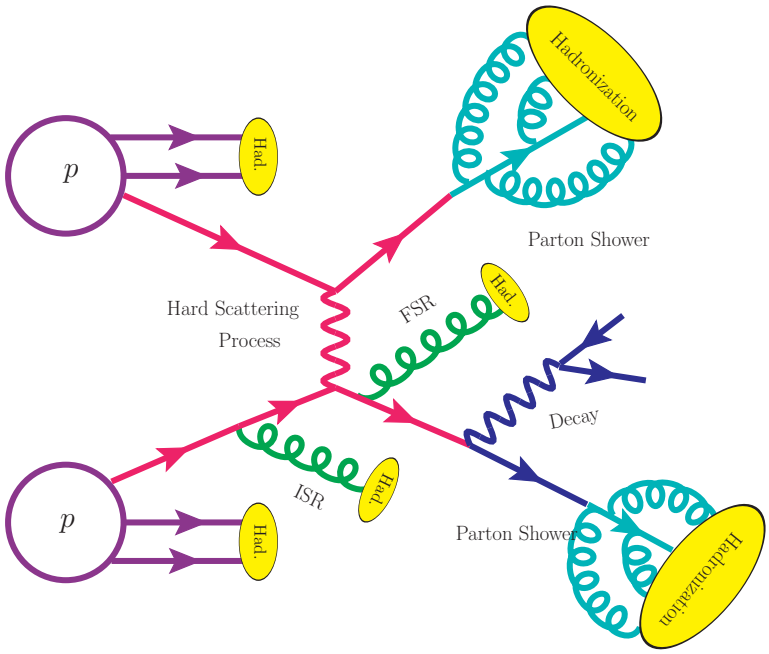

Figure 18: Schematic overview of a simulated event. The incoming protons p are shown in purple. The hard scattering process, in this case a t-channel event, is shown in red. After the hard interaction, any heavy particles are decayed, shown in blue. Then, the remaining particles are showered, shown in teal. Finally, all colored particles are hadronized to form colorless hadrons. This is shown in yellow. Also shown is the Initial and Final State Radiation, ISR and FSR, respectively. Not shown is the possibility of an underlying event.

Carlo (MC) methods. The advantage of using MC methods for integration is that the uncertainty of the MC integration is proportional to the inverse of the number of events generated, independent of the integral's dimensionality. Therefore, the

uncertainty can be reduced by increasing the number of generated events. The hard interaction process consists of the interaction of the partons going to some predefined final state. In addition, some ME generators can also decay heavy on-shell particles. This is also done perturbatively as part of the hard process. Otherwise, specific tools for the decay of heavy resonance can be used such as MadSpin [60], Tauola [61] or EvtGen [62]. MadSpin also keeps track of spin correlations between initial particles and their decay products. Tauola and EvtGen are specific tools for for the decay of tau leptons and heavy flavor particles such as B and D mesons, respectively.

Once the hard interaction is calculated, the remaining particles are showered. All colored particles created in the event can initiate gluon radiation, which can in turn radiate more gluons or quark anti-quark pairs. This is called the Final State Radiation (FSR). Besides the final states, also the initial states can radiate gluons, This is called Initial State Radiation (ISR). The collective process of soft gluon radiation is called the Parton Shower (PS). Here, any remaining unstable particles are also decayed. An unstable particle as defined in ATLAS is any particle with a mean life greater than $0.3 \cdot 10^{-10}$ s or $c\tau \approx 10$ mm. Once the colored particles are showered, that means they not have enough energy to radiate off more gluons, they form stable hadron. This process is called Hadronization. The collection of particles created from an initial quark or gluon is called a jet. Examples of Parton Showering tools are Herwig [63, 64, 65] and Pythia [66]. These are in principle also ME generators, but are commonly linked to other ME generators such as Powheg and MadGraph for the purpose of showering.

In principle the is also the possibility of an Underlying Event (UE). This is the additional low energy QCD interaction between other partons from the initial protons. Further, there is the possibility of pile-up. This is when more than one proton-proton

collision per proton bunch occurs. In 2018 the mean number of interactions per event was around 35 and it can go as high as 130 -140 at the High Luminocity LHC (HL-LHC). This can impact the reconstruction of the event, but will not be discussed further since no full simulation is used in this analysis.

2.4 The Measurements

In the following section, the top quark measurements relevant for this analysis will be discussed. First, the single top cross section is summarized and all important aspects are pointed out. This includes the number of contributing operators and how they contribute. Second, the single top decay distribution measurement is discussed, again focusing on the the contributing operators. On overview is also given on which regions of the EFT parameter space can be constrained by the single top decay distribution measurement alone. Lastly, the W polarization measurement is reviewed. Also here, the different aspects relevant for this analysis are addressed and the constraints set by the W helicity measurement. Also discussed in this section are the specific input parameters used in the fit for each one of the measurements.

2.4.1 Single Top Quark Production

In Section 1.3.1 the production of a single top quarks was discussed, in particular, the single top production in which the top quark or anti-quark is produced through t-channel scattering of a b-quark and a light quark, mediated by a W boson in the t-channel. In this section, the experimental details of the single top cross section measurement used for this analysis is given in more detail. The single top t-channel

	Predicted	Measured
$\sigma\,(tq)$	$54.9^{+2.3}_{-1.9}$ pb	$56.7^{+4.3}_{-3.8}$ pb
$\sigma\,(\bar{t}q)$	$29.7^{+1.7}_{-1.5}$ pb	$32.9^{+3.0}_{-2.7}$ pb

Table 7: Predicted and measured values of the total top quark and top anti-quark cross section. The theoretical predictions correspond to next-to-leading (NLO) calculations in QCD (See Section 2.9.3). The experimental uncertainties correspond to total statistical + systematic uncertainties.

cross section has been measured at ATLAS at a center-of-mass energy of $\sqrt{s} = 8$ TeV [31]. The total, fiducial and differential cross section was measured. Here, focus is placed on the total and fiducial cross section. The total cross section corresponds to the inclusive cross section, and the fiducial cross is defined through a set of fiducial cuts that are closely related to the geometrical properties of the ATLAS detector and the analysis strategy used. In this particular case, analysis strategy refers i.a. to the specific decay channels of the top quark and W boson. Therefore, the fiducial cross section not only measures the production, but also the decay of the top quark. More details about the fiducial region are given later in this section. The relation between fiducial and total cross section is given by

$$\sigma_{\text{fid}} = A_{\text{fid}}\sigma_{\text{tot}}, \tag{2.8}$$

where A_{fid} is the fiducial acceptance given by

$$A_{\text{fid}} = \frac{N_{\text{fid}}}{N_{\text{tot}}}. \tag{2.9}$$

where N_{tot} is the total number of events and N_{fid} is the number of events that pass the fiducial cuts.

There are a number of advantages and disadvantages for choosing either the total or fiducial cross section for the EFT combination. The total cross section has the advantage that it only includes the production of the top quark or anti-quark. From Figure 5 one can see that this implies that the expression for the cross section is at most quadratic in the EFT coefficients, since the matrix element only contains one Wtb vertex and

$$\mathcal{M}_{\text{tot}} \propto c_i, \tag{2.10}$$

$$\Rightarrow \sigma_{\text{tot}} \propto c_i^2. \tag{2.11}$$

where c_i can be any of the Wtb related EFT coefficients. An expression for the total cross section in terms of the EFT coefficients is given in Eq. C.6 of Appendix C. To use this expression in the fit, the coefficients κ in the parameterization of the cross section in Eq. C.6 have to be calculated. Details for the calculation of the coefficients κ for the fiducial cross section are given in Section 2.8. For the total cross section, there are 8 combinations of EFT coefficients that contribute to the cross sections, as can be seen in Eq. C.6. All other combinations are zero. The reason is that in the 5-flavor scheme, for vanishing b-quark mass the terms that includes a combination of a left- and right-handed EFT coefficients vanish. Consequently, 8 different coefficients κ need to be determined. The disadvantage of using the total cross section is, that the dependence of the acceptance on the EFT coefficients is not known and has to be evaluated. The total cross section involves the extrapolation from the signal region to the full phase space. This extrapolation is usually done assuming Standard Model acceptance. However, the EFT operators can modify the

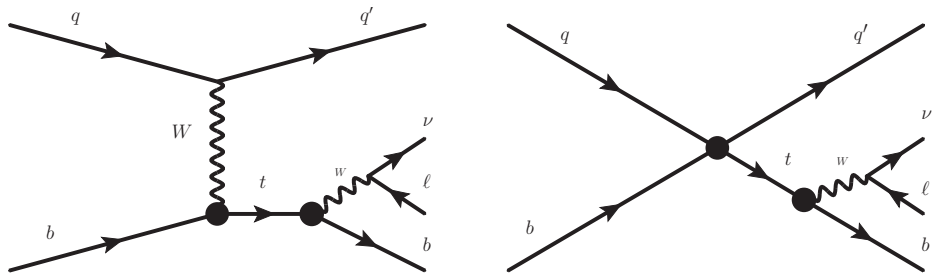

Figure 19: Single top quark production and subsequent decay in the 5-flavor scheme. The black dots represent EFT vertices. Left: t-channel single top production. Right: Single top production through a four-quark interaction.

kinematics of the process and therefore change the acceptance which makes an interpretation of the cross section result difficult if the acceptance in terms of the EFT coefficients is unknown.

The fiducial cross section on the other hand suffers less from this problem, since no extrapolation is required. Therefore, the dependency on the EFT coefficients is expected to be much smaller. The lack of an extrapolation also reduces the Monte Carlo generator uncertainties of the fiducial cross section that enter through the calculation of the fiducial acceptance. The disadvantage of including the fiducial cross section is that the parameterization of the cross section in term of the EFT coefficients is more complex. Since the fiducial cross section includes both the production and decay of the top quark or anti-quark, EFT coefficients can enter the amplitude in two vertices depicted as block dots in Figure 19. The Wtb vertex governs both the production and decay of the single top quark or anti-quark. In addition the four-quark operator can also contribute to the production of the top quark or anti-

	Measured
$\sigma_{\text{fid}}(tq)$	(9.78 ± 0.57) pb
$\sigma_{\text{fid}}(\bar{t}q)$	(5.77 ± 0.45) pb

Table 8: Measured fiducial top quark and anti-quark cross section [31].

$A_{\text{fid}}(tq)$	$A_{\text{fid}}(\bar{t}q)$
$17.26^{+0.46}_{-0.21}$	$17.52^{+0.45}_{-0.20}$

Table 9: Fiducial acceptance in % calculated with POWHEG-BOX + PYTHIA6 [31].

quark. Therefore, the expression of the cross section is a quartic function in the EFT coefficients. This increases the number of coefficients κ that need to be computed. For the fiducial cross section there are a total of 61 coefficients κ. Detail on these coefficients and their calculation are given in Section 2.8.

Both the fiducial and total cross section measure total rates and therefore the cross sections provide constraints on absolute values of the EFT coefficients. Consequently, no phases of the EFT coefficients can be constraint. The cross sections are also the only observables that can put constraints on both the Standard Model like EFT coefficient $c_{\varphi Q}^{(3)}$ and the four-quark coefficient $c_{Qq}^{3,1}$.

	Predicted	Measured
F_0	0.687 ± 0.005	0.709 ± 0.019
F_L	0.311 ± 0.005	0.299 ± 0.015
F_R	0.0017 ± 0.0001	-0.008 ± 0.014

Table 10: Predicted [46] and measured [67, 68] values of the three W helicity fractions.

2.4.2 W Helicity Fractions

The theoretical background of the W helicity fraction was discussed in Section 1.3.2.1. Since the decay of the top quark proceeds via the Wtb vertex, this also provides an opportunity to constrain EFT coefficients that could potentially modify that vertex. The W helicity fractions have been measured at ATLAS in $t\bar{t}$ events at a center-of-mass energy of $\sqrt{s} = 8$ TeV [67, 68]. Specifically, the analysis studied $t\bar{t}$ events where one top quark decays into a bottom quark and a W which subsequently decays into a charged lepton and a neutrino. The charged lepton serves as the analyzer as discussed in Section 1.3.2.1. The W coming from the other top quark decays hadronically into a light quark and anti-quark. The case of a hadronic analyzer, where instead of the charged lepton the down quark is used as the analyzer, is also studied and measured. However, these results do have considerably larger uncertainties. This is because the two light quarks from the W boson decay are hard to separate and correctly identify. Therefore, only the leptonic analyzer is considered in this work. The results of the W helicity fraction measurement is detailed

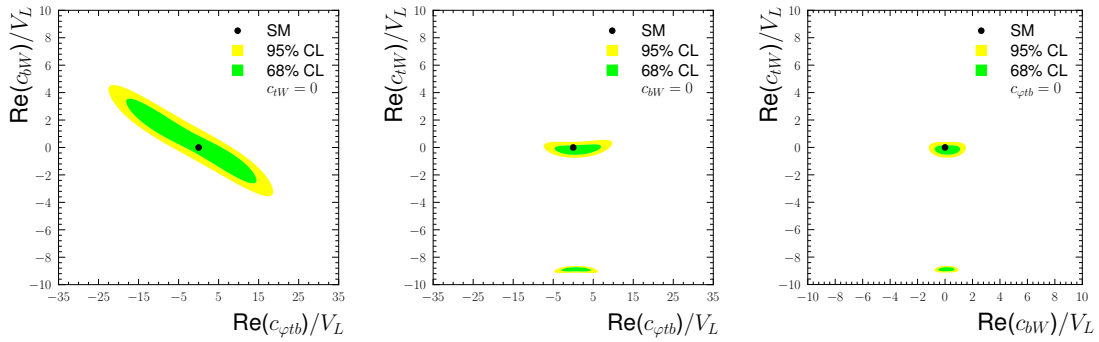

(a) (b) (c)

Figure 20: Marginalized confidence limits on pairs of EFT coefficients from the W helicity fractions. For each plot, the remaining coefficient is set to zero. All coefficients are assumed to be real. Also shown is the Standard Model point.

in Table 10. Listed are the predicted and measured values and their respective uncertainties. Uncertainties of the measured helicity fractions correspond to statistical and systematic uncertainties. The predicted values correspond to next-to-next-to-leading order (NNLO) calculations in QCD [46]. Constraints on the EFT coefficients can already be made by solely looking at the W helicity fractions. However, some care needs to be taken. The three helicity fractions are constrained to add up to one,

$$F_0 + F_L + F_R = 1, \tag{2.12}$$

so that only two independent observables remain. Therefore, the W helicity fractions can only constrain pairs of EFT coefficients, while the remaining coefficients are set to their respective Standard Model values. Further, the W helicity fractions measure

only ratios of couplings. Typically, the ratio is taken with respect to $V_L = V_{tb} \approx 1$. This can be seen from Eq. 1.43 in Section 1.3.2.1. Including the effects of the EFT coefficients, Eq. 1.43 are modified as

$$F_0 = \frac{|V_L - x_W g_R|^2 + |V_R - x_W g_L|^2}{|V_L - x_W g_R|^2 + |V_R - x_W g_L|^2 + 2\,|x_W V_L - g_R|^2 + 2\,|x_W V_R - g_L|^2}$$

$$F_L = \frac{2\,|x_W V_L - g_R|^2}{|V_L - x_W g_R|^2 + |V_R - x_W g_L|^2 + 2\,|x_W V_L - g_R|^2 + 2\,|x_W V_R - g_L|^2}$$

$$F_R = \frac{2\,|x_W V_R - g_L|^2}{|V_L - x_W g_R|^2 + |V_R - x_W g_L|^2 + 2\,|x_W V_L - g_R|^2 + 2\,|x_W V_R - g_L|^2}, \quad (2.13)$$

where the EFT coefficients are written in terms of the anomalous couplings, see Eq. 1.34. Expressions for the W helicity fractions in terms of the anomalous couplings for massive b-quarks can be found in Appendix A. Furthermore, the W helicity fractions are real so that limits can only be set on real parts of EFT coefficients. Putting everything together, this allows to put limits on pairs of three real EFT coefficients $c_{\varphi tb}$, c_{bW} and c_{tW}. Figure 20 shows the limits on all possible combinations of the EFT coefficients. In this special case, where all coefficients are real and only two couplings are non-zero at a time, the limits on the coefficients are fairly strong. It is also possible to see the strong anti-correlations between the left-handed coefficients $c_{\varphi tb}$ and c_{bW} in Figure 20 (a) as is expected from Eq. 2.13 (Note that there is a relative minus sign between the definition of g_L and c_{bW}). Limits on the anomalous couplings were set by the measurement under the assumption that $V_L = 1$, all couplings are real, and only one couplings is active at a time. These limits are given by

$$\begin{aligned} V_R &\in [-0.17, 0.25]\,, \\ g_L &\in [-0.11, 0.08]\,, \\ g_R &\in [-0.03, 0.06]\,, [0.74, 0.78]\,. \end{aligned} \quad (2.14)$$

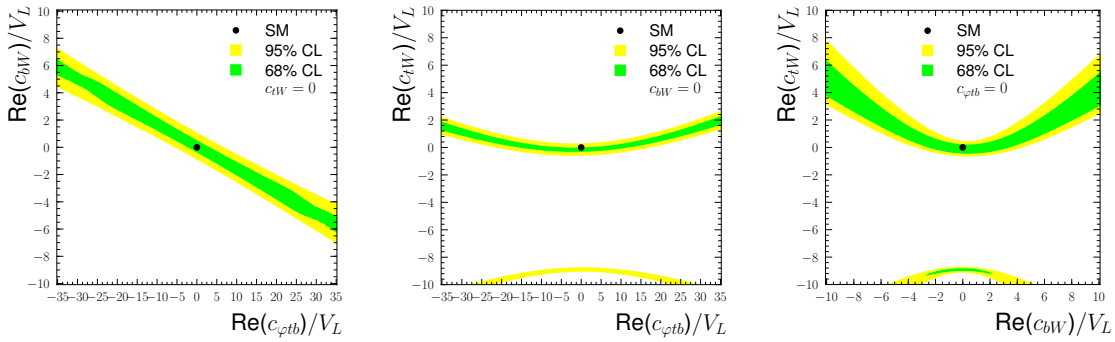

Figure 21: Marginalized confidence limits on pairs real of EFT coefficients from the W helicity fractions. Varying the real parts of $c_{\varphi tb}$, c_{bW} and c_{tW} freely significantly increases the allowed regions of the coefficients. Note that the constraints on $\mathrm{Re}\,(c_{bW})$ are due to the limited range of $\mathrm{Re}\,(c_{\varphi tb})$.

These limits can be translated into EFT coefficients by using Eq. 1.34 so that

$$\begin{aligned} c_{\varphi tb} &\in [-6.51, 8.25]\,, \\ c_{bW} &\in [-0.93, 1.28]\,, \\ c_{tW} &\in [-9.10, -8.63]\,, [-0.70, 0.34]\,, \end{aligned} \tag{2.15}$$

where $c_{\varphi tb}$, c_{bW} and c_{tW} are real. Note the sign change due to the sign difference between anomalous couplings and EFT coefficients.

Some of the constraints can also be loosened in order to evaluate how the limits change. Specifically, the restriction of setting the remaining coefficient to zero can be dropped. Figure 21 shows the same plots as Figure 20, with the difference that the remaining coupling is not fixed to zero, but instead is marginalized. It is clear that removing this constraint significantly increases the limits of the EFT parameters in

Eq. 2.15 and no definite limits can be obtained. This is to be expected, since it is not possible to constrain more than two parameters with only two independent observables. Furthermore, once the coefficients are allowed to be complex valued, the parameter space is too large and determining the confidence regions of the EFT coefficients through marginalization is not possible.

2.4.3 Single Top Quark Decay Distribution

In the previous section, the W helicity fractions measured in top quark decay distributions was discussed. This section covers a more generalized measurement of the top quarks angular decay distributions. The theoretical background was given in Section 1.3.2.2. This section discusses the experimental aspects, which EFT coefficients can be constrained and what the limits on those coefficients are.

The generalized fractions and phases in Section 1.51 were measured at ATLAS in single top quark events at a center-of-mass energy of $\sqrt{s} = 8$ TeV [69]. Table 11 shows the predicted and measured values of the fractions and phases. The predicted values are leading-order (LO) expression [46, 70]. Measured values are only available for f_1 and δ_-. Upper bounds are set on f_1^+ and f_0^+. Due to this, there was no sensitivity on the phase δ_+. As with the W helicity fractions, the single top decay distributions measure ratios of couplings taken with respect to $V_L \approx 1$. However, the number of observables is larger. Having three generalized helicity fractions and two phases allows to constrain almost the full parameter space of the Wtb vertex. One limitation lies in the number of complex phases. This will be the topic the following Section 2.5. Figure 22 shows limits on some of the EFT coefficients. In all plots, $V_L = 1$ while all other coefficients are varied freely. In Section 1.3.2.2, Eq. 1.54 the relations between W helicity fractions and the generalized fractions was discussed.

	Predicted	Measured
f_1	0.304	$0.296^{+0.048}_{-0.051}$
f_1^+	0.001	< 0.120 (95%CL)
f_0^+	$6 \cdot 10^{-5}$	< 0.085 (95%CL)
δ_+	0.0	
δ_-	0.0	$0.002\pi^{+0.016\pi}_{-0.0017\pi}$

Table 11: Predicted [46, 70] and measured [69] values of the three generalized fractions and phases.

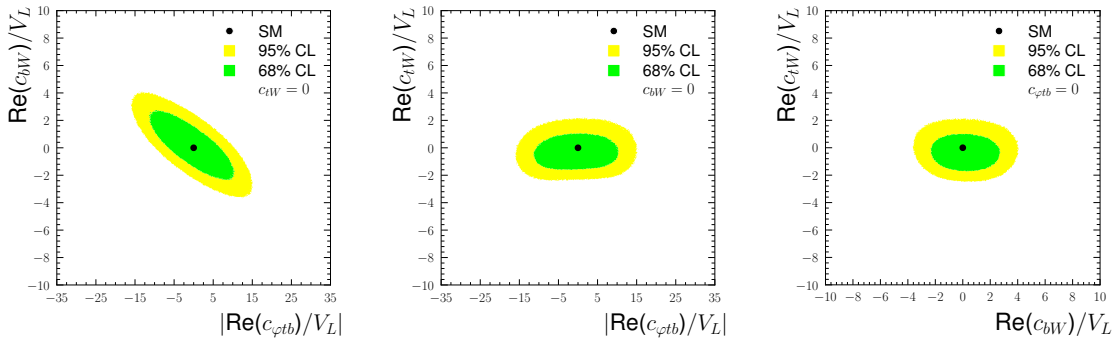

Figure 22: Limits on EFT coefficients from the single top decay distributions. All other coefficients are marginalized.

Here we can see how this relation is reflected in the probability distributions of the EFT coefficients. Figure 20 (a) and Figure 22 (a), both showing the real parts of $c_{\varphi tb}$ and c_{bW}, exhibit the same behaviour. One important difference is that in the former

the remaining coefficient c_{tW} is set to zero, while it is a free parameter in the latter.

The measurement of the generalized fraction f_1 and the phase δ_- also puts limits on the range of the anomalous couplings and therefore on the EFT coefficients. The ratio of the real and imaginary part of the coupling g_R was constraint to the confidence interval

$$\mathrm{Re}\left[\frac{g_R}{V_L}\right] \in [-0.12, 0.17] \quad \mathrm{Im}\left[\frac{g_R}{V_L}\right] \in [-0.07, 0.06]\,, \tag{2.16}$$

and by Eq. 1.34 the limits on the EFT coefficients are

$$\mathrm{Re}\left[\frac{c_{tW}}{V_L}\right] \in [-1.98, 1.40] \quad \mathrm{Im}\left[\frac{c_{tW}}{V_L}\right] \in [-0.70, 0.82]\,. \tag{2.17}$$

Upper limits have also been set on the magnitude of the ratios

$$\begin{aligned} \left|\frac{V_R}{V_L}\right| &< 0.37 \quad (95\%\mathrm{CL}), \\ \left|\frac{g_L}{V_L}\right| &< 0.29 \quad (95\%\mathrm{CL}), \end{aligned} \tag{2.18}$$

and again for the EFT coefficients

$$\begin{aligned} \left|\frac{c_{\varphi tb}}{V_L}\right| &< 12.21 \quad (95\%\mathrm{CL}), \\ \left|\frac{c_{bW}}{V_L}\right| &< 3.38 \quad (95\%\mathrm{CL}). \end{aligned} \tag{2.19}$$

All limits are for the coefficients with respect to the Standard Model couplings V_L and could change once V_L is taken as a free parameter. Limits for the top quark polarization are also given at

$$\begin{aligned} P &< 0.72 \quad (95\%\mathrm{CL}), \\ P &< 0.86 \quad (95\%\mathrm{CL}). \end{aligned} \tag{2.20}$$

All limits are in accordance with the Standard Model predictions.

2.5 Choice Of Parameters

As seen in Section 1.1, the dimension 6 operators contributing to the top quark interactions considered in this analysis are

$$\mathcal{O}_{\varphi Q}^{(3)}, \qquad \mathcal{O}_{\varphi tb}, \qquad \mathcal{O}_{bW}, \qquad \mathcal{O}_{tW}, \qquad \mathcal{O}_{Qq}^{3,1}. \tag{2.21}$$

The corresponding EFT coefficients $c_{\varphi Q}^{(3)}$ and $c_{Qq}^{3,1}$ are real, $c_{\varphi tb}$, c_{bW}, and c_{tW} are complex, giving a total of 7 free parameters. However, the measurements discussed in Sections 2.4.1–2.4.3 do not constrain sufficiently many complex parameters. Both the cross sections and the W helicity measurement only measure real observables. The single top decay distributions constrain three real factions and two complex phases. It is therefore necessary to reduce the number of complex parameters in the EFT coefficient space. In the measurements of the single top decay distributions as well as the W helicity fractions the dominant terms are proportional to linear combinations of either V_L and c_{tW} or $c_{\varphi tb}$ and c_{bW}, see Eq. 2.13 for the W helicity fractions and their relation to the generalized fractions of the single top decay distributions in Eq. 1.54. Both V_L and c_{tW} correspond to left-handed and both $c_{\varphi tb}$ and c_{bW} correspond to right-handed couplings. Therefore, the coefficients can be divided into two sectors, a left-handed sector V_L - c_{tW} and a right-handed sector $c_{\varphi tb}$ - c_{bW}. The coefficient c_{tW} interferes directly with the purely real Standard Model contribution V_L. Therefore, the single top decay distribution measurement could determine the phase difference of c_{tW} with respect V_L. However, due do the small magnitude of both $c_{\varphi tb}$ and c_{bW}, there was little sensitivity for the phase between the left-handed and right-handed sector and the phase difference between the two coefficients of the right-handed sector.

To study the effect of the phases on the EFT parameter limits, the EFT pa-

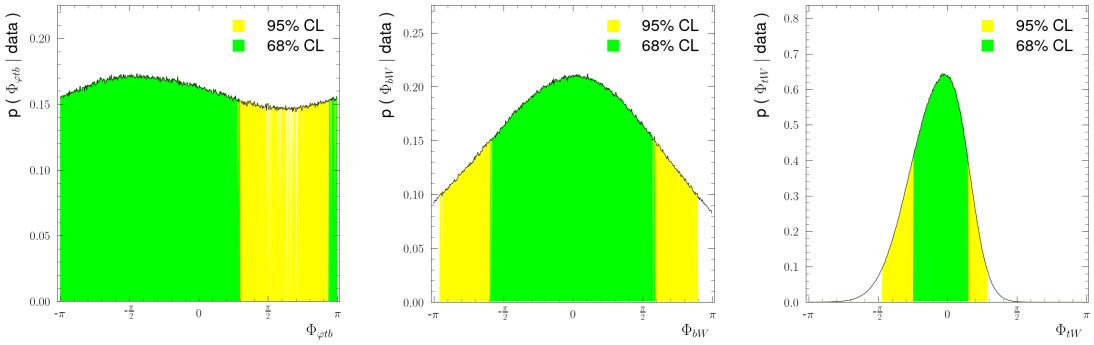

(a) (b) (c)

Figure 23: Probability distribution of the phases of the EFT coefficients $c_{\varphi tb}$ (a), c_{bW} (b) and c_{tW} (c) from the single top decay distribution measurement. The phases of $c_{\varphi tb}$ and c_{bW} are unconstrained due to the interference with the Standard Model term V_L.

rameters are written in this section in polar form as

$$c_j = \mathrm{Re}\,(c_j) + i\,\mathrm{Im}\,(c_j) \quad \Rightarrow \quad c_j = \rho_j e^{i\Phi_j}, \tag{2.22}$$

where ρ_j and Φ_j are the magnitude and phase of coefficient $j = \varphi tb,\ bW,\ tW$. The arguments are allowed to vary freely between 0 and 2π in the fits. Figure 23 shows the probability distributions of the phases of the EFT coefficient $c_{\varphi tb}$, c_{bW} and c_{tW} coming from the single top decay distribution measurement. Both the phases of $c_{\varphi tb}$ and c_{bW} are unconstrained. The phase of c_{tW}, however, is constraint around the Standard Model value of zero. The distributions were generated with the EFT*fitter* tool taking only the single top decay distribution measurement as input. Adding the W helicity fraction measurement and/or the cross sections does not change the distributions.

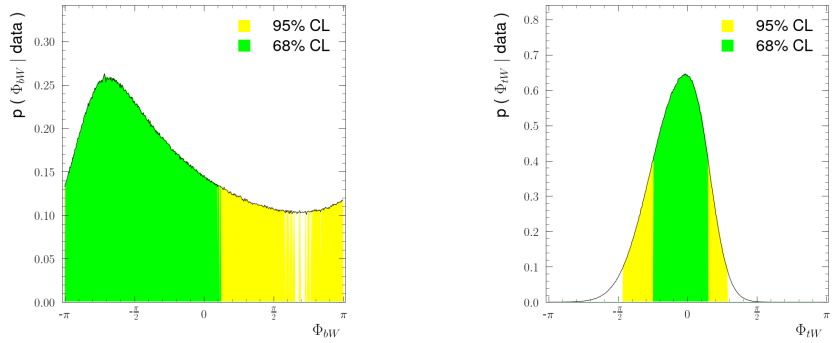

(a) (b)

Figure 24: Probability distribution of the phases of the EFT coefficients c_{bW} (a) and c_{tW} (b) for $\phi_{ptb} = 0$. Fixing the phase of $c_{\varphi tb}$ does not affect the phase of c_{tW}. The phase of c_{bW} is still largely unconstrained.

This is expected, since the single top decay distribution measurement is the only measurement giving any constraints for the imaginary parts of the coefficients.

Since the phase of $c_{\varphi tb}$ is unconstrained, it is fixed to zero, making $c_{\varphi tb}$ a real, positive parameter. This leaves two imaginary parameters that can in principle be constrained by the single top decay distribution measurement. Of course, there is still the issue that only one of the two phases in the single top decay distribution measurement was actually measured (the phase δ_- in Table 11), which means that also in this analysis, only one of them can be constrained. As can be seen in Figure 24 the phase that is constrained is the phase of the coefficient c_{tW}, while the phase of c_{bW} is still largely unconstrained. The phase of c_{bW}, will be kept as a free parameter, since fixing ϕ_{bW} has a large effects on the probability distribution of the left-handed coefficients. This can be seen in Figure 25, where the probability distribution of the

magnitude of $c_{\varphi tb}$ and c_{bW} is shown for different values of their respective phases. Fixing the phases also fixes the relative sign, which strongly affects the correlation between $c_{\varphi tb}$ and c_{bW}. Contrarily, solely fixing the phase of $c_{\varphi tb}$ has no effect on the magnitude or phase of c_{tW}, as can be seen when comparing Figure 23 and Figure 24. This is also true for the remainder of the free parameters, that is the magnitudes of the coefficients $c_{\varphi tb}$, c_{bW} and c_{tW} as well as the polarization. In conclusion, the free parameters in the fit are given by

$$c_{\varphi Q}^{(3)}, \quad c_{Qq}^{3,1} \quad \text{real} \tag{2.23}$$

$$c_{bW}, \quad c_{tW} \quad \text{complex} \tag{2.24}$$

$$c_{\varphi tb} \quad \text{real, positive} \tag{2.25}$$

where $c_{\varphi Q}^{(3)}$ and $c_{Qq}^{3,1}$ are real parameters, c_{bW} and c_{tW} are complex parameters and $c_{\varphi tb}$ is a real, positive parameter. Note that fixing $c_{\varphi tb}$ is done in the fit for purely practical purposes and does not constrain the coefficient $c_{\varphi tb}$ to positive or even real values. Multiplying $c_{\varphi tb}$ with an arbitrary phase does not change the posterior probability distributions of the fit as long as c_{bW} is multiplied by the same phase. The only quantity that is fixed is the absolute phase of $c_{\varphi tb}$ and c_{bW} to reduce the number of complex parameters.

At this point, a few words should also be said about the effects of other dimension 6 operators. As seen in Section 1.2 the list of dimension 6 operators contributing to top quark physics is long and in principle other operators could be included in a global fit. Further, additional measurements that are sensitive to the operators in Eq. 2.21. For example, the top quark production in association with a W boson is also sensitive to the Wtb couplings. However, the Wt production also gets a contribution from other operators such as the top gluon coupling c_{tG}. This operator

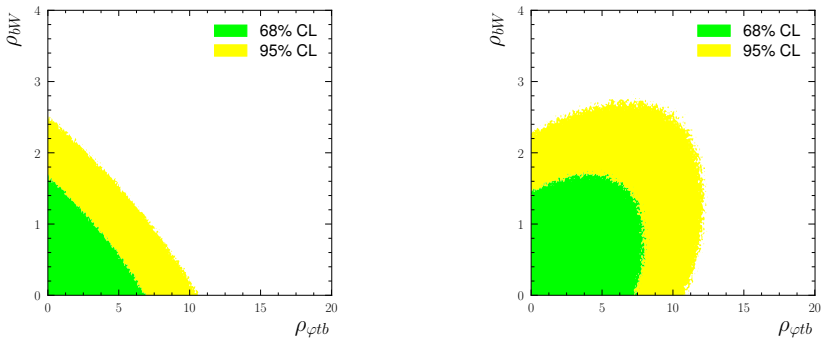

(a) (b)

Figure 25: Fixing both phases of the left-handed sector, $\phi_{\varphi tb}$ and ϕ_{bW}, has a strong impact on the limits of the magnitudes of the respective coefficients. Each plot shows the probability distribution of the magnitudes of $c_{\varphi tb}$ and c_{bW}, while the phase $\phi_{\varphi tb}$ is fixed to $\phi_{\varphi tb} = 0$, and the phases $\phi_{bW} = 0$ (a) and the phases $\phi_{bW} = \pi$ (b).

in turn is also constrained by the $t\bar{t}$ cross section, so inclusion thereof would be required as well. Both processes can be seen in Figure 26, where the Wt production shows an alternative Feynman diagram to the one shown in Figure 4. This would vastly increase both the number of observables and the parameter space. This could be the subject of a wider effort and is beyond the scope of this work. Therefore, this analysis is restricted to the observables listed in Section 2.4 and the parameters discussed in this section.

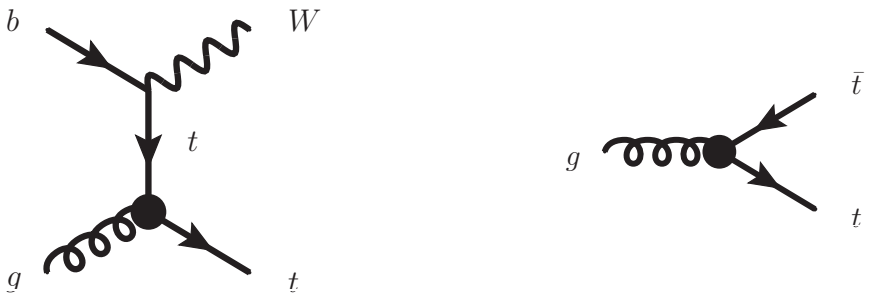

Figure 26: Single top quark production in association with a W boson and top pair production receive contributions from dimension 6 the top-gluon operator $\mathcal{O}_{tG}$. (a) shows the Wt production, (b) shows the top pair production.

2.5.1 Dependency Of The Top Quark Polarization On The EFT Coefficients

The polarization in the context of the top quark was discussed in Section 1.3.1. In this section, the dependency of the EFT coefficients on the polarization and its effects on the combined fit is evaluated. The polarization directly appears in the expressions of the angular coefficients in Eq. 1.56 in the single top decay distribution analysis, where a lower bound of $P > 0.72$ at 95% CL [69] was found. In this analysis, the polarization can be treated in two ways in the fit. It can be defined as one of the free parameters in the fit. Then, the polarization will be varied within its allowed range and marginalized when calculating the allowed regions of the remaining EFT coefficients. Alternatively, the polarization can be parameterized in terms of the EFT coefficients. This has been done in the literature for the anomalous couplings of the Wtb vertex [71] and the four-quark operators contributing to single top production

[72]. The four-quark operator considered in this analysis does not have a significant effect on the polarization and is therefore not further investigated.

However, the anomalous couplings can have a sizable effect on the polarization. To study this effect, expressions of the polarization taken from Ref. [71] have been included in the combined fit. After performing the fit, the resulting probability distributions of the EFT coefficients were compared with the distributions of the fit when marginalizing over the polarization. Figure 27 shows the comparison for the coefficients $c_{\varphi Q}^{(3)}$, $\mathrm{Re}\,(c_{bW})$, and $c_{\varphi tb}$. These coefficients show a slight shift when marginalizing over the polarization. All other coefficients show no shift in the distribution. The reason that the variation of the polarization in terms of the EFT coefficients is only slightly noticeable is due to the uncertainty of the polarization, which is still larger than the predicted variation of the polarization in terms of the EFT coefficients. More precise measurements of the polarization can provide valuable input for future combinations of measurements. In particular, measurements of the polarization directions P_x and P_y could provide unique information on the coefficient c_{tW}. Here, the more conservative method is chosen and the polarization is treated as a free parameter in this fit and marginalized when stating confidence regions of the EFT coefficients.

2.6 Previous Combinations

Many studies have been done in the past to constrain EFT coefficients by combining different measurements. In this section, a short review of the latest combinations that put constraints on one or more of the dimension 6 operator coefficients discussed in the previous sections is given.

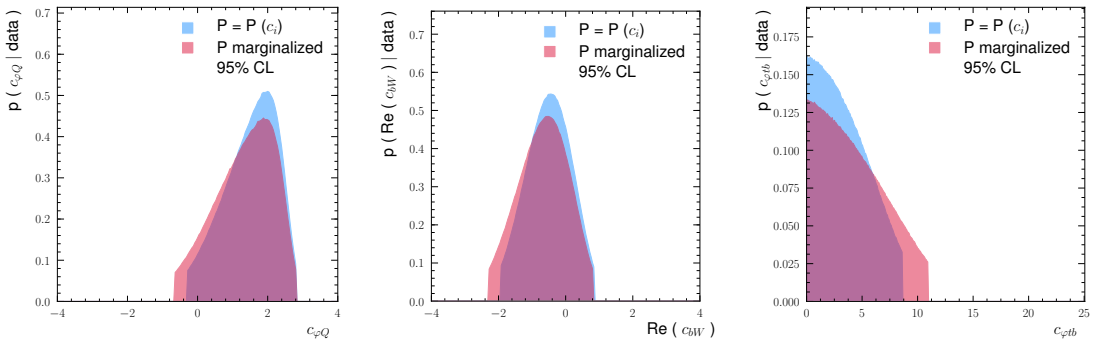

(a) (b) (c)

Figure 27: Comparison of the 1D probability distributions when varying the polarization according to Ref. [71] (red) and when marginalizing over the polarization (blue). Three of the EFT coefficients show slight shifts in their distributions, $c_{\varphi Q}^{(3)}$ (a), $\mathrm{Re}\,(c_{bW})$ (b), and $c_{\varphi tb}$ (c), all other coefficients do not change. All plots show a combination of W helicity fractions, single top decay distributions and 8 TeV cross sections.

Most recently, a combination of the top pair production cross section in association with a photon $\sigma\,(t\bar{t}\gamma)$ with the $\bar{B} \to X_s\gamma$ branching ratio was performed [73]. Limits were set on the EFT coefficients c_{uB}, c_{uG}, and c_{uW}. Both individual and marginalized limits are given. Individual limits are obtained by setting non-zero one coefficient at a time, while the marginalized limits come from a simultaneous fit of all three coefficients at once. Limits on the 90% confidence intervals on the coefficient $\widetilde{C}_{uW} = \frac{v^2}{\Lambda^2} c_{uW}$ range from approximately $\widetilde{C}_{uW} \in [-0.50, -0.18]\,, [-0.14, 1.4]$ for the marginalized limits, to $\widetilde{C}_{uW} \in [-0.4, 0.8]$ for the individual limits. In terms of the notation used in the analysis presented here, these limits translate

to $c_{uW} \in [-8.2, -3.0], [-2.3, 2.3]$ for the marginalized limits, to $c_{uW} \in [-6.6, 13.2]$ for the individual limits. Assumptions were made in that the coefficients were restricted to be real and no four-quark operators contribute. Correlations between the measurements were not calculated, but instead estimated by varying the correlation coefficient in the fit. It was found that the correlation can have an effect on the size of the confidence regions by as large as 30%, but the general shape and location is unchanged.

A more global analysis was performed by fitting more than 30 measurements to a total of 34 EFT coefficients [74]. Assumptions include that all coefficients are real and correlations between the measurements are not taken into account. The 95% confidence limits set by this global fit are $c_{\varphi Q}^{(3)} \in [-5.5, 5.8]$, $c_{\varphi tb} \in [-27, 8.7]$, $c_{bW} \in [-2.6, 3.1]$, $c_{tW} \in [-1.8, 0.9]$, and $c_{Qq}^{3,1} \in [-1.1, 1.3]$. These limits correspond to the marginalized limits. The individual limits on one coefficient at a time are given by $c_{\varphi Q}^{(3)} \in [-0.9, 0.6]$, $c_{\varphi tb} \in [-9.4, 9.5]$, $c_{bW} \in [-0.6, 0.2]$, $c_{tW} \in [-0.4, 0.2]$, and $c_{Qq}^{3,1} \in [-0.1, 0.09]$.

In addition, the single top decay distribution and W helicity fraction measurements set limits on the Wtb related EFT coefficients. These limits were stated in Eqs. 2.16–2.19 of Section 2.4.3 and Eq. 2.15 of Section 2.4.2, respectively.

2.7 Parameterization Of The Cross Section

In Section 2.4.1, the single top production cross section measurement was discussed and it was found that the inclusion of the cross sections in the combined fit requires that the expression for the cross sections in terms of the EFT coefficients is known. This section discusses the full parameterization of the cross section in terms

of the EFT coefficients and the calculation of the coefficients $\boldsymbol{\kappa}$, that are needed for this parameterization. In general, the cross section can be written as

$$\sigma_{\text{fid}}(\boldsymbol{g}) = \sigma_{\text{fid,SM}}\left(V_L^4 + \boldsymbol{g}\cdot\boldsymbol{\kappa}\right), \tag{2.26}$$

for the fiducial and

$$\sigma_{\text{tot}}(\boldsymbol{g}') = \sigma_{\text{tot,SM}}\left(V_L^2 + \boldsymbol{g}'\cdot\boldsymbol{\kappa}'\right), \tag{2.27}$$

for the total cross section. The vector $\boldsymbol{g} = \boldsymbol{g}(\boldsymbol{p})$ contains all possible combinations of EFT coefficients evaluated at a point in the EFT coefficient space, here defined as

$$\boldsymbol{p} = \left(\text{Re}\left(c_{tW}\right), c_{Qq}^{3,1}, \text{Re}\left(c_{\varphi tb}\right), \text{Re}\left(c_{bW}\right), \text{Im}\left(c_{tW}\right), \text{Im}\left(c_{bW}\right)\right). \tag{2.28}$$

Detailed expressions for $\boldsymbol{g}$ and $\boldsymbol{g}'$, the possible combinations of EFT coefficients for the fiducial and total cross sections in terms of $\boldsymbol{p}$ can be found in Appendix C.3. In case of the fiducial cross section, the components of $\boldsymbol{g}$ are products of four EFT coefficients. For the total cross section, the components are products of two EFT coefficients. The coefficients $\boldsymbol{\kappa}$ include all contributions to the cross sections that are not contained in the Standard Model cross section σ_{SM}. Therefore, to parameterize the cross section and include it into the combination, the coefficients $\boldsymbol{\kappa}$ need to be computed.

In the following, only the fiducial cross section is considered and therefore σ refers to σ_{fid}, unless otherwise stated. The calculation of the coefficients $\boldsymbol{\kappa}$ can be accomplished by first factoring out the SM-like coupling V_L. Then, $\boldsymbol{g}$ depends on the ratio of the remaining 6 EFT coefficients with respect to V_L. For the fiducial cross section, $\boldsymbol{g}$ has in principle

$$\binom{n+m}{n} = 210 \tag{2.29}$$

components, where $n = 4$ for a quartic function and $m = 6$ is the number of EFT coefficients. However, not all of the components in $\boldsymbol{g}$ contribute to the cross section. First of all, since the cross section is calculated in the 5 flavor-scheme with $m_b = 0$ only certain combinations of left- and right-handed couplings are non-zero. More specifically, if there is an odd number of left- or right-handed EFT coefficients in any component of $\boldsymbol{g}$ then this component vanishes. Secondly, since the cross section is a CP-conserving observable, imaginary parts of the EFT coefficients should only appear in either a square or quartic combination. Any component of $\boldsymbol{g}$ that is linear or cubic in the imaginary parts vanishes. Lastly, the four-quark coupling $c_{Qq}^{3,1}$ only contributes to the production of the top quark or anti-quark. Therefore, this coupling can only appear up to a quadratic in the cross section. After applying all of these restrictions, there are 61 remaining, non-zero components in $\boldsymbol{g}$, shown in Appendix C.3. In the next step, the 61 coefficients $\boldsymbol{\kappa}$ are calculated by solving a system of 61 coupled equations for the cross section evaluated at different values of the EFT coefficients $\boldsymbol{p}$. The system of equations is given by

$$\sigma_{\mathrm{MG},i} = \sigma_{\mathrm{fid,SM}} V_L^4 \left(1 + \sum_j g_j(p_i^{gen}) \kappa_j \right), \tag{2.30}$$

where, $j = 1, \ldots, 61$ and $\sigma_{\mathrm{MG},i}$ are cross sections calculated in MadGraph at 61 different coupling points p_i^{gen}. More on the calculation of the cross sections in MadGraph will be given in Section 2.8. In vector form this equation can be written as

$$\boldsymbol{\sigma}_{\mathrm{MG}} = \sigma_{\mathrm{fid,SM}} V_L^4 \left(\boldsymbol{J}_{1,61} + \boldsymbol{M} \cdot \boldsymbol{\kappa} \right), \tag{2.31}$$

where $\boldsymbol{J}_{1,61}$ is an all-ones column vector of length 61. The matrix $\boldsymbol{M}_{ij} = g_j(p_i^{gen})$ is a square matrix that has as its row elements all 61 combinations of EFT coefficients

where each row is evaluated at a different, generated point p_i^{gen}. Details on the generation of these points is given below. Further, in Eq. 2.31, V_L has been factored out, so the EFT coefficients in $\boldsymbol{g}$ and $\boldsymbol{M}$ are now ratios of EFT coefficients with respect to V_L. Then, the coefficients $\boldsymbol{\kappa}$ are simply given by inversion of Eq. 2.31 as

$$\boldsymbol{\kappa} = \boldsymbol{M}^{-1} \left(\frac{\boldsymbol{\sigma}_{\mathrm{MG}}}{\sigma_{\mathrm{fid,SM}}} - \boldsymbol{J}_{1,61} \right), \tag{2.32}$$

and the uncertainty on the coefficients $\boldsymbol{\kappa}$ is given by

$$\delta^2_{\kappa_j} = \frac{1}{\sigma^2_{\mathrm{fid,SM}}} \left[\left(\boldsymbol{M}^{-1} \frac{\boldsymbol{\sigma}_{\mathrm{MG}}}{\sigma_{\mathrm{fid,SM}}} \right)^2_j \delta^2_{\sigma_{\mathrm{fid,SM}}} + \left(\boldsymbol{M}^{-1} \mathcal{C}_{\sigma_{\mathrm{MG}}} \left(\boldsymbol{M}^{-1} \right)^T \right)_{jj} \right], \tag{2.33}$$

where $\delta_{\sigma_{\mathrm{fid,SM}}}$ is the uncertainty of the Standard Model cross section and $\mathcal{C}_{\sigma_{\mathrm{MG}}}$ is the covariance matrix of the MadGraph calculation. Table 12 lists all coefficients $\boldsymbol{\kappa}$ and their uncertainties. At this point, the question arises on how to choose the 61 points at which to evaluate the cross sections. From Eq. 2.32 it is clear that the matrix $\boldsymbol{M}$ which is constructed from the 61 generated points, needs to be invertible. Further, the generated points should be spread throughout the coupling space in such a way as to minimize the uncertainty on the cross section evaluated at a point of interest. Points of interest in this case are points within the EFT parameter space other than the 61 generated points. In other words, the maximum uncertainty of the cross section within the parameter space should be minimized. The next section will discuss in detail how the uncertainty is calculated and ways to optimize the generation of the 61 points to minimize the uncertainty.

	$\kappa(t)$	$\delta\kappa(t)$	$\kappa(\bar{t})$	$\delta\kappa(\bar{t})$	$g\,(p)$
κ_1	0.018929	0.000287	-0.073498	0.000216	$c_{tW}^{\mathrm{R}} V_L^3$
κ_2	-0.459320	0.000657	-0.372440	0.000241	$c_{Qq}^{3,1} V_L^3$
κ_3	0.030647	0.000097	0.017244	0.000052	$\left(c_{tW}^{\mathrm{R}}\right)^2 V_L^2$
κ_4	-0.013769	0.000068	0.004523	0.000048	$c_{Qq}^{3,1} c_{tW}^{\mathrm{R}} V_L^2$
κ_5	0.116716	0.000167	0.065442	0.000041	$\left(c_{Qq}^{3,1}\right)^2 V_L^2$
κ_6	0.002465	0.000008	0.002197	0.000004	$V_L^2 c_{\varphi tb}^2$
κ_7	-0.000408	0.000012	-0.002479	0.000009	$c_{bW}^{\mathrm{R}} V_L^2 c_{\varphi tb}$
κ_8	0.017933	0.000057	0.025086	0.000037	$\left(c_{bW}^{\mathrm{R}}\right)^2 V_L^2$
κ_9	0.005544	0.000059	0.002239	0.000041	$\left(c_{tW}^{\mathrm{I}}\right)^2 V_L^2$
κ_{10}	0.007029	0.000055	0.016299	0.000041	$\left(c_{bW}^{\mathrm{I}}\right)^2 V_L^2$
κ_{11}	-0.000095	0.000003	0.000325	0.000002	$\left(c_{tW}^{\mathrm{R}}\right)^3 V_L$
κ_{12}	0.000470	0.000002	0.000426	0.000002	$c_{Qq}^{3,1} \left(c_{tW}^{\mathrm{R}}\right)^2 V_L$
κ_{13}	-0.000910	0.000002	-0.000421	0.000001	$\left(c_{Qq}^{3,1}\right)^2 c_{tW}^{\mathrm{R}} V_L$
κ_{14}	0.000006	0.000000	-0.000003	0.000000	$c_{tW}^{\mathrm{R}} V_L c_{\varphi tb}^2$
κ_{15}	-0.000034	0.000000	-0.000016	0.000000	$c_{bW}^{\mathrm{R}} c_{tW}^{\mathrm{R}} V_L c_{\varphi tb}$
κ_{16}	-0.000258	0.000002	-0.000134	0.000001	$\left(c_{bW}^{\mathrm{R}}\right)^2 c_{tW}^{\mathrm{R}} V_L$

Continued on next page

Table 12: Coefficients κ_i and uncertainties $\delta\kappa_i$ for the 8 TeV fiducial top quark and anti-quark cross section. Also shown is the combination of EFT coefficients $g_i\,(p)$ associated with each κ_i.

	$\kappa(t)$	$\delta\kappa(t)$	$\kappa(\bar{t})$	$\delta\kappa(\bar{t})$	$g\,(p)$
κ_{17}	0.000261	0.000001	0.000235	0.000001	$\left(c_{tW}^{\mathrm{I}}\right)^2 c_{tW}^{\mathrm{R}} V_L$
κ_{18}	-0.000107	0.000002	-0.000298	0.000002	$\left(c_{bW}^{\mathrm{I}}\right)^2 c_{tW}^{\mathrm{R}} V_L$
κ_{19}	-0.000016	0.000000	0.000004	0.000000	$c_{Qq}^{3,1} V_L c_{\varphi tb}^2$
κ_{20}	-0.000020	0.000000	-0.000008	0.000000	$c_{Qq}^{3,1} c_{bW}^{\mathrm{R}} V_L c_{\varphi tb}$
κ_{21}	0.000157	0.000003	-0.000099	0.000002	$c_{Qq}^{3,1} \left(c_{bW}^{\mathrm{R}}\right)^2 V_L$
κ_{22}	0.000553	0.000002	0.000359	0.000001	$c_{Qq}^{3,1} \left(c_{tW}^{\mathrm{I}}\right)^2 V_L$
κ_{23}	0.000148	0.000002	-0.000092	0.000002	$c_{Qq}^{3,1} \left(c_{bW}^{\mathrm{I}}\right)^2 V_L$
κ_{24}	-0.000027	0.000000	-0.000004	0.000000	$c_{bW}^{\mathrm{I}} c_{tW}^{\mathrm{I}} V_L c_{\varphi tb}$
κ_{25}	0.000114	0.000001	0.000030	0.000001	$c_{bW}^{\mathrm{I}} c_{bW}^{\mathrm{R}} c_{tW}^{\mathrm{I}} V_L$
κ_{26}	-0.000084	0.000001	-0.000014	0.000001	$\left(c_{tW}^{\mathrm{R}}\right)^4$
κ_{27}	0.000072	0.000001	0.000018	0.000000	$c_{Qq}^{3,1} \left(c_{tW}^{\mathrm{R}}\right)^3$
κ_{28}	-0.000096	0.000000	-0.000078	0.000000	$\left(c_{Qq}^{3,1}\right)^2 \left(c_{tW}^{\mathrm{R}}\right)^2$
κ_{29}	-0.000003	0.000000	-0.000003	0.000000	$\left(c_{tW}^{\mathrm{R}}\right)^2 c_{\varphi tb}^2$
κ_{30}	-0.000018	0.000000	-0.000014	0.000000	$c_{bW}^{\mathrm{R}} \left(c_{tW}^{\mathrm{R}}\right)^2 c_{\varphi tb}$
κ_{31}	-0.000041	0.000000	-0.000025	0.000000	$\left(c_{bW}^{\mathrm{R}}\right)^2 \left(c_{tW}^{\mathrm{R}}\right)^2$
κ_{32}	-0.000004	0.000000	0.000010	0.000000	$\left(c_{tW}^{\mathrm{I}}\right)^2 \left(c_{tW}^{\mathrm{R}}\right)^2$

Continued on next page

Table 12: Coefficients κ_i and uncertainties $\delta\kappa_i$ for the 8 TeV fiducial top quark and anti-quark cross section. Also shown is the combination of EFT coefficients $g_i\,(p)$ associated with each κ_i

	$\kappa(t)$	$\delta\kappa(t)$	$\kappa(\bar{t})$	$\delta\kappa(\bar{t})$	$g\,(p)$
κ_{33}	-0.000036	0.000000	0.000002	0.000000	$\left(c_{bW}^{\mathrm{I}}\right)^2 \left(c_{tW}^{\mathrm{R}}\right)^2$
κ_{34}	0.000001	0.000000	0.000002	0.000000	$c_{Qq}^{3,1} c_{tW}^{\mathrm{R}} c_{\varphi tb}^2$
κ_{35}	-0.000002	0.000000	-0.000000	0.000000	$c_{Qq}^{3,1} c_{bW}^{\mathrm{R}} c_{tW}^{\mathrm{R}} c_{\varphi tb}$
κ_{36}	-0.000041	0.000000	-0.000048	0.000000	$c_{Qq}^{3,1} \left(c_{bW}^{\mathrm{R}}\right)^2 c_{tW}^{\mathrm{R}}$
κ_{37}	-0.000040	0.000000	-0.000023	0.000000	$c_{Qq}^{3,1} \left(c_{tW}^{\mathrm{I}}\right)^2 c_{tW}^{\mathrm{R}}$
κ_{38}	0.000030	0.000000	0.000031	0.000000	$c_{Qq}^{3,1} \left(c_{bW}^{\mathrm{I}}\right)^2 c_{tW}^{\mathrm{R}}$
κ_{39}	-0.000002	0.000000	-0.000001	0.000000	$c_{bW}^{\mathrm{I}} c_{tW}^{\mathrm{I}} c_{tW}^{\mathrm{R}} c_{\varphi tb}$
κ_{40}	0.000008	0.000000	0.000001	0.000000	$c_{bW}^{\mathrm{I}} c_{bW}^{\mathrm{R}} c_{tW}^{\mathrm{I}} c_{tW}^{\mathrm{R}}$
κ_{41}	-0.000003	0.000000	-0.000003	0.000000	$\left(c_{Qq}^{3,1}\right)^2 c_{\varphi tb}^2$
κ_{42}	0.000019	0.000000	0.000009	0.000000	$\left(c_{Qq}^{3,1}\right)^2 c_{bW}^{\mathrm{R}} c_{\varphi tb}$
κ_{43}	0.000051	0.000000	0.000041	0.000000	$\left(c_{Qq}^{3,1}\right)^2 \left(c_{bW}^{\mathrm{R}}\right)^2$
κ_{44}	0.000023	0.000000	-0.000008	0.000000	$\left(c_{Qq}^{3,1}\right)^2 \left(c_{tW}^{\mathrm{I}}\right)^2$
κ_{45}	0.000006	0.000000	-0.000008	0.000000	$\left(c_{Qq}^{3,1}\right)^2 \left(c_{bW}^{\mathrm{I}}\right)^2$
κ_{46}	-0.000000	0.000000	-0.000000	0.000000	$c_{Qq}^{3,1} c_{bW}^{\mathrm{I}} c_{tW}^{\mathrm{I}} c_{\varphi tb}$
κ_{47}	-0.000002	0.000000	0.000001	0.000000	$c_{Qq}^{3,1} c_{bW}^{\mathrm{I}} c_{bW}^{\mathrm{R}} c_{tW}^{\mathrm{I}}$
κ_{48}	-0.000001	0.000000	-0.000000	0.000000	$c_{\varphi tb}^4$

Continued on next page

Table 12: Coefficients κ_i and uncertainties $\delta\kappa_i$ for the 8 TeV fiducial top quark and anti-quark cross section. Also shown is the combination of EFT coefficients $g_i\,(p)$ associated with each κ_i

	$\kappa(t)$	$\delta\kappa(t)$	$\kappa(\bar{t})$	$\delta\kappa(\bar{t})$	$g\,(p)$
κ_{49}	0.000001	0.000000	0.000001	0.000000	$c_{bW}^{\mathrm{R}} c_{\varphi tb}^{3}$
κ_{50}	-0.000007	0.000000	-0.000006	0.000000	$\left(c_{bW}^{\mathrm{R}}\right)^{2} c_{\varphi tb}^{2}$
κ_{51}	-0.000001	0.000000	0.000002	0.000000	$\left(c_{tW}^{\mathrm{I}}\right)^{2} c_{\varphi tb}^{2}$
κ_{52}	-0.000002	0.000000	0.000002	0.000000	$\left(c_{bW}^{\mathrm{I}}\right)^{2} c_{\varphi tb}^{2}$
κ_{53}	-0.000003	0.000000	-0.000001	0.000000	$\left(c_{bW}^{\mathrm{R}}\right)^{3} c_{\varphi tb}$
κ_{54}	-0.000003	0.000000	-0.000002	0.000000	$c_{bW}^{\mathrm{R}} \left(c_{tW}^{\mathrm{I}}\right)^{2} c_{\varphi tb}$
κ_{55}	-0.000006	0.000000	0.000003	0.000000	$\left(c_{bW}^{\mathrm{I}}\right)^{2} c_{bW}^{\mathrm{R}} c_{\varphi tb}$
κ_{56}	-0.000021	0.000000	0.000017	0.000000	$\left(c_{bW}^{\mathrm{R}}\right)^{4}$
κ_{57}	0.000020	0.000000	-0.000013	0.000000	$\left(c_{bW}^{\mathrm{R}}\right)^{2} \left(c_{tW}^{\mathrm{I}}\right)^{2}$
κ_{58}	-0.000014	0.000000	-0.000062	0.000000	$\left(c_{bW}^{\mathrm{I}}\right)^{2} \left(c_{bW}^{\mathrm{R}}\right)^{2}$
κ_{59}	0.000007	0.000000	0.000020	0.000000	$\left(c_{tW}^{\mathrm{I}}\right)^{4}$
κ_{60}	0.000065	0.000000	0.000049	0.000000	$\left(c_{bW}^{\mathrm{I}}\right)^{2} \left(c_{tW}^{\mathrm{I}}\right)^{2}$
κ_{61}	0.000037	0.000001	0.000010	0.000000	$\left(c_{bW}^{\mathrm{I}}\right)^{4}$

Table 12: Coefficients κ_i and uncertainties $\delta\kappa_i$ for the 8 TeV fiducial top quark and anti-quark cross section. Also shown is the combination of EFT coefficients $g_i\,(p)$ associated with each κ_i

2.7.1 Uncertainty Of The Cross Section

Eq. 2.26 gives the fiducial cross section in terms of the EFT coefficients. However, since the coefficients $\boldsymbol{\kappa}$ have been determined through a minimal set of generated points, any cross section that lies between the generated points might have a sizable uncertainty due to interpolation effects. In this section, the uncertainty on the cross section for any point in the parameter space of the EFT coefficients is derived. To start, Eq. 2.26 is rewritten in terms of the cross sections generated in MadGraph as

$$\sigma_{\text{fid}}\left(\boldsymbol{g}\right) = \sigma_{\text{fid,SM}} V_L^4 \left[1 + \boldsymbol{g}\boldsymbol{M}^{-1}\left(\frac{\boldsymbol{\sigma}_{\text{MG}}}{\sigma_{\text{fid,SM}}} - \boldsymbol{J}\right)\right] \tag{2.34}$$

where again V_L is factored out and $\boldsymbol{\sigma}_{\text{MG}}$ are the cross sections calculated in MadGraph. The uncertainty squared on the cross section $\sigma_{\text{fid}}\left(\boldsymbol{g}\right)$ is given by

$$\delta^2_{\sigma_{\text{fid}}} = \left(\frac{\partial\sigma_{\text{fid}}\left(\boldsymbol{g}\right)}{\partial\sigma_{\text{fid,SM}}}\right)^2 \delta^2_{\sigma_{\text{fid,SM}}} + \left(\frac{\partial\sigma_{\text{fid}}\left(\boldsymbol{g}\right)}{\partial\boldsymbol{\sigma}_{\text{MG}}}\right) \mathcal{C}_{\sigma_{\text{MG}}} \left(\frac{\partial\sigma_{\text{fid}}\left(\boldsymbol{g}\right)}{\partial\boldsymbol{\sigma}_{\text{MG}}}\right)^T, \tag{2.35}$$

where $\delta_{\sigma_{\text{fid,SM}}}$ is the uncertainty of the SM cross section and $\mathcal{C}_{\sigma_{\text{MG}}}$ is the variance matrix of the MadGraph calculation. Taking the derivatives in Eq. 2.35 we get

$$\frac{\partial\sigma_{\text{fid}}\left(\boldsymbol{g}\right)}{\partial\sigma_{\text{MG},j}} = V_L^4 \boldsymbol{g}_k \boldsymbol{M}^{-1}_{k,j}, \tag{2.36}$$

and

$$\frac{\partial\sigma_{\text{fid}}\left(\boldsymbol{g}\right)}{\partial\sigma_{\text{fid,SM}}} = V_L^4\left(1 - \boldsymbol{g}\boldsymbol{M}^{-1}\boldsymbol{J}\right) \tag{2.37}$$

where $\boldsymbol{g}^T\boldsymbol{M}^{-1}\boldsymbol{J} = \sum_k \left(\boldsymbol{g}\boldsymbol{M}^{-1}\right)_k$ is the sum of the elements of the vector $\boldsymbol{g}^T\boldsymbol{M}^{-1}$. Then, Eq. 2.35 takes the form

$$\delta^2_{\sigma_{\text{fid}}} = V_L^8\left(1 - \boldsymbol{g}\boldsymbol{M}^{-1}\boldsymbol{J}\right)^2 \delta^2_{\sigma_{\text{fid,SM}}} + V_L^8\left(\boldsymbol{g}\boldsymbol{M}^{-1}\right)\mathcal{C}_{\sigma_{\text{MG}}}\left(\boldsymbol{g}\boldsymbol{M}^{-1}\right)^T. \tag{2.38}$$

This equation allows to calculate the uncertainty on the fiducial cross section at any point in the parameter space of the EFT coefficients. To evaluate the behavior of the uncertainty of the cross section in the EFT coefficients parameter space, a grid search over the parameters was done to confirm that the uncertainty does not blow up at any point. This grid search was done as follows. Each EFT parameter was varied independently between its minimum and maximum value. For each set of parameters, the fiducial cross section and the uncertainty on the cross section at that point were calculated. If the cross section plus its uncertainty at that point is smaller than half the Standard Model cross section, that point is disregarded. The same applies to a point where the cross section minus the uncertainty is twice the Standard Model cross section. In particular, this excludes cross sections that are very small and have a relatively large uncertainty. These uncertainties are not compatible with the measured cross sections and therefore will not enter the fit. In the remaining parameter region, the relative uncertainty on the cross section is calculated.

It is found, that the relative uncertainty does not go above 0.5%. In fact, the highest values of the uncertainties are in the regions where at least several EFT coefficients take on values at the larger end of their ranges. For the parameter region, where none of the EFT coefficients is larger that half its allowed value, the maximum uncertainty is below 0.3%.

2.7.2 Generation Of The Set Of Points

To generate the set of 61 points, the range of the EFT coefficients is first set to be $-1 \leq c \leq 1$ for the coefficients $c = c_{\varphi Q}^{(3)}$, $\mathrm{Re}\,(c_{tW})$, $\mathrm{Re}\,(c_{tW})$, $\mathrm{Im}\,(c_{tW})$ and $c_{Qq}^{3,1}$ and $0 \leq c \leq 1$ for $c_{\varphi tb}$ and $\mathrm{Im}\,(c_{tW})$. The reason for the positive range of $c_{\varphi tb}$ is that this coefficient is defined to be positive, see Section 2.5. The imaginary part

of the coefficient c_{tW} can be restricted to positive values, since it always appears as either a square or quartic with itself or the imaginary part of c_{bW}. Therefore, only the relative sign between the two imaginary parts contributes. Once an optimal set of points is found, the range of the couplings can be scaled to their desired values. This scaling does not affect the invertibility of the matrix $\boldsymbol{M}$ and therefore does not affect the set of points. The generation of the set of points takes part in three stages. First, an initial set of points is generated. This initial set is chosen manually in such a way that

1. as many points as possible are set at the corners and edges of the parameter space,
2. the resulting matrix $\boldsymbol{M}$ is not singular.

In the second stage, the initial set of points is optimized by moving one point at a time while

1. reducing the 2-norm condition number of the matrix $\boldsymbol{M}$ constructed from the set of points. The condition number gives a measure on the uncertainty of the result of the matrix inversion;
2. reducing the maximum approximate uncertainty of the cross section in the parameter space.

The approximate uncertainty of the cross section is given by

$$\delta_\sigma^2 = \delta_{\sigma_{\mathrm{SM}}}^2 \left[\left(1 - \boldsymbol{g}\boldsymbol{M}^{-1}\boldsymbol{J}\right)^2 + \left(\boldsymbol{g}\boldsymbol{M}^{-1}\right) \right]. \tag{2.39}$$

This approximate uncertainty is derived from the full uncertainty of the cross section at any point in the parameter space, Eq. 2.38, by assuming the uncertainty of any cross section in the parameter space is equal to the uncertainty of the Standard

Model cross section. This is certainly not the case and the uncertainty can deviate significantly from the Standard Model uncertainty. However, the approximate uncertainty can still give a measure on how large the uncertainty at a point in the parameter space grows with respect to the uncertainty of the Standard Model cross section. It also serves as a measure to determine the uncertainty at a point before and after moving one point. After the second stage, the set of points is already optimized to a good degree. Therefore, this set is used in the third stage, to perform the calculation of the cross sections in Eq. 2.31. This calculation is done in MadGraph with a reduced number of events. In this particular case, the calculation was done with 50,000 events. The reason to keep the number of events low is that a full calculation in MadGraph is time and resource consuming and should only be done in the last step, when the most optimal set of points is found. Once the calculation is done the cross section at any point in the EFT coefficient space can be parameterized according to Eq. 2.34 and the uncertainty is given by Eq. 2.38. From this uncertainty, another approximate uncertainty can be derived, that utilizes the cross sections and coefficients $\boldsymbol{\kappa}$ previously calculated.

For N generated events, the statistical uncertainty δ_i on the cross section σ_i is

$$\delta_i = \frac{\sigma_i}{\sqrt{N}}, \tag{2.40}$$

and the relative uncertainty on the cross section should not vary too much in the EFT coefficient space if all cross sections are calculated with the same number of events. Then, the relative uncertainty of the cross section at any point can be related to the relative uncertainty of the Standard Model cross section as

$$\frac{\delta^2_{\sigma_{\text{fid}}}}{\sigma^2_{\text{fid}}} \approx \frac{\delta^2_{\sigma_{\text{fid,SM}}}}{\sigma^2_{\text{fid,SM}}} \tag{2.41}$$

It is then possible to write the variance matrix $\mathcal{C}_{\sigma_{\mathrm{MG}}}$ in Eq. 2.38 as

$$\begin{aligned}
\left(\mathcal{C}_{\sigma_{\mathrm{MG}}}\right)_{ij} &= \delta^2_{\sigma_{\mathrm{MG},i}}\delta_{ij} \\
&\approx \frac{\sigma^2_{\mathrm{MG},i}}{N}\delta_{ij} \\
&\approx \frac{\delta^2_{\sigma_{\mathrm{fid,SM}}}}{\sigma^2_{\mathrm{fid,SM}}}\sigma^2_{\mathrm{MG},i}\delta_{ij}, \\
\mathcal{C}_{\sigma_{\mathrm{MG}}} &\approx \frac{\delta^2_{\sigma_{\mathrm{fid,SM}}}}{\sigma^2_{\mathrm{fid,SM}}}\boldsymbol{I}\bar{\boldsymbol{\sigma}}_{\mathrm{MG}}.
\end{aligned} \tag{2.42}$$

Here, $\delta^2_{\sigma_{\mathrm{MG},i}}$ are the uncertainties squared of the generated cross sections and δ_{ij} is the Kronecker delta. $\boldsymbol{I}$ is the identity matrix and

$$\bar{\boldsymbol{\sigma}}_{\mathrm{MG}} = \left\{\sigma^2_{\mathrm{MG},0}, \sigma^2_{\mathrm{MG},1}, \sigma^2_{\mathrm{MG},2}, \sigma^2_{\mathrm{MG},3}, \dots\right\} \tag{2.43}$$

is the vector that holds the squares of the generated cross sections. Then, the uncertainty squared on $\sigma_{\mathrm{fid}}(\boldsymbol{g})$ in Eq. 2.38 becomes

$$\delta^2_{\sigma_{\mathrm{fid}}} = V_L^8\left(1-\boldsymbol{g}\boldsymbol{M}^{-1}\boldsymbol{J}\right)^2\delta^2_{\sigma_{\mathrm{fid,SM}}} + V_L^8\left(\boldsymbol{g}\boldsymbol{M}^{-1}\right)\frac{\delta^2_{\sigma_{\mathrm{fid,SM}}}}{\sigma^2_{\mathrm{fid,SM}}}\left(\boldsymbol{I}\bar{\boldsymbol{\sigma}}_{\mathrm{MG}}\right)\left(\boldsymbol{g}\boldsymbol{M}^{-1}\right)^T. \tag{2.44}$$

Further, the relative uncertainty on $\sigma_{\mathrm{fid}}(\boldsymbol{g})$ can be calculated as

$$\frac{\delta^2_{\sigma_{\mathrm{fid}}}}{\sigma_{\mathrm{fid}}(\boldsymbol{g})^2} = \frac{\delta^2_{\sigma_{\mathrm{fid,SM}}}}{\sigma_{\mathrm{fid}}(\boldsymbol{g})^2}V_L^8\left[\left(1-\boldsymbol{g}\boldsymbol{M}^{-1}\boldsymbol{J}\right)^2 + \left(\boldsymbol{g}\boldsymbol{M}^{-1}\right)\frac{\boldsymbol{I}\bar{\boldsymbol{\sigma}}_{\mathrm{MG}}}{\sigma^2_{\mathrm{fid,SM}}}\left(\boldsymbol{g}\boldsymbol{M}^{-1}\right)^T\right]. \tag{2.45}$$

Plugging in the general expression for the cross section $\sigma_{\mathrm{fid}}(\boldsymbol{g}) = \sigma_{\mathrm{fid,SM}}(1+\boldsymbol{g}\cdot\boldsymbol{\kappa})$ this leads to

$$\frac{\delta^2_{\sigma_{\mathrm{fid}}}}{\sigma_{\mathrm{fid}}(\boldsymbol{g})^2} = \frac{\delta^2_{\sigma_{\mathrm{fid,SM}}}}{\sigma^2_{\mathrm{fid,SM}}}\frac{V_L^8}{(1+\boldsymbol{g}\cdot\boldsymbol{\kappa})^2}\left[\left(1-\boldsymbol{g}\boldsymbol{M}^{-1}\boldsymbol{J}\right)^2 + \left(\boldsymbol{g}\boldsymbol{M}^{-1}\right)\frac{\boldsymbol{I}\bar{\boldsymbol{\sigma}}_{\mathrm{MG}}}{\sigma^2_{\mathrm{fid,SM}}}\left(\boldsymbol{g}\boldsymbol{M}^{-1}\right)^T\right]. \tag{2.46}$$

In this expression, $\bar{\boldsymbol{\sigma}}_{\mathrm{MG}}$ depends on the generated cross sections and can be expressed as

$$\boldsymbol{\sigma}_{\mathrm{MG},i} = \sigma_{\mathrm{fid,SM}} \left(1 + \boldsymbol{g}_i' \cdot \boldsymbol{\kappa}\right), \tag{2.47}$$

where $\boldsymbol{g}_i'$ depends on the choice of the ith point generated in the second stage. Eq. 2.46 now only depends on the coefficients $\boldsymbol{\kappa}$ and the choice of points generated in the second stage. Even though the set calculated in the second stage and thereby the coefficients $\boldsymbol{\kappa}$ are not the most optimal set, they do provide a good approximation for the uncertainties of the cross sections. Finally, Eq. 2.46 can be used to find a new set of points that minimizes the relative uncertainty at every point in the parameter space.

2.8 Monte Carlo Simulations Of The Cross Section

In the previous section the generation of a set of points to calculate the coefficients $\boldsymbol{\kappa}$ in the parameterization of the fiducial cross section defined in Eq. 2.26 was discussed. In this section, the generated set of points is used to compute the coefficients $\boldsymbol{\kappa}$ according to Eq. 2.32. Each entry in $\boldsymbol{\sigma}_{\mathrm{MG}}$ of Eq. 2.32 corresponds to a cross section calculated at a specific point $\boldsymbol{p}$ in the EFT coefficient space, where $\boldsymbol{p}$ is defined in Eq. 2.28. This set of cross sections corresponding the the set of generated points was calculated in MadGraph5 (version 2.6.2) [56, 57]. The events are then decayed using MadSpin [60] and subsequently showered with Pythia8 (v8.235) [66]. MadSpin ensures that the spin correlations between the top quark and its decay products are preserved. Event generation and showering was done in

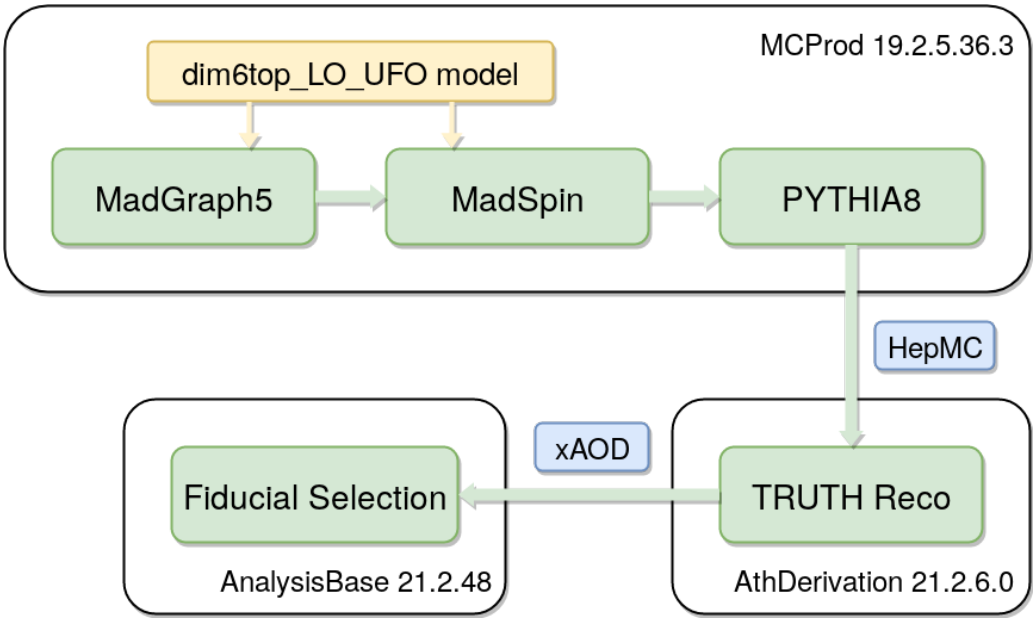

Figure 28: Workflow of the Monte Carlo generation. Events are generated in MadGraph5 then decayed with MadSpin. Both steps use the `dim6top_LO_UFO` model. Events are then showered in Pythia8 which generated HepMC and xAOD files as output. The xAOD files are then reconstructed at TRUTH level. The reconstructed events are then processed by an Athena algorithm for fiducial selection.

Athena [75] release `MCProd` 19.2.5.36.3. To include the effect of the dimension 6 operators, the Universal FeynRules Output (UFO) model `dim6top_LO_UFO` Ref. [17] was used. This UFO model is an implementation of all dimension 6 operators including at least one top quark and is based on the Warsaw basis of dimension 6 operators [16]. In the last step, the showered events are reconstructed at truth level to convert

SM inputs	
$\alpha_{\mathrm{EW}}^{-1}$	132.2332298
G_F	1.16639×10^{-5} GeV^{-2}
α_s	0.1181
Masses	
m_b	0.0
m_t	172.5 GeV
PDF set	
PDF	CT10 [76]
EFT inputs	
Λ	1 TeV

Table 13: Input values for the MadGraph event generation.

the final state particles into physics objects that are measured in the detector. The complete workflow from event generation to fiducial selection is shown in Figure 28. Also show are the data formats of the output after each section. More details on the data formats are given below. In the following, details of the individual steps of this event generation chain are given.

Matrix Element Generator: The generation of the top quark or anti-quark in MadGraph is according to the 5 flavor-scheme t-channel processes shown in

Figure 5 in Section 2.4.1

$$pp \to tj, \quad pp \to \bar{t}j, \tag{2.48}$$

where the proton and spectator jet are defined as

$$p = \left\{u, \bar{u}, d, \bar{d}, s, \bar{s}, c, \bar{c}, b, \bar{b}\right\}, \tag{2.49}$$

$$j = \left\{u, \bar{u}, d, \bar{d}, s, \bar{s}, c, \bar{c}\right\}. \tag{2.50}$$

The spectator jet j is a jet initiated by a light quark. All input values for the event generation are given in Table 13. Some of these input values were chosen in such a way as to reproduce known physical quantities. In particular, the Fermi constant G_F (Eq. 1.15) and α_{EW}^{-1} (Eq. 1.19) are adjusted such that the W boson mass is set to $m_W = 80.39$ GeV. This also fixes the value of the vacuum expectation value to $v = 246.2$ GeV. The renormalization and factorization scale is set to its default value. By default, both scales are calculated event-by-event according to

$$\mu_R = \mu_F = \sqrt{m^2 + p_T^2}, \tag{2.51}$$

where μ_R is the renormalization scale and μ_F is the factorization scale defined in Section 1.1.1. Eq. 2.51 is used as is for a single particle and corresponds to the geometric mean for a pair of heavy particles. In case of a massless particle the renormalization and factorization scales are equal to the transverse momentum of that particle. With these settings, a total of one million events has been generated for each of the 61 generated points in the EFT parameter space plus the Standard Model point. After the event generation in MadGraph, the top quark is then decayed using MadSpin according to the decay chain

$$t \to Wb, \quad W \to \ell\nu \tag{2.52}$$

where $\ell = e, \mu, \tau$ and ν_ℓ is the respective neutrino. The top quark is assumed to decay into a W boson and a b quark 100% of the time. This is due to the relative size of the CKM matrix elements V_{tb}, V_{ts} and, V_{td} as discussed in Section 1.1 and Section 1.3.2.1. No restrictions are made for the decay of the tau lepton, which decays both leptonically and hadronically. The missing lepton in the case of a hadronic decay of the tau lepton is taken care of in the fiducial event selection, discussed further down in this section.

Showering and Hadronization: After the events have been generated and the top quarks are decayed, the events are showered using PYTHIA8 to account for initial and final state radiation. PYTHIA8 showers all remaining unstable particles such as the b quarks and tau leptons. In addition to the showering, PYTHIA8 also adds initial and final state radiation to the events. See Section 2.3 for more details on Monte Carlo event generation.

Reconstruction: After showering, the event file only consists of stable particles that can be measured in the detector. In principle, the events need to be passed though detector simulation and reconstruction. Full detector simulation and reconstruction however is computationally very expensive. For this analysis, a truth reconstruction is sufficient. In truth reconstruction, all final state particles that are stored in a HepMC [77] format after showering are converted into an xAOD [78] format. The xAOD format stores the physics objects in terms of physics analysis objects such as jets and dressed leptons that are reconstructed from the HepMC record. The physics analysis objects can then be used to perform the fiducial selection. The main physics object containers used in this analysis are the *TruthElectrons* and *TruthMuons* container, which hold the records of the electrons and muons, respectively, and the truth jet container. Specifically, the truth jets used are the *AntiKt4TruthDressedWZJets*. The jets stored in this con-

tainer are small-R jets with an anti-k_t radius 0.4 and a transverse momentum of $p_T > 20$ GeV. To identify b-tagged jets, the *TrueFlavor* decoration is used. This corresponds to a merging of the two decorations, one by the Heavy Flavor (HF) tagging group for identifying a jet as b- or c-tagged at particle level and the other by the jet group for identifying a jet as quark- or gluon-initiated. Truth reconstruction was done in Athena release `AthDerivation` 21.2.6.0.

Once the reconstructed data sets were generated, the fiducial cuts were applied. For that, an Athena algorithm using Athena release `AnalysisBase` 21.2.48 was developed. The fiducial acceptance was then calculated from the total number of events generated N_{tot} and the number of events that passed the fiducial cuts N_{fid} as

$$A_{\text{fid}} = \frac{N_{\text{fid}}}{N_{\text{tot}}}. \tag{2.53}$$

The fiducial cuts are defined in such a way as to resemble the experiments constraints as closely as possible. Here, a short review of the fiducial cuts is given.

Decay Chain: As discussed before, the top quark is assumed to decay into a W boson and a b-quark 100% of the time. The W subsequently decays leptonically into an electron, muon or tau and the respective neutrino. In case of the decay into a tau lepton, only those events pass the fiducial cuts, where the tau decays leptonically into an electron or muon.

Leptons: Exactly one electron or muon with transverse momentum of $p_{\text{T}} > 25$ GeV and $|\eta| < 2.5$ is required. In principle, the decay chain is defined in such a way that the W boson only decays leptonically. However, in the case of a hadronic tau, there is no lepton associated with the W decay and the event is a background event.

Jets: There have to be two jets with a transverse momentum of $p_{\mathrm{T}} > 30$ GeV. Exactly one of the jets is required to be tagged as a b-jet. In addition, the light jet is required to lie within $|\eta| < 4.5$ and the b-jet is required to lie within $|\eta| < 2.5$.

Separation: If the lepton is found within a cone size of $\Delta R < 0.4$ of a jet the event is removed since the lepton is likely to be originated from that jet. Here, ΔR is given by $\Delta R = \sqrt{(\Delta\eta)^2 + (\Delta\phi)^2}$.

Invariant Mmass: The invariant mass of the lepton - b-jet system is required to be $m_{\ell b} < 160$ GeV. This is because current Monte Carlo event generators are not able to model off-shell effect of the top decay above this region.

With this, the fiducial cross section at each point in the EFT parameter space was calculated according to Eq. 2.8 and the coefficients $\boldsymbol{\kappa}$ used as input for the fit were calculated as described in Section 2.7.

To verify the calculation, coefficients $\hat{\kappa}$ calculated at 7 TeV and 14 TeV for the total cross section have been compared to the literature. The coefficients for the 7 TeV cross section are compared to the coefficients taken from the default example in the EFT*fitter* code [79]. A comparison is given in Table 15 where sign differences in the definition of the dim. 6 operators as discussed in Section 1.2 are taken into account. The coefficients of the 14 TeV cross section are compared with coefficients calculated in Ref. [18] and shown in Table 14. Again, sign differences from different definitions of the dim. 6 operators are taken into account. In both cases, generally good agreement between the coefficients $\boldsymbol{\kappa}$ is found. One sign difference is present in the coefficients $\boldsymbol{\kappa}$ of the 14 TeV cross section. The coefficient corresponding to the cross term between V_R and g_L in the top anti-quark cross section has an opposite sign. This does not occur when comparing the coefficients with EFT*fitter*.

	MG5 $\sigma(tj)$	Ref. $\sigma(tj)$	MG5 $\sigma(\bar{t}j)$	Ref. $\sigma(\bar{t}j)$
$V_L g_R$	-0.461	-(0.348 - 0.365)	-0.006	-(0.038 - 0.040)
g_R^2	2.219	2.18	1.866	1.75 - 1.77
V_R^2	0.883	0.916 - 0.923	1.111	1.082 - 1.084
$V_R g_L$	-0.035	-(0.006 - 0.008)	0.485	-(0.399 - 0.408)
g_L^2	1.680	1.75 - 1.79	2.372	2.16 - 2.17

Table 14: Comparison of coefficients $\hat{\kappa}$ for the 14 TeV total cross section. MG5 stand for the coefficients calculated in MadGraph5 in this work. Ref. stands for the coefficients taken from Ref. [18].

	MG5 $\sigma(tj)$	EFT*fitter* $\sigma(tj)$	MG5 $\sigma(\bar{t}j)$	EFT*fitter* $\sigma(\bar{t}j)$
$V_L g_R$	-0.536	-0.537	0.035	0.002
g_R^2	2.080	1.829	1.545	1.366
V_R^2	0.864	0.863	1.158	1.139
$V_R g_L$	0.102	0.050	-0.639	-0.597
g_L^2	1.287	1.199	2.271	2.008

Table 15: Comparison of coefficients $\hat{\kappa}$ for the 7 TeV total cross section. MG5 stand for the coefficients calculated in MadGraph5 in this work. EFT*fitter* stands for the coefficients taken from the EFT*fitter* code in Ref. [79].

Furthermore, the event generation was verified with additional control plots. These plots included distributions of kinematic variables such as the transverse momentum of the leptons and jets, their pseudorapidity distributions and the separation of leptons and jets. In addition to this, control plots were made reproducing the distributions of the neural network input variables of the 8 TeV cross section measurement. All checks were done on the fiducial and the full phase space. The input variables of the neural network in the cross section analysis consisted of the invariant mass of the light jet and the b-jet, $m(jb)$; the absolute value of the pseudorapidity $|\eta(j)|$ of the light jet; the top quark mass reconstructed from the charged lepton, neutrino and b-jet, $m(\ell\nu b)$; the transverse mass of the reconstructed W boson $m_T\left(\ell E_T^{\text{miss}}\right)$[1]; the absolute value of the difference in pseudorapidity of the reconstructed W boson and the b-jet, $\Delta\eta(\ell\nu, b)$; the invariant mass of the charged lepton and the b-jet, $m(\ell b)$; the cosine of the polarization angle θ^* between the charged lepton and the spectator jet in the rest-frame of the top quark, $\cos\theta^*(\ell, j)$ (see Section 1.3.1). In addition to these variables, control plots of the W boson helicity angle (see Section 1.3.2.1, that is the angle between the charged lepton and the b-jet in the W boson rest frame were made. These plots ensured that the decay of the top quark and W boson are as expected. This specifically helped in identifying an issue in the decay with MadSpin and to evaluate the sign differences discussed in Section 1.2. Figures 29–32 shows the various distributions for the fiducial and total phase space for different values of the real part of the EFT coefficient c_{tW}.The

[1] The transverse mass of the W boson is given by

$$m_T(\ell\nu) = \sqrt{(p_{T,\ell} + p_{T,\nu})^2 - (p_{x,\ell} + p_{x,\nu})^2 - (p_{y,\ell} + p_{y,\nu})^2},$$

where $p_{T,\ell}$ and $p_{T,\nu}$ is the transverse momentum and $p_{x,\ell}$ and $p_{x,\nu}$ is the x component of the momentum of the charged lepton and the neutrino, respectively. Similarly for the y components $p_{y,\ell}$ and $p_{y,\nu}$.

values chosen are $\mathrm{Re}\,(c_{tW}) = \pm 2, \pm 5$. These values do lie outside of the confidence limits found in as seen in Section 2.11. However, they are chosen in such a way as to see the change in the distributions with respect of the EFT parameters. For the coefficient $c_{\varphi tb}$ only positive values of $c_{\varphi tb} = 10, 25$ are chosen since this coefficient is restricted to positive values, see Section 2.5. All other coefficients were set to their Standard Model values. This ensures that the specific features of one EFT operator does not overshadow or cancel another. For most variables variations of $\mathrm{Re}\,(c_{tW})$ do not affect the distributions of that variable. In some cases the large coefficient values lead to slight deviations in the distributions without changing the overall behaviour. Overall, the deviations are less severe in the fiducial region than when considering the whole phase space. The largest deviations is in the distributions of the angles $\cos\theta^*\,(\ell, j)$. However, only large coefficients values of $\mathrm{Re}\,(c_{tW}) = \pm 5$ lead to a sizable deviation, while the smaller values of $\mathrm{Re}\,(c_{tW}) = \pm 2$ are still close to the Standard Model. Therefore, deviations in the $\cos\theta^*\,(\ell, j)$ distribution due to $\mathrm{Re}\,(c_{tW})$ should not affect the acceptance correction of the neural network of the 8 TeV cross section analysis. The imaginary part of c_{tW} has a similar behavior as the real part. A few more deviations in the remaining coupling shown in Appendix E should be mentioned here. The four-quark operator corresponding to coefficient $c_{Qq}^{3,1}$ in Figures 67–70 does show large deviations from the Standard Model distributions in several variables. Most notably these are the η distribution of the spectator jet. In the Standard Model, as with the remaining EFT coefficients, the single top production goes via a t-channel process. Due to the nature of the t-channel process, the η distribution of the spectator jet is shifted towards large values of η, that is the direction of the beam pipe. The four-quark operator $c_{Qq}^{3,1}$ corresponds to a point interaction where the direction of the spectator jet is uniformly distributed. In addition, the transpose momentum of the spectator jet takes larger values. This behavior

is predominant for a large positive value of $c_{Qq}^{3,1}$. Figures 71–74 of Appendix E also shows the distributions of the input variables when varying the Standard Model like coefficient $c_{\varphi Q}^{(3)}$. This coefficient however only affects the normalization, but not the shape of the distributions.

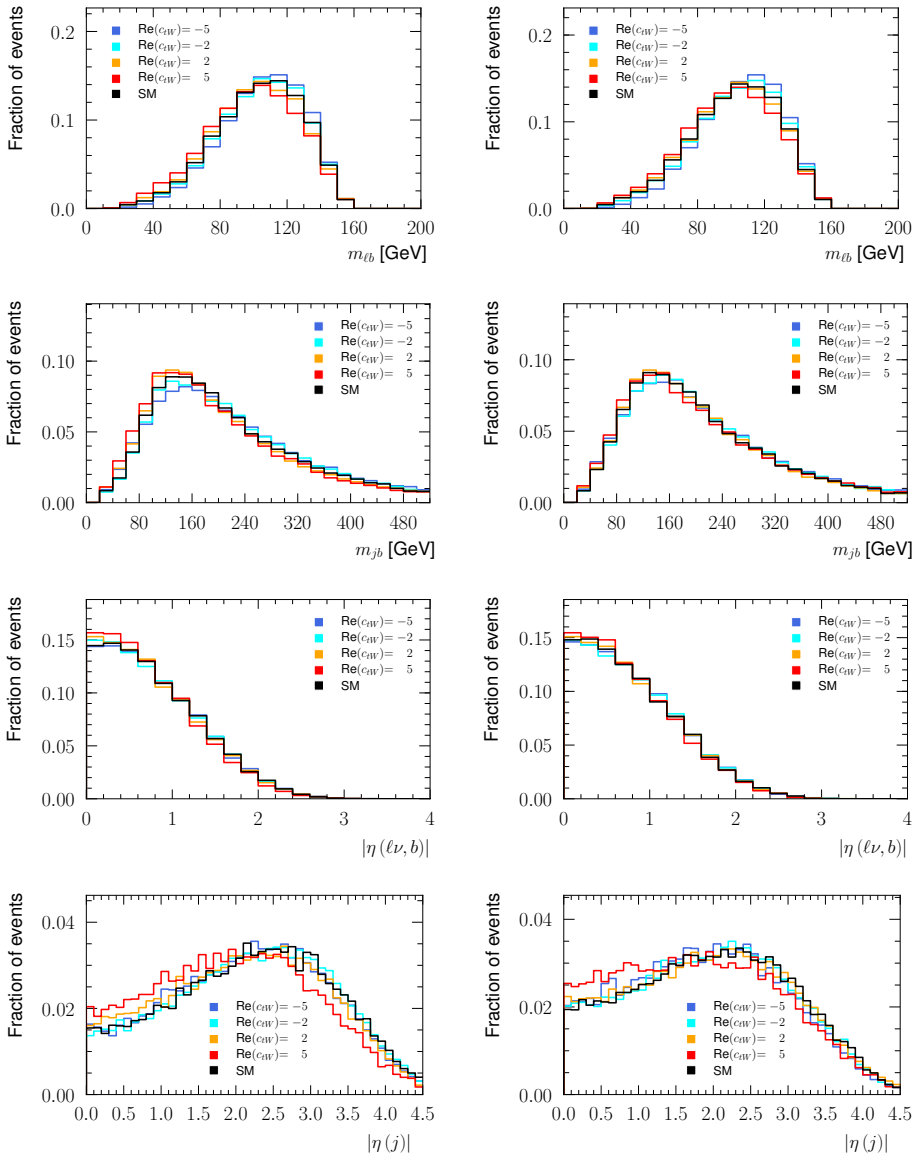

Figure 29: Control plots of simulated top quark (left) and top anti-quark (right) events when varying $\mathrm{Re}(c_{tW})$ in the fiducial phase space. Shown are, from top to bottom row, the input variables $m(\ell b)$, $m(jb)$, $\Delta\eta(\ell\nu, b)$, $|\eta(j)|$.

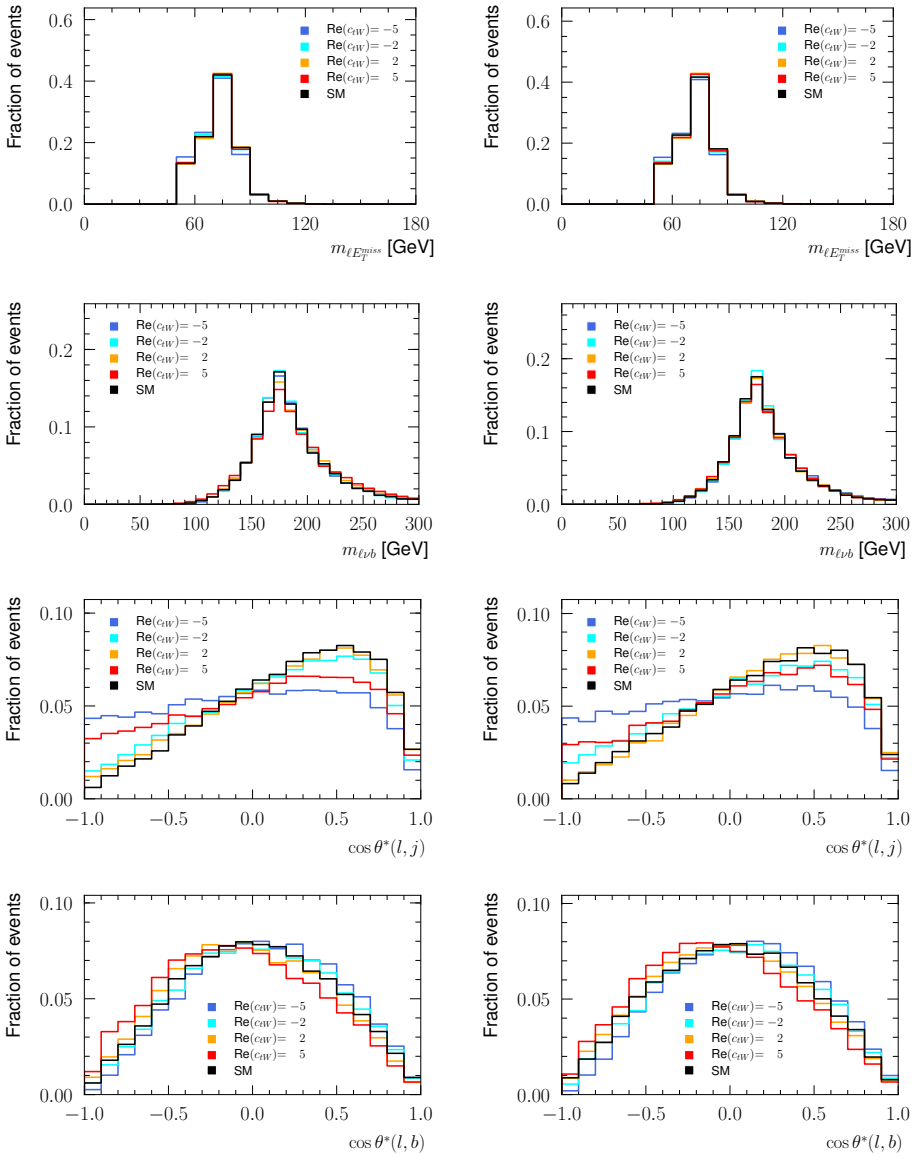

Figure 30: Control plots of simulated top quark (left) and top anti-quark (right) events when varying $\mathrm{Re}\,(c_{tW})$ in the fiducial phase space. Shown are, from top to bottom row, the input variables $m_T\left(\ell E_T^{\mathrm{miss}}\right)$, $m\,(\ell\nu b)$, $\cos\theta^*\,(\ell, j)$, $\cos\theta^*\,(\ell, b)$.

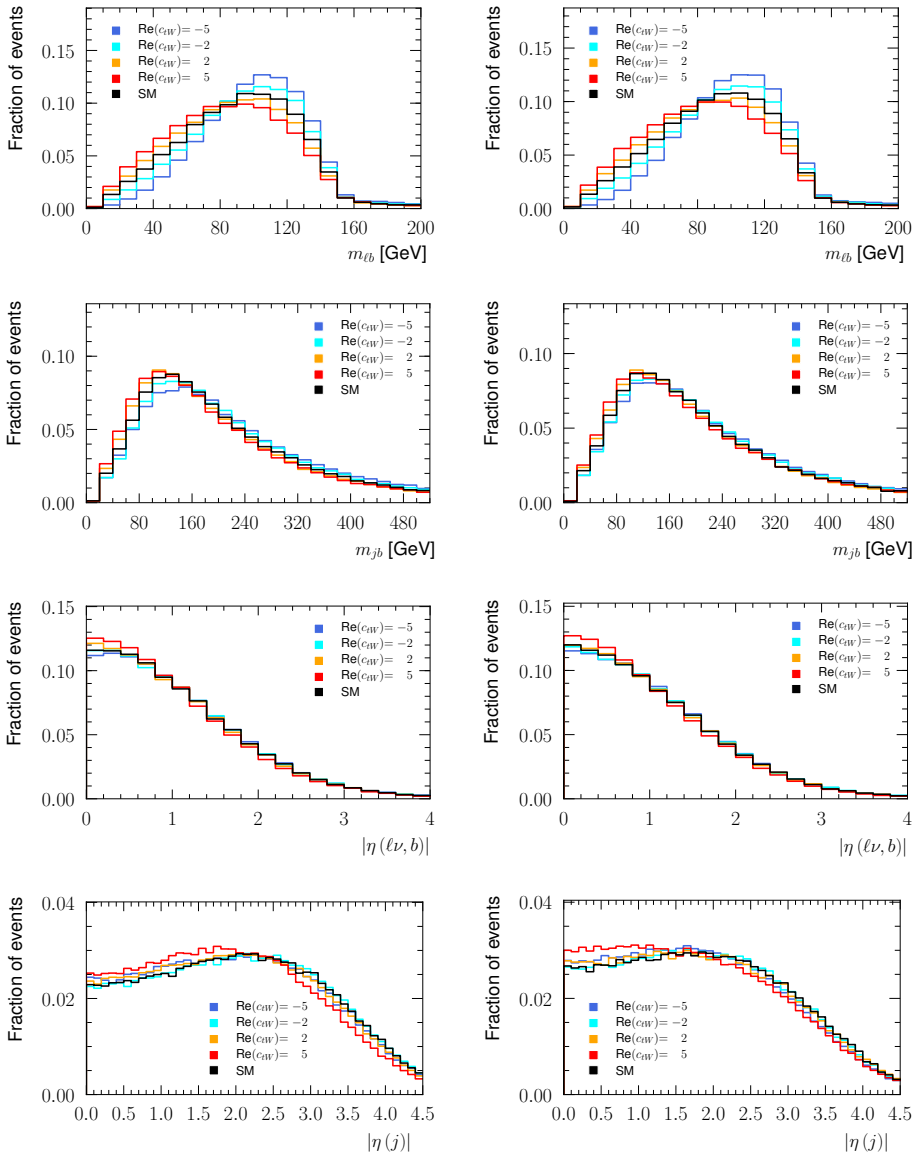

Figure 31: Control plots of simulated top quark (left) and top anti-quark (right) events when varying $\mathrm{Re}(c_{tW})$ in the full phase space. Shown are, from top to bottom row, the input variables $m(\ell b)$, $m(jb)$, $\Delta\eta(\ell\nu, b)$, $|\eta(j)|$.

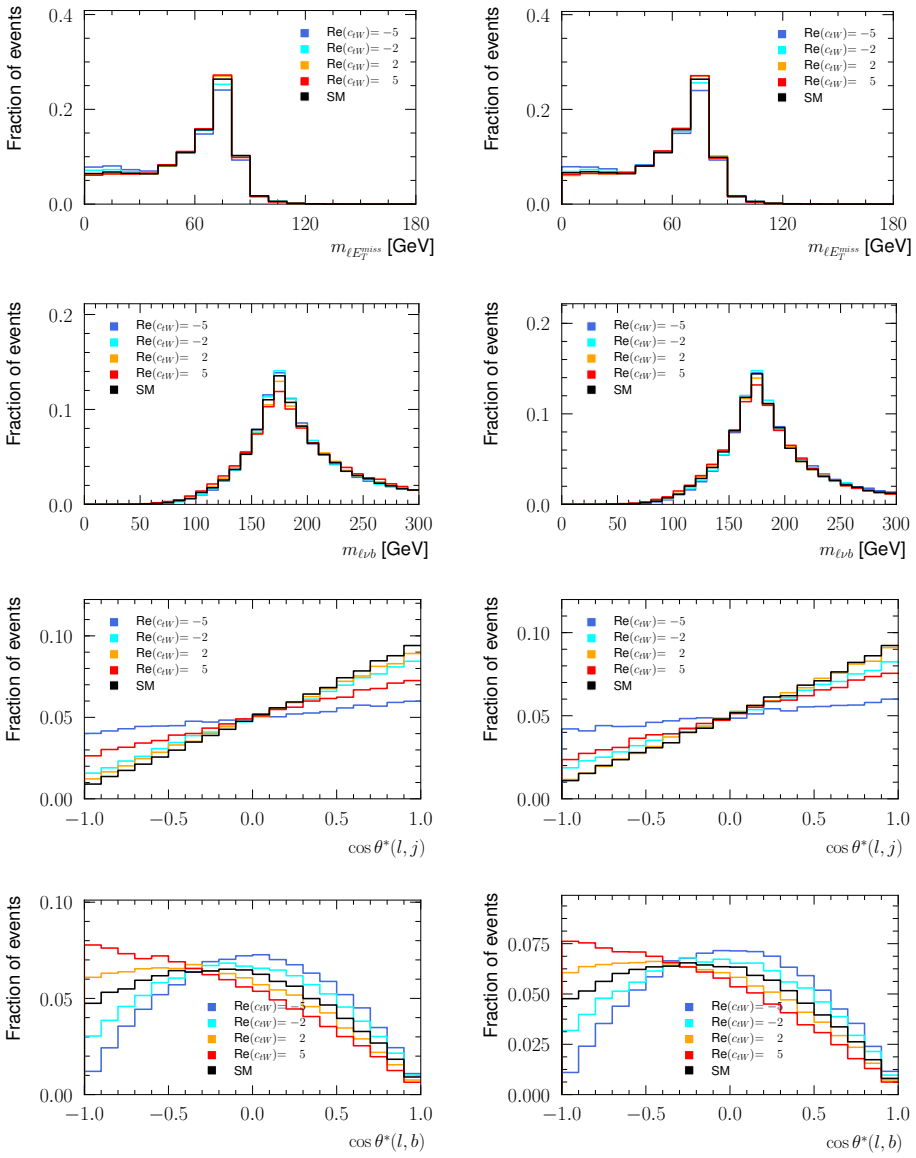

Figure 32: Control plots of simulated top quark (left) and top anti-quark (right) events when varying $\mathrm{Re}\,(c_{tW})$ in the full phase space. Shown are, from top to bottom row, the input variables $m_T\left(\ell E_T^{\mathrm{miss}}\right)$, $m\,(\ell\nu b)$, $\cos\theta^*\,(\ell, j)$, $\cos\theta^*\,(\ell, b)$.

2.9 Uncertainties

This section gives an overview of the systematic uncertainties of the measurements described in Section 2.4. Further, the correlations between observables within one measurement and the correlations between observables of different measurements are discussed. In order to get reliable bounds on the EFT coefficients all the correlations between the different measurements need to be taken into account. Many of the systematic uncertainties are potentially correlated. To account for these correlations, the up and down variations of each uncertainty of every observable in all measurements are checked to determine whether they vary in a correlated or anti-correlated way. Then, their correlation coefficient is set to be either $+1$ in the correlated or -1 in the anti-correlated case. The up and down variations of a systematic uncertainty are variations of the nominal value of an observable when one of the systematic uncertainties is varied within its $\pm\sigma$ bounds. If a systematic uncertainty can only be varied in one direction, this variation is taken as both up and down variation. Examples for these systematic uncertainties are resolution uncertainties like jet energy resolution or lepton momentum resolution. Some systematic uncertainties do not have variations, but instead the nominal value of the observable is compared to the value of that observable computed using a different technique. Examples for these variations are the Monte Carlo event generator and parton showering tools. Appendix I lists all systematic uncertainties for the measurements discussed in Section 2.4 that contribute to the correlations between these measurements In the next sections, details of the different measurements, their systematic uncertainties and correlations between their observables are given. After that, details on the calculation of the total systematic correlation matrix used in the combined fit are give.

2.9.1 W Helicity Fractions Systematic Uncertainties

In this section, the uncertainties of the W helicity fractions as well as their correlations are discussed. Uncertainties that enter the combined fit come from both, the experimental uncertainties of the W helicity fraction measurement and the theoretical uncertainties that enter the fit through the parameterization of the helicity fractions in terms of the EFT coefficients. First, the mean values and uncertainties, both experimental and theoretical, of the W helicity fractions that are used in EFT*fitter* are discussed. When parameterizing the W helicity fractions in terms of the EFT coefficients, they are normalized to their predicted values as

$$F_i = F_i^{\mathrm{NNLO}} \frac{F_i^{\mathrm{EFT}}}{F_i^{\mathrm{SM}}}, \tag{2.54}$$

where $i = 0, L$. F_i^{NNLO} is the theoretical prediction at next-to-next-to-leading-order (NNLO) in the strong coupling constant [46], and F_i^{EFT} and F_i^{SM} are the helicity fractions in terms of the EFT coefficients and in terms of only SM parameters, respectively. Expressions for F_i^{EFT} can be found in Appendix A. The NNLO predictions are given by

$$F_0^{\mathrm{NNLO}} = 0.687 \pm 0.005, \tag{2.55}$$

$$F_L^{\mathrm{NNLO}} = 0.311 \pm 0.005, \tag{2.56}$$

$$F_R^{\mathrm{NNLO}} = 0.0017 \pm 0.0001, \tag{2.57}$$

for $m_b = 4.8$ GeV and $m_t = 172.8$ GeV. F_R is listed here for completeness. These predictions come with a theoretical uncertainty and therefore lead to another uncertainty in the combined fit. An additional, theoretical uncertainty on the experimental

value of 0.73% for F_0 and 1.6% for F_L is assigned. Therefore, the experimental values for the helicity fractions used in EFT*fitter* are

$$\begin{aligned} F_0 &= 0.709 \pm 0.012\,(\text{stat.+bkg.}) \pm {}^{+0.015}_{-0.014}\,(\text{syst.}) \pm 0.005\,(\text{th.})\,, \\ &= 0.709 \pm 0.020, \end{aligned} \tag{2.58}$$

and

$$\begin{aligned} F_L &= 0.299 \pm 0.008\,(\text{stat.+bkg.}) \pm {}^{+0.013}_{-0.012}\,(\text{syst.}) \pm 0.005\,(\text{th.})\,, \\ &= 0.299 \pm 0.016, \end{aligned} \tag{2.59}$$

where the statistics, background and systematic uncertainties are taken from [67, 68] and the theoretical uncertainty corresponds the uncertainty discussed above. All systematic uncertainties of the W helicity fractions that contribute to the correlations with the other measurements are listed in Table 29 of Appendix I.

Next, a detailed look at the systematic uncertainties of the W helicity fractions is given, in order to calculate the correlations between the helicity fractions and the remaining measurements. For the majority of the systematic uncertainties in the W helicity fraction analysis up and down variations are available. The correlation coefficients of the helicity fractions with other observables can therefore be calculated in a straight forward way, see Section 2.9.4. In case no up and down variations are given, the sign of the variation needs to be evaluated in another way. In the following, details of the uncertainties with no up and down variations and the calculation of the signs are given.

Initial and Final State Radiation: The initial and final state radiation uncertainty corresponds to the scale uncertainties from the parton shower generator and is labeled *radLo* and *radHi* in the systematics table. These correspond to the up and down variations, respectively.

ME Generator: The variation of the central values of F_0 and F_L when switching from the default matrix element generator POWHEG to the alternative generator MC@NLO are given in the W helicity fraction analysis. It shows that the central value of F_0 decreases, while the central value value of F_L increases. Since the PDF variation is one-directional, a negative sign is assigned to the variation of F_0 and a positive sign is assigned to the variation of F_L.

Parton Shower: The variation of the central values values of F_0 and F_L when switching from the default parton shower generator PYTHIA to the alternative generator HERWIG is given in the W helicity fraction analysis. Under this variation, F_0 increases and F_L decreases and therefore F_0 gets assigned a positive and F_L gets assigned a negative sign.

PDF: Variations of the helicity fractions with respect to the different PDF's are available. These show that going from the default PDF CT10 NLO to either of the other PDF, MSTW2008 68% CL NLO or NNPDF 2.3 NLO increases the values of F_0 and decreases the values of F_L. Therefore, the variation of F_0 is assigned a positive sign and the variation of F_L a negative sign.

Top Mass: The variation of the helicity fractions with respect to the top mass is available. The fraction F_0 increases with increasing m_t and F_L decreases with increasing m_t. Therefore, the variations of F_0 is assigned a positive sign and F_L is assigned a negative sign.

Lastly, the correlation coefficients between the two helicity fractions is discussed. This correlation coefficient is not calculated here, but instead the value is taken from the analysis. The correlation coefficient is given by

$$\rho_{F_0 F_L} = -0.82 \tag{2.60}$$

and includes both systematic and statistical correlations.

	Mean value	Uncertainty
a_{010}	-0.058381	0.016316
a_{020}	-0.055868	0.016787
a_{100}	0.045245	0.017026
a_{110}	0.027649	0.018197
a_{120}	-0.045311	0.015230
$\mathrm{Re}(a_{111})$	-0.066725	0.015932
$\mathrm{Im}(a_{111})$	0.035573	0.004670
$\mathrm{Re}(a_{121})$	0.008963	0.015141
$\mathrm{Im}(a_{121})$	0.001532	0.005956

Table 16: Mean values and total uncertainties of the measured angular coefficients $a_{k,l,m}$.

2.9.2 Single Top Decay Distribution Systematic Uncertainties

The mean values and total uncertainties of the angular coefficients $a_{k,l,m}$ of the single top decay distribution measurement are listed in Table 16. Similar to the W helicity fractions, the angular coefficients are normalized to their Standard Model predictions as

$$a_{k,l,m} = a^{\mathrm{LO}}_{k,l,m} \frac{a^{\mathrm{EFT}}_{k,l,m}}{a^{\mathrm{SM}}_{k,l,m}}, \tag{2.61}$$

for all $a_{k,l,m}$, except for the imaginary parts of a_{111} and a_{121}, where the $a^{\mathrm{SM}}_{k,l,m} = 0$. In Eq. 2.61 $a^{\mathrm{EFT}}_{k,l,m}$ is the angular coefficient parameterized by the EFT coefficients

as given by Eq. B.1 in Appendix B and $a^{\mathrm{LO}}_{k,l,m}$ are the angular coefficients given in Eq. 1.55 and Eq. 1.56 of Section 1.3.2.2 evaluated at the leading-order Standard Model predictions [70, 80] of

$$f_1 = 0.304 \qquad \delta_+ = 0 \tag{2.62}$$

$$f_1^+ = 0.001 \qquad \delta_- = 0 \tag{2.63}$$

$$f_0^+ = 6 \times 10^{-5} \qquad P = 0.9 \tag{2.64}$$

Detailed information on all systematic uncertainties considered for correlations with the remaining measurements can be found in Tables 31–35 of Appendix I. To evaluate the correlations with the other measurements, the up and down variations of the systematic uncertainties are considered. Up and down variations are available for all systematic uncertainties and the sign of the correlation coefficients can be determined in a straight forward way, see Section 2.9.4.

The correlation coefficients between the angular coefficients $a_{k,l,m}$ is taken from the single top decay distribution analysis. The full correlation matrix is shown in Table 17.

2.9.3 Cross Section Systematic Uncertainties

The cross section systematic uncertainties are available as symmetrized uncertainties only. No up and down variations are given. There, the behavior of the cross section when varying one of the systematics within its allowed range has to be evaluated. For that, the single top decay distribution measurement can be used. In the single top decay distribution measurement, the signal fraction of the t-channel process was measured. The change of the signal fraction when varying on of the systematic uncertainties follows the same sign as the cross section, when varying that

	a_{010}	a_{020}	a_{100}	a_{110}	a_{120}	a_{111}^{R}	a_{111}^{I}	a_{121}^{R}	a_{121}^{I}
a_{010}	1.00	-0.45	0.69	-0.65	0.52	0.42	0.06	-0.16	-0.08
a_{020}	-0.45	1.00	-0.43	0.61	-0.39	-0.28	0.16	-0.07	0.12
a_{100}	0.69	-0.43	1.00	-0.68	0.42	0.45	-0.09	-0.01	0.21
a_{110}	-0.65	0.61	-0.68	1.00	-0.60	-0.62	0.15	0.25	0.11
a_{120}	0.52	-0.39	0.42	-0.60	1.00	0.33	-0.06	-0.21	0.00
a_{111}^{R}	0.42	-0.28	0.45	-0.62	0.33	1.00	-0.26	-0.23	0.03
a_{111}^{I}	0.06	0.16	-0.09	0.15	-0.06	-0.26	1.00	0.05	-0.26
a_{121}^{R}	-0.16	-0.07	-0.01	0.25	-0.21	-0.23	0.05	1.00	0.07
a_{121}^{I}	-0.08	0.12	0.21	0.11	0.00	0.03	-0.26	0.07	1.00

Table 17: Correlation matrix of the angular coefficient [69]. Superscripts R and I stand for real and imaginary parts, respectively.

same uncertainty. Therefore, a study of the signal fraction gives an estimate of the sign of the up and down variations of the cross section. The signs calculated this way can then be combined with the symmetrized uncertainties taken from the cross section analysis.

Not all uncertainties of the cross section measurement have a corresponding uncertainty in the single top decay distribution measurement. However, uncertainties that do not have a corresponding one in the other measurements are not correlated with these. In particular, the uncertainties $b\bar{b}$ acceptance and electron charge ID are not present in either the single top decay distribution or the W helicity fraction analysis. These uncertainties then only contribute to the correlation between the

top and anti-top cross section. Since the correlation between the two cross sections is evaluated in a different way (see further down in this section) the uncertainties $b\bar{b}$ acceptance and electron charge ID do not need any further evaluation here. One exception is the multijet normalization uncertainty which is present in both the cross section and the single top decay distribution measurement. However, the uncertainty is negligible for all angular coefficients $a_{k,l,m}$ in the single top decay distribution analysis and therefore does not lead to correlations with the cross sections.

To account for the theoretical uncertainties of the predicted cross section, an additional uncertainty similar to the one in the W helicity fraction is applied. In EFT*fitter*, the cross sections are normalized to the theoretical predictions. At next-to-leading-order (NLO) in the strong coupling constant, the total top quark and antiquark cross sections are predicted to be

$$\begin{aligned} \sigma\left(tq\right) &= 54.9^{+2.3}_{-1.9}\,\text{pb}, \\ \sigma\left(\bar{t}q\right) &= 29.7^{+1.7}_{-1.5}\,\text{pb}, \end{aligned} \tag{2.65}$$

for $m_t = 172.5$ GeV. They are calculated with the HatHor v2.1 tool [25] and work based on [81]. To get the prediction of the fiducial cross sections, the total cross sections are multiplied by the respective fiducial acceptances, given by

$$\begin{aligned} A_{\text{fid}}\left(tq\right) &= \left(17.26^{+0.46}_{-0.21}\right)\,\%, \\ A_{\text{fid}}\left(\bar{t}q\right) &= \left(17.52^{+0.45}_{-0.20}\right)\,\%, \end{aligned} \tag{2.66}$$

taken from [31]. Therefore, the predicted values for the fiducial cross sections are

$$\begin{aligned} \sigma_{\text{fid}}\left(tq\right) &= 9.48 \pm 0.41\,\text{pb}, \\ \sigma_{\text{fid}}\left(\bar{t}q\right) &= 5.20 \pm 0.30\,\text{pb}, \end{aligned} \tag{2.67}$$

From this, an additional uncertainty on the cross sections of 4.4% for top quark and 5.7% for top anti-quark is calculated and applied to the experimental cross sections. The experimental, fiducial cross sections used in EFT*fitter* are therefore

$$\begin{aligned}\sigma_{\text{fid}}\left(tq\right) &= 9.78 \pm 0.57\,(\text{exp.}) \pm 0.43\,(\text{th.})\ \text{pb}, \\ &= 9.78 \pm 0.71\ \text{pb},\end{aligned} \tag{2.68}$$

and

$$\begin{aligned}\sigma_{\text{fid}}\left(\bar{t}q\right) &= 5.77 \pm 0.45\,(\text{exp.}) \pm 0.33\,(\text{th.})\ \text{pb}, \\ &= 5.77 \pm 0.56\ \text{pb},\end{aligned} \tag{2.69}$$

where the experimental uncertainty is taken from [31] and the theoretical uncertainty is the additional uncertainty due to the theoretical predictions calculated above.

The correlation coefficient between the two cross sections is not known from the analysis. Here, we take the statistical and systematic uncertainties from the analysis and calculate the correlation coefficient by assuming the statistical uncertainties to be uncorrelated and the systematic uncertainties 100% correlated. This leads to a correlation coefficient

$$\rho_{\sigma_t\sigma_{\bar{t}}} = 0.91. \tag{2.70}$$

As a check, the correlation coefficient has been varied between $0 \leq \rho_{\sigma_t\sigma_{\bar{t}}} < 1$ and no significant change in the combined fit was found.

2.9.4 Constructing The Correlation Matrix

In the following, the construction of the total correlation matrix from the up and down variations of the different measurements is described. To combine the systematic uncertainties of the measurements into a single correlation matrix, all the uncertainty categories that are present in the different measurements have to be matched onto each other. As described in the previous sections, detailed tables of all uncertainty categories are available for the W helicity fraction and single top decay distribution measurements. For the cross sections, the up and down variations have been calculated from information available from the single top decay distribution analysis, see Section 2.9.6.

Matching the uncertainty categories onto each other proceeds in different steps. First, all categories that have a one-to-one correspondence in two or more measurements are matched. This matching is done by simply adjusting the uncertainty name. Comparing the W helicity fractions and single top decay distributions, uncertainty categories that can be directly matched are listed in Table 18. A detailed list matched uncertainties between the single top decay distributions and the cross sections can be found in Tables 22–25. In the second step, uncertainties that are only present in one of the measurements are dropped, since they do not contribute to the correlations between observables of different measurements. Finally, some of the uncertainties are divided into sub-categories in some of the measurements, but only listed as a total uncertainty in other measurements. An example for this is the jet energy resolution uncertainty, which is a single uncertainty in the single top decay distribution measurement, but has 11 distinct sub-categories in the cross section and W helicity fraction measurements. For these uncertainties, the sub-categories have to be combined first, before they can be matched onto each other. The procedure

single top decay distribution	W helicity fractions
jes_Modelling1	JES modelling/theory (1)
jes_RhoTopology	JES pile-up (rho term)
jes_FlavourComp	JES flavour composition
jes_FlavourResponse	JES flavour response
jvf	JES Jet vertex fraction
jes_EtaIntercalibration_TotalStat	JES eta inter-calibration (stat. term)
jes_Statistical1	JES statistics (1)
ELE_ID	Electron scale factor id
ELE_RECO	Electron scale factor reco
ELE_TRIGGER	Electron scale factor trigger
MUON_ID	Muon scale factor id
MUON_RECO	Muon scale factor reco
MUON_TRIGGER	Muon scale factor trigger
ME Generator	ttbar NLO modelling
Parton Shower	ttbar hadronization

Table 18: Comparison of the uncertainty categories present in both W helicity fractions and single top decay distribution measurements.

for combining the sub-categories is described in Section 2.9.5.

Once the uncertainty categories are matched, the covariance matrix for these

categories can be constructed. For this, first a covariance matrix from the up variations and one from the down variations is constructed. Each covariance matrix is the result of the outer product of the vector of up/down variations. Thus, e.g. the covariance matrix from the up variations is

$$\mathcal{C}_i^{\text{up}} = \left(\boldsymbol{v}^{\text{up}}\right)^T \boldsymbol{v}^{\text{up}}, \tag{2.71}$$

where $\boldsymbol{v}$ is the vector containing all up variations of all the observables in one uncertainty category. The index $i = 1, \ldots, N$, where N is the number of uncertainty categories. Similarly, the covariance matrix from the down variations is constructed. To calculate the total covariance matrix for each uncertainty category, the up and down covariance matrices are averaged as in

$$\mathcal{C}_i = \frac{1}{2}\left(\mathcal{C}_i^{\text{up}} + \mathcal{C}_i^{\text{down}}\right). \tag{2.72}$$

Once the the covariance matrices for all uncertainty categories are constructed, the total covariance matrix can be computed by summing the individual covariance matrices for all uncertainty categories

$$\mathcal{C} = \sum_{i=1}^{N} \mathcal{C}_i. \tag{2.73}$$

Again, N is the number of uncertainty categories. From this covariance matrix, the respective correlation matrix is constructed

$$corr = \left(diag\left(\mathcal{C}\right)\right)^{-\frac{1}{2}} \mathcal{C} \left(diag\left(\mathcal{C}\right)\right)^{-\frac{1}{2}} \tag{2.74}$$

and then used in EFT*fitter* for the combined fit. Here, $diag\left(\mathcal{C}\right)$ is the matrix that contains only the diagonal elements of $\mathcal{C}$. In order to calculate the correlation matrix in Eq. 2.74, all uncertainties that are present in both the W helicity fraction and

the single top decay distribution measurement have to be matched. We already saw that many of the uncertainty categories easily map onto each other. Other categories however, need a more careful approach. In particular, the uncertainties related to the jet energy scale, jet energy resolution, the b-tagging related uncertainties and some of the uncertainties related to lepton reconstruction need to be treated separately.

2.9.5 Matching Uncertainties With Sub-Categories

Some of the uncertainty categories, are divided into sub-categories in some of the measurements, while in other measurements they are only given as a single uncertainty value. An example for this is the jet energy resolution uncertainties, which are split into matching sub-categories for both the cross sections and W helicity fractions, but only appear as one category in the single top decay distribution analysis. In this section, the general strategy of combining systematic uncertainties of this kind is shown using the example of the jet energy resolution. Table 19 shows the jet energy resolution sub-categories and up and down variations for the cross sections and W helicity fractions. To add all uncertainties into a single covariance matrix, the sub-categories of the cross sections and W helicity fractions have to be combined first. To construct the covariance matrices of the up variations, the outer product of all up variations of each category in Table 19 is taken. Next, all these covariance matrices are summed up to get one single covariance matrix for the up variations. Similarly, one covariance matrix for the down variations is constructed. Finally, the up and down variation covariance matrices are added according to Eq. 2.72. This is essentially the same procedure as shown in the last section. In the next step, the covariance matrix of the cross sections and W helicity fractions needs to be combined with the single top decay distribution uncertainties to get the total covariance matrix

	F_0 up	F_L up	F_0 down	F_L down
JER_DataMC_Diff	-0.0021	0.0002	-0.0021	0.0002
JER_NP0	0.0013	-0.0044	-0.0021	0.0002
JER_NP1	-0.0021	0.0002	-0.0019	-0.0003
JER_NP2	-0.0013	-0.0016	-0.0018	0.0000
JER_NP3	-0.0025	0.0001	-0.0004	-0.0012
JER_NP4	-0.0013	-0.0001	-0.0024	-0.0006
JER_NP5	-0.0020	-0.0004	-0.0018	-0.0003
JER_NP6	-0.0025	0.0004	-0.0006	-0.0009
JER_NP7	-0.0028	-0.0000	-0.0013	-0.0005
JER_NP8	-0.0021	0.0002	-0.0018	-0.0001
JER_Noise_FwdReg	-0.0020	0.0003	-0.0020	0.0003

Table 19: Up and down variations of the jet energy resolution in the W helicity fractions measurement.

of the jet energy resolution uncertainty.

The total covariance matrix for the jet energy resolution can be written as

$$\mathcal{C} = \begin{pmatrix} \mathcal{C}_{\mathrm{WHF},\sigma} & P \\ P^T & \mathcal{C}_{\mathrm{STDD}} \end{pmatrix}, \tag{2.75}$$

where P includes the correlations between the single top decay distributions and the cross sections and W helicity fractions. $\mathcal{C}_{\mathrm{WHF},\sigma}$ is the combined covariance matrix of the cross sections and W helicity fractions and $\mathcal{C}_{\mathrm{STDD}}$ is the covariance matrix from

the single top decay distributions. Since at this point the information on the up and down variations is not available anymore, it must be deducted in another way. To get a hold on the up/down variations of the total jet energy resolution of the cross sections and W helicity fractions, the up/down variations for each observable are added up. The sign of this result determines the sign of the variation. In that way, each entry in P can be calculated as

$$P_{ij}^{up} = \rho_{ij}^{up} = \mathrm{sgn}\left(\mathcal{C}_{\mathrm{STDD},ii}^{up}\right) \mathrm{sgn}\left(\sum \mathcal{C}_{\mathrm{WHF},\sigma,ii}^{up}\right) \sqrt{\mathcal{C}_{\mathrm{STDD},ii}} \sqrt{\mathcal{C}_{\mathrm{WHF},\sigma,ii}}. \tag{2.76}$$

Here $\mathcal{C}_{\mathrm{STDD},ii}^{up}$ is the i'th coefficient of the single top decay distributions $a_{k,l,m}$ and $\sum \mathcal{C}_{\mathrm{WHF},\sigma,ii}^{up}$ is the sum over all the up variations of one of either one of the cross sections or W helicity fractions. As an example, the covariance of the single top decay distribution coefficient a_{010} and the W helicity fraction F_0 for the up values is given by

$$\rho_{a_{010}F_0^{up}} = \mathrm{sgn}\left(\delta_{a_{010}^{up}}\right) \mathrm{sgn}\left(\sum_i \delta_{F_{0,i}^{up}}\right) \sqrt{\delta_{a_{010}^{up}}^2} \sqrt{\delta_{F_0^{up}}^2}, \tag{2.77}$$

where $\delta_{a_{010}^{up}} = -0.0043$ is the up variation of a_{010} in Table 20 and $\sum_i \delta_{F_{0,i}^{up}} = -0.0194$ is the sum over all entries of the column F_0 up in Table 19. This ensures, that the sign of the covariance follows the overall sign of the up values of F_0. $\delta_{F_0^{up}}^2 = \sum_i \delta_{F_{0,i}^{up}}^2$ is the variance of F_0^{up} coming from the sum of the covariance matrices $\mathcal{C}_{\mathrm{WHF},\sigma,ii}$. Putting everything together, the covariance is

$$\begin{aligned} \rho_{a_{010}F_0^{up}} &= (-1)\,(-1)\,(0.0043)\,\sqrt{0.000047} \\ &= 0.000029. \end{aligned} \tag{2.78}$$

In this way, all entries of P are calculated and the covariance matrix for each systematic uncertainty is calculated.

a_{010}	a_{020}	a_{100}	a_{110}	a_{120}	a_{111}^{R}	a_{111}^{I}	a_{121}^{R}	a_{121}^{I}
-0.0043	0.0082	0.0009	0.0028	0.001	0.0003	-0.0006	-0.0027	0.0023

Table 20: Up variations of the jet energy resolution in the single top decay distributions. Superscript R and I stand for real and imaginary part, respectively.

a_{010}	a_{020}	a_{100}	a_{110}	a_{120}	a_{111}^{R}	a_{111}^{I}	a_{121}^{R}	a_{121}^{I}
-0.0043	0.0082	0.0009	0.0028	0.001	0.0003	-0.0006	-0.0027	0.0023

Table 21: Down variations of the jet energy resolution in the single top decay distributions. Superscript R and I stand for real and imaginary part, respectively.

2.9.6 Estimation Of Cross Section Up/Down Variations

In this section, the estimation of the sign of the up and down variations of the cross section uncertainties is described. As discussed in Section 2.9.3, only symmetrized values are given for the cross section uncertainties. Therefore, the sign has to be estimated in a different way. The measurement of the single top decay distributions was performed at a center-of-mass energy $\sqrt{s} = 8$ TeV using t-channel single top events. Therefore, the signal fraction measured in the single top decay distribution analysis is directly related to the cross section. In the single top decay distribution analysis, the variation of the signal fraction when varying one of the systematic uncertainties was saved as ROOT files. These ROOT files can be used to calculate the sign of the change in signal fraction and therefore as an estimate of the sign of the change in the cross section for each variation of systematic uncertainty.

In the first step, the different systematic uncertainties of the cross section and the single top decay distribution analyses need to be matched. Tables 22–24 show a comparison between all systematic uncertainties that have been matched between the analyses. Uncertainties that only contribute to one of the two analyses are not listed since they do not lead to a correlation between the observables of the two measurements. Next, the signal fraction of every matched systematic uncertainty is calculated. The do this, four ROOT files are needed, the ROOT file containing the up/down varied combined weight of the signal, the file containing the nominal combined weight of the signal and both the containing the nominal and the up/down varied combined weight of the background. In the following, all the sample files used to determine the signs of the matched uncertainty categories are listed. All signal and background sample files are divided into electron and muon channels. When calculating the signal fraction, both channels are combined unless a specific uncertainty only treats one of the two. Here, only the samples for the electron channel are listed. Further, for the signal samples, equivalent files exist for both top and antitop samples, unless otherwise stated. The sample files contain information on the combined weights and the associated scale factors. With this information, the signal fraction is calculated as

$$SF = \frac{w_s}{w_s + w_b}, \tag{2.79}$$

where SF is the signal fraction and w_s and w_b is the combined weight times the scale factor of the signal and background, respectively. Variations of the systematic uncertainties will affect the signal weight, background weight or both. The sign of the change in the signal fraction is taken as the sign of the change in cross section.

Single top decay dist.	t-channel cross section
JES b-tagging	b-jet energyscale
JES single-particle	JES single particle
JES pile-up (μ)	JES pile-up (μ)
JES pile-up ($n_{vertices}$)	JES pile-up (n_{vtx})
JES pile-up (p_T term)	JES pile-up (Pt)
JES pile-up (ρ term)	JES pile-up (ρ)
JES punch through	JES PunchThrough
JES flavor composition	JES flavour composition
JES flavor response	JES flavour response
JES η intercalibration (stat. term)	JES η intercal. statistical
JES η intercalibration (modelling term)	JES η intercalibration
JES detector (1)	JES detector 1
JES detector (2)	JES detector 2
JES detector (3)	JES detector 3)
JES detector and modelling (1)	JES mixed detector and modelling 1
JES detector and modelling (2)	JES mixed detector and modelling 2
JES detector and modelling (3)	JES mixed detector and modelling 3
JES detector and modelling (4)	JES mixed detector and modelling 4
JES modelling/theory (1)	JES physics modelling 1
JES modelling/theory (2)	JES physics modelling 2
JES modelling/theory (3)	JES physics modelling 3
JES modelling/theory (4)	JES physics modelling 4
JES statistics (1)	JES statistical 1
JES statistics (2)	JES statistical 2
JES statistics (3)	JES statistical 3
JES statistics (4)	JES statistical 4
Jet vertex fraction	Jet vertex fraction

Table 22: Comparison of the jet energy scale uncertainties taken from the single top decay distribution analysis and the t-channel cross section analysis.

Single top decay dist.	t-channel cross section
Jet b-tagging scale factor	b-tag scalefactorC0
	b-tag scalefactorC1
	b-tag scalefactorC2
	b-tag scalefactorC3
	b-tag scalefactorC4
	b-tag scalefactorC5
	b-tag scalefactorC6
	b-tag scalefactorC7
	b-tag scalefactorC8
Jet c-tagging scale factor	c-tag scalefactorC0
	c-tag scalefactorC1
	c-tag scalefactorC2
	c-tag scalefactorC3
Jet mis-tagging scale factor	mis-tag scalefactorC0
	mis-tag scalefactorC1
	mis-tag scalefactorC2
	mis-tag scalefactorC3
	mis-tag scalefactorC4
	mis-tag scalefactorC5
	mis-tag scalefactorC6
	mis-tag scalefactorC7
	mis-tag scalefactorC8
	mis-tag scalefactorC9
	mis-tag scalefactorC10
	mis-tag scalefactorC11

Table 23: Comparison of the flavor tagging uncertainties taken from the single top decay distribution analysis and the t-channel cross section analysis. Each category, b-tagging, c-tagging and mis-tagging only has one uncertainty in the single top decay distribution analysis.

Single top decay dist.	t-channel cross section
t-channel NLO modelling	tq NLO matching method
t-channel hadronization	tq Parton-Shower model
t-channel scale variation	μ variation of tq process
$t\bar{t}$ NLO modelling	$t\bar{t}$, Wt, $t\bar{b}$ NLO matching method
$t\bar{t}$ hadronization	$t\bar{t}$, Wt Parton-Shower model
$t\bar{t}$ scale variation	μ variation of $t\bar{t}$, Wt, $t\bar{b}$ process

Table 24: Comparison of the generator related uncertainties taken from the single top decay distribution analysis and the t-channel cross section analysis.

The following sample files are used as nominal samples, unless otherwise stated. For the signal, the nominal file is

`mc12_8TeV_2jetbin.sig.powheg_pythia_top.SM.SEL.nominal.el.root`

and the corresponding file for antitop. Further, this file corresponds to the electron channel. A separate file was used for the muon channel. For the background, the nominal file is

`mc12_8TeV_2jetbin.bkg.nominal.mu.root`

for the electron channel and a corresponding file for the muon channel. In the following, all categories of systematic uncertainties are discussed. For each systematic, the the sample files containing the systematic up variation of the electron channel of both signal and background are listed. Unless otherwise stated, a corresponding file for the down variation as well as files for the muon channel exist. If a nominal sample other than the ones stated above is used, these are also listed here.

Jet Energy Resolution and Jet Reconstruction Efficiency: The samples

Single top decay dist.	t-channel cross section
Jet energy resolution	Jet energy resolution
Jet reconstruction efficiency	Jet efficiency
Muon momentum resolution (id.)	Muon momentum resolution (ID)
Muon momentum scale	Muon momentum scale
Muon momentum smearing resolution	Muon momentum resolution
Electron energy resolution	Electron energy resolution
Electron energy scale	Electron energy scale
Electron scale factor (trigger)	Lepton Trigger SF
Muon scale factor (trigger)	
Electron scale factor (id.)	Lepton ID SF
Muon scale factor (id.)	
Electron scale factor (recon.)	Lepton Reco SF
Muon scale factor (recon.)	
E_T^{miss} (cell-out + soft jet resolution)	E_T^{miss} CellOut + SoftJet Resolution
E_T^{miss} (cell-out + soft jet scale)	E_T^{miss} CellOut + SoftJet Scale
Z-jets normalization	Z+jets heavy flavour norm.
Luminosity	Luminosity

Table 25: Comparison of the remaining uncertainties taken from the single top decay distribution analysis and the t-channel cross section analysis. The lepton scale factor uncertainties are split into electron and muon channel in the single top decay distribution analysis.

used to estimate the sign of the jet energy resolution and jet reconstruction efficiency uncertainties are

```
mc12_8TeV_2jetbin.sig.powheg_pythia_top.SM.SEL.jer.el.root
mc12_8TeV_2jetbin.sig.powheg_pythia_top.SM.SEL.jeff.el.root
```

for top and antitop quark samples. No up or down variation is given since the jet energy resolution can only be decreased. The background sample is

```
mc12_8TeV_2jetbin.bkg.jer.el.root
mc12_8TeV_2jetbin.bkg.jeff.el.root
```

Jet Energy Scale: The signal samples used to estimate the sign of the jet energy scale uncertainties are

```
mc12_8TeV_2jetbin.sig.powheg_pythia_top.SM.SEL.BJesUnc_up.el.root
mc12_8TeV_2jetbin.sig.powheg_pythia_top.SM.SEL.SinglePart_up.el.root
mc12_8TeV_2jetbin.sig.powheg_pythia_top.SM.SEL.Pileup_OffsetMu_up.el.root
mc12_8TeV_2jetbin.sig.powheg_pythia_top.SM.SEL.Pileup_OffsetNPV_up.el.root
mc12_8TeV_2jetbin.sig.powheg_pythia_top.SM.SEL.Pileup_Pt_up.el.root
mc12_8TeV_2jetbin.sig.powheg_pythia_top.SM.SEL.Pileup_Rho_up.el.root
mc12_8TeV_2jetbin.sig.powheg_pythia_top.SM.SEL.PunchThrough_up.el.root
mc12_8TeV_2jetbin.sig.powheg_pythia_top.SM.SEL.flavor_comp_up.el.root
mc12_8TeV_2jetbin.sig.powheg_pythia_top.SM.SEL.flavor_response_up.el.root
mc12_8TeV_2jetbin.sig.powheg_pythia_top.SM.SEL.jvf_up.el.root
mc12_8TeV_2jetbin.sig.powheg_pythia_top.SM.SEL.EtaIntercalibrationModel_up.el.root
mc12_8TeV_2jetbin.sig.powheg_pythia_top.SM.SEL.EtaIntercalibrationTotalStat_up.el.root
mc12_8TeV_2jetbin.sig.powheg_pythia_top.SM.SEL.JesEffectiveDet1_up.el.root
mc12_8TeV_2jetbin.sig.powheg_pythia_top.SM.SEL.JesEffectiveDet2_up.el.root
mc12_8TeV_2jetbin.sig.powheg_pythia_top.SM.SEL.JesEffectiveDet3_up.el.root
mc12_8TeV_2jetbin.sig.powheg_pythia_top.SM.SEL.JesEffectiveMix1_up.el.root
mc12_8TeV_2jetbin.sig.powheg_pythia_top.SM.SEL.JesEffectiveMix2_up.el.root
mc12_8TeV_2jetbin.sig.powheg_pythia_top.SM.SEL.JesEffectiveMix3_up.el.root
mc12_8TeV_2jetbin.sig.powheg_pythia_top.SM.SEL.JesEffectiveMix4_up.el.root
mc12_8TeV_2jetbin.sig.powheg_pythia_top.SM.SEL.JesEffectiveModel1_up.el.root
mc12_8TeV_2jetbin.sig.powheg_pythia_top.SM.SEL.JesEffectiveModel2_up.el.root
mc12_8TeV_2jetbin.sig.powheg_pythia_top.SM.SEL.JesEffectiveModel3_up.el.root
mc12_8TeV_2jetbin.sig.powheg_pythia_top.SM.SEL.JesEffectiveModel4_up.el.root
mc12_8TeV_2jetbin.sig.powheg_pythia_top.SM.SEL.JesEffectiveStat1_up.el.root
mc12_8TeV_2jetbin.sig.powheg_pythia_top.SM.SEL.JesEffectiveStat2_up.el.root
mc12_8TeV_2jetbin.sig.powheg_pythia_top.SM.SEL.JesEffectiveStat3_up.el.root
mc12_8TeV_2jetbin.sig.powheg_pythia_top.SM.SEL.JesEffectiveStat4_up.el.root
```

and the background samples used are

```
mc12_8TeV_2jetbin.bkg.BJesUnc_up.el.root
mc12_8TeV_2jetbin.bkg.SinglePart_up.el.root
mc12_8TeV_2jetbin.bkg.Pileup_OffsetMu_up.el.root
mc12_8TeV_2jetbin.bkg.Pileup_OffsetNPV_up.el.root
mc12_8TeV_2jetbin.bkg.Pileup_Pt_up.el.root
mc12_8TeV_2jetbin.bkg.Pileup_Rho_up.el.root
mc12_8TeV_2jetbin.bkg.PunchThrough_up.el.root
mc12_8TeV_2jetbin.bkg.flavor_comp_up.el.root
mc12_8TeV_2jetbin.bkg.flavor_response_up.el.root
mc12_8TeV_2jetbin.bkg.jvf_up.el.root
mc12_8TeV_2jetbin.bkg.EtaIntercalibrationModel_up.el.root
mc12_8TeV_2jetbin.bkg.EtaIntercalibrationTotalStat_up.el.root
mc12_8TeV_2jetbin.bkg.JesEffectiveDet1_up.el.root
mc12_8TeV_2jetbin.bkg.SEL.JesEffectiveDet2_up.el.root
mc12_8TeV_2jetbin.bkg.SEL.JesEffectiveDet3_up.el.root
mc12_8TeV_2jetbin.bkg.SEL.JesEffectiveMix1_up.el.root
mc12_8TeV_2jetbin.bkg.SEL.JesEffectiveMix2_up.el.root
mc12_8TeV_2jetbin.bkg.SEL.JesEffectiveMix3_up.el.root
mc12_8TeV_2jetbin.bkg.SEL.JesEffectiveMix4_up.el.root
mc12_8TeV_2jetbin.bkg.SEL.JesEffectiveModel1_up.el.root
mc12_8TeV_2jetbin.bkg.JesEffectiveModel2_up.el.root
mc12_8TeV_2jetbin.bkg.JesEffectiveModel3_up.el.root
mc12_8TeV_2jetbin.bkg.SEL.JesEffectiveModel4_up.el.root
mc12_8TeV_2jetbin.bkg.JesEffectiveStat1_up.el.root
```

mc12_8TeV_2jetbin.bkg.JesEffectiveStat2_up.el.root
mc12_8TeV_2jetbin.bkg.JesEffectiveStat3_up.el.root
mc12_8TeV_2jetbin.bkg.JesEffectiveStat4_up.el.root

Different samples we used as nominals for signal and background. For the jet flavor composition and jet flavor response uncertainties, the nominals used are

mc12_8TeV_2jetbin.sig.powheg_pythia_top.SM.SEL.nominal_JESflavor_nominal.el.root
mc12_8TeV_2jetbin.bkg.JESflavor_nominal.el.root

For the jet vertex fraction uncertainty, the nominals used are

mc12_8TeV_2jetbin.sig.powheg_pythia_top.SM.SEL.nominal.el.root
mc12_8TeV_2jetbin.bkg.nominal.el.root

The remaining jet energy scale uncertainties use the default nominals

mc12_8TeV_2jetbin.sig.powheg_pythia_top.SM.SEL.nominal_JES_nominal.el.root
mc12_8TeV_2jetbin.bkg.JES_nominal.el.root

Flavor Tagging: The signal samples used to estimate the sign of the flavor tagging uncertainties are

mc12_8TeV_2jetbin.sig.powheg_pythia_top.SM.SEL.jet_SF_btag_up.el.root
mc12_8TeV_2jetbin.sig.powheg_pythia_top.SM.SEL.jet_SF_ctag_up.el.root
mc12_8TeV_2jetbin.sig.powheg_pythia_top.SM.SEL.jet_SF_mistag_up.el.root

and the background samples used are

mc12_8TeV_2jetbin.bkg.jet_SF_btag_up.el.root
mc12_8TeV_2jetbin.bkg.jet_SF_ctag_up.el.root
mc12_8TeV_2jetbin.bkg.jet_SF_mistag_up.el.root

The nominal samples used are the default samples.

Lepton Reconstruction: The signal samples used to estimate the sign of the lepton scale factor uncertainties are

mc12_8TeV_2jetbin.sig.powheg_pythia_top.SM.SEL.el_SF_Id.el.root
mc12_8TeV_2jetbin.sig.powheg_pythia_top.SM.SEL.el_SF_reco.el.root
mc12_8TeV_2jetbin.sig.powheg_pythia_top.SM.SEL.el_trigger_SF.el.root

and the background samples used are

mc12_8TeV_2jetbin.bkg.el_SF_Id_up.el.root
mc12_8TeV_2jetbin.bkg.el_SF_reco_up.el.root
mc12_8TeV_2jetbin.bkg.el_trigger_SF_up.el.root

The nominal samples are the default samples. Further, there are specific uncertainties for electrons and muons separately. For those the signal and background samples are given by

mc12_8TeV_2jetbin.sig.powheg_pythia_top.SM.SEL.el_ees_up.el.root
mc12_8TeV_2jetbin.sig.powheg_pythia_top.SM.SEL.el_eer_up.el.root

mc12_8TeV_2jetbin.bkg.el_ees_up.el.root
mc12_8TeV_2jetbin.bkg.el_eer_up.el.root

for the electron energy scale and resolution and

mc12_8TeV_2jetbin.sig.powheg_pythia_top.SM.SEL.mu_musc_up.mu.root

mc12_8TeV_2jetbin.bkg.mu_musc_up.mu.root

for the muon momentum scale. In addition, there are muon specific uncertainties that only have a one-sided variation with respect to the nominal. The uncertainties are the muon momentum resolution ID and muon momentum smearing resolution. The signal samples used for these are given by

mc12_8TeV_2jetbin.sig.powheg_pythia_top.SM.SEL.mu_muid_res.mu.root
mc12_8TeV_2jetbin.sig.powheg_pythia_top.SM.SEL.mu_mums_res.mu.root

and the background samples are

mc12_8TeV_2jetbin.bkg.mu_muid_res.mu.root
mc12_8TeV_2jetbin.bkg.mu_mums_res.mu.root

MC Generator Uncertainties: In both analyses, single top decay distribution and cross section, the MC generator uncertainty comes from the difference between the default generator POWHEG and the alternative generator MC@NLO both interfaced with HERWIG. Therefore, to get the sign of that variation, we take the difference of the signal fraction calculated from the MC@NLO sample file and the signal fraction calculated from the POWHEG sample, both with their respective background samples.

mc12_8TeV_2jetbin.sig.amcatnlo_herwig.SM_AFII.SEL.nominal.el.root
mc12_8TeV_2jetbin.sig.powheg_herwig_top.SM_AFII.SEL.nominal.el.root
mc12_8TeV_2jetbin.bkg.tchannel_aMCatNLOHerwig_AFII.el.root
mc12_8TeV_2jetbin.bkg.tchannel_PowhegHerwig_AFII.el.root

Similarly, the sign for the MC generator uncertainty of the $t\bar{t}$ background is calculated from the following samples:

mc12_8TeV_2jetbin.bkg.ttbar_MCatNLOfHerwig.el.root
mc12_8TeV_2jetbin.bkg.ttbar_PowhegfHerwig_hdampInf_AFII.el.root
mc12_8TeV_2jetbin.sig.powheg_herwig_top.SM_AFII.SEL.nominal.el.root

where the last sample is the signal sample used in this case.

Parton Shower Uncertainties: As for the MC generator uncertainties, the parton shower uncertainties are calculated from the difference in two parton shower generators. In both analyses, the is the difference between the default PYTHIA and the alternative generator HERWIG. In both cases, the MC generator is POWHEG. The sample files used to calculate the sign of the change in the signal fraction are

```
mc12_8TeV_2jetbin.sig.powheg_herwig_top.SM_AFII.SEL.nominal.el.root
mc12_8TeV_2jetbin.sig.powheg_pythia_top.SM_AFII.SEL.nominal.el.root
mc12_8TeV_2jetbin.bkg.tchannel_PowhegHerwig_AFII.el.root
mc12_8TeV_2jetbin.bkg.tchannel_PowhegPythia_AFII.el.root
```

For the $t\bar{t}$ background, the

```
mc12_8TeV_2jetbin.bkg.ttbar_PowhegfHerwig_hdampInf_AFII.el.root
mc12_8TeV_2jetbin.bkg.ttbar_PowhegPythia_hdampInf_AFII.el.root
mc12_8TeV_2jetbin.sig.powheg_pythia_top.SM_AFII.SEL.nominal.el.root
```

where again the last sample is the signal sample used.

Scale and Initial/Final-State Radiation Uncertainties: Uncertainties from the variation of the renormalization and factorization scale of the MC and parton shower generators in both analyses, the MC generator POWHEG interfaced with the showering generator PYTHIA is used and the scales are varied according to Perugia 2011 tunes. The up and down variation correspond to a variation of the scale by a factor of two, called P2012radLo, and a variation by a factor of 0.5, called P2012radHi, respectively. The signal samples used to calculate the sign are

```
mc12_8TeV_2jetbin.sig.powheg_pythia_top.facsc2_rensc2_P2012radLo_AFII.SEL.nominal.el.root
mc12_8TeV_2jetbin.sig.powheg_pythia_top.facsc0p5_rensc0p5_P2012radHi_AFII.SEL.nominal.el.root
```

for the up and down variation, respectively. The nominal signal sample used is

```
mc12_8TeV_2jetbin.sig.powheg_pythia_top.P2012_AFII.SEL.nominal.el.root
```

Similarly, for the background the samples used are

```
mc12_8TeV_2jetbin.bkg.tchannel_PowhegPythiaP2012radLo_AFII.el.root
mc12_8TeV_2jetbin.bkg.tchannel_PowhegPythiaP2012radHi_AFII.el.root
```

with the nominal background sample

```
mc12_8TeV_2jetbin.bkg.tchannel_PowhegPythiaP2012_AFII.el.root
```

For the scale uncertainty from the $t\bar{t}$ background, the samples used to calculate the signs are

```
mc12_8TeV_2jetbin.bkg.ttbar_hdamp172p5_scale2_P2012radLo.el.root
mc12_8TeV_2jetbin.bkg.ttbar_hdamp345p0_scale0p5_P2012radHi.el.root
```

with the default nominal samples for signal and background.

E_T^{miss} and Luminosity: The signal samples used to estimate the sign of the E_T^{miss} soft jet resolution and scale as well as the Luminosity uncertainties are

```
mc12_8TeV_2jetbin.sig.powheg_pythia_top.SM.SEL.res_soft_up.el.root
mc12_8TeV_2jetbin.sig.powheg_pythia_top.SM.SEL.sc_soft_up.el.root
mc12_8TeV_2jetbin.sig.powheg_pythia_top.SM.SEL.lumi_up.el.root
```

and the background samples are

```
mc12_8TeV_2jetbin.bkg.res_soft_up.el.root
mc12_8TeV_2jetbin.bkg.sc_soft_up.el.root
mc12_8TeV_2jetbin.bkg.lumi_up.el.root
```

in combination with the default nominals.

PDF: The cross section analysis gives a table of different generators using different PDF sets. However, the variation of the cross section has no clear trend, meaning that the ranking of the PDF sets according to their cross section also depends on the generator. Unfortunately, the generator used in the single top decay distribution analysis, Protos + Pythia, is not listed in the cross section analysis. Therefore, no direct comparison can be made and no sign of the correlation can be estimated. The PDF uncertainties are therefore taken as uncorrelated between the single top decay distribution and cross section measurements.

Background Normalization Uncertainties: The background normalization uncertainties are small in both the single top decay distribution and cross section measurements. A possible correlation between those does not have an effect on the limits of the EFT coefficient and is therefore not included.

2.9.7 Total Correlation Matrix

In the previous sections the strategy for combining all systematic uncertainties into a single covariance matrix was discussed. Once this is achieved, the covariance matrix needs to be converted into a correlation matrix, using Eq. 2.74, as input for the EFT*fitter* tool. Table 26 shows the total correlation matrix used in the fit.

	F_0	F_L	a_{010}	a_{020}	a_{100}	a_{110}	a_{120}	a^{R}_{111}	a^{R}_{111}	a^{R}_{121}	a^{I}_{121}	$\sigma_{\mathrm{fid}}(t)$	$\sigma_{\mathrm{fid}}(\bar{t})$
F_0	1.000	-0.820	0.053	-0.056	0.092	-0.098	0.063	0.101	-0.120	-0.022	-0.022	0.018	0.016
F_L	-0.820	1.000	-0.032	0.032	-0.053	0.061	-0.035	-0.057	0.053	0.011	0.010	-0.028	-0.021
a_{010}	0.053	-0.032	1.000	-0.446	0.686	-0.651	0.518	0.418	0.061	-0.157	-0.080	0.249	0.112
a_{020}	-0.056	0.032	-0.446	1.000	-0.430	0.614	-0.393	-0.275	0.163	-0.066	0.123	-0.163	-0.035
a_{100}	0.092	-0.053	0.686	-0.430	1.000	-0.675	0.417	0.452	-0.088	-0.008	0.208	0.256	0.093
a_{110}	-0.098	0.061	-0.651	0.614	-0.675	1.000	-0.604	-0.621	0.152	0.254	0.114	-0.319	-0.157
a_{120}	0.063	-0.035	0.518	-0.393	0.417	-0.604	1.000	0.330	-0.065	-0.205	0.001	0.223	0.109
a^{R}_{111}	0.101	-0.057	0.418	-0.275	0.452	-0.621	0.330	1.000	-0.261	-0.230	0.030	0.337	0.228
a^{I}_{111}	-0.120	0.053	0.061	0.163	-0.088	0.152	-0.065	-0.261	1.000	0.053	-0.259	-0.124	-0.223
a^{R}_{121}	-0.022	0.011	-0.157	-0.066	-0.008	0.254	-0.205	-0.230	0.053	1.000	0.068	-0.138	-0.107
a^{I}_{121}	-0.022	0.010	-0.080	0.123	0.208	0.114	0.001	0.030	-0.259	0.068	1.000	0.158	0.224
$\sigma_{\mathrm{fid}}(t)$	0.018	-0.028	0.249	-0.163	0.256	-0.319	0.223	0.337	-0.124	-0.138	0.158	1.000	0.905
$\sigma_{\mathrm{fid}}(\bar{t})$	0.016	-0.021	0.112	-0.035	0.093	-0.157	0.109	0.228	-0.223	-0.107	0.224	0.905	1.000

Table 26: Total correlation matrix including both systematic and statistical uncertainties. The superscripts R and I stand for real and imaginary parts, respectively.

2.10 Dependence Of The Migration Matrix In The Single Top Decay Distribution Analysis On The EFT Coefficients

In this section the dependency of the migration matrix in the single top decay distribution analysis is discussed. The χ^2 function used in the single top decay distribution analysis to determine the generalized helicity fractions and phases defined in Section 2.4.3 consists of two pieces. The first piece describes the fit of angular coefficients $a_{k,l,m}$ parameterized in terms of the physics parameters $\vec{\alpha}$ to the measured angular coefficients and is given by

$$\chi_1^2 = \left(\vec{\nu}\left(\vec{\alpha}\right) - \vec{\nu}_0\right)^T \cdot \mathbf{V}^{-1} \cdot \left(\vec{\nu}\left(\vec{\alpha}\right) - \vec{\nu}_0\right), \tag{2.80}$$

where ν_0 is the vector of measured angular coefficients $a_{k,l,m}$ and $\vec{\nu}\left(\vec{\alpha}\right)$ are the angular coefficients parameterized by $\vec{\alpha} = \left\{f_1, f_1^+, f_0^+, \delta_+, \delta_-, P\right\}$, the generalized helicity fractions and phases. The matrix $\mathbf{V}$ is the covariance matrix of the measured coefficients. The second piece of the χ^2 function accounts for the dependency of the migration matrix on the physics parameters. The migration matrix $\mathbf{G}$ takes the reconstructed coefficients $\vec{\mathcal{A}}$ to their true values $\vec{a}$, where both are vectors of angular coefficients. This step is necessary to remove effects of the detector on the measurements and is parameterized by the migration matrix. The relation between reconstructed and deconvolved coefficients is given by

$$\vec{\mathcal{A}} = \mathbf{G} \cdot \vec{a}, \tag{2.81}$$

where $\vec{\mathcal{A}}$ is the vector of reconstructed coefficients and $\vec{a}$ is the vector of deconvolved coefficients. However, the number of reconstructed coefficients is generally larger

than the true coefficients, which means Eq. 2.81 can not be inverted. Instead, the true coefficients $\vec{a}$ can be determined by minimizing the χ^2 function

$$\chi_2^2 = \left(\vec{\mathcal{A}} - \mathbf{G} \cdot \vec{a}\right)^T \cdot \mathbf{W} \cdot \left(\vec{\mathcal{A}} - \mathbf{G} \cdot \vec{a}\right), \tag{2.82}$$

where χ_2^2 is now the second piece of the total χ^2. The second χ_2^2 gives a measure on how well a set of physics parameters describes the deconvolution of the detector effects. The total χ^2 was then given by

$$\chi^2 = \chi_1^2 + \chi_2^2 \tag{2.83}$$

The angular coefficients used for the combined fit in EFT*fitter* are the deconvolved coefficients $\vec{a}$. The deconvolution of these coefficients was done with a Standard Model migration matrix. Therefore, additional information on the dependency of the deconvolved coefficients on the EFT coefficients needs to be included in EFT*fitter*. Furthermore, the second piece of the χ^2 function in Eq. 2.82 needs to be included in EFT*fitter* to account for the dependency of the migration matrix on the EFT coefficients.

2.10.1 Parameterizing The Second Piece Of The χ^2 In Terms Of The EFT Coefficients

To minimize the total χ^2 in Eq. 2.83 a fit using Markov Chain Monte Carlo (MCMC) calculation was performed. The Markov Chain stored both pieces of the χ^2 function, deconvolved angular coefficients in terms of the varied physics parameters, and the physics parameters themselves. Therefore, it is possible to parameterize χ_2^2 in terms of the physics parameters. This parameterization was done by fitting a

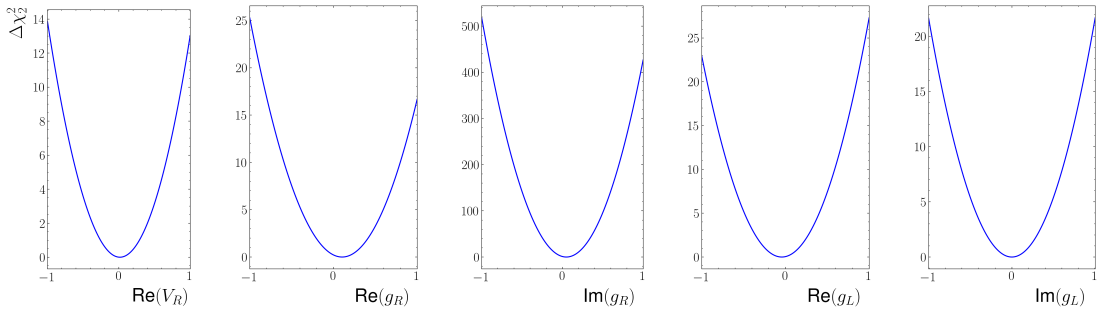

Figure 33: Variation $\Delta\chi^2_2$ due to the anomalous couplings. In each plot, the remaining couplings are set to zero.

polynomial of second degree including cross terms in terms of the anomalous couplings to χ^2_2. The anomalous couplings were chosen here, since the single top decay distribution analysis parameterizes the dimension 6 operator's effects in terms of these. The fit results were then checked with a additional Markov chains and good was agreement found. Once the dependency of χ^2_2 in terms of the anomalous couplings is found, Eq. 1.34 can be used to rewrite it in terms of the EFT coefficients. Figure 33 shows the resulting variation $\Delta\chi^2_2$ in terms of each of the anomalous couplings. In each figure, all the remaining couplings are set to zero. Figure 34 also shows the marginalized probability distributions of the EFT coefficients when adding χ^2_2. Most of the coefficients do not change much. The distributions of the coefficients $c^{(3)}_{\varphi Q}$, $\mathrm{Re}\,(c_{bW})$, and $c^{3,1}_{Qq}$ slightly decrease. Only the imaginary part of c_{tW} gets a significant shift towards the SM value of $\mathrm{Im}\,(c_{tW}) = 0$ as expected from the increase in χ^2_2.

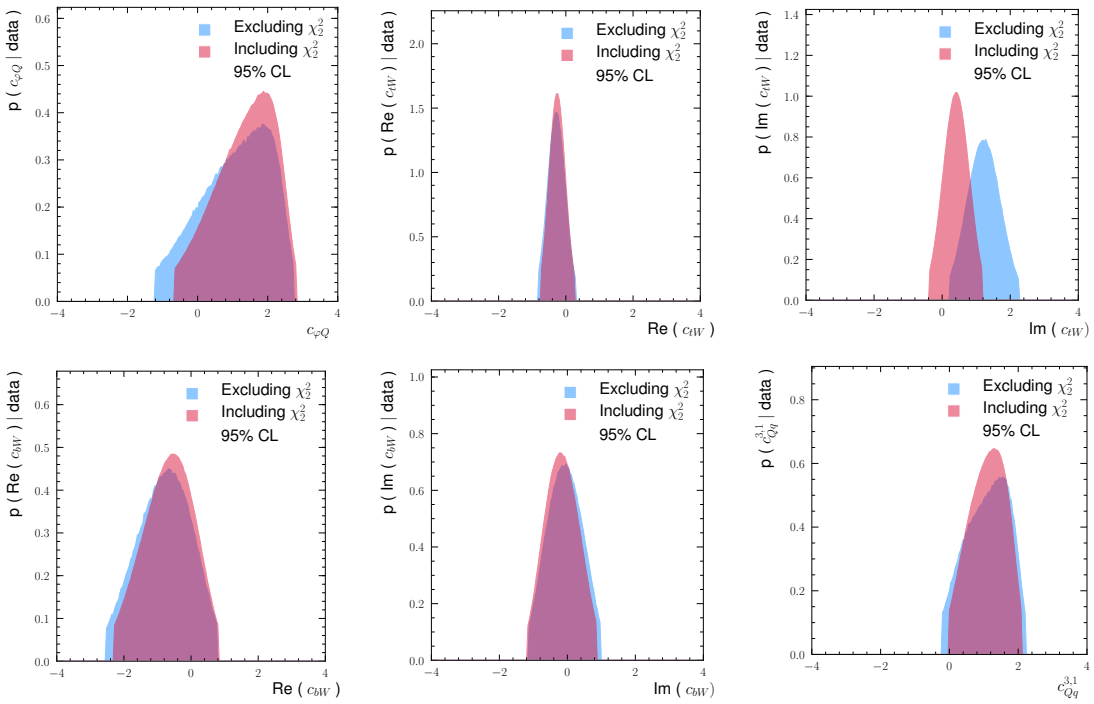

Figure 34: Comparison of the marginalized probability distributions of the EFT coefficients when including the additional χ^2_2 in Eq. 2.83. Only the imaginary part of c_{tW} is significantly impacted and the distribution shifts towards the SM value.

2.10.2 Dependency Of The Deconvolved Angular Coefficients On The EFT Coefficients

The parameterization of the deconvolved angular coefficients in terms of the anomalous couplings can again be constructed from the output of the MCMC calculation. For each angular coefficient $a_{k,l,m}$, the points in EFT space of the Markov chain are simultaneously fitted to a polynomial of degree 4. Again, the resulting

fit was checked with test data from different Markov chains and good agreement was found. Appendix F shows the fits for each angular coefficient $a_{k,l,m}$ and each anomalous coupling. In each plot, all other couplings are set to zero. Also shown are point along the axis of the specific EFT coupling. These points are selected in such a way that all other couplings are as close to zero as possible. However, the MCMC does not necessarily evaluate the coefficients at these points. In fact, it is unlikely for the Markov chain to pick points where only one coupling has a large value and the remaining ones are close to zero, since this combination will likely lead to a large χ^2 value. Furthermore, as was seen in the previous section, the imaginary part of g_R leads to a steep increase in the χ^2 such that the MCMC does not choose large values in $\mathrm{Im}(g_R)$. Therefore, the spread of the MCMC points in the $\mathrm{Im}(g_R)$ direction is relatively small, particularly if the other couplings are required to be close to zero. In addition to the fitted curves, each plot also shows the angular coefficient $a_{k,l,m}$ deconvolved with a Standard Model migration matrix, including their uncertainties. This allows to compare the fitted curves to the uncertainties of the measured coefficients and in most cases the variation of the angular coefficients with respect to the anomalous couplings does no exceed the uncertainties of the measured angular coefficients by much. In the cases where the dependency does have a potentially large effect, that effect only exceeds the uncertainty of the measured coefficient at coupling values beyond the expected allowed ranges of that coupling. From the polynomial coefficients of the fit, the dependency of the angular coefficients $a_{k,l,m}$ in terms of the EFT coefficients $c_{\varphi tb}$, c_{bW} and c_{tW} can then be determined from Eq. 1.34 and used in EFT*fitter*. Checking the posterior probability distributions in EFT*fitter*, no difference could be observed after including the EFT dependency of the angular coefficients.

2.11 Results

The following sections discuss the combination of the measurements listed in Section 2.4. First, the combination of the single top decay distribution and W helicity measurements will be discussed. The fit is performed using the EFT*fitter* tool discussed in Section 2.2. A set of $N_{\text{par}} = 5$ EFT coefficients is fitted to a total of $N_{\text{obs}} = 11$ observables. Details about the contributing EFT coefficients and the allowed regions of these will be given. Next, the t-channel fiducial cross section is added to the fit. This increases the number of independent observables to $N_{\text{obs}} = 13$, while also increasing the number of free parameters $N_{\text{par}} = 7$. Finally, a case study is conducted by adding s-channel single top cross section to the fit.

2.11.1 Combination Of Single Top Decay Distributions And W Helicity Fractions

This section discusses the combination of the single top decay distribution and W helicity fraction measurements. Both analyses measure angular distributions of the top quark decay products and therefore only ratios of coefficients with respect to V_L can be constrained. In addition, both of the measurements measure only the top quark decay and therefore the four-quark operator $c_{Qq}^{3,1}$ does not contribute. This leaves the remaining coefficients $c_{\varphi tb}$, c_{bW}, and c_{tW} as free parameters of the fit, where $c_{\varphi tb}$ is real and positive and c_{bW} and c_{tW} are complex as discussed in Section 2.5. Figure 35 shows marginalized, two-dimensional probability distributions of combinations of the ratios of the real parts of the EFT coefficients $c_{\varphi tb}$, c_{bW} and c_{tW} with V_L. Each figure shows the 95% confidence region that can be constrained by the W helicity fraction measurement (WHEL), the single top decay distribution measure-

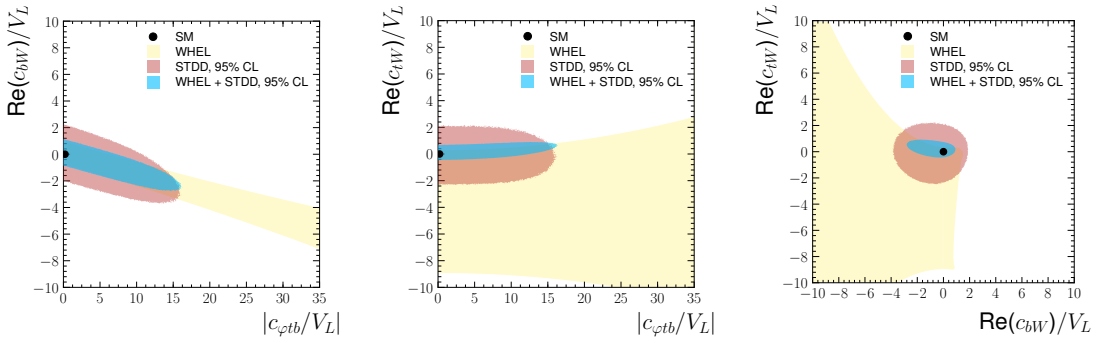

(a) (b) (c)

Figure 35: Marginalized, two-dimensional probability distribution of the ratio of the EFT coefficients (a) $c_{\varphi tb}$ and $\mathrm{Re}\,(c_{bW})$, (b) $c_{\varphi tb}$ and $\mathrm{Re}\,(c_{tW})$, (c) $\mathrm{Re}\,(c_{bW})$ and $\mathrm{Re}\,(c_{tW})$, with V_L. Also shown is the Standard Model point.

ment (STDD), and the combination of the two measurements (WHEL + STDD). As discussed in Section 2.4, the coefficients $c_{\varphi tb}$ and $\mathrm{Re}\,(c_{bW})$ show a significant anti-correlation. This can be seen in Figure 35 (a) for both the W helicity fractions and the single top decay distributions. The constraints on the EFT coefficients coming from the W helicity fractions alone are shown in yellow. The W helicity fractions do not provide enough constraints to determine the confidence regions for complex EFT coefficients. Rather, the regions in yellow correspond to regions where the posterior probability distribution has non-negligible values. In Figure 35 (c) the coefficient $\mathrm{Re}\,(c_{bW})$ is constrained to mostly negative values. The reason for this is that $c_{\varphi tb}$ is set real and positive and therefore the coefficient $\mathrm{Re}\,(c_{bW})$ is essentially forced to negative values, due to the anti-correlations between $c_{\varphi tb}$ and c_{bW}. This behavior only appears when looking at the W helicity fractions alone, since in the other

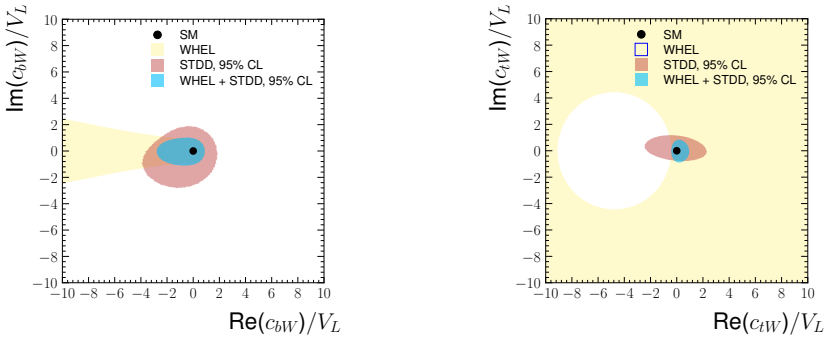

(a) (b)

Figure 36: Marginalized, two-dimensional probability distribution of the ratio of the EFT coefficients (a) $\mathrm{Re}\,(c_{bW})$ and $\mathrm{Im}\,(c_{bW})$, (b) $\mathrm{Re}\,(c_{tW})$ and $\mathrm{Im}\,(c_{tW})$, with V_L. Also shown is the Standard Model point.

measurements the coefficients $c_{\varphi tb}$ and c_{bW} also appear in other combinations. Figure 35 also demonstrates how important correlations are in determining individual limits on EFT coefficients. Neglecting correlations in the combination of the two measurements would severely overestimate the smallness of the confidence limit on the real part of c_{tW} (blue region in (a)). The single top decay distributions can in principle constrain all coefficients but adding the W helicity significantly improves the size of the confidence regions. Figure 36 shows the marginalized two-dimensional confidence regions of the two complex coefficients c_{bW} and c_{tW}. In (a), the real part of c_{bW} is plotted against the imaginary part of c_{bW}, and in (b), the real part of c_{tW} is plotted against the imaginary part of c_{tW}. In Figure 36 (a) the same behaviour of $\mathrm{Re}\,(c_{bW})$ is seen as in Figure 35 (c), where $\mathrm{Re}\,(c_{bW})$ is constrained to negative values. The W helicity fractions can only exclude a region in the negative $\mathrm{Re}\,(c_{tW})$

plane. Adding the single top decay distributions individually constrains the real and imaginary parts and pins the allowed region around the Standard Model point.

Limits are set on the ratios of the coefficients $c_{\varphi tb}$, c_{bW} and c_{tW} with respect to V_L. The 68% and 95% confidence limits on the right-handed vector coefficients $c_{\varphi tb}$ are

$$\begin{aligned} \left|\frac{c_{\varphi tb}}{V_L}\right| &< 7.92 \quad (68\%\text{CL})\,, \\ \left|\frac{c_{\varphi tb}}{V_L}\right| &< 13.57 \quad (95\%\text{CL})\,, \end{aligned} \tag{2.84}$$

the limits on the right-handed tensor coefficient c_{bW} are

$$\begin{aligned} \text{Re}\left[\frac{c_{bW}}{V_L}\right] &\in [-1.44, 0.14] \quad (68\%\text{CL})\,, \\ \text{Re}\left[\frac{c_{bW}}{V_L}\right] &\in [-2.33, 0.67] \quad (95\%\text{CL})\,, \\ \text{Im}\left[\frac{c_{bW}}{V_L}\right] &\in [-0.48, 0.43] \quad (68\%\text{CL})\,, \\ \text{Im}\left[\frac{c_{bW}}{V_L}\right] &\in [-0.89, 0.84] \quad (95\%\text{CL})\,, \end{aligned} \tag{2.85}$$

and the limits on the left-handed tensor coefficient c_{tW} are

$$\begin{aligned} \text{Re}\left[\frac{c_{tW}}{V_L}\right] &\in [-0.05, 0.50] \quad (68\%\text{CL})\,, \\ \text{Re}\left[\frac{c_{tW}}{V_L}\right] &\in [-0.29, 0.80] \quad (95\%\text{CL})\,, \\ \text{Im}\left[\frac{c_{tW}}{V_L}\right] &\in [-0.36, 0.34] \quad (68\%\text{CL})\,, \\ \text{Im}\left[\frac{c_{tW}}{V_L}\right] &\in [-0.70, 0.68] \quad (95\%\text{CL})\,. \end{aligned} \tag{2.86}$$

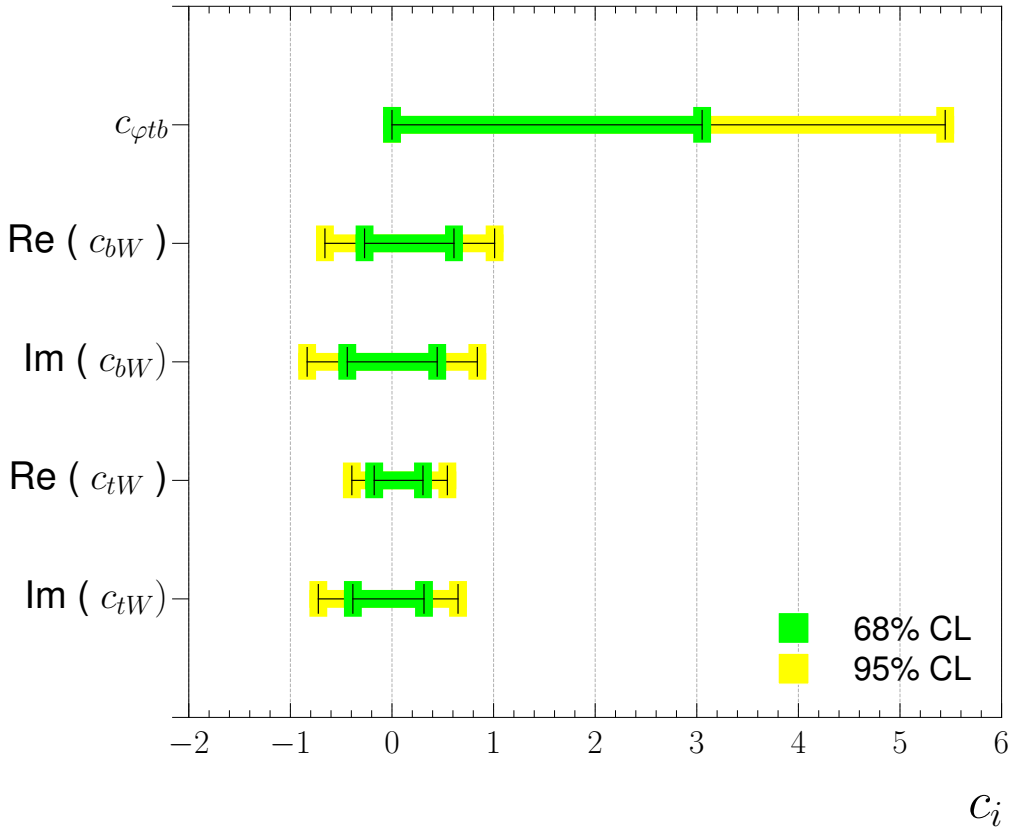

Figure 37: Individual 95% (yellow) and 68% (green) confidence limits on the EFT coefficients for the combination of the W helicity fractions and single top decay distributions.

All limits are in accordance with the Standard Model. Appendix G shows the marginalized two-dimensional probability distributions of the EFT coefficients. Limits on individual coefficients can also be given. Individual limits correspond to the limits set on one of the EFT coefficients, while all other coefficients are set to their

Standard Model values. Figure 37 shows the limits on the individual coefficients. The larges effect of constraining the coefficients individually is in the coefficients $c_{\varphi tb}$ and c_{bW}. As stated earlier, this is due to the correlation between the two coefficients.

In this section it was demonstrated that it is possible to set tight limits on the EFT coefficients by combining the W helicity fraction and single top decay distribution measurements. However, these limits are given with respect to V_L. To constrain the limits of the couplings themselves requires the addition of observables that measure total rates, such as the cross section. This will be the topic of the following section.

2.11.2 Combination Of The Single Top Decay Distributions, W Helicity Fractions And Fiducial Cross Section

In the previous section the combination of the W helicity fractions and the single top decay distributions was discussed. To be able to set constraints on the EFT coefficients themselves and not just the ratio with respect to V_L, the $\sqrt{s} = 8$ TeV fiducial t-channel cross sections are added to the combination. This also allows to constrain the four-quark coefficient $c_{Qq}^{3,1}$, which only contributes to the production and not to the decay of the top quark. Therefore, the full EFT parameter space $c_{\varphi Q}^{(3)}$, $c_{\varphi tb}$, c_{bW}, c_{tW}, and $c_{Qq}^{3,1}$ can be constrained. Figure 38 shows how the 68% and 95% confidence limits on the Wtb coefficients $c_{\varphi tb}$, c_{bW} and c_{tW} change when constraining them with either only the single top decay distributions (STDD), a combination of single top decay distributions and W helicity fractions (STDD + WHEL), or a combination that also adds the cross sections (STDD + WHEL + XSEC). In most cases, adding the cross section does not improve the limits by much. However, it is important to keep in mind that in the combination with the cross

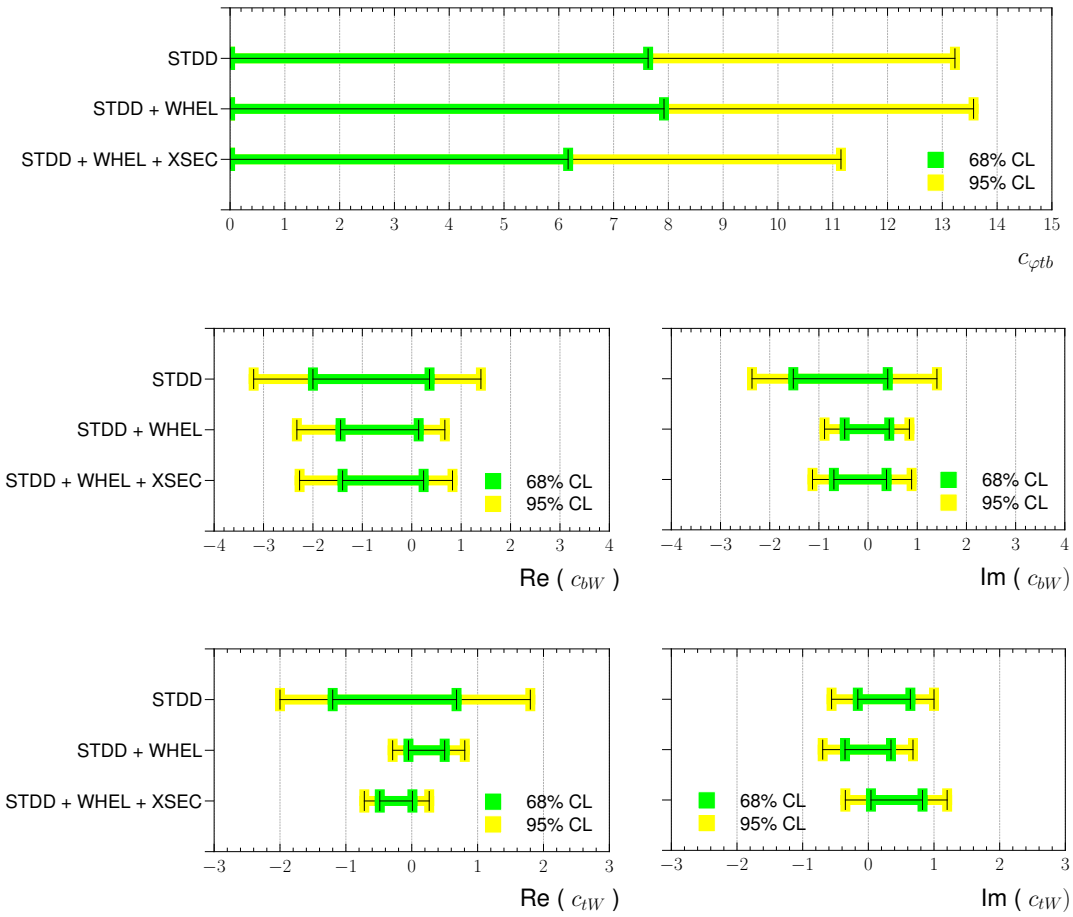

Figure 38: Comparison of the EFT coefficients constraining the Wtb vertex. In each plot, the marginalized 68% CL and 95% CL set by the single top decay distributions (STDD), the combination of single top decay distributions and W helicity fractions (STDD + WHEL), and the combination of single top decay distributions, W helicity fractions and cross sections (STDD + WHEL + XSEC).

section any assumptions on V_L are dropped. Even with less assumptions, the limits still improve slightly. For the tensor coefficients, the largest improvement comes from adding the W helicity fractions. This is most prominent in the real part of c_{tW}. The imaginary part of c_{tW} is solely fixed by the single top decay distributions, since this is the only measurement sensitive to imaginary coefficients. The imaginary part of c_{bW} is not that well constrained by either of the two angular measurements, but combining the two decreases the limit by decreasing the overall magnitude of the coefficient c_{bW}. Figure 39 also shows the one-dimensional probability distributions of all EFT coefficients and the polarization. Each plot shows the 68% and 95% confidence intervals. From the marginalized distributions the following limits on the EFT coefficients are set. For the Standard Model like coefficient $c_{\varphi Q}^{(3)}$, the limits are found to be

$$\begin{aligned} c_{\varphi Q}^{(3)} &\in [0.68, 2.49] \quad (68\%\text{CL}) \,, \\ c_{\varphi Q}^{(3)} &\in [-0.64, 2.83] \quad (95\%\text{CL}) \,. \end{aligned} \tag{2.87}$$

The magnitude of the right-handed vector coefficient $c_{\varphi tb}$ the upper limits are

$$\begin{aligned} c_{\varphi tb} &< 6.17 \quad (68\%\text{CL}) \,, \\ c_{\varphi tb} &< 11.15 \quad (95\%\text{CL}) \,. \end{aligned} \tag{2.88}$$

For the real and imaginary parts of the coefficient right-handed tensor coefficient c_{bW} limits are found at

$$\begin{aligned} \text{Re}\,(c_{bW}) &\in [-1.40, 0.24] \quad (68\%\text{CL}) \,, \\ \text{Re}\,(c_{bW}) &\in [-2.27, 0.82] \quad (95\%\text{CL}) \,, \\ \text{Im}\,(c_{bW}) &\in [-0.70, 0.37] \quad (68\%\text{CL}) \,, \\ \text{Im}\,(c_{bW}) &\in [-1.13, 0.88] \quad (95\%\text{CL}) \,, \end{aligned} \tag{2.89}$$

and for the left-handed tensor coefficient c_{tW} at

$$\begin{aligned}
&\mathrm{Re}\,(c_{tW}) \in [-0.49, 0.01] \quad (68\%\mathrm{CL})\,, \\
&\mathrm{Re}\,(c_{tW}) \in [-0.72, 0.26] \quad (95\%\mathrm{CL})\,, \\
&\mathrm{Im}\,(c_{tW}) \in [0.04, 0.82] \quad (68\%\mathrm{CL})\,, \\
&\mathrm{Im}\,(c_{tW}) \in [-0.35, 1.20] \quad (95\%\mathrm{CL})\,.
\end{aligned} \tag{2.90}$$

The four-quark coefficient $c_{Qq}^{3,1}$ is bound between

$$\begin{aligned}
&c_{Qq}^{3,1} \in [0.61, 1.79] \quad (68\%\mathrm{CL})\,, \\
&c_{Qq}^{3,1} \in [0.00, 2.11] \quad (95\%\mathrm{CL})\,.
\end{aligned} \tag{2.91}$$

All limits are in accordance with the Standard Model prediction. Since the polarization has been treated as a free parameter, the confidence limits from the marginalization are also stated here,

$$\begin{aligned}
&P > 0.86 \quad (68\%\mathrm{CL})\,, \\
&P > 0.73 \quad (95\%\mathrm{CL})\,,
\end{aligned} \tag{2.92}$$

these limits are in accordance with the limits on the polarization from the single top decay distribution measurement, given in Eq. 2.4.3. As was mentioned before, several of the EFT coefficient are correlated in some of the measurements. Specifically, the right-handed coefficients are correlated in the W helicity fraction measurement and the single top decay distributions. It is therefore important to study the correlations of the coefficients in the final result. Table 27 shows the correlations between the EFT coefficients. The high correlation between the two right-handed coefficients $c_{\varphi tb}$ and $\mathrm{Re}\,(c_{bW})$ as discussed in Section 2.4.2 and Section 2.4.3 is reflected here. Similarly, the Standard Model like coefficient $c_{\varphi Q}^{(3)}$ and the four-quark coefficient $c_{Qq}^{3,1}$

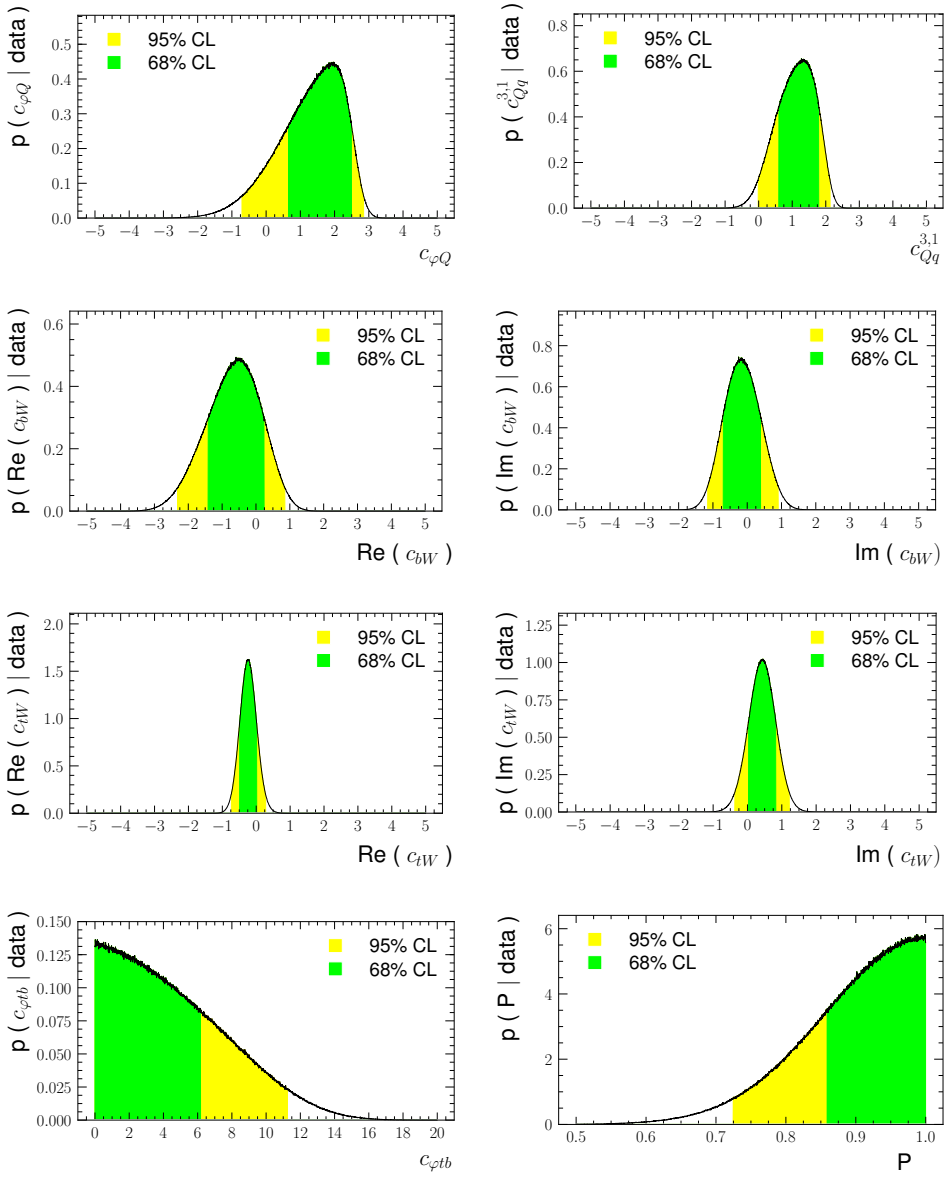

Figure 39: Marginalized, one-dimensional probability distribution of the EFT coefficients and the polarization.

	$c_{\varphi Q}^{(3)}$	$c_{\varphi tb}$	c_{bW}^{R}	c_{bW}^{I}	c_{tW}^{R}	c_{tW}^{I}	$c_{Qq}^{3,1}$	P
$c_{\varphi Q}^{(3)}$	1	−0.58	0.48	0.09	−0.32	0.05	0.70	−0.12
$c_{\varphi tb}$	−0.58	1	−0.79	−0.18	0.35	−0.04	0.01	0.12
c_{bW}^{R}	0.48	−0.79	1	0.13	−0.32	0.05	−0.01	−0.08
c_{bW}^{I}	0.09	−0.18	0.13	1	−0.11	0.08	−0.01	−0.05
c_{tW}^{R}	−0.32	0.35	−0.32	−0.11	1	−0.07	−0.07	0.14
c_{tW}^{I}	0.05	−0.04	0.05	0.08	−0.07	1	0.05	0.09
$c_{Qq}^{3,1}$	0.70	0.01	−0.01	−0.01	−0.07	0.05	1	−0.01
P	−0.12	0.12	−0.08	−0.05	0.14	0.09	−0.01	1

Table 27: Correlations between the EFT coefficients and the polarization P. The superscripts R and I stand for real and imaginary parts, respectively.

show a fairly strong correlation. In Table 12 of Section 2.7 lists the coefficients $\boldsymbol{\kappa}$ that parameterize the fiducial cross section in terms of the EFT coefficients. Given the two coefficients connecting $c_{\varphi Q}^{(3)}$ and $c_{Qq}^{3,1}$ are κ_2 and κ_4 (see Appendix C.3) a correlation coefficient as in Table 27 is expected. Some medium sized correlations exist between $c_{\varphi Q}^{(3)}$ and the right-handed coefficients $c_{\varphi tb}$ and $\mathrm{Re}\,(c_{bW})$. As expected, the imaginary parts are not correlated strongly with any of the other coefficients. Also the polarization does not exhibit a strong correlation with any of the EFT coefficients. Figure 40 shows the two-dimensional marginalized probability distributions of the coefficients $c_{\varphi tb}$ and $\mathrm{Re}\,(c_{bW})$ as well as the coefficients $c_{\varphi Q}^{(3)}$ and $c_{Qq}^{3,1}$. In both cases the correlations can be seen. From this it is also clear, that a complete description of the confidence limits of the EFT coefficients can only be done when taking

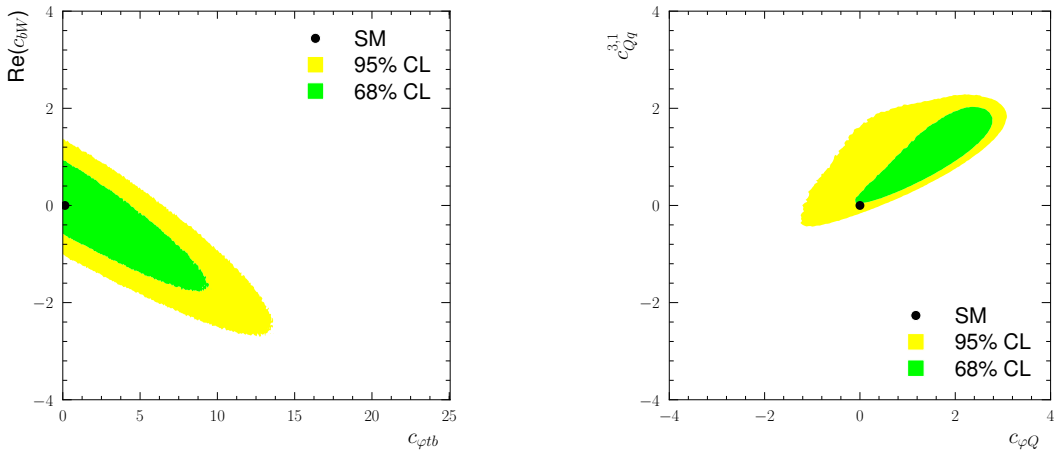

(a) (b)

Figure 40: Two-dimensional probability distributions of the EFT coefficients (a) $c_{\varphi tb}$ and $\mathrm{Re}\,(c_{bW})$, (b) $c_{\varphi Q}^{(3)}$ and $c_{Qq}^{3,1}$. In both cases the correlation seen in Table 27 is visible.

into account the correlations between them. Without correlations, care needs to be taken when interpreting the limits. The remaining pairs of coefficients are shown in Figures 83–87 of Appendix H.

In addition to the marginalized confidence limits, also the individual limits are shown. Figure 41 shows the individual 95% and 68% confidence limits of the EFT coefficients. The Standard Model like coefficient $c_{\varphi Q}^{(3)}$ and the four-quark coefficient $c_{Qq}^{3,1}$ are affected the most. For both coefficients the 95% CL decreases by roughly 70%. This can be explained by the large correlation between these two coefficients. If one of the two is fixed to the Standard Model value, then the allowed region for the one other should decrease accordingly. Further the right-handed vector coefficient

$c_{\varphi tb}$ decreases by roughly 60% and the real part right-handed tensor coefficient c_{bW} by roughly 35%. Again, these two coefficients are correlated, which affects their limits when looked at individually. The limits on the coefficient c_{tW} for both real and imaginary part is decreased by roughly 20%. Finally, the imaginary part of c_{bW} is not affected by fixing the remaining coefficients to their Standard Model values.

Impact Of The Correlations Between The Measurements

The results of the combination of the single top decay distribution, W helicity fraction, and fiducial cross section take into account all correlations between the individual observables but in particular also between the different measurements. Details on the correlations were discussed in Section 2.9.4. In this section, the impact of the correlations on the confidence limits of the EFT coefficients is shown. Figure 42 shows how the one-dimensional 95% confidence regions shift when adding the correlations between the measurement in the fit. Shown are the confidence limits of the real and imaginary parts of the coefficients c_{tW} and the polarization. There is no noticeable change from the correlations on the remaining EFT coefficients. For the real part of c_{tW}, the adding the correlations results in a slight shift of the confidence interval towards more negative values, while the imaginary part of c_{tW} shifts towards more positive values. The confidence limit of the polarization decreases slightly when adding the correlations. Nevertheless, the impact of the correlations between the different measurements is small.

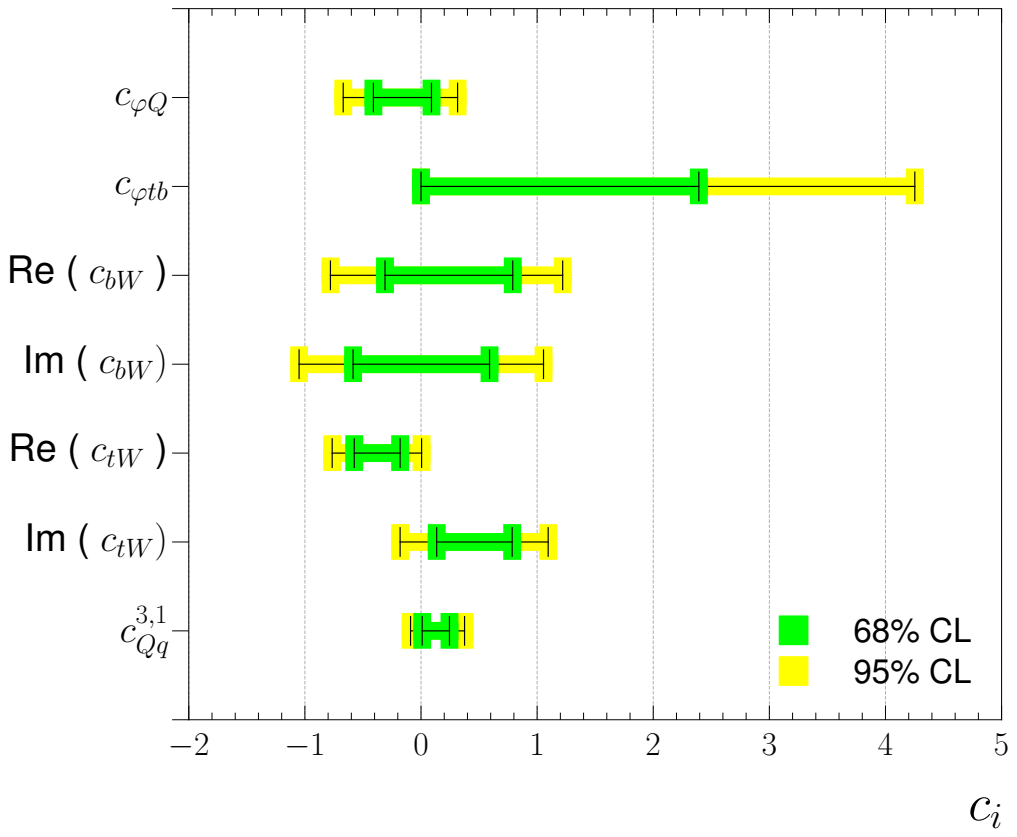

Figure 41: Individual 95% (yellow) and 68% (green) confidence limits on the EFT coefficients for the combination of the W helicity fractions, the single top decay distributions and the cross section.

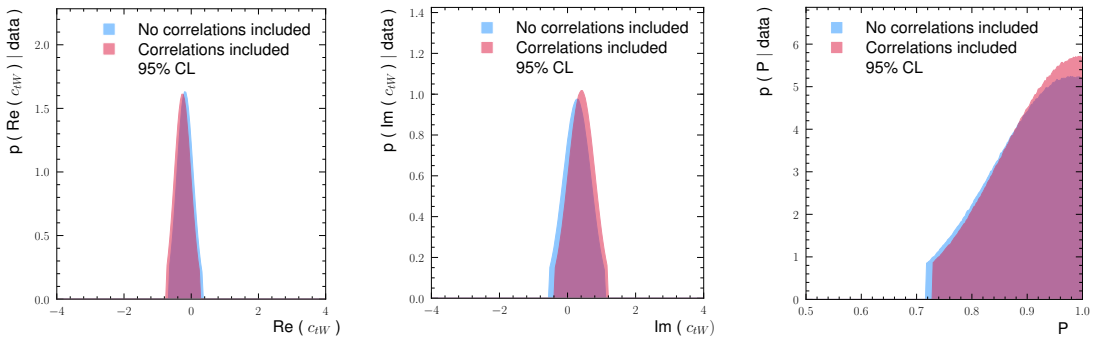

(a) (b) (c)

Figure 42: Comparison of the marginalized, one-dimensional probability distribution of the EFT coefficients (a) $\mathrm{Re}\,(c_{tW})$, (b) $\mathrm{Im}\,(c_{tW})$, and the polarization P when including correlations between the measurements (red) and when neglecting correlations between the measurements (blue). Correlations between the observables within a measurement are always included.

2.11.3 Case Study: Adding the S-Channel Single Top Production Cross Section

The confidence limits of the four-quark coefficient $c_{Qq}^{3,1}$ found in the previous section can in principle be improved by adding the $\sqrt{s} = 8$ TeV s-channel top + anti-top cross section [40] to the fit. The s-channel cross section was discussed in Section 1.3.1. Since the uncertainties of the s-channel cross section are still fairly large it does not provide strong constraints on the EFT coefficients related to the Wtb interaction. However, the s-channel cross section is sensitive to the four-quark coefficient $c_{Qq}^{3,1}$. In the Standard Model, the s-channel cross section is suppressed

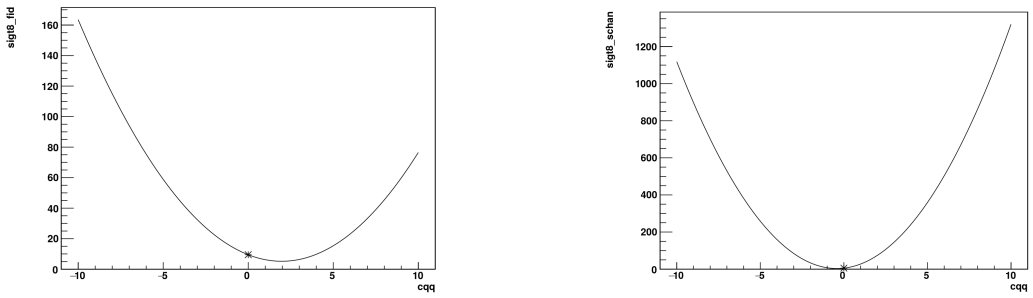

(a) (b)

Figure 43: Dependency of the t-channel top quark cross section (a) and s-channel top + anti-top cross section (b) on the four-quark coefficient $c_{Qq}^{3,1}$. Figures taken from EFT*fitter* output.

due to the intermediate W boson which is highly off-shell. This suppression does not exist for the four-quark interaction, which is why small values of $c_{Qq}^{3,1}$ can lead to a large increase of the cross section. The dependency of both the t-channel and s-channel cross section is shown in Figure 43. The increase with $c_{Qq}^{3,1}$ is almost an order of magnitude higher for the s-channel than it is for the t-channel in the same range of the coefficient.

To parameterize the s-channel cross section in terms of the EFT coefficients a similar approach as discussed in Section 2.7 and Section 2.8 is used. There are some differences in the combinations of EFT coefficients that can appear in the parameterization of the s-channel cross section. Here, combinations of left- and right-handed coefficients do not vanish, even for massless b-quark. A list of coefficients $\boldsymbol{\kappa}$ for the s-channel cross section is given in Table 28. The coefficients κ_3 and κ_5

	κ		κ
κ_1	0.4583	κ_8	0.0000
κ_2	0.0833	κ_9	0.0009
κ_3	1.9268	κ_{10}	0.0002
κ_4	0.4738	κ_{11}	-0.0003
κ_5	2.3176	κ_{12}	-0.0004
κ_6	0.0001	κ_{13}	-0.0140
κ_7	0.0001	κ_{14}	0.0835

Table 28: Coefficients κ for the s-channel cross section. The full expression of the cross section is given in Appendix D.

corresponding to the interference with the Standard Model and the quadratic term in $c_{Qq}^{3,1}$, respectively. Both are significantly larger than the κ's corresponding to the remaining EFT coefficients. The full expression of the s-channel cross section in terms of the EFT coefficients is given in Appendix D.

For the s-channel cross section, correlations are not taken into account with the remaining measurements. As seen in the previous section, the correlations do not affect the fit by much and it is assumed here that also the s-channel cross section is not affected too much.

One remaining issue is the possible affect of the detector acceptance due to changes in the kinematics from the EFT coefficients. Since the measured s-channel is a total cross sections, acceptance effects could play a role. Nevertheless, as a case study the s-channel is added to the fit here, to investigate the affects on the limits

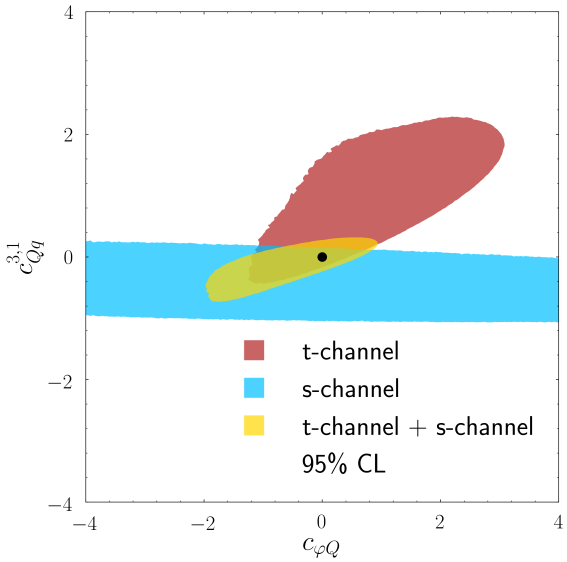

Figure 44: Comparison of the two-dimensional probability distribution of the EFT coefficients $c_{\varphi Q}^{(3)}$ and $c_{Qq}^{3,1}$. Shown is the combination of the single top decay distributions and the W helicity fractions together with the t-channel fiducial cross section (red), the s-channel cross section (blue), and the combination of t-channel and s-channel cross section.

of the EFT coefficients. Figure 44 shows a comparison of the two-dimensional probability distribution of the single top decay distributions and the W helicity fractions with either the t-channel, the s-channel or a combination of t-channel and s-channel cross section. The coefficient $c_{\varphi Q}^{(3)}$ is not directly constrained by the s-channel cross section in the limits studied in the previous sections. However, adding the s-channel cross section does put strong constraints on the four-quark coefficient $c_{Qq}^{3,1}$. Since $c_{Qq}^{3,1}$ and $c_{\varphi Q}^{(3)}$ are correlated, this in turn puts stronger limits on $c_{\varphi Q}^{(3)}$, as seen in Figure 44.

2.12 Conclusion

This analysis studies the combination of different ATLAS top quark measurements and the effect of this combination on the confidence limits of a set of EFT coefficients. The EFT coefficients are the Wilson coefficients of an EFT expansion in the Standard Model fields. The EFT coefficients considered here are a set of dimension 6 operators giving contributions to the Wtb and four-quark interactions. The analysis relies on results of the single top decay distribution measurement, which measures a set of generalised helicity fractions and phases in the top quark decay, the W helicity fraction measurement, which measures the fractions of transversely and longitudinally polarized W bosons in top quark decays, and the $\sqrt{s} = 8$ TeV single top t-channel fiducial cross sections. Each of the measurements provides its own advantages. The single top decay distribution measurement can constraint three of the four Wtb related EFT coefficients at once. The Standard Model like coefficient $c_{\varphi Q}^{(3)}$ is taken as the normalization of the remaining coefficients. In addition, the angular coefficients of the single top decay distributions are the only measured quantities able to determine complex observables. Therefore, in this analysis, also complex EFT coefficients could be constrained. The W helicity fraction measurement is more precise and allows for tighter bounds on the Wtb interaction coefficients $\mathrm{Re}\,(c_{tW})$ and $\mathrm{Re}\,(c_{bW})$ when combined with the single top decay distributions. The cross sections add the ability to constrain the magnitude of the EFT coefficients and therefore also measure the Standard Model like coefficient $c_{\varphi Q}^{(3)}$, which has to be fixed to its Standard Model value in the measurements of the single top decay distribution and W helicity fraction. Further, the cross sections are sensitive to the four-quark interaction $c_{Qq}^{3,1}$ and therefore allow the constraint of an additional coefficient.

Care was taken in the study and implementation of the correlations between

the measurements. For this, all categories of systematic uncertainties have been matched between the different measurements and correlations have been evaluated. It was found that the correlations between measurements do not affect the posterior probability distributions of the EFT coefficients in a significant way. A naive combination neglecting correlations between different measurements already leads to reasonable results.

Finally, limits were set on the EFT coefficients that are in accordance with the Standard Model predictions. At 95% confidence limit, the Standard Model like coefficients was determined as $c_{\varphi Q}^{(3)} \in [-0.64, 2.83]$, the right-handed vector coefficient $c_{\varphi tb} < 11.15$, the real and imaginary parts of the right-handed tensor coefficient $\mathrm{Re}\,(c_{bW}) \in [-2.27, 0.82]$, $\mathrm{Im}\,(c_{bW}) \in [-1.13, 0.88]$, and the real and imaginary parts of the left-handed tensor coefficient $\mathrm{Re}\,(c_{tW}) \in [-0.72, 0.26]$, $\mathrm{Im}\,(c_{tW}) \in [-0.35, 1.20]$. Limits were also set on the four-quark coefficient $c_{Qq}^{3,1} \in [0.00, 2.11]$. All of these limits improve on the limits set by the recent global fit [74] discussed in Section 2.6. In obtaining these limits and adding the fiducial cross section to the combination no assumptions are put on the EFT coefficients. However, as discussed in Section 2.4, the fiducial cross section was chosen because the dependence of the acceptance on the EFT coefficients is expected to be small. Due to technical restrictions, the neural network used in the cross section analysis as a signal/background discriminant could not be used to estimate the dependency of the acceptance on the EFT coefficients. In case the acceptance does have a sizeable effect, variations in the allowed regions could still occur. This effect could be further investigated in future combinations of measurements. Nevertheless, the combination of the single top decay distributions and the W helicity fractions discussed in Section 2.11.1 still provides constraints on the Wtb related EFT coefficients without relying on the cross section.

Besides setting limits on EFT coefficients, the analysis presented here serves an-

other role within the experiment. It presents as a study on how future analyses can be conducted in such a way as to simplify combinations with other measurement. This concerns in particular the treatment of the systematic uncertainties and correlations. Besides this, the treatment of anomalous or EFT coefficients can also be optimized for example in parameterizing the analyses' procedures in terms of the EFT coefficients; Do quantities such as the detector acceptance or deconvolution depend in a significant way on the EFT parameters? Having the ability to combine a greater variety of measurement in a systematic way would provide the ability to constrain a larger set of EFT parameters at once and lead the way to a more global fit without the need for assumptions on the EFT coefficients.

3.0 VP1-Light

The following chapter discusses the new standalone ATLAS 3D event display VP1-Light and the standalone GeoModel package. Both applications were presented at the 23rd Computing in High Energy and Nuclear Physics 2018 conference in Sofia, Bulgaria [82, 83].

3.1 The VP1 Event Display And Why ATLAS Needs A Light Version

Displaying a particle physics event has been crucial part of an analysis since the very beginning of particle physics. In the early days, track of charged particles were both measured and visualized in Wilson or cloud chambers. The chambers consisted of supersaturated vapor of water or alcohol. A charged particle passing through the chamber ionizes the gas along its trajectory . The vapor condensates along the ionized vapor which is then visible to the eye or a camera. Figure 45 (a) shows a picture of a track in a Wilson chamber that led to the discovery of the positron in 1933 [84]. With the advent of computer graphics, software too took the place of photographic images. These tool to visualize particle physics events are usually called event displays. Figure 45 (b) shows an event display of a Higgs boson candidate recorded by the ATLAS experiment in June 2012. The Higgs event is displayed by the ATLAS 3D event display VP1 [85, 86]. VP1 is one of the general purpose event displays used in ATLAS. It is tightly integrated in the experiment's offline software framework Athena [75] to access all kinds of experimental data. This integration has many advantages in terms of data access. VP1 can display the experimental data at

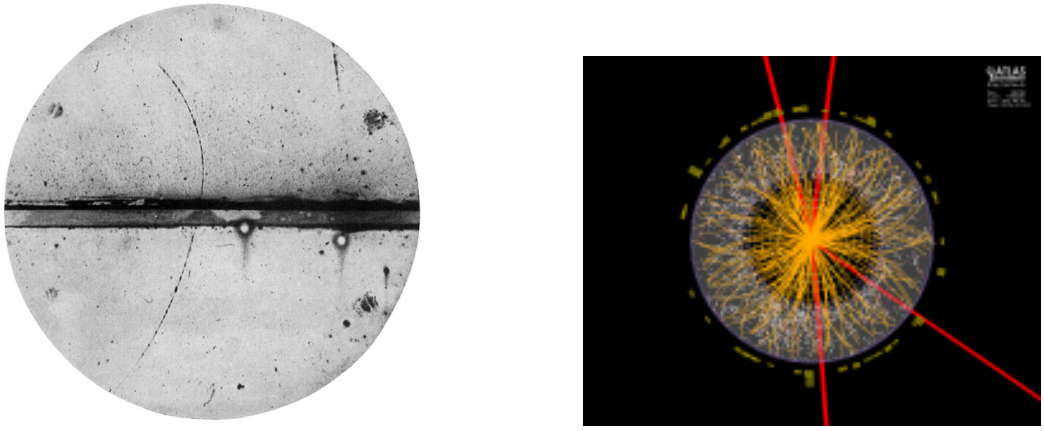

(a) (b)

Figure 45: Event displays from then and now. (a) A photographic display of a track in a Wilson chamber that led to the discovery of the positron [84]. (b) Higgs boson candidate event in the ATLAS event display VP1 [85, 86].

every step of the data chain without the need of additional converters. Figure 46 gives an overview of the data chain. The upper branch corresponds to the flow of the data recorded by the ATLAS detector. The lower branch corresponds to the flow of the simulated data. In between every step, VP1 can access and display the data. Access to the detector geometry is given through the GeoModel [87] package which builds the geometry on the fly from C++ code upon request. Some of the other advantages are the direct access to other services such as the online geometry and alignment database, conditions data for data taking, and track extrapolation tools for the complex magnetic field. However, this tight integration also puts limits when visualizing the geometry and developing or modernizing the code. VP1 can

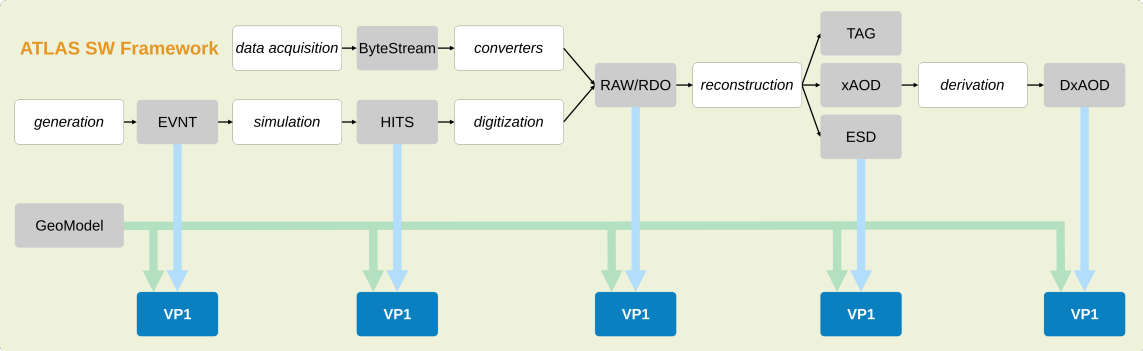

Figure 46: Data collected or generated through simulation by ATLAS. At every step, VP1 can access and display the data that is processed within the ATLAS software framework Athena. The GeoModel-based ATLAS geometry is also stored and accessed through Athena.

only be used on platforms supported by the ATLAS software framework's code[1]. Many end-users do not have these platforms installed on their personal computers and can therefore not run VP1 locally. They have to run VP1 either remotely or in a virtual machine. This comes with several drawbacks. The performance can be slow over the network when run remotely, since a lot of 3D data is sent back and forth. On the other hand, for VP1 in a virtual machine not all graphics options are available since the 3D rendering is done on the software rather than the hardware side. Consequently, the quality of the resulting images is not as high as it could be if VP1 were to be run natively. In addition, performance can still become an issue

[1] At the time of writing, the ATLAS software framework can be fully compiled only on Scientific Linux 6 (SLC6) and CERN Centos7 (CC7), CERN-customized versions of RedHat Linux 6 and Centos7, respectively.

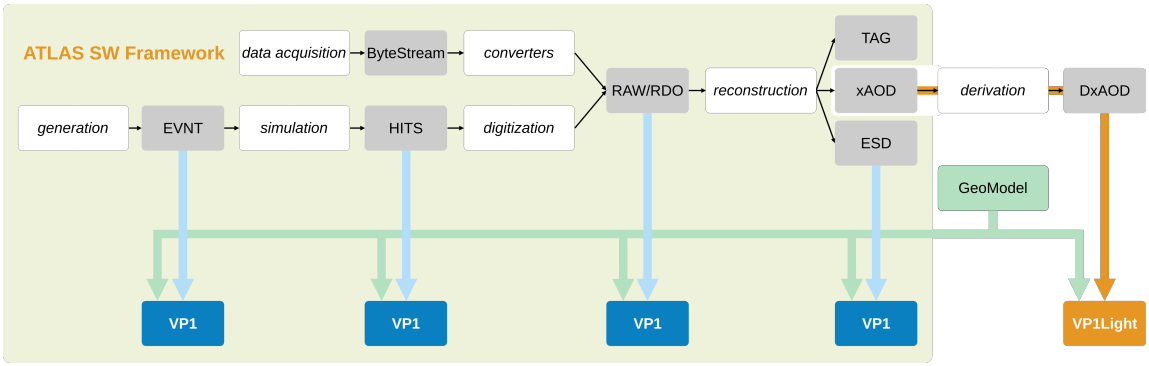

Figure 47: An updated view of the flow chart shown in Figure 46. VP1-Light can access xAOD and DxAOD files in standalone mode, while taking the geometry information from the persistent copy from the new standalone GeoModel packages, without the need for the experiment's software framework.

in a virtual machine, depending on the user's hardware. Another disadvantage of the integration of VP1 into Athena is the complex run time dependency that VP1 inherits from Athena. This makes the initialization of VP1 a lengthy process, taking several minutes and significantly slowing down the start-up of VP1. All of this makes VP1 a cumbersome tool for physics analysis users but also developers.

However, users who primarily run data analysis jobs on their custom filtered event data on their personal computers do not use or need most of services accessed by VP1 through Athena. A user who wants to debug an event or generate an event display usually does not need the latest version of the detector geometry or detailed alignment information. Similarly, They do not need access to every intermediate data format of the ATLAS data process shown in Figure 46. These users would benefit by being able to run the data visualization application VP1 on the same platform

as their analysis. The data used for physics analyses are usually stored in xAOD [78] files, and its derivatives DxAOD files, in a ROOT format [88], which does not require full access to the ATLAS Athena framework.

For this purpose, and leveraging the use of the new experiment-agnostic GeoModel library and of the standalone detector description persistification mechanism, the standalone, lightweight version of VP1, called VP1-Light, was developed. Figure 47 shows an updated version of the drawing shown in Figure 46, illustrating framework-independent use of VP1-Light the standalone GeoModel. More one the standalone GeoModel in the following section.

3.2 Display Of The ATLAS Detector

The full ATLAS event display VP1 uses the GeoModel package to display the ATLAS geometry. GeoModel provides a detailed ATLAS detector description, not just to VP1, but to a variety of ATLAS applications, including simulation and data reconstruction. GeoModel provides both raw geometry data and time-dependent alignment corrections. The geometry is built on the fly from C++ code while the geometry data is stored in the ATLAS Geometry Database. This database is integrated into the ATLAS software framework and therefore GeoModel is required to run inside the framework as well. In order to build the ATLAS geometry in a standalone application, a standalone version of GeoModel was also required.

A standalone GeoModel was developed by extracting the GeoModel kernel from the Athena framework. Fortunately, GeoModel did not have any dependencies on other Athena software components, so the extraction did not pose any major complications. In the process, the only external dependency on the CLHEP [89] library

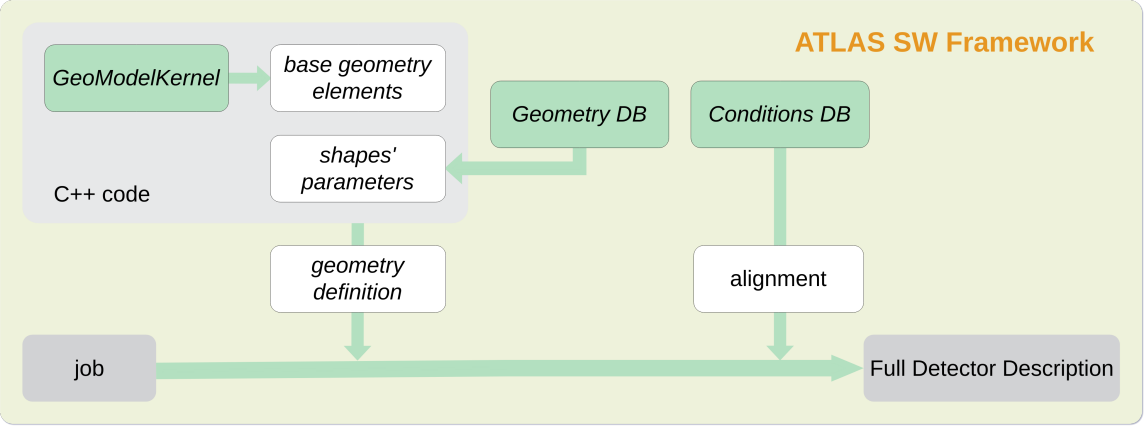

Figure 48: Overview of the ATLAS detector description. An Athena job, such as simulation, reconstruction, or VP1 requests the ATLAS geometry. The raw detector geometry is built on the fly from C++ code. On top of that, time-dependent alignment data is applied from the Conditions DB.

was dropped and instead the Eigen [90] library was used. Since the standalone GeoModel package does not have access to the ATLAS Geometry DB, a new mechanism to store the geometry data was implemented. A persistent version of the detector geometry is generated in inside the experiments software framework that can then be imported into the standalone application. Two different file format were chosen to store the persistent detector geometry. The SQLite format [91], designed to store the geometry in an optimized and compact way. The SQlite format therefore results in relatively small file sizes. As an example, the full ATLAS geometry used by VP1-Light is stored in a SQLite file of only about 50 MB. The second format is the JSON format [92]. It is a human readable format that can easily be split in multiple files. This allows users to directly edit individual components of the geometry. Since

the standalone GeoModel is independent of ATLAS software it can be use as an experiment-agnostic detector description, serving other experiments as well.

VP1-Light is the first application to use both the standalone GeoModel package and the persistification mechanism to visualize the the ATLAS detector geometry. Views of the full ATLAS detector and its sub-detectors are shown in Section 1.4.2.

3.3 Display Of Physics Objects

Physics objects that can be displayed are jets, inner detector tracks, muon tracks calorimeter clusters, primary and secondary vertices. These are the main collection of objects. Each collection has different categories. These categories depend on the input file and which object collections are saved during reconstruction and/or slimming and thinning. Slimming and thinning is the reduction of a files size by removing objects that are not needed. E.g. an analysis might not need Inner Detector tracking information and thus this is removed from the xAOD file. Here, a short overview of the physics object category is given.

Jets are displayed as as cones starting from the production vertex. The size is proportional to the jet energy. b-tagging information is available and b-tagged jets can be displayed in a separate color.

Calorimeter Clusters are displayed as columns in the respective $\eta - \phi$ direction in the region of the calorimeters. The length of the column corresponds the the energy deposited and can be scaled as desired.

Vertices are shown as small spheres in the interaction region. Different collections such as primary or secondary vertices and displaced vertices are available.

Inner Detector Track Particles are shown as curved lines in the ID region. The curvature depends on the particles momentum. Track parameters can also be shown. These parameters correspond to the different points of measurement, such as first or last measurement or entry point of the calorimeter.

Electrons are essentially the same as track particles, kept in a different collections. This allows to draw them separately from the remaining track particles.

Muons are displayed similar to other track particles. However, their range goes beyond the Inner Detector and the track curve all the way through the calorimeter to the muon spectrometer.

MET or Missing Transverse Energy is displayed as dashed lines in the $(\rho - \phi)$ plane. Depending on the input file, a range of MET collections are available, such as MET from the tracks, calorimeters or reconstructed jets.

Figure 49 gives an overview of all the physics objects and how they are displayed in VP1-Light. In addition to simply displaying the objects, users can also make selection cuts on the physics objects. Selections on jet and calorimeter clusters can be made according to their minimum or maximum (transverse) energy. Muons, electrons and other track particles can be selected according to their (transverse) momentum. η and ϕ cuts can be made on all these objects. This allows the user to only view the objects used in an analysis. Further, information on the objects can be viewed by selection. This will print out the selected objects properties, such as energy, momentum, or invariant mass.

3.4 Development

VP1-Light, just as VP1, is a C++ based modular framework, build as a collection of packages each with its own function. `VP1Systems` packages enable the access to the data, such as the xAOD files through the `VP1AODSystems` package or the detector geometry through the `VP1GeometrySystems`. The GUI views are handled by the `VP1Plugin` which store dedicated views for the detector geometry, the physics objects or a combination of both. To make VP1-Light a standalone application, all relevant packages needed to be extracted from the Athena framework. For the 3D visualization of the geometry and the physics objects Coin [93], which is a free software Open Inventor clone, is used. For the graphical user interface (GUI) the Qt5 libraries [94] are utilized.

VP1-Light was embedded into a CMake build system for development. This provided a sandbox environment for the implementation of the required functionalities. The initial version of VP1-Light, that was basically just the packages extracted from Athena, only displayed the detector geometry. For this, the new standalone GeoModel was used. This made VP1-Light the first application to use the standalone persistification mechanism. Access to physics objects was not initially available, since the full VP1 version has access to the physics data through the Athena framework. Therefore, a new implementation of the `VP1AODSystems` had to be developed that can access xAOD files independent from the software framework. Similarly, some of the event access routines had to be rewritten. This is because the full VP1 runs as an Athena algorithm, stepping through a data file one event at a time. However, VP1-Light uses direct access to the xAOD files and it is therefore possible to browses the event file. This allows the user to view any given event in the file without the need to proceed through the file one event at a time. Other functionalities were added as

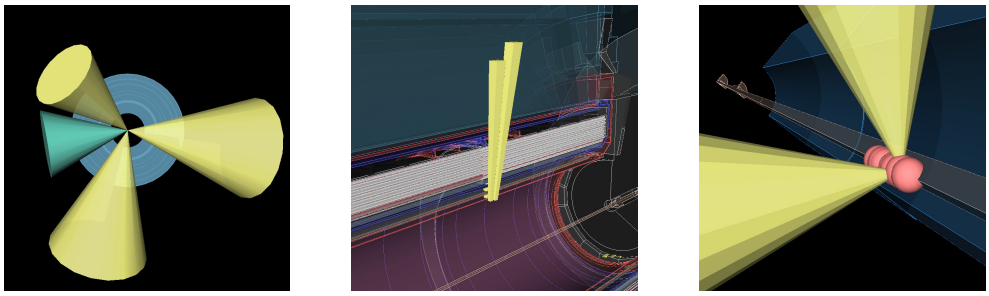

(a) Jets (b) Calorimeter Clusters (c) Vertices

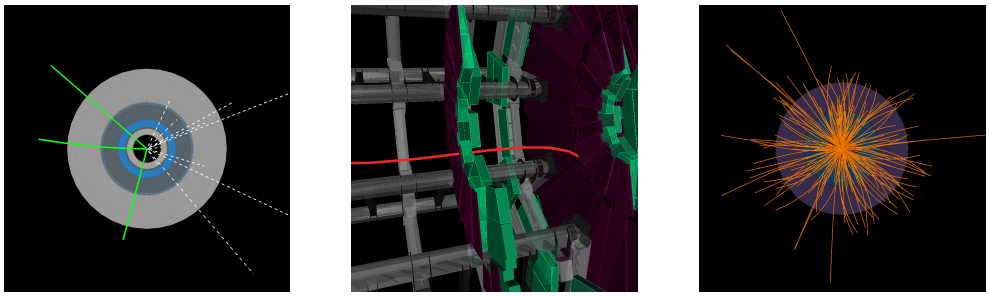

(d) Electrons & MET (e) Muons (f) ID Track Particles

Figure 49: Overview of the physics objects available in VP1-Light. (a) shows a set of 3 jets (yellow) and one b-jet (turquoise). The background shows a cross sectional view of the Tile calorimeter. (b) shows a set of calorimeters clusters in the calorimeter region. (c) shows the primary vertices (red) and a set of jets (yellow). The background shows a sectional view of the SCT and the beam pipe. (d) shows a set of electron tracks (green) and missing transverse energy (white). The background shows a cross sectional view of the SCT and TRT. (e) shows a Muon track (red) passing the Muon Spectrometer's end-caps. (f) shows a set of mostly low energetic track particles (orange). The background shows a again the SCT and TRT.

well, such as settings dialogs for options that were set via environment variables in full VP1. All of the developments make VP1-Light a more user-friendly application that behaves more like a standard desktop application. Figure 50 shows a use case of VP1-Light with a new settings dialog. The new event controls can also be seen at the bottom left of the GUI.

Once the main features of VP1-Light were developed all packages were reintegrated into the ATLAS software framework. The decision to take this step was based on the many advantages in having VP1-Light in the Athena build system.

- Since VP1-Light is based on the VP1 packages, the code base of VP1 and VP1-Light is still the same. In the parts where they differ, a preprocessor flag determines whether VP1 or VP1-Light is compiled.
- Development can be done simultaneously on VP1 and VP1-Light.
- Code maintenance is kept to a minimum, since VP1 and VP1-Light share the same code.
- External packages (Coin, Qt, ROOT, etc.) can be directly compiled from the Athena code base. This makes the compilation and installation process much easier for users and developers.

Reintegration into the Athena build system does not reintroduce a dependency of VP1-Light on the framework. Once VP1-Light is compiled, it runs in standalone mode without access to the framework.

Since VP1-Light is independent of the software framework, it is also free of its the platform restriction. This makes VP1-Light a cross-platform application that is supported for both Linux and macOS. Both of these operating systems are widely used platforms for ATLAS physics analysis users. Figure 50 shows VP1-Light running on macOS.

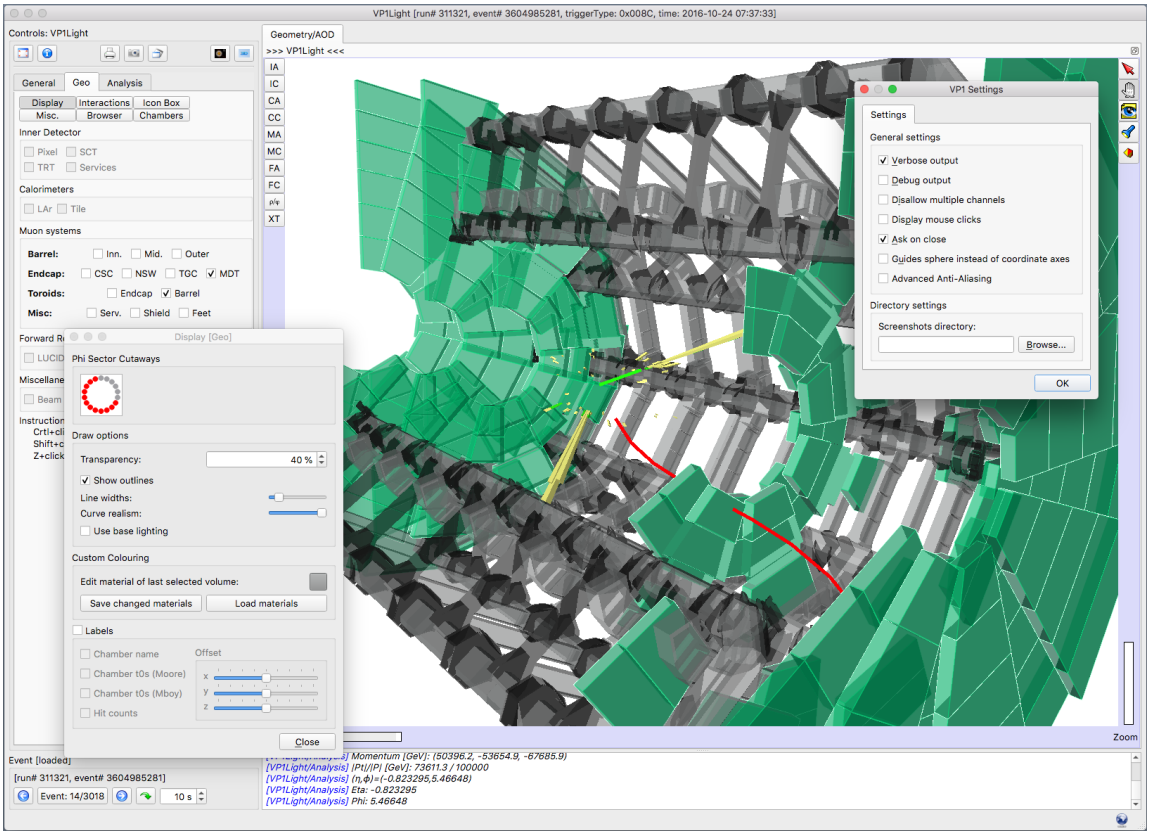

Figure 50: View of the VP1-Light GUI on a macOS system. The 3D viewer is showing parts of the ATLAS detector geometry (toroids and MS) and some physics objects (calorimeter clusters, muon, electron). In the bottom left corner, new event controls are added which allow the user to switch between events more easily. In the foreground, a new settings dialog for general program settings is shown as well as a dialog to adjust the geometry display.

Besides its usage as an event display for end-users, VP1-Light is also designed as a test-bed for new technologies. Being a standalone, lightweight application that only takes a short time to start greatly simplifies improvement of visualization techniques, engines, libraries, compared to the development workflow in a large framework such as Athena. For a start, VP1-Light will be used to test new 3D graphics engines. Currently, VP1 and VP1-Light are based on Coin3D, an aging library which will have to be replaced eventually since it is causing compatibility issues with new software releases. One promising candidate is Qt 3D which is now available as a stable version. Further investigation needs to be done to ensure it fulfills all requirements.

3.5 Distribution

VP1-Light was developed with a focus on usability. Users should get an easy to use application that is free of the of the drawbacks of the full VP1 application. In Section 3.4, the reintegration of VP1-Light into the ATLAS Athena build system was described. This reintegration into Athena does make the compilation of VP1-Light straightforward. However, many user might still get shied away by the prospect of compiling VP1-Light including its external requirements. Especially the compilation of ROOT and the installation of Qt5 is a lengthy process. Therefore, a mechanism to package the VP1-Light and external packages binaries into an application bundle was developed. In a first step, the VP1-Light and external binaries were packaged into an AppImage [95] bundle for Linux systems and an Apple Disk Image for macOS systems. These app bundles are essentially mountable volumes that the user directly run out of the box. In the second step, dedicated package managers of the operating systems are used for the distribution of the VP1-Light packages. On the Linux side,

VP1-Light is available for selected Long-Time Support (LTS) Ubuntu distributions. Distribution is done through the Personal Package Archives (PPA). The user can simply install the VP1-Light external dependencies and the main application and use VP1-Light like a native Ubuntu application. For macOS, the distribution is done through the HomeBrew [96] package manager in a similar way.

3.6 Conclusion

With the development of VP1-Light, all ATLAS analysis users, developers, outreach experts and more have a standalone 3D event display at their disposal that is easy to get, easy to install and easy to use. VP1-Light is a standalone version of the general purpose event display VP1. It has been detached from the ATLAS software framework. Physics data is accessed from xAOD files in ROOT format. The ATLAS detector geometry is is stored and read in by the standalone GeoModel package in a SQLite database format. This format allows the persistification of the entire ATLAS detector geometry in one file of order 50 MB.

VP1-Light is available for ATLAS users through dedicated package managers of both Ubuntu Linux and macOS. It can also be installed on many other Linux distributions.

Appendix A

W Helicity Fractions To $\mathcal{O}(x_b^4)$

The W helicity fraction in terms of the EFT coefficients to $\mathcal{O}(x_b^4)$ are given by

$$F_0 = \frac{A_0}{A_0 + 2B_0}, \tag{A.1}$$

$$F_L = \frac{B_0 - 2x_q B_1}{A_0 + 2B_0}, \tag{A.2}$$

$$F_R = \frac{B_0 + 2x_q B_1}{A_0 + 2B_0}. \tag{A.3}$$

where

$$x_q = \sqrt{x_E^2 - x_W^2}, \tag{A.4}$$

$$x_E = \frac{1 + x_W^2 - x_b^2}{2}. \tag{A.5}$$

and $x_W = \frac{m_W}{m_t}$ and $x_b = \frac{m_b}{m_t}$.

The form factors up to $\mathcal{O}(x_b^4)$ are given by

$$
\begin{aligned}
A_0 = & \frac{1}{x_W^2}\left(|V_L|^2+|V_R|^2\right)\left(1-x_W^2-2x_b^2-x_W^2x_b^2+x_b^4\right) \\
& + \left(|g_L|^2+|g_R|^2\right)\left(1-x_W^2+x_b^2\right) - 4x_b\,\mathrm{Re}\left(V_LV_R^*+g_Lg_R^*\right) \\
& - \frac{2}{x_W}\,\mathrm{Re}\left(V_Lg_R^*+V_Rg_L^*\right)\left(1-x_W^2-x_b^2\right), \\
& + \frac{2}{x_W}x_b\,\mathrm{Re}\left(V_Lg_L^*+V_Rg_R^*\right)\left(1+x_W^2-x_b^2\right), \qquad \text{(A.6)} \\
A_1 = & \frac{1}{(x_W^2}\left(|V_L|^2-|V_R|^2\right)\left(1-x_b^2\right) - \left(|g_L|^2-|g_R|^2\right) - \frac{2}{x_W}\,\mathrm{Re}\left(V_Lg_R^*-V_Rg_L^*\right) \\
& + \frac{2}{x_W}x_b\,\mathrm{Re}\left(V_Lg_L^*-V_Rg_R^*\right), \qquad \text{(A.7)} \\
B_0 = & \left(|V_L|^2+|V_R|^2\right)\left(1-x_W^2+x_b^2\right) \\
& + \frac{1}{x_W^2}\left(|g_L|^2+|g_R|^2\right)\left(1-x_W^2-2x_b^2-x_W^2x_b^2+x_b^4\right) \\
& - 4x_b\,\mathrm{Re}\left(V_LV_R^*+g_Lg_R^*\right) - \frac{2}{x_W}\,\mathrm{Re}\left(V_Lg_R^*+V_Rg_L^*\right)\left(1-x_W^2-x_b^2\right) \\
& + \frac{2}{x_W}x_b\,\mathrm{Re}\left(V_Lg_L^*+V_Rg_R^*\right)\left(1+x_W^2-x_b^2\right), \qquad \text{(A.8)} \\
B_1 = & -\left(|V_L|^2-|V_R|^2\right) + \frac{1}{x_W^2}(|g_L|^2-|g_R|^2)(1-x_b^2) + \frac{2}{x_W}\,\mathrm{Re}\left(V_Lg_R^*-V_Rg_L^*\right) \\
& + \frac{2}{x_W}x_b\,\mathrm{Re}\left(V_Lg_L^*-V_Rg_R^*\right), \\
C_0 = & \left(|V_L|^2+|V_R|^2+|g_L|^2+|g_R|^2\right)\left(1-x_W^2-x_b^2\right) \\
& - 2x_b\,\mathrm{Re}\left(V_LV_R^*+g_Lg_R^*\right)\left(1+x_W^2-x_b^2\right) \\
& - \frac{1}{x_W}\,\mathrm{Re}\left(V_Lg_R^*+V_Rg_L^*\right)\left(1-2x_b^2-x_W^4+x_b^4\right) + 4x_Wx_b\,\mathrm{Re}\left(V_Lg_L^*+V_Rg_R^*\right), \\
& \qquad \text{(A.9)} \\
C_1 = & 2(-|V_L|^2+|V_R|^2+|g_L|^2-|g_R|^2) + \frac{2}{x_W}\,\mathrm{Re}\left(V_Lg_R^*-V_Rg_L^*\right)\left(1+x_W^2-x_b^2\right), \\
& \qquad \text{(A.10)}
\end{aligned}
$$

$$D_0 = \frac{1}{x_W} \operatorname{Im}\left(V_L g_R^* + V_R g_L^*\right)\left(1 - 2x_W^2 - 2x_b^2 - 2x_W^2 x_b^2 + x_W^4\right), \tag{A.11}$$

$$D_1 = -4x_b \operatorname{Im}\left(V_L V_R^* + g_L g_R^*\right) - \frac{2}{x_W} \operatorname{Im}\left(V_L g_R^* - V_R g_L^*\right)\left(1 - x_W^2 - x_b^2\right), \tag{A.12}$$

Appendix B

Single Top Decay Distribution To $\mathcal{O}\left(x_b^4\right)$

The coefficients of the angular expansion of the single top decay distribution analysis $a_{k,l,m}$ are given in Section 1.3.2.2 in terms of the generalized helicity fractions and phases. The coefficients $a_{k,l,m}$ in terms of the form factors defined in Eq. A.10 are given by

$$
\begin{aligned}
a_{0,1,0} &= \sqrt{\frac{3}{8\pi}}\frac{2x_q B_1}{A_0+2B_0}, \\
a_{0,2,0} &= \frac{1}{\sqrt{40\pi}}\frac{B_0-A_0}{A_0+2B_0}, \\
a_{1,0,0} &= +P\frac{1}{\sqrt{24\pi}}\frac{2x_q\left(A_1+2B_1\right)}{A_0+2B_0}, \\
a_{1,1,0} &= +P\frac{1}{\sqrt{32\pi}}\frac{2B_0}{A_0+2B_0}, \\
a_{1,2,0} &= +P\frac{1}{\sqrt{480\pi}}\frac{4x_q\left(B_1-A_1\right)}{A_0+2B_0}, \\
\mathrm{Re}\left(a_{1,1,1}\right) &= -P\frac{1}{\sqrt{8\pi}}\frac{1}{x_W}\frac{C_0}{A_0+2B_0}, \\
\mathrm{Im}\left(a_{1,1,1}\right) &= -P\frac{1}{\sqrt{8\pi}}\frac{1}{x_W}\frac{x_q D_1}{A_0+2B_0}, \\
\mathrm{Re}\left(a_{1,2,1}\right) &= -P\frac{1}{\sqrt{40\pi}}\frac{1}{x_W}\frac{x_q C_1}{A_0+2B_0}, \\
\mathrm{Im}\left(a_{1,2,1}\right) &= -P\frac{1}{\sqrt{40\pi}}\frac{1}{x_W}\frac{D_0}{A_0+2B_0}.
\end{aligned}
\tag{B.1}
$$

In addition, the generalized helicity fractions and phases can be written in terms of the form factors as

$$\begin{aligned} f_1 &= \frac{2B_0}{A_0 + 2B_0}, \\ f_1^+ &= \frac{B_0 + 2x_q B_1}{2B_0}, \\ f_0^+ &= \frac{A_0 - 2x_q A_1}{2A_0}, \\ \tan\delta_- &= \frac{D_0 - x_q D_1}{C_0 - x_q C_1}, \\ \tan\delta_+ &= \frac{D_0 + x_q D_1}{C_0 + x_q C_1}. \end{aligned} \tag{B.2}$$

Appendix C

Fiducial And Total Cross Section In Terms Of EFT Coefficients

The fiducial cross section in terms of the Wilson coefficients is then given by

$$\sigma_{\text{fid}} = \sigma_{\text{fid}}^{\text{SM}} \left(V_L^4 + \boldsymbol{g}(\boldsymbol{p}) \cdot \boldsymbol{\kappa} \right), \tag{C.1}$$

where $\boldsymbol{g}(\boldsymbol{p})$ is a column vector which components are quartic functions of the Wilson coefficients. The explicit for of $\boldsymbol{g} \cdot \boldsymbol{\kappa}$, here written as

$$\boldsymbol{g}(\boldsymbol{p}) \cdot \boldsymbol{\kappa} = \left(\boldsymbol{g}(\boldsymbol{p}) \cdot \boldsymbol{\kappa}\right)_1 + \left(\boldsymbol{g}(\boldsymbol{p}) \cdot \boldsymbol{\kappa}\right)_2, \tag{C.2}$$

is

$$\begin{aligned}
\left(\boldsymbol{g}(\boldsymbol{p}) \cdot \boldsymbol{\kappa}\right)_1 = {} & \kappa_1 \mathrm{Re}\left(c_{tW}\right) V_L^3 + \kappa_2 c_{Qq}^{3,1} V_L^3 + \kappa_3 \mathrm{Re}\left(c_{tW}\right)^2 V_L^2 + \kappa_4 c_{Qq}^{3,1} \mathrm{Re}\left(c_{tW}\right) V_L^2 \\
& + \kappa_5 \left(c_{Qq}^{3,1}\right)^2 V_L^2 + \kappa_6 V_L^2 c_{\varphi tb}^2 + \kappa_7 \mathrm{Re}\left(c_{bW}\right) V_L^2 c_{\varphi tb} + \kappa_8 \mathrm{Re}\left(c_{bW}\right)^2 V_L^2 \\
& + \kappa_9 \mathrm{Im}\left(c_{tW}\right)^2 V_L^2 + \kappa_{10} \mathrm{Im}\left(c_{bW}\right)^2 V_L^2 + \kappa_{11} \mathrm{Re}\left(c_{tW}\right)^3 V_L \\
& + \kappa_{12} c_{Qq}^{3,1} \mathrm{Re}\left(c_{tW}\right)^2 V_L + \kappa_{13} \left(c_{Qq}^{3,1}\right)^2 \mathrm{Re}\left(c_{tW}\right) V_L + \kappa_{14} \mathrm{Re}\left(c_{tW}\right) V_L c_{\varphi tb}^2 \\
& + \kappa_{15} \mathrm{Re}\left(c_{bW}\right) \mathrm{Re}\left(c_{tW}\right) V_L c_{\varphi tb} + \kappa_{16} \mathrm{Re}\left(c_{bW}\right)^2 \mathrm{Re}\left(c_{tW}\right) V_L \\
& + \kappa_{17} \mathrm{Im}\left(c_{tW}\right)^2 \mathrm{Re}\left(c_{tW}\right) V_L + \kappa_{18} \mathrm{Im}\left(c_{bW}\right)^2 \mathrm{Re}\left(c_{tW}\right) V_L + \kappa_{19} c_{Qq}^{3,1} V_L c_{\varphi tb}^2 \\
& + \kappa_{20} c_{Qq}^{3,1} \mathrm{Re}\left(c_{bW}\right) V_L c_{\varphi tb} + \kappa_{21} c_{Qq}^{3,1} \mathrm{Re}\left(c_{bW}\right)^2 V_L + \kappa_{22} c_{Qq}^{3,1} \mathrm{Im}\left(c_{tW}\right)^2 V_L \\
& + \kappa_{23} c_{Qq}^{3,1} \mathrm{Im}\left(c_{bW}\right)^2 V_L + \kappa_{24} \mathrm{Im}\left(c_{bW}\right) \mathrm{Im}\left(c_{tW}\right) V_L c_{\varphi tb} \\
& + \kappa_{25} \mathrm{Im}\left(c_{bW}\right) \mathrm{Re}\left(c_{bW}\right) \mathrm{Im}\left(c_{tW}\right) V_L + \kappa_{26} \mathrm{Re}\left(c_{tW}\right)^4 + \kappa_{27} c_{Qq}^{3,1} \mathrm{Re}\left(c_{tW}\right)^3
\end{aligned} \tag{C.3}$$

$$
\begin{aligned}
(\boldsymbol{g}(\boldsymbol{p})\cdot\boldsymbol{\kappa})_2 = {} & \kappa_{28}\left(c_{Qq}^{3,1}\right)^2\mathrm{Re}\left(c_{tW}\right)^2+\kappa_{29}\mathrm{Re}\left(c_{tW}\right)^2c_{\varphi tb}^2+\kappa_{30}\mathrm{Re}\left(c_{bW}\right)\mathrm{Re}\left(c_{tW}\right)^2c_{\varphi tb}\\
& +\kappa_{31}\mathrm{Re}\left(c_{bW}\right)^2\mathrm{Re}\left(c_{tW}\right)^2+\kappa_{32}\mathrm{Im}\left(c_{tW}\right)^2\mathrm{Re}\left(c_{tW}\right)^2\\
& +\kappa_{33}\mathrm{Im}\left(c_{bW}\right)^2\mathrm{Re}\left(c_{tW}\right)^2+\kappa_{34}c_{Qq}^{3,1}\mathrm{Re}\left(c_{tW}\right)c_{\varphi tb}^2\\
& +\kappa_{35}c_{Qq}^{3,1}\mathrm{Re}\left(c_{bW}\right)\mathrm{Re}\left(c_{tW}\right)c_{\varphi tb}+\kappa_{36}c_{Qq}^{3,1}\mathrm{Re}\left(c_{bW}\right)^2\mathrm{Re}\left(c_{tW}\right)\\
& +\kappa_{37}c_{Qq}^{3,1}\mathrm{Im}\left(c_{tW}\right)^2\mathrm{Re}\left(c_{tW}\right)+\kappa_{38}c_{Qq}^{3,1}\mathrm{Im}\left(c_{bW}\right)^2\mathrm{Re}\left(c_{tW}\right)\\
& +\kappa_{39}\mathrm{Im}\left(c_{bW}\right)\mathrm{Im}\left(c_{tW}\right)\mathrm{Re}\left(c_{tW}\right)c_{\varphi tb}\\
& +\kappa_{40}\mathrm{Im}\left(c_{bW}\right)\mathrm{Re}\left(c_{bW}\right)\mathrm{Im}\left(c_{tW}\right)\mathrm{Re}\left(c_{tW}\right)+\kappa_{41}\left(c_{Qq}^{3,1}\right)^2c_{\varphi tb}^2\\
& +\kappa_{42}\left(c_{Qq}^{3,1}\right)^2\mathrm{Re}\left(c_{bW}\right)c_{\varphi tb}+\kappa_{43}\left(c_{Qq}^{3,1}\right)^2\mathrm{Re}\left(c_{bW}\right)^2+\kappa_{44}\left(c_{Qq}^{3,1}\right)^2\mathrm{Im}\left(c_{tW}\right)^2\\
& +\kappa_{45}\left(c_{Qq}^{3,1}\right)^2\mathrm{Im}\left(c_{bW}\right)^2+\kappa_{46}c_{Qq}^{3,1}\mathrm{Im}\left(c_{bW}\right)\mathrm{Im}\left(c_{tW}\right)c_{\varphi tb}\\
& +\kappa_{47}c_{Qq}^{3,1}\mathrm{Im}\left(c_{bW}\right)\mathrm{Re}\left(c_{bW}\right)\mathrm{Im}\left(c_{tW}\right)+\kappa_{48}c_{\varphi tb}^4+\kappa_{49}\mathrm{Re}\left(c_{bW}\right)c_{\varphi tb}^3\\
& +\kappa_{50}\mathrm{Re}\left(c_{bW}\right)^2c_{\varphi tb}^2+\kappa_{51}\mathrm{Im}\left(c_{tW}\right)^2c_{\varphi tb}^2+\kappa_{52}\mathrm{Im}\left(c_{bW}\right)^2c_{\varphi tb}^2\\
& +\kappa_{53}\mathrm{Re}\left(c_{bW}\right)^3c_{\varphi tb}+\kappa_{54}\mathrm{Re}\left(c_{bW}\right)\mathrm{Im}\left(c_{tW}\right)^2c_{\varphi tb}\\
& +\kappa_{55}\mathrm{Im}\left(c_{bW}\right)^2\mathrm{Re}\left(c_{bW}\right)c_{\varphi tb}+\kappa_{56}\mathrm{Re}\left(c_{bW}\right)^4+\kappa_{57}\mathrm{Re}\left(c_{bW}\right)^2\mathrm{Im}\left(c_{tW}\right)^2\\
& +\kappa_{58}\mathrm{Im}\left(c_{bW}\right)^2\mathrm{Re}\left(c_{bW}\right)^2+\kappa_{59}\mathrm{Im}\left(c_{tW}\right)^4\\
& +\kappa_{60}\mathrm{Im}\left(c_{bW}\right)^2\mathrm{Im}\left(c_{tW}\right)^2+\kappa_{61}\mathrm{Im}\left(c_{bW}\right)^4, \qquad \text{(C.4)}
\end{aligned}
$$

where the point $\boldsymbol{p}$ holds the couplings

$$
\boldsymbol{p}=\left(V_L,\mathrm{Re}\left(c_{tW}\right),c_{Qq}^{3,1},\mathrm{Re}\left(c_{\varphi tb}\right),\mathrm{Re}\left(c_{bW}\right),\mathrm{Im}\left(c_{tW}\right),\mathrm{Im}\left(c_{bW}\right)\right). \qquad \text{(C.5)}
$$

The total cross section in terms of the EFT coefficients can be written as

$$
\sigma_{\mathrm{tot}}=\sigma_{\mathrm{tot}}^{\mathrm{SM}}\left(V_L^2+\boldsymbol{g}(\boldsymbol{p})\cdot\boldsymbol{\kappa}\right), \qquad \text{(C.6)}
$$

where

$$\boldsymbol{g}(\boldsymbol{p}) \cdot \boldsymbol{\kappa} = \kappa_1 \mathrm{Re}\left(c_{tW}\right) V_L + \kappa_2 \left(\mathrm{Re}\left(c_{tW}\right)^2 + \mathrm{Im}\left(c_{tW}\right)^2\right) + \kappa_3 V_L c_{Qq}^{3,1} + \kappa_4 \mathrm{Re}\left(c_{tW}\right) c_{Qq}^{3,1} + \kappa_5 \left(c_{Qq}^{3,1}\right)^2 + \kappa_6 c_{\varphi tb}^2 + \kappa_7 c_{\varphi tb} \mathrm{Re}\left(c_{bW}\right) + \kappa_8 \left(\mathrm{Re}\left(c_{bW}\right)^2 + \mathrm{Im}\left(c_{bW}\right)^2\right), \tag{C.7}$$

where $\boldsymbol{p}$ is given by Eq. C.5.

Appendix D

S-Channel Cross Section In Terms Of EFT Coefficients

The s-channel single top cross section in terms of the EFT coefficients is given by

$$\sigma_{\text{s-chan.}} = \sigma^{\text{SM}}_{\text{s-chan.}} \left(V_L^2 + \boldsymbol{g}(\boldsymbol{p}) \cdot \boldsymbol{\kappa} \right), \tag{D.1}$$

where

$$\begin{aligned} \boldsymbol{g}(\boldsymbol{p}) \cdot \boldsymbol{\kappa} = {} & V_L^2 + \kappa_1 \text{Re}\left(c_{tW}\right) V_L + \kappa_2 \left(\text{Re}\left(c_{tW}\right) + \text{Im}\left(c_{tW}\right)\right)^2 + \kappa_3 V_L c_{Qq}^{3,1} \\ & + \kappa_4 \text{Re}\left(c_{tW}\right) c_{Qq}^{3,1} + \kappa_5 \left(c_{Qq}^{3,1}\right)^2 + \kappa_6 V_L V_R + \kappa_7 \text{Re}\left(c_{tW}\right) V_R + \kappa_8 c_{Qq}^{3,1} V_R \\ & + \kappa_9 V_R^2 + \kappa_{10} V_L \text{Re}\left(c_{bW}\right) + \kappa_{11} \left(\text{Re}\left(c_{tW}\right) \text{Re}\left(c_{bW}\right) + \text{Im}\left(c_{tW}\right) \text{Im}\left(c_{bW}\right)\right) \\ & + \kappa_{12} c_{Qq}^{3,1} \text{Re}\left(c_{bW}\right) + \kappa_{13} V_R \text{Re}\left(c_{bW}\right) + \kappa_{14} \left(\text{Re}\left(c_{bW}\right) + \text{Im}\left(c_{bW}\right)\right)^2 . \end{aligned} \tag{D.2}$$

Appendix E

Monte Carlo Generation: Control Plots

This section shows the remaining control plots discussed in Section 2.8.

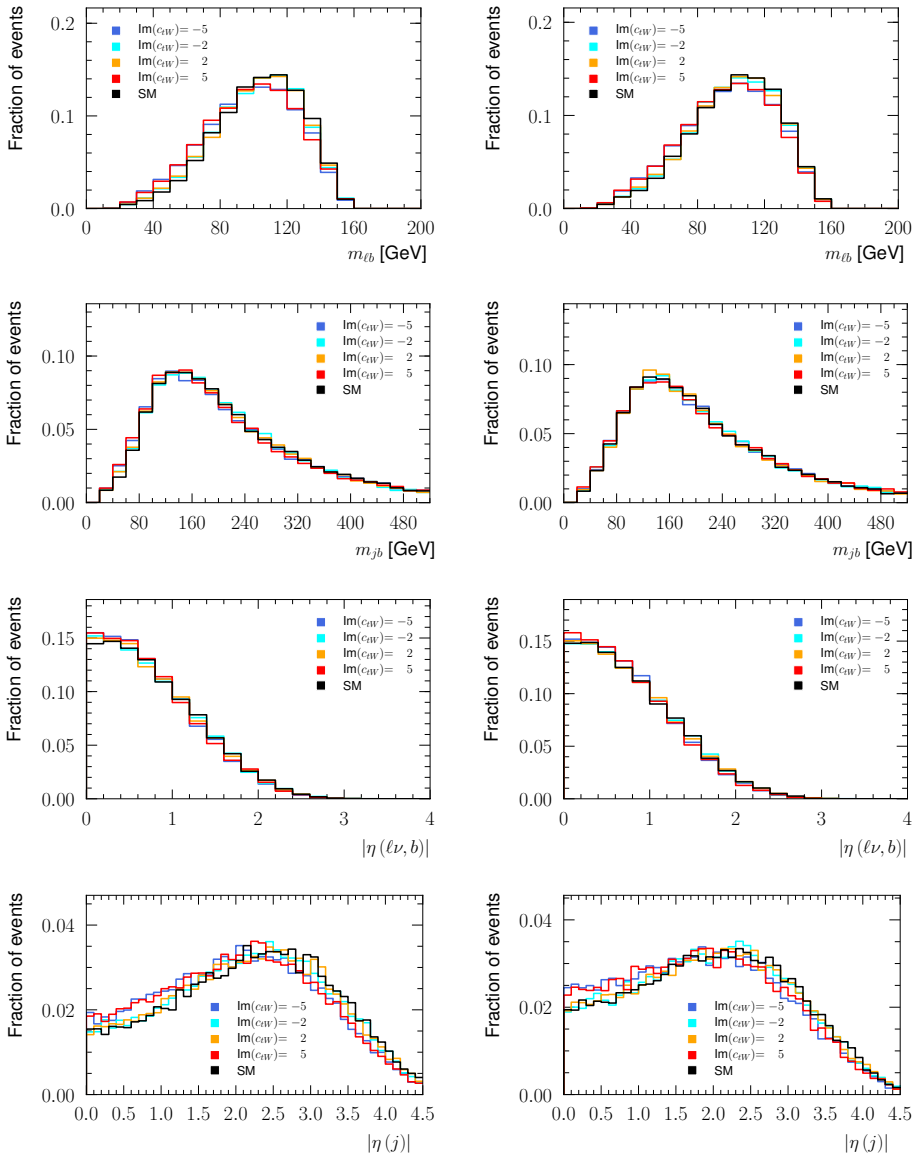

Figure 51: Control plots of simulated top quark and top anti-quark events when varying $\mathrm{Im}\,(c_{tW})$ in the fiducial phase space. Shown are, from top to bottom row, the input variables $m\,(\ell b)$, $m\,(jb)$, $\Delta\eta\,(\ell\nu, b)$, $|\eta\,(j)|$.

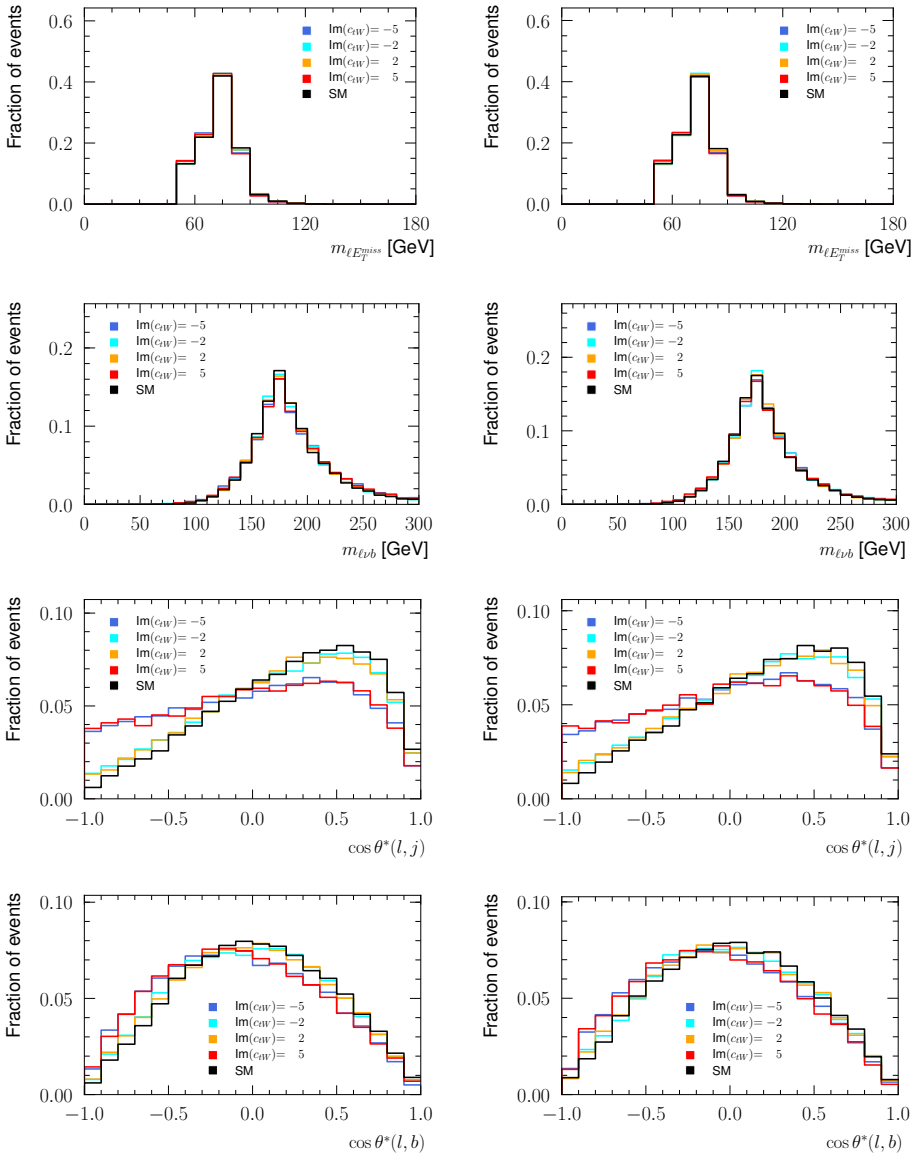

Figure 52: Control plots of simulated top quark and top anti-quark events when varying $\mathrm{Im}\,(c_{tW})$ in the fiducial phase space. Shown are, from top to bottom row, the input variables $m_T\left(\ell E_T^{\mathrm{miss}}\right)$, $m\,(\ell\nu b)$, $\cos\theta^*\,(\ell, j)$, $\cos\theta^*\,(\ell, b)$.

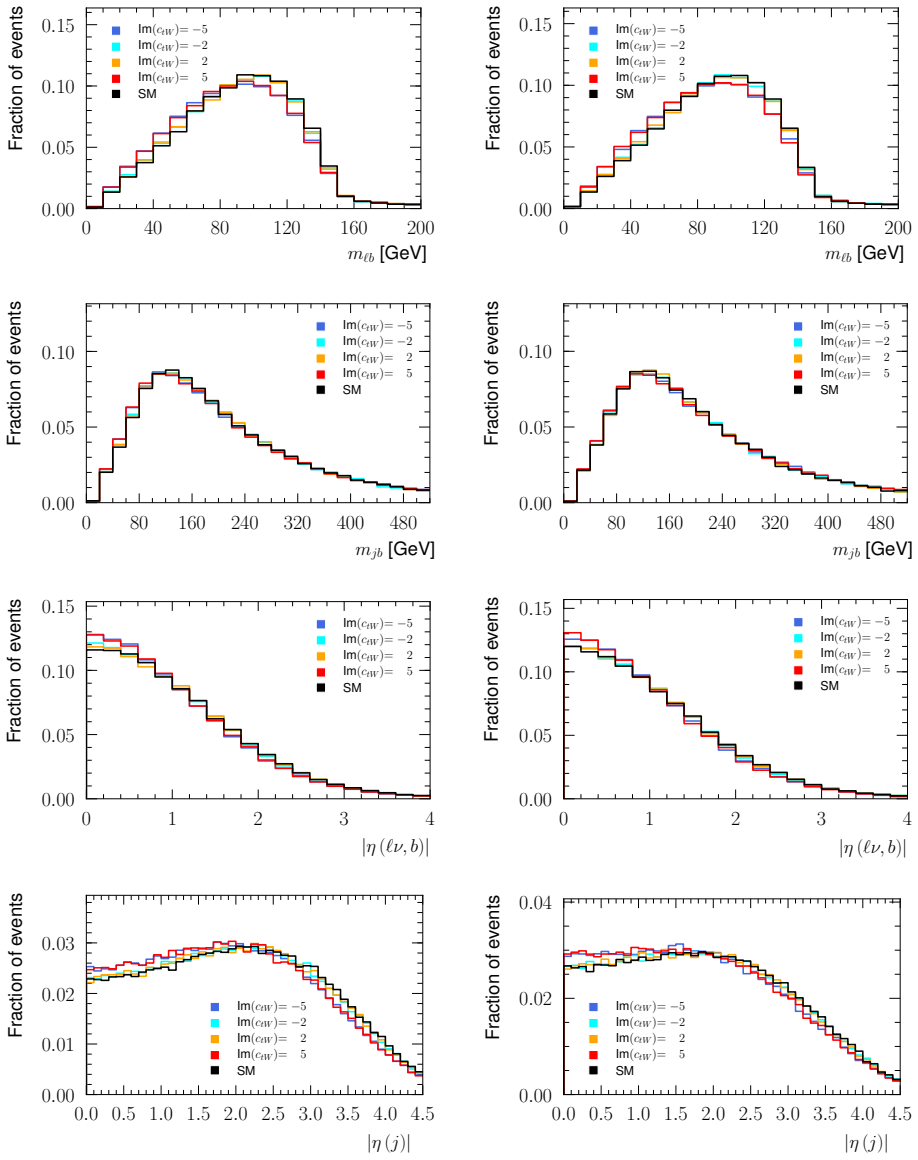

Figure 53: Control plots of simulated top quark and top anti-quark events when varying $\mathrm{Im}\,(c_{tW})$ in the full phase space. Shown are, from top to bottom row, the input variables $m\,(\ell b)$, $m\,(jb)$, $\Delta\eta\,(\ell\nu, b)$, $|\eta\,(j)|$.

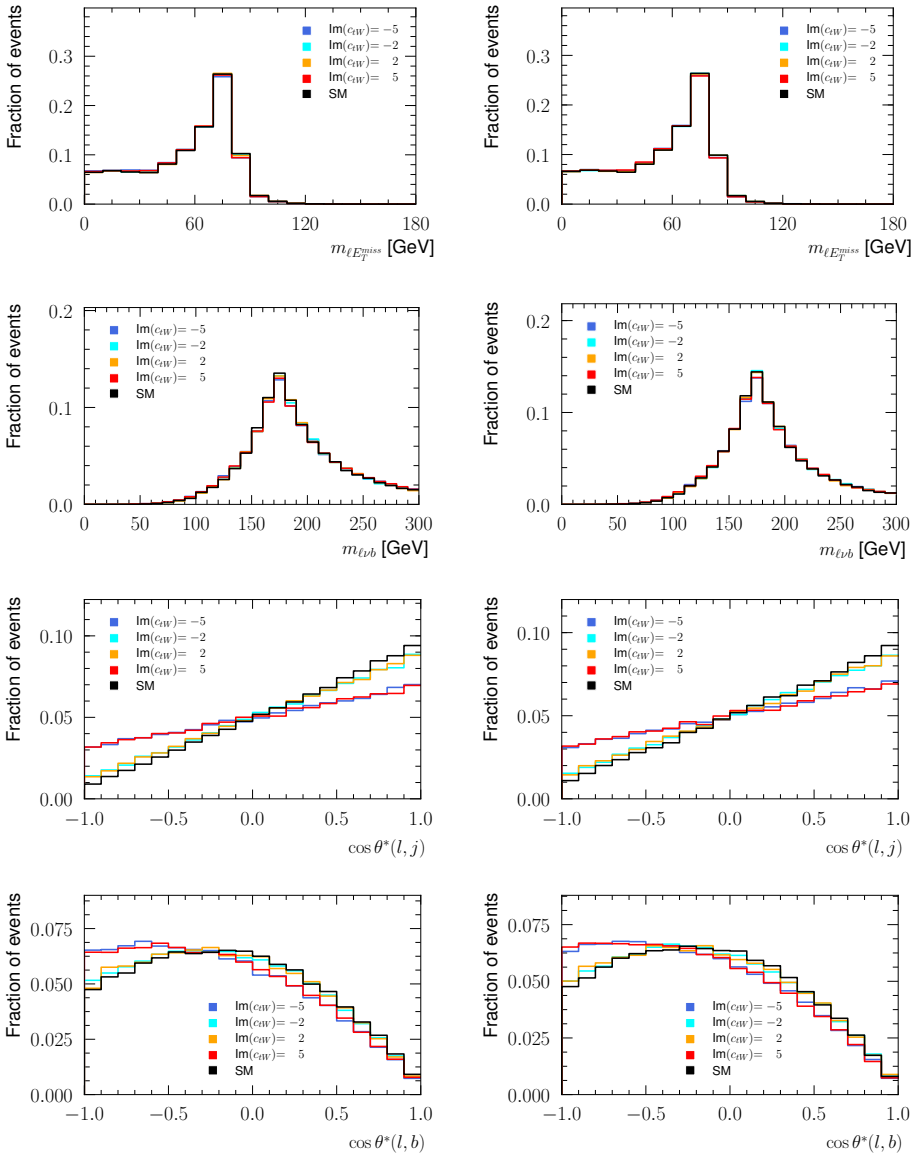

Figure 54: Control plots of simulated top quark and top anti-quark events when varying Im (c_{tW}) in the full phase space. Shown are, from top to bottom row, the input variables $m_T\left(\ell E_T^{\text{miss}}\right)$, $m\left(\ell\nu b\right)$, $\cos\theta^*\left(\ell,j\right)$, $\cos\theta^*\left(\ell,b\right)$.

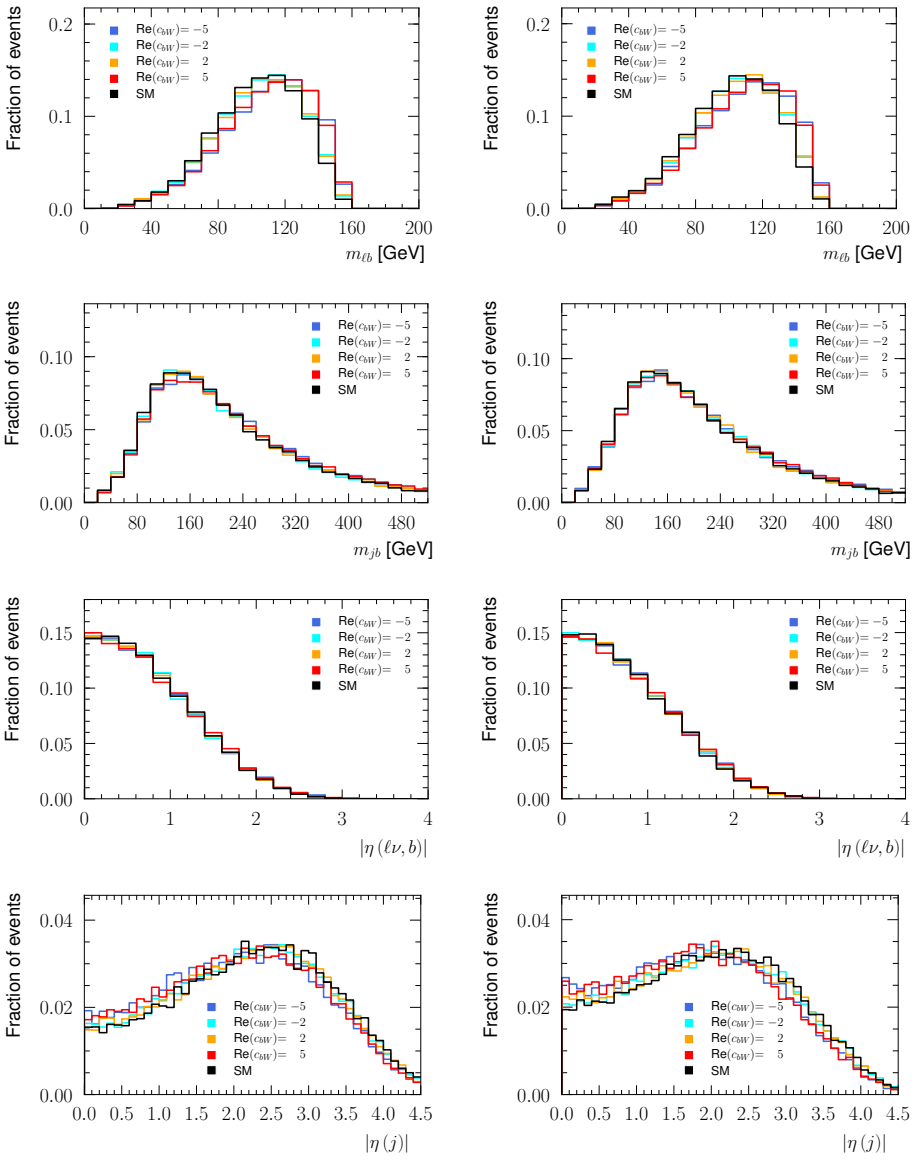

Figure 55: Control plots of simulated top quark and top anti-quark events when varying $\mathrm{Re}(c_{bW})$ in the fiducial phase space. Shown are, from top to bottom row, the input variables $m(\ell b)$, $m(jb)$, $\Delta\eta(\ell\nu, b)$, $|\eta(j)|$.

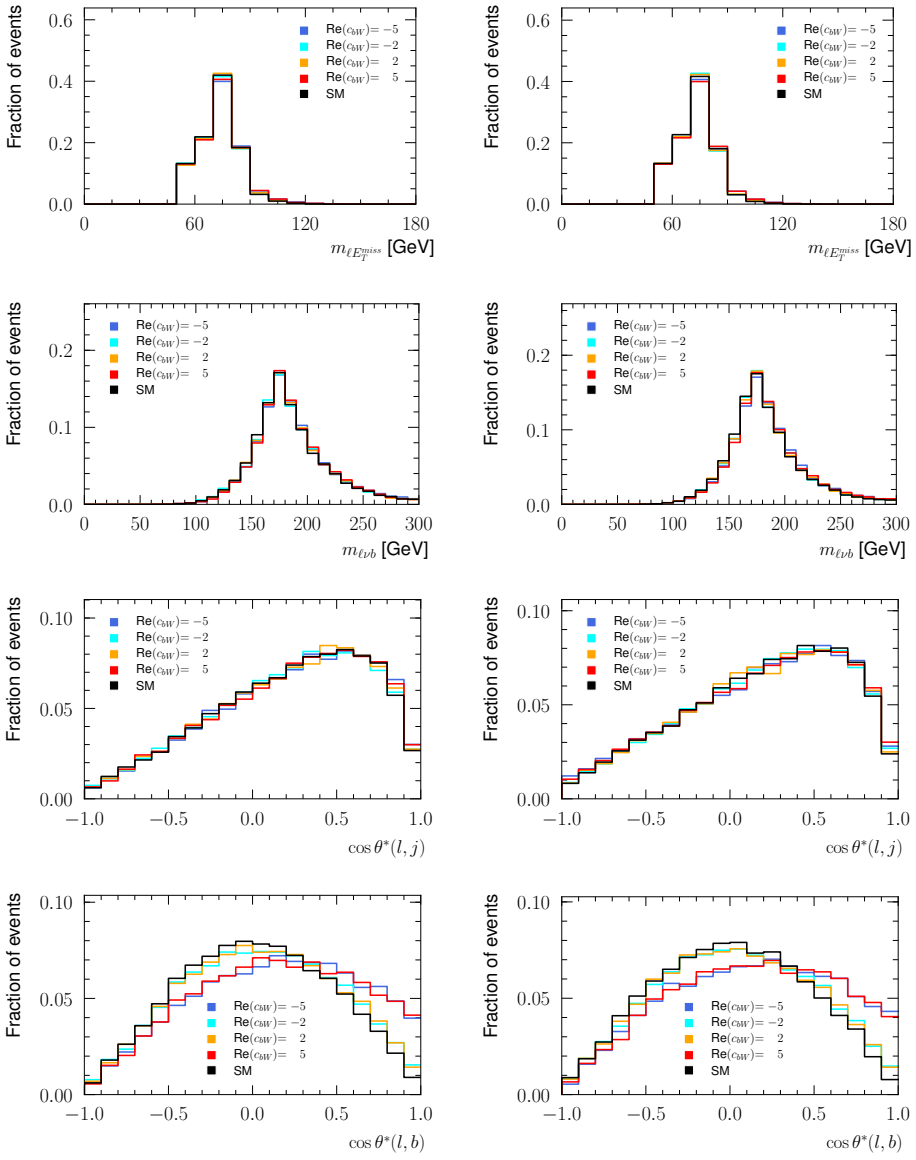

Figure 56: Control plots of simulated top quark and top anti-quark events when varying $\mathrm{Re}\,(c_{bW})$ in the fiducial phase space. Shown are, from top to bottom row, the input variables $m_T\left(\ell E_T^{\mathrm{miss}}\right)$, $m\,(\ell\nu b)$, $\cos\theta^*\,(\ell, j)$, $\cos\theta^*\,(\ell, b)$.

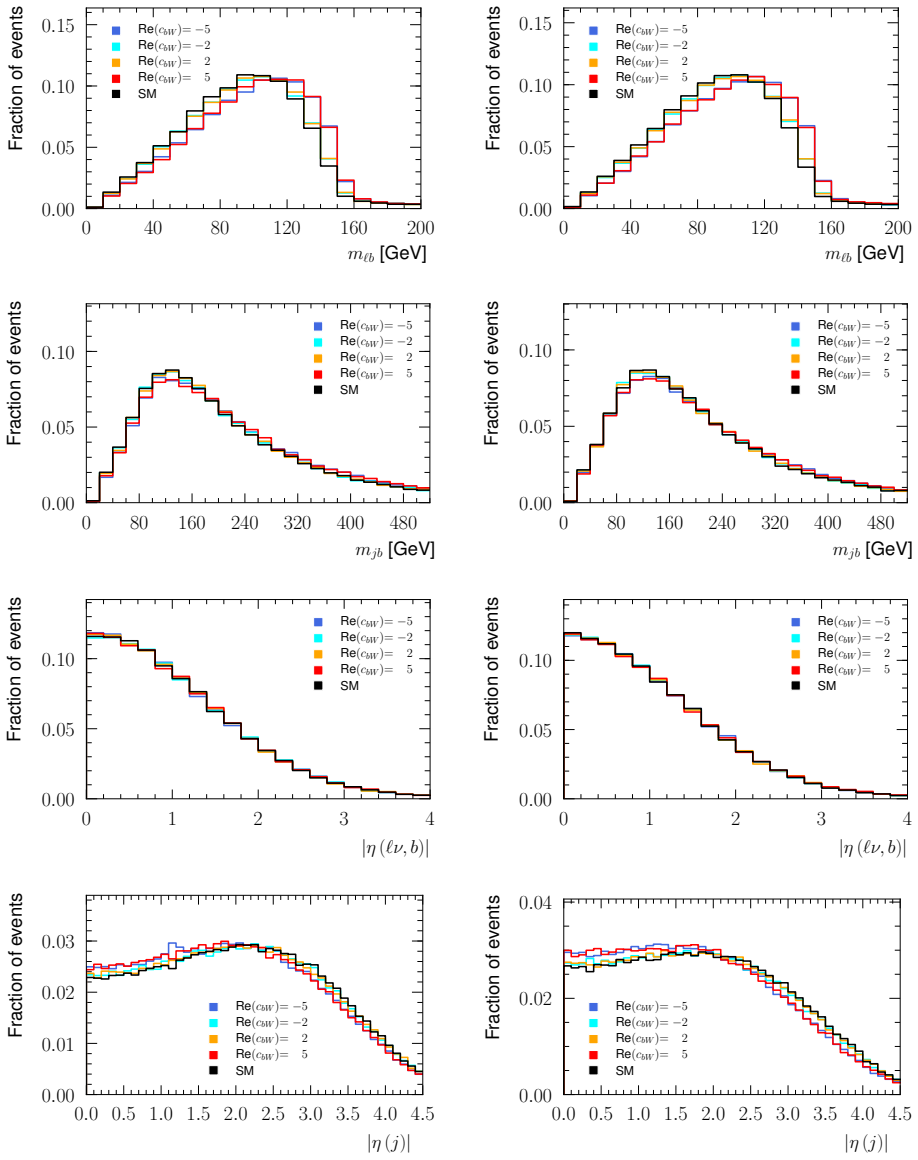

Figure 57: Control plots of simulated top quark and top anti-quark events when varying $\mathrm{Re}\,(c_{bW})$ in the full phase space. Shown are, from top to bottom row, the input variables $m\,(\ell b)$, $m\,(jb)$, $\Delta\eta\,(\ell\nu, b)$, $|\eta\,(j)|$.

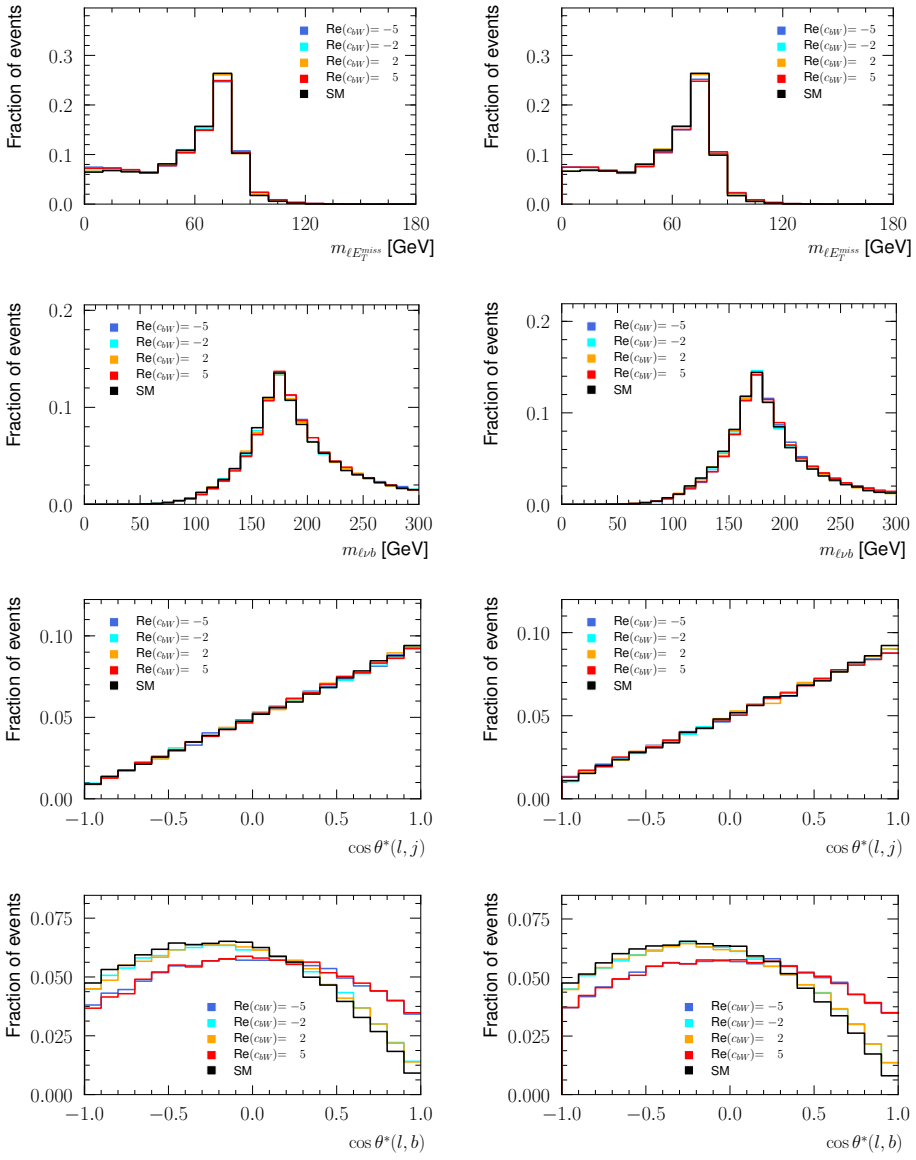

Figure 58: Control plots of simulated top quark and top anti-quark events when varying Re (c_{bW}) in the full phase space. Shown are, from top to bottom row, the input variables $m_T\left(\ell E_T^{\text{miss}}\right)$, $m\left(\ell\nu b\right)$, $\cos\theta^*\left(\ell,j\right)$, $\cos\theta^*\left(\ell,b\right)$.

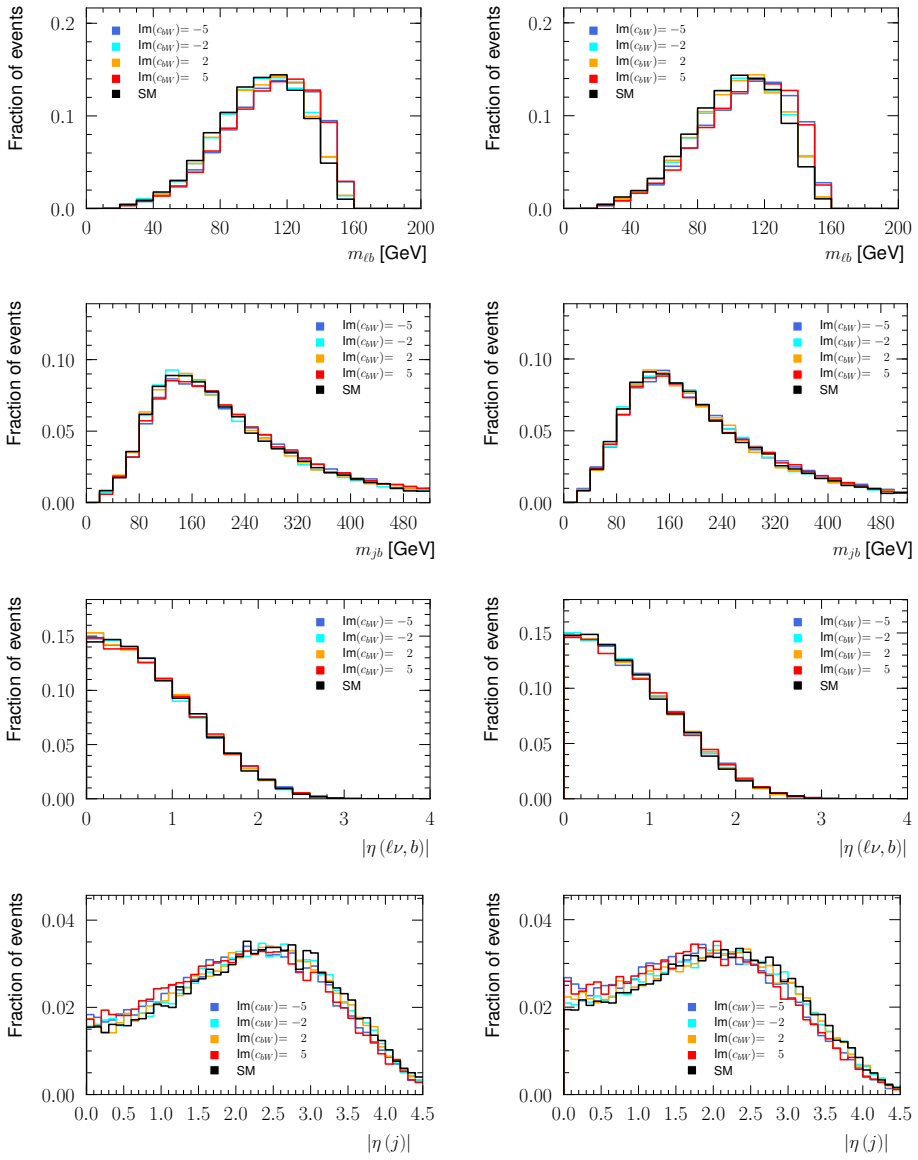

Figure 59: Control plots of simulated top quark and top anti-quark events when varying $\mathrm{Im}\,(c_{bW})$ in the fiducial phase space. Shown are, from top to bottom row, the input variables $m\,(\ell b)$, $m\,(jb)$, $\Delta\eta\,(\ell\nu, b)$, $|\eta\,(j)|$.

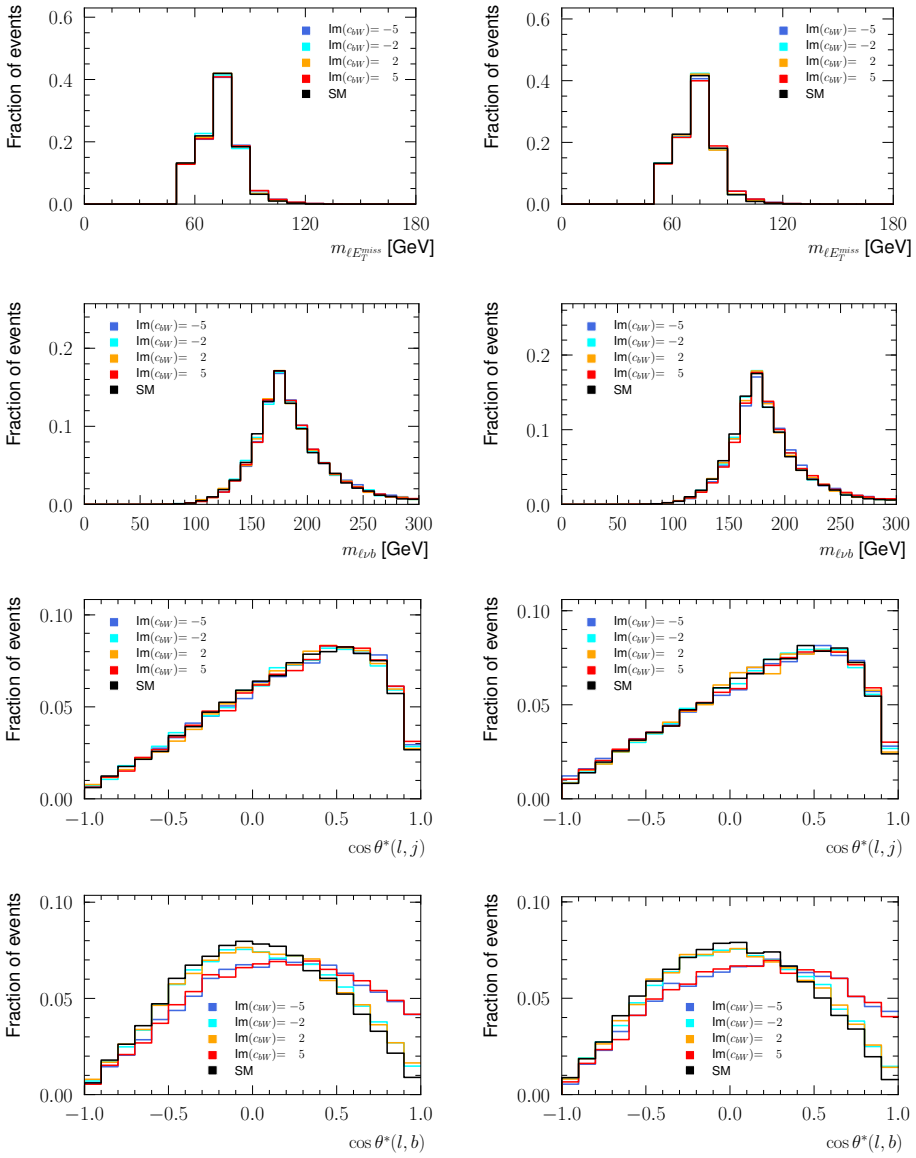

Figure 60: Control plots of simulated top quark and top anti-quark events when varying $\mathrm{Im}\,(c_{bW})$ in the fiducial phase space. Shown are, from top to bottom row, the input variables $m_T\left(\ell E_T^{\mathrm{miss}}\right)$, $m\,(\ell\nu b)$, $\cos\theta^*\,(\ell, j)$, $\cos\theta^*\,(\ell, b)$.

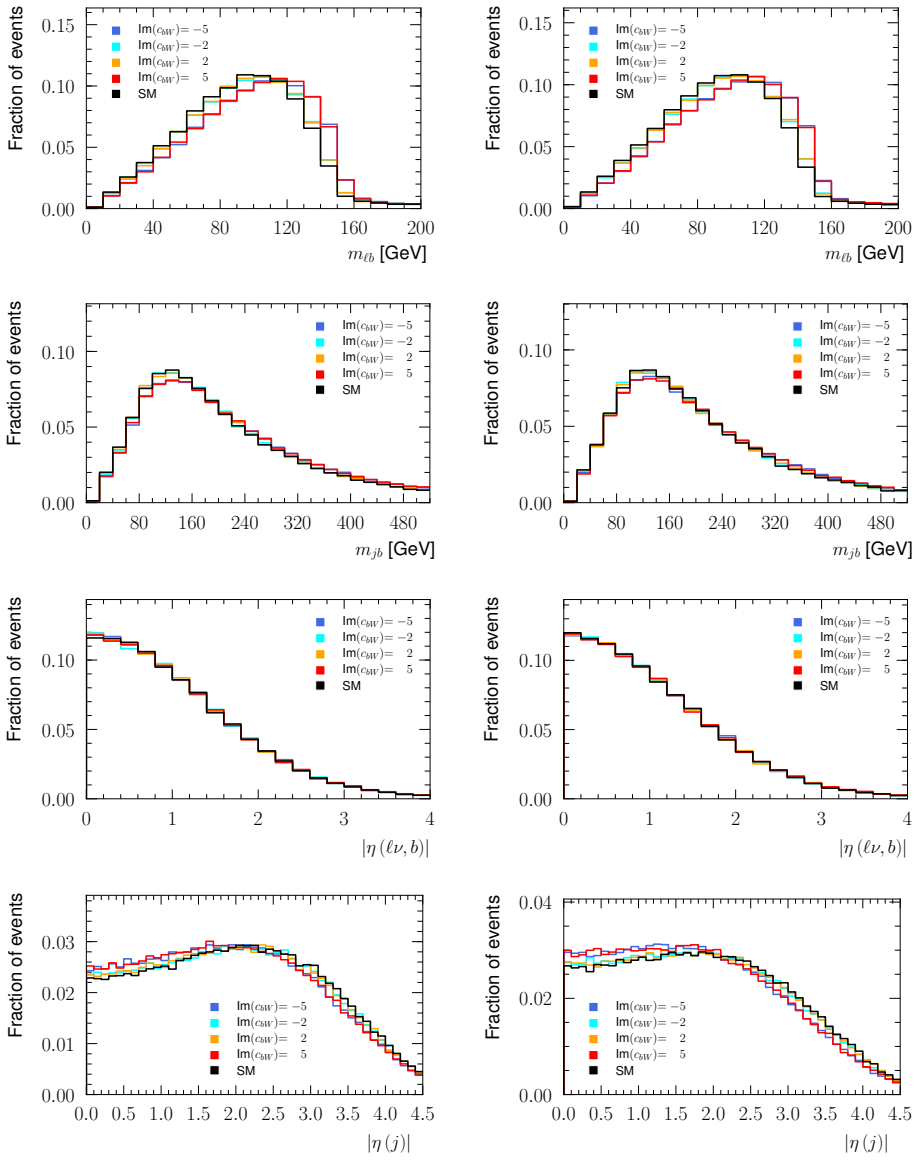

Figure 61: Control plots of simulated top quark and top anti-quark events when varying $\mathrm{Im}\,(c_{bW})$ in the full phase space. Shown are, from top to bottom row, the input variables $m\,(\ell b)$, $m\,(jb)$, $\Delta\eta\,(\ell\nu, b)$, $|\eta\,(j)|$.

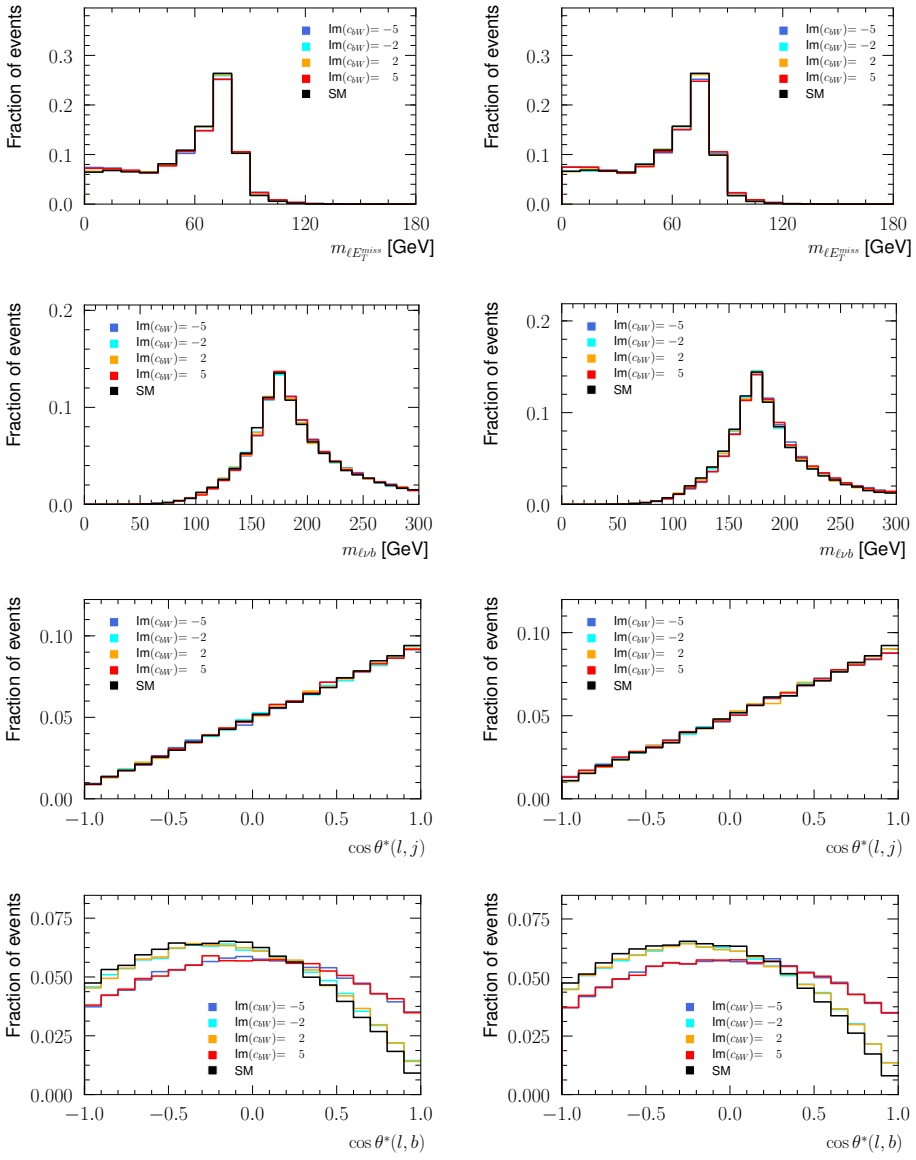

Figure 62: Control plots of simulated top quark and top anti-quark events when varying $\mathrm{Im}\,(c_{bW})$ in the full phase space. Shown are, from top to bottom row, the input variables $m_T\left(\ell E_T^{\mathrm{miss}}\right)$, $m\,(\ell\nu b)$, $\cos\theta^*\,(\ell,j)$, $\cos\theta^*\,(\ell,b)$.

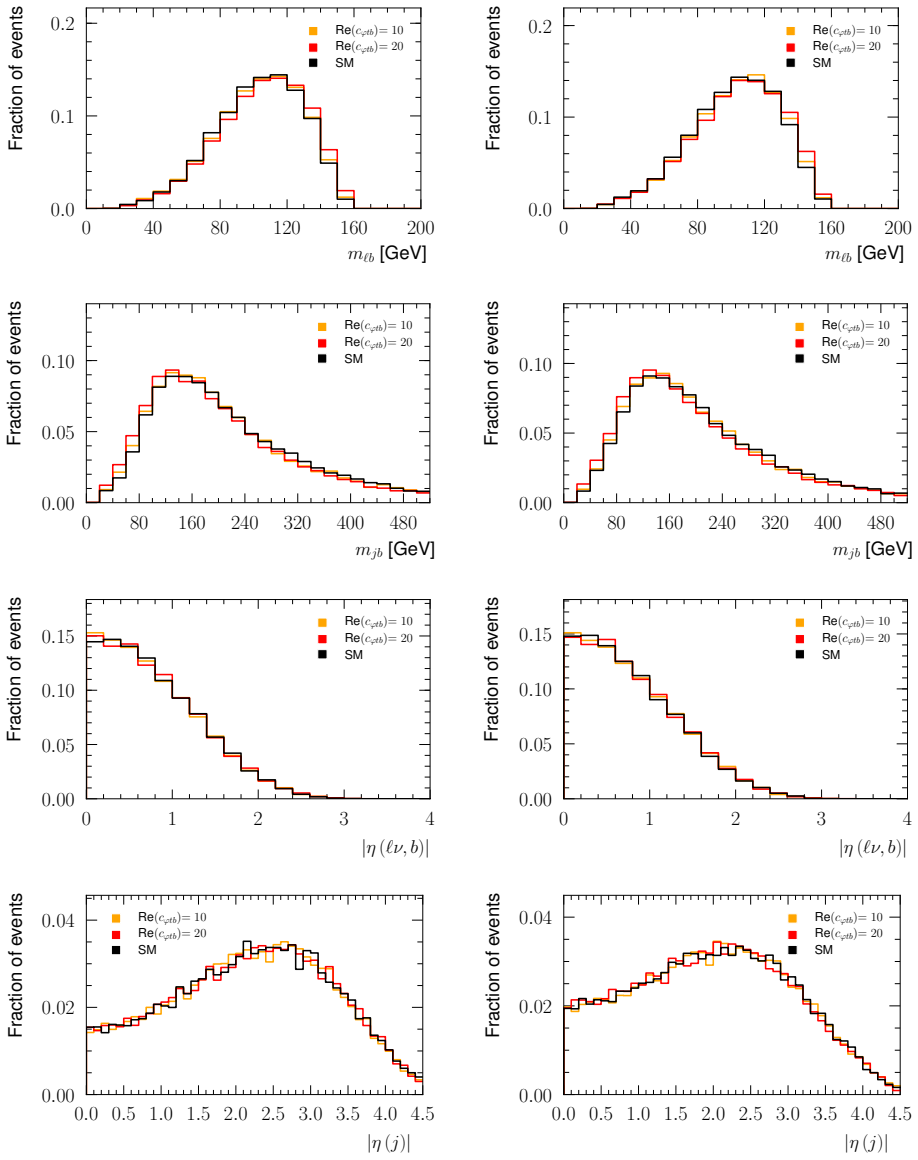

Figure 63: Control plots of simulated top quark and top anti-quark events when varying $c_{\varphi tb}$ in the fiducial phase space. Shown are, from top to bottom row, the input variables $m(\ell b)$, $m(jb)$, $\Delta\eta(\ell\nu, b)$, $|\eta(j)|$.

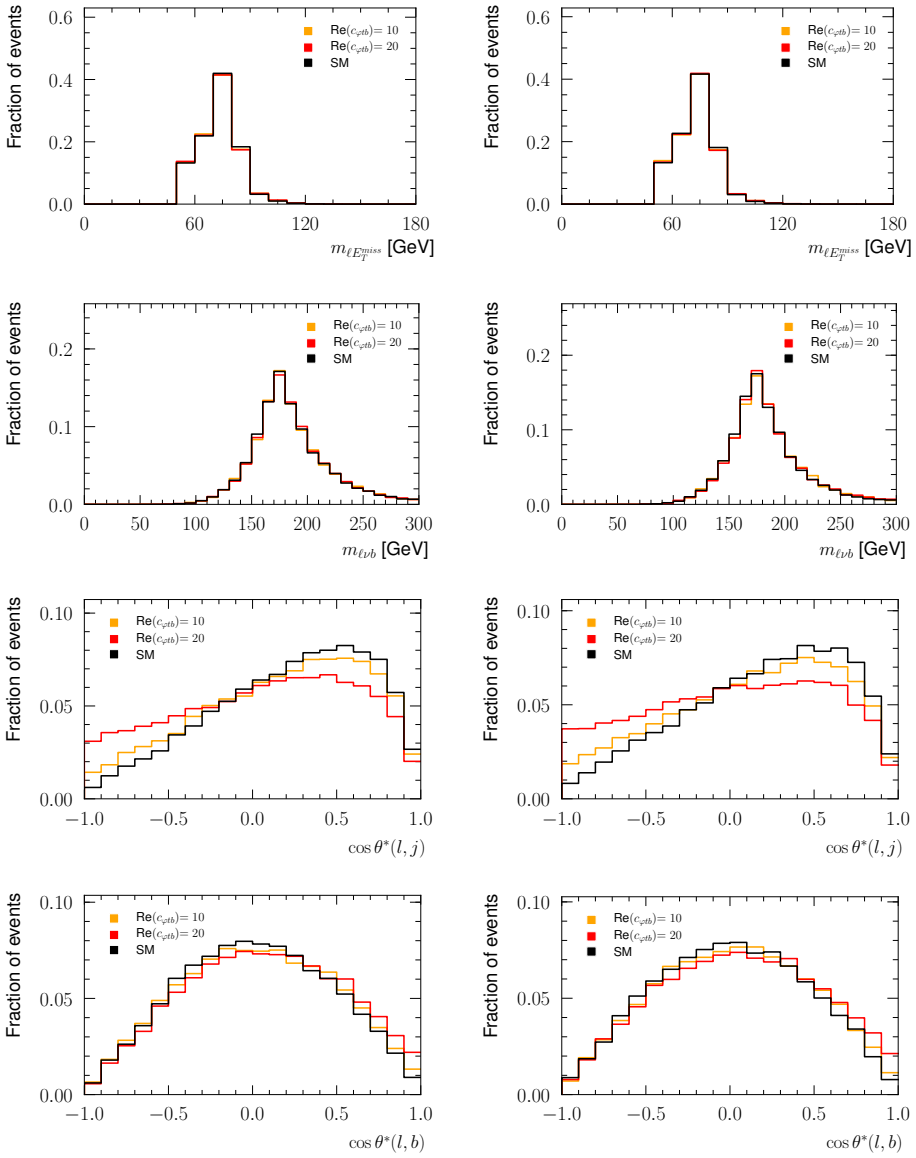

Figure 64: Control plots of simulated top quark and top anti-quark events when varying $c_{\varphi tb}$ in the fiducial phase space. Shown are, from top to bottom row, the input variables $m_T\left(\ell E_T^{\text{miss}}\right)$, $m\left(\ell\nu b\right)$, $\cos\theta^*\left(\ell, j\right)$, $\cos\theta^*\left(\ell, b\right)$.

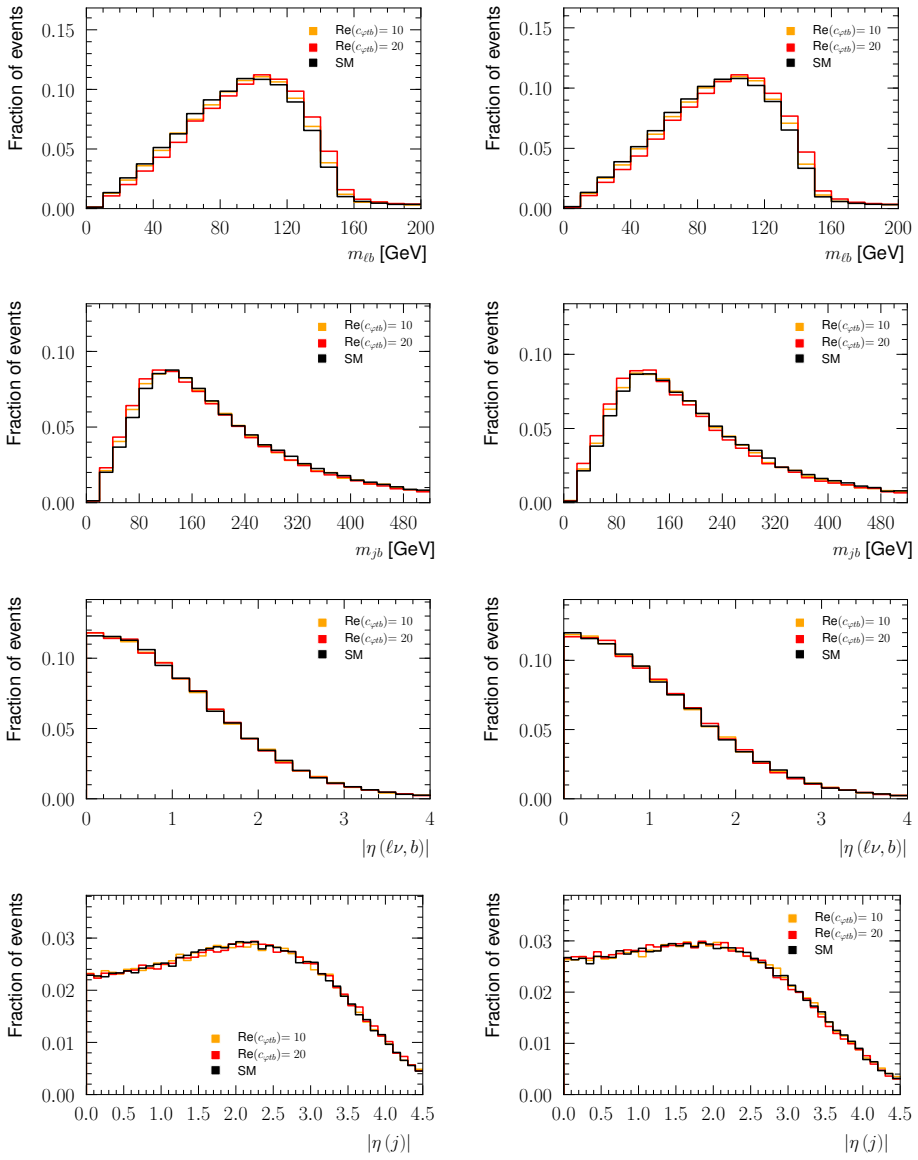

Figure 65: Control plots of simulated top quark and top anti-quark events when varying $c_{\varphi tb}$ in the full phase space. Shown are, from top to bottom row, the input variables $m(\ell b)$, $m(jb)$, $\Delta\eta(\ell\nu, b)$, $|\eta(j)|$.

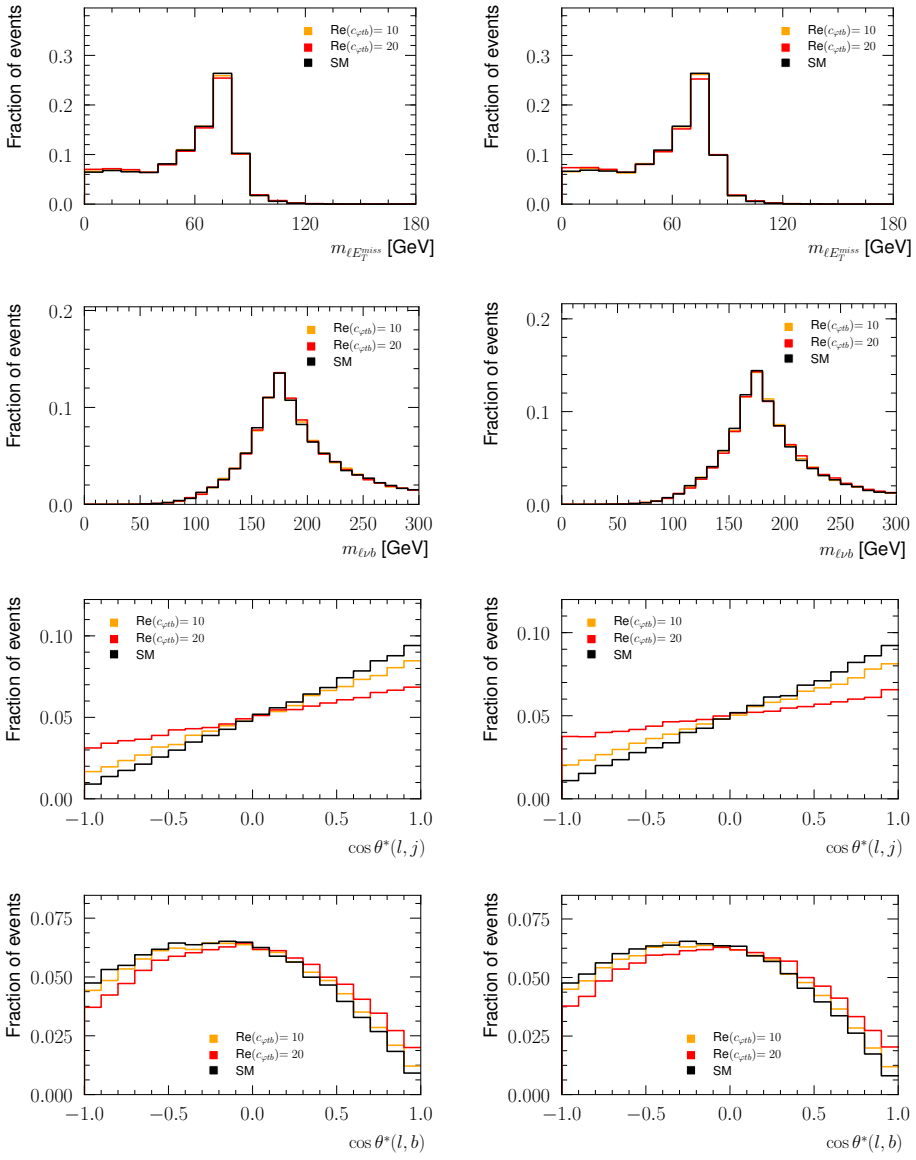

Figure 66: Control plots of simulated top quark and top anti-quark events when varying $c_{\varphi tb}$ in the full phase space. Shown are, from top to bottom row, the input variables $m_T\left(\ell E_T^{\text{miss}}\right)$, $m\left(\ell\nu b\right)$, $\cos\theta^*\left(\ell,j\right)$, $\cos\theta^*\left(\ell,b\right)$.

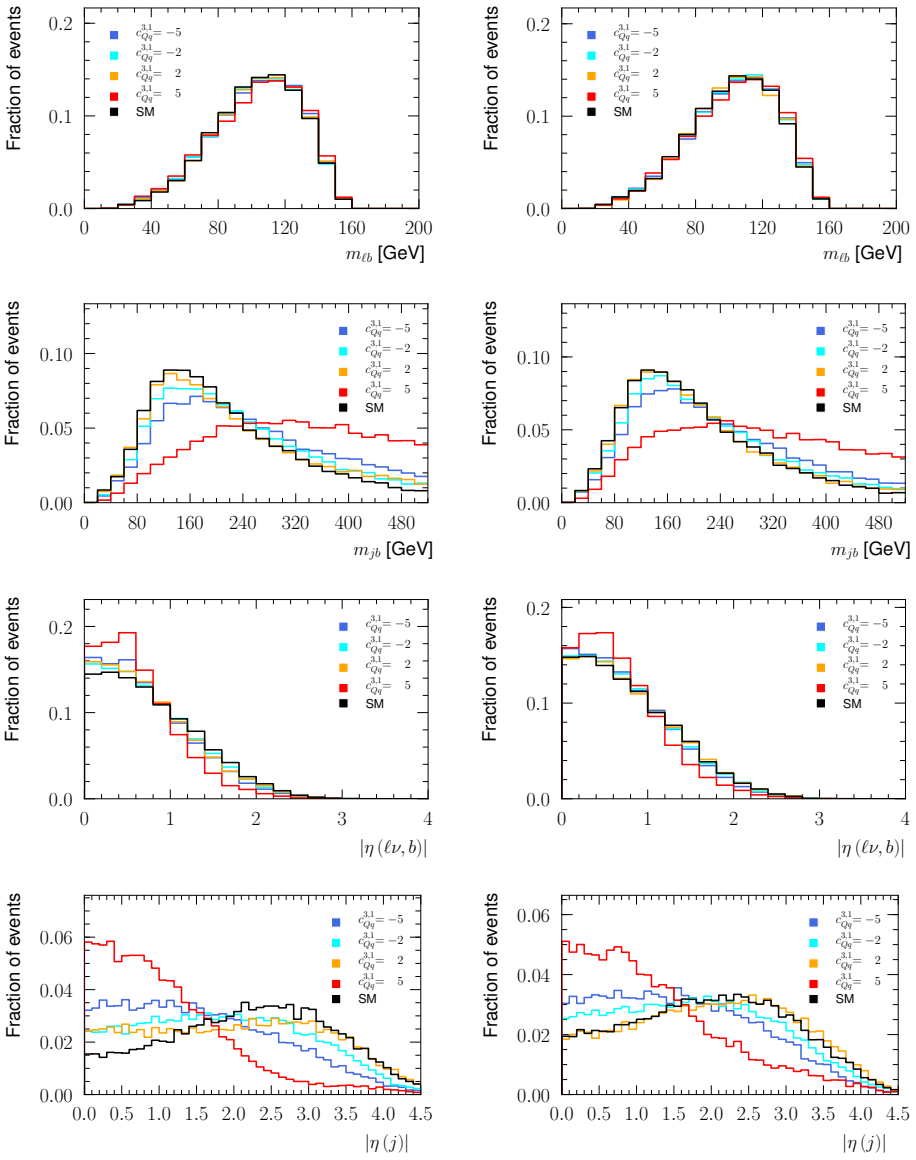

Figure 67: Control plots of simulated top quark and top anti-quark events when varying $c_{Qq}^{3,1}$ in the fiducial phase space. Shown are, from top to bottom row, the input variables $m(\ell b)$, $m(jb)$, $\Delta\eta(\ell\nu, b)$, $|\eta(j)|$.

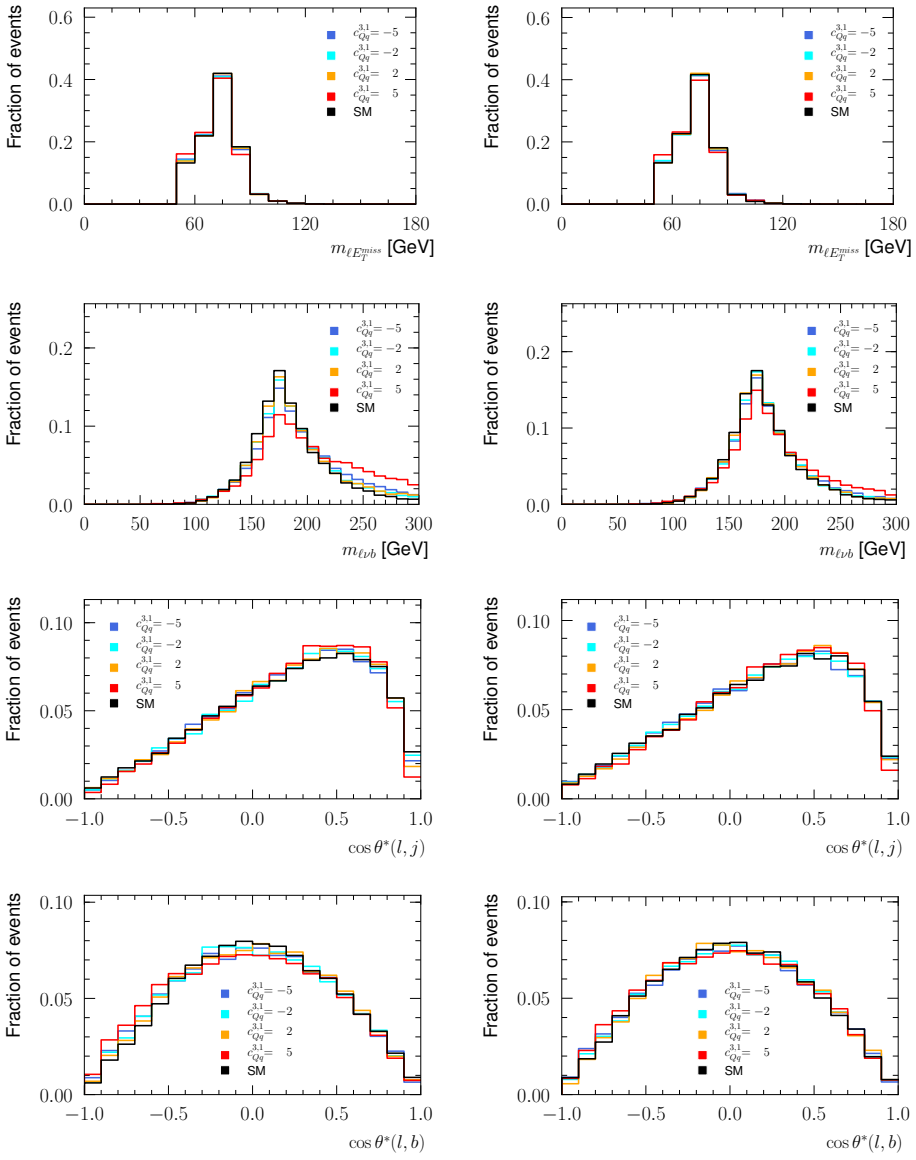

Figure 68: Control plots of simulated top quark and top anti-quark events when varying $c_{Qq}^{3,1}$ in the fiducial phase space. Shown are, from top to bottom row, the input variables $m_T\left(\ell E_T^{\text{miss}}\right)$, $m\left(\ell\nu b\right)$, $\cos\theta^*\left(\ell, j\right)$, $\cos\theta^*\left(\ell, b\right)$.

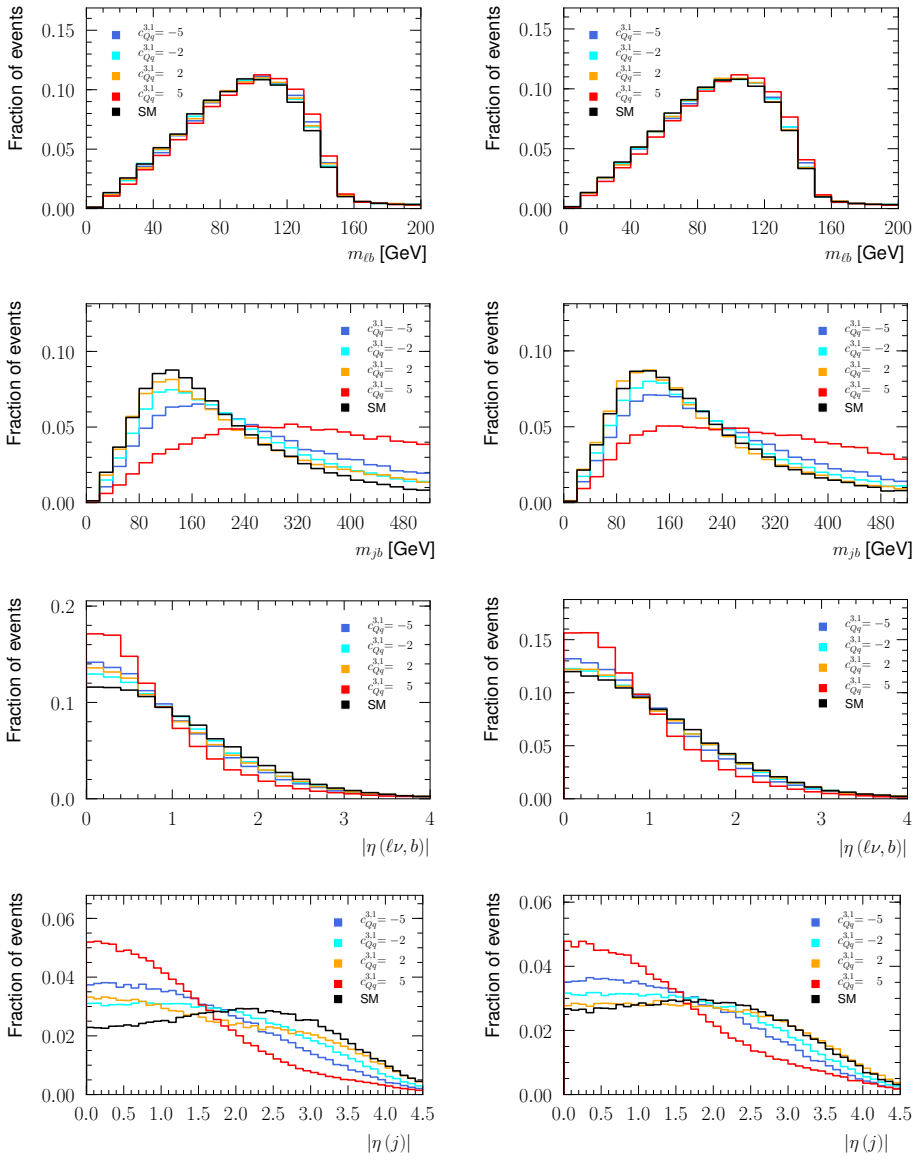

Figure 69: Control plots of simulated top quark and top anti-quark events when varying $c_{Qq}^{3,1}$ in the full phase space. Shown are, from top to bottom row, the input variables $m(\ell b)$, $m(jb)$, $\Delta\eta(\ell\nu, b)$, $|\eta(j)|$.

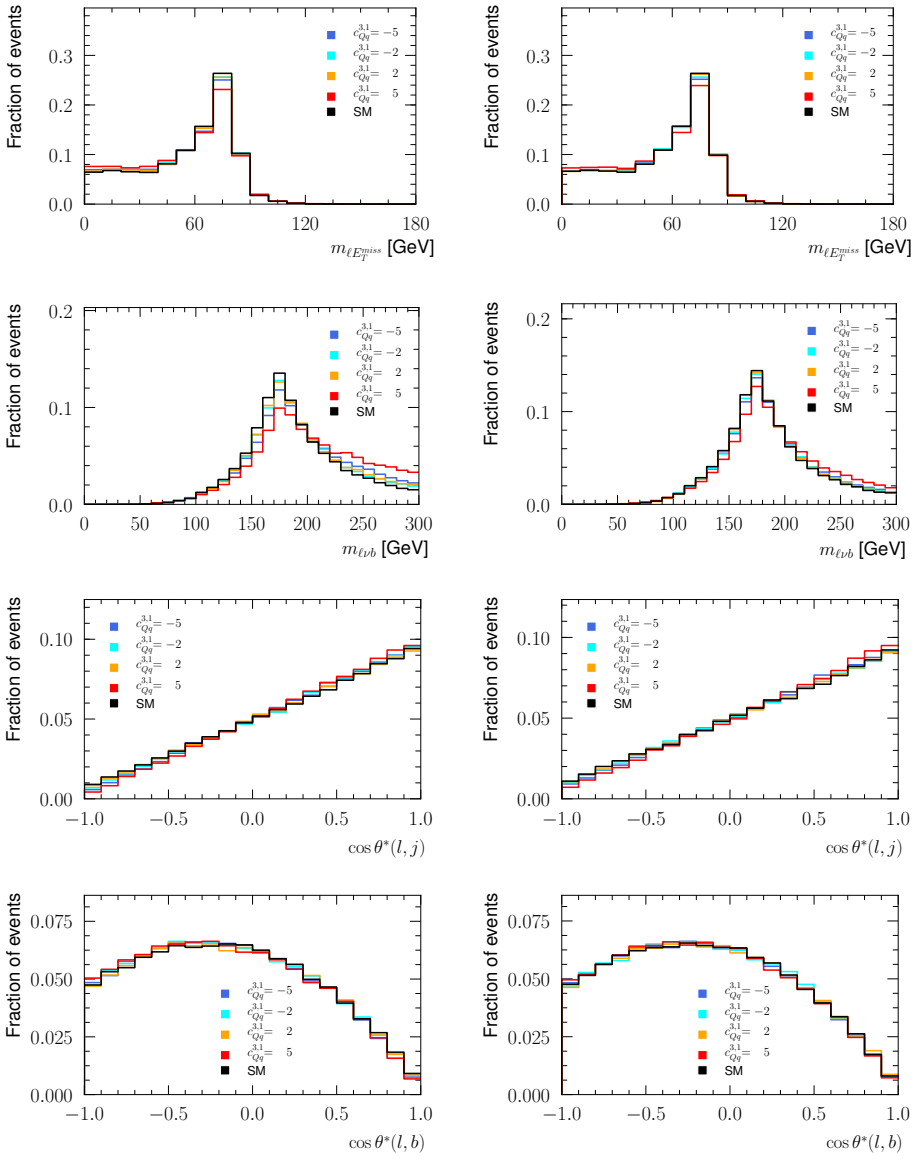

Figure 70: Control plots of simulated top quark and top anti-quark events when varying $c_{Qq}^{3,1}$ in the full phase space. Shown are, from top to bottom row, the input variables $m_T\left(\ell E_T^{\text{miss}}\right)$, $m\left(\ell\nu b\right)$, $\cos\theta^*\left(\ell, j\right)$, $\cos\theta^*\left(\ell, b\right)$.

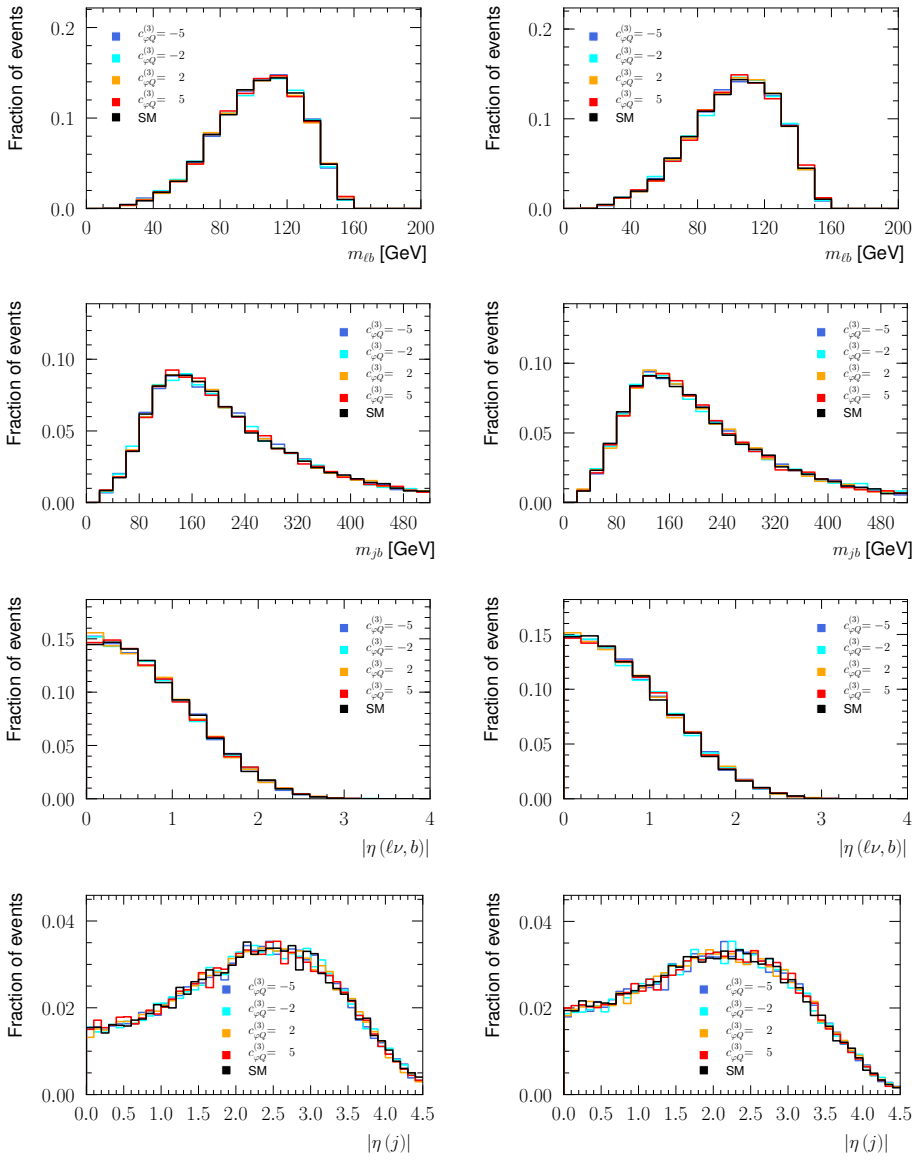

Figure 71: Control plots of simulated top quark and top anti-quark events when varying $c_{\varphi Q}^{(3)}$ in the fiducial phase space. Shown are, from top to bottom row, the input variables $m(\ell b)$, $m(jb)$, $\Delta\eta(\ell\nu, b)$, $|\eta(j)|$.

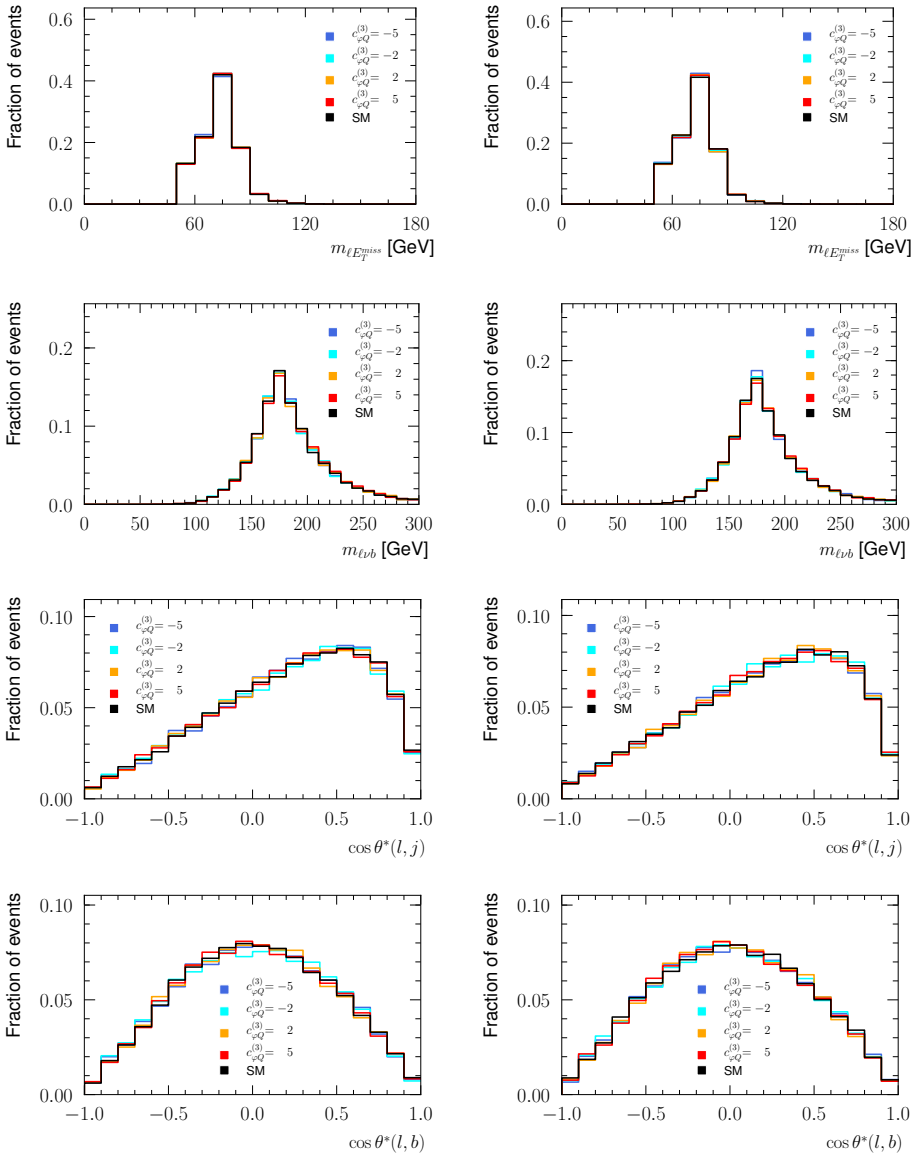

Figure 72: Control plots of simulated top quark and top anti-quark events when varying $c_{\varphi Q}^{(3)}$ in the fiducial phase space. Shown are, from top to bottom row, the input variables $m_T\left(\ell E_T^{\text{miss}}\right)$, $m\left(\ell\nu b\right)$, $\cos\theta^*\left(\ell, j\right)$, $\cos\theta^*\left(\ell, b\right)$.

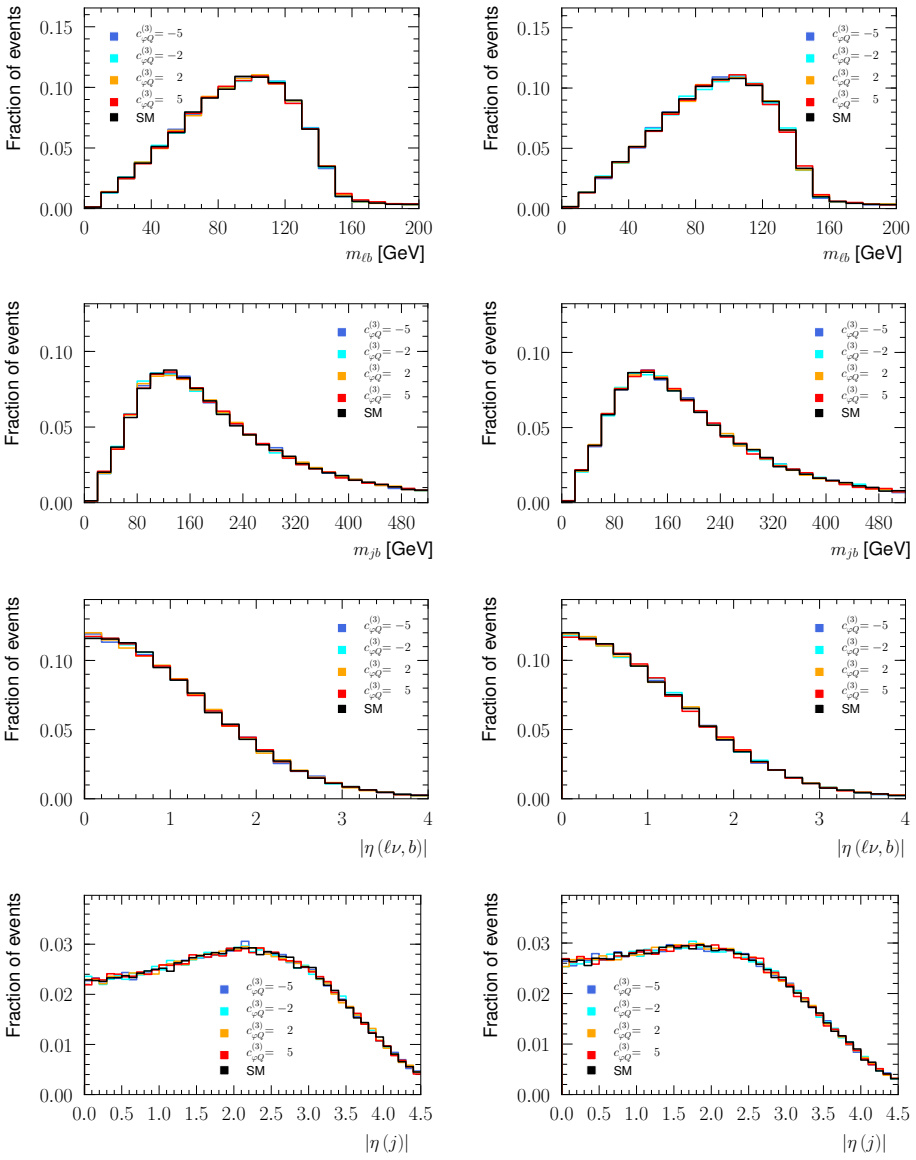

Figure 73: Control plots of simulated top quark and top anti-quark events when varying $c_{\varphi Q}^{(3)}$ in the full phase space. Shown are, from top to bottom row, the input variables $m(\ell b)$, $m(jb)$, $\Delta\eta(\ell\nu, b)$, $|\eta(j)|$.

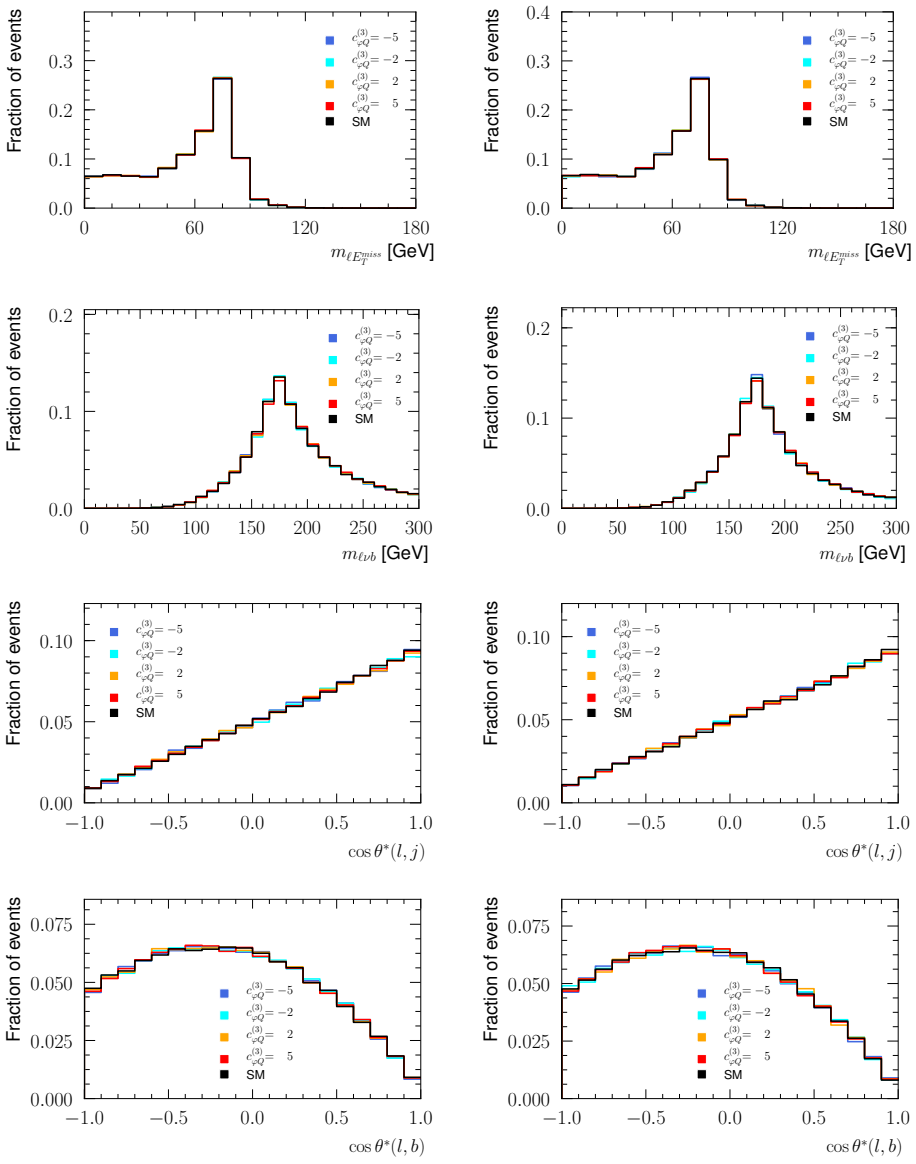

Figure 74: Control plots of simulated top quark and top anti-quark events when varying $c_{\varphi Q}^{(3)}$ in the full phase space. Shown are, from top to bottom row, the input variables $m_T\left(\ell E_T^{\text{miss}}\right)$, $m\left(\ell\nu b\right)$, $\cos\theta^*\left(\ell, j\right)$, $\cos\theta^*\left(\ell, b\right)$.

Appendix F

Dependency Of Angular Coefficients On Anomalous Couplings

This section shows all fits of the deconvolved angular coefficients in terms of the anomalous couplings. The light green points are the points in the Markov chain selected for each coupling as described in Section 2.10.2 and the blue curve is the fitted function. Also shown in red is the measured angular coefficient at the Standard Model point including the uncertainty.

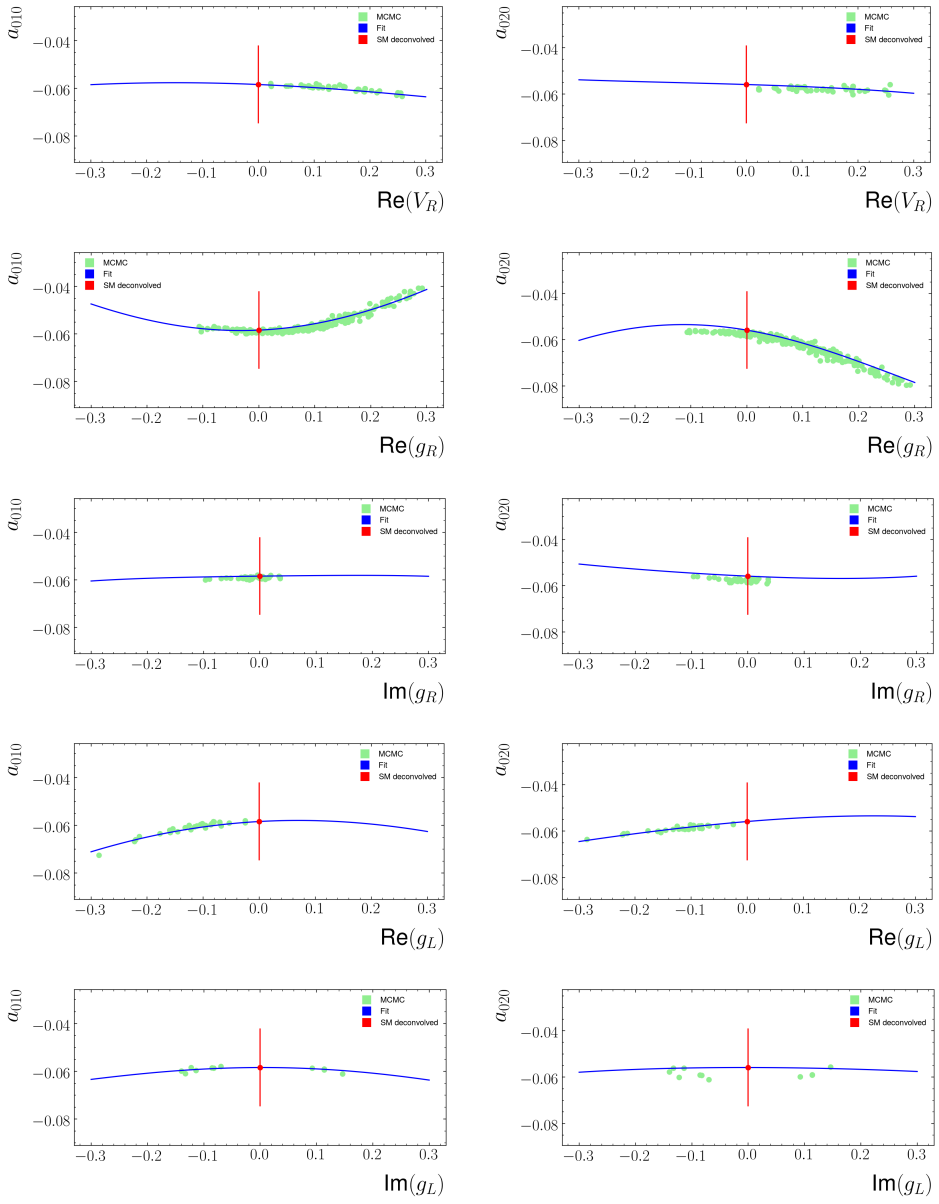

Figure 75: Dependency of the angular coefficients a_{010} and a_{020} on the EFT coefficients.

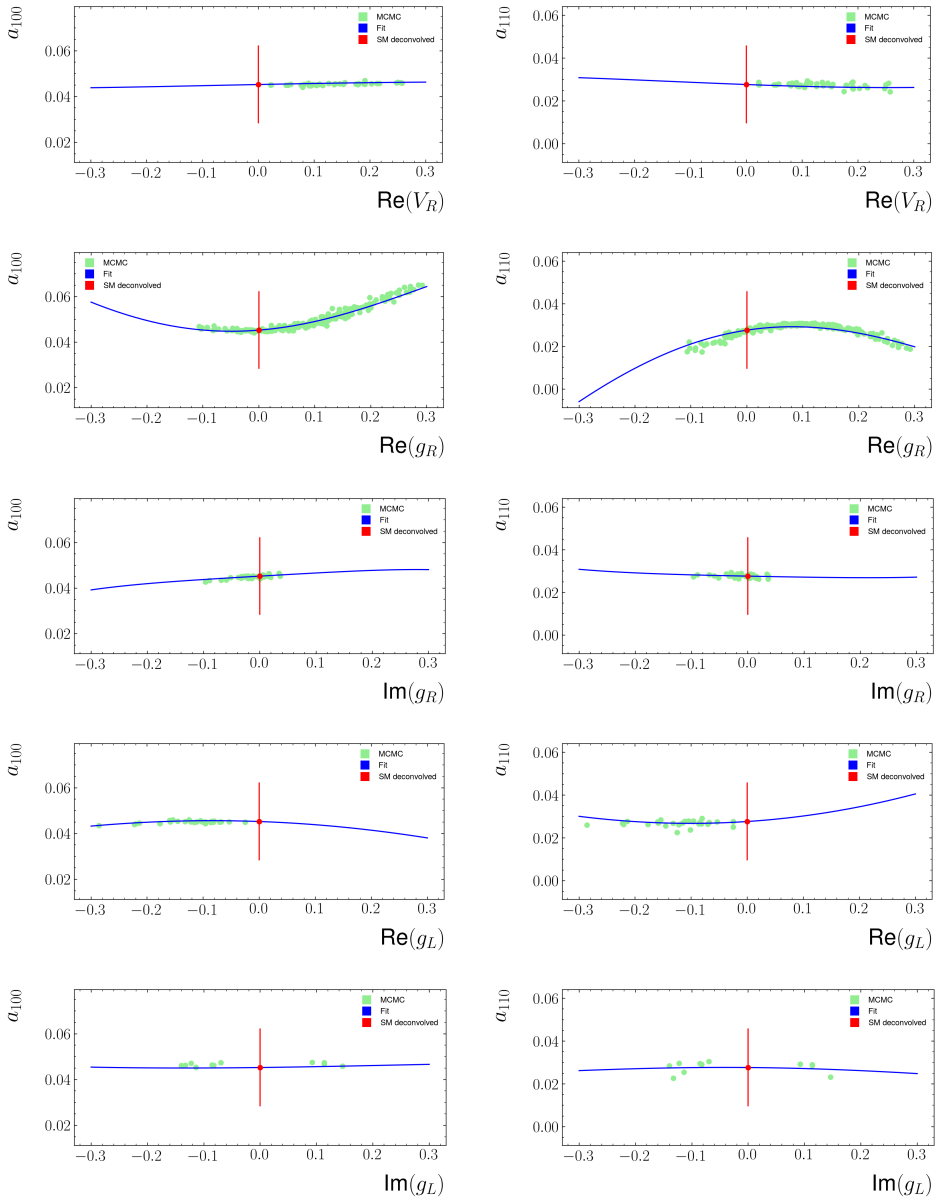

Figure 76: Dependency of the angular coefficients a_{100} and a_{110} on the EFT coefficients.

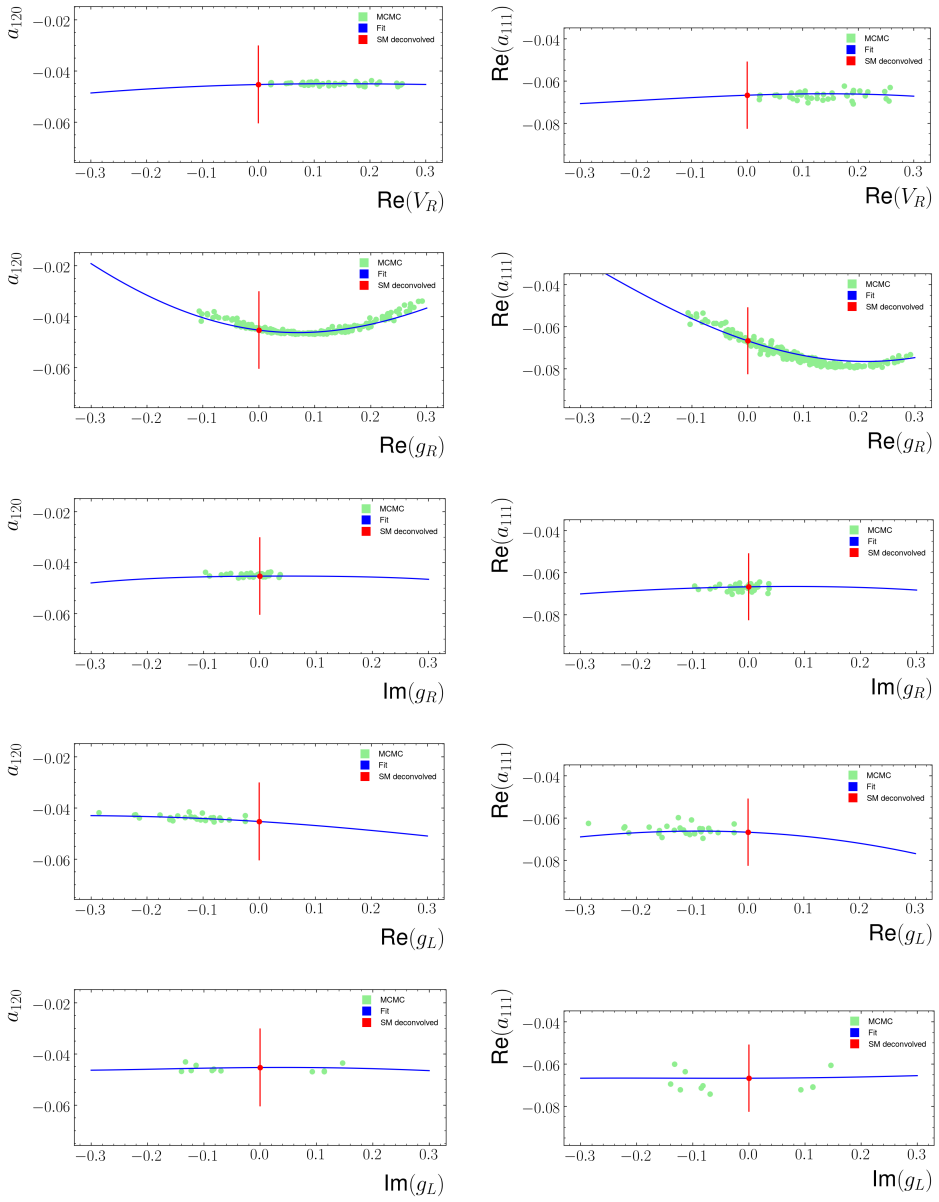

Figure 77: Dependency of the angular coefficients a_{120} and $\mathrm{Re}(a_{111})$ on the EFT coefficients.

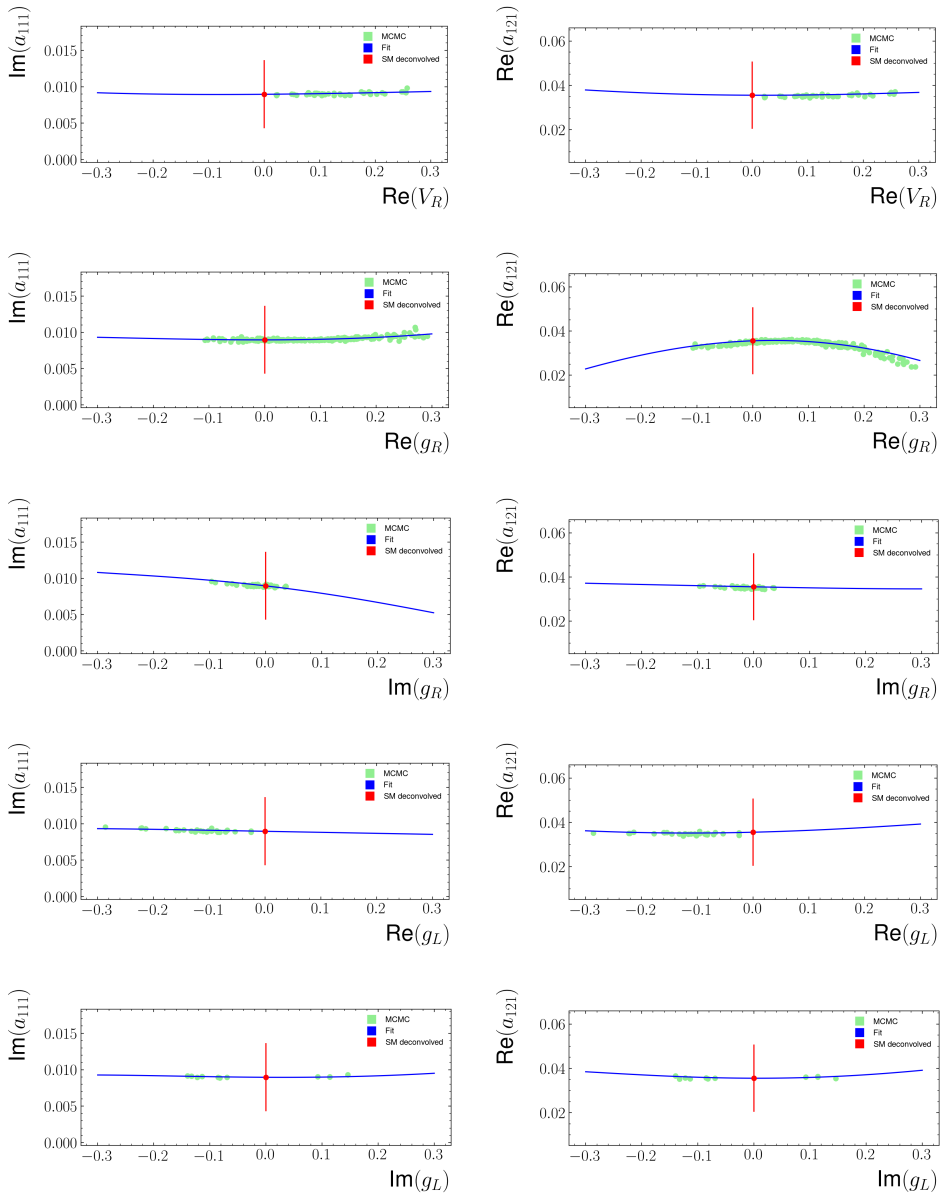

Figure 78: Dependency of the angular coefficients $\mathrm{Im}(a_{111})$ and $\mathrm{Re}(a_{121})$ on the EFT coefficients.

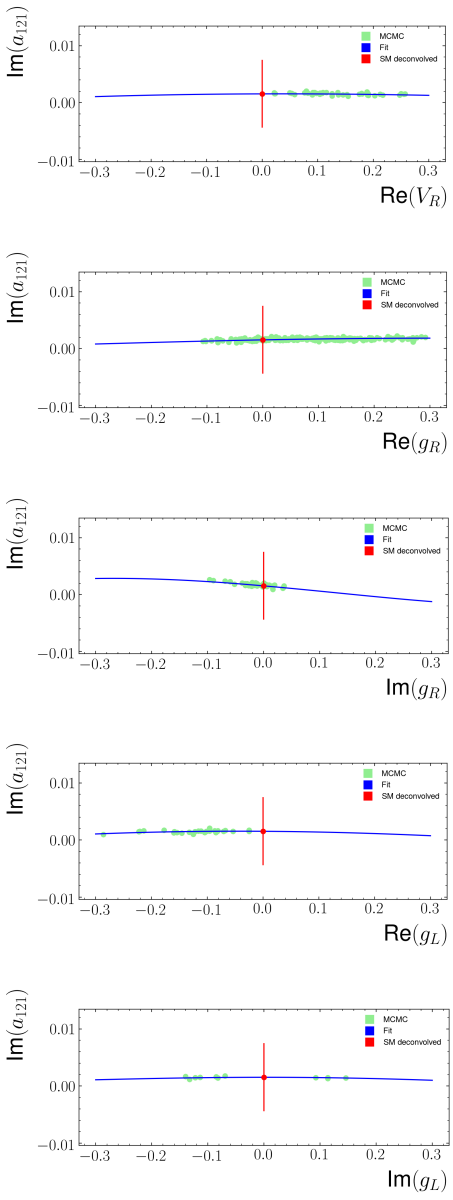

Figure 79: Dependency of the angular coefficients $\mathrm{Im}(a_{121})$ on the EFT coefficients.

Appendix G

2D Probability Distributions Of The Combination Of The Single Top Decay Distributions And W Boson Helicity Fractions

This section shows the two-dimensional marginalized probability distributions of the ratio of the EFT coefficients with respect to V_L corresponding to Section 2.11.1.

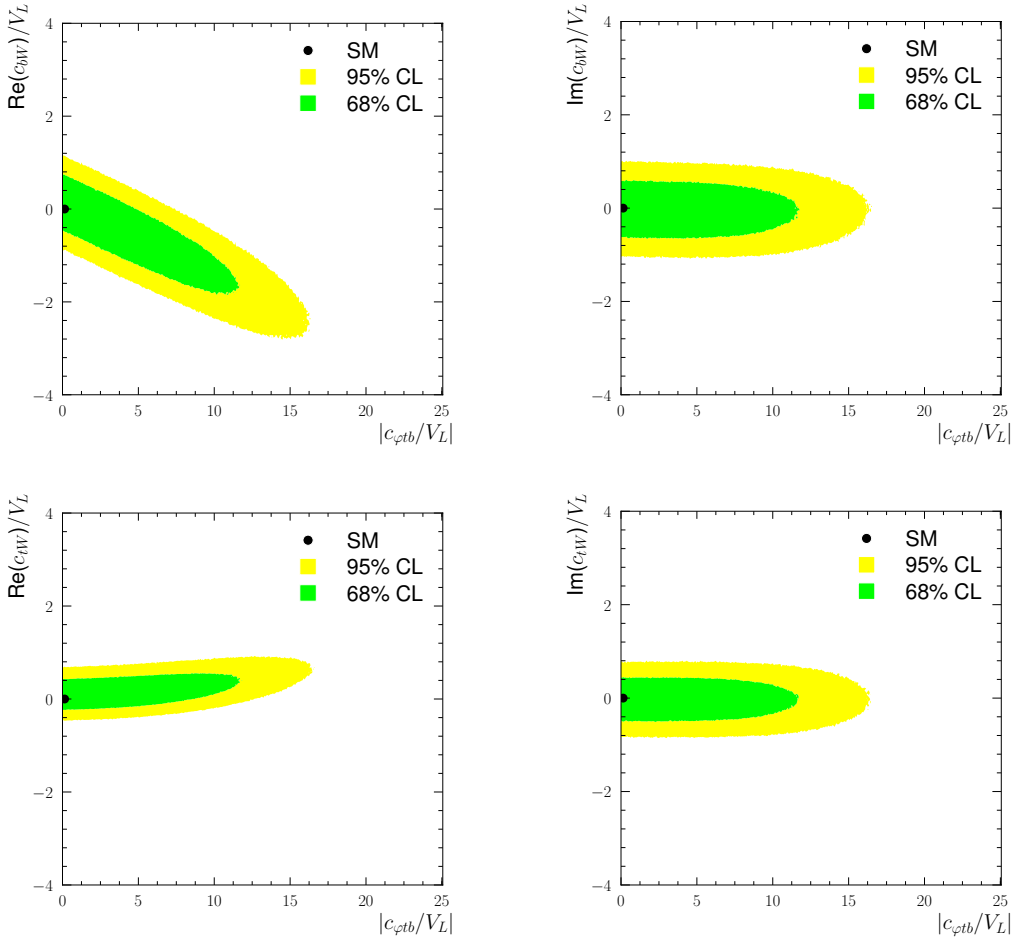

Figure 80: Two-dimensional marginalized 68% (green) and 95% (yellow) confidence regions of the EFT coefficients.

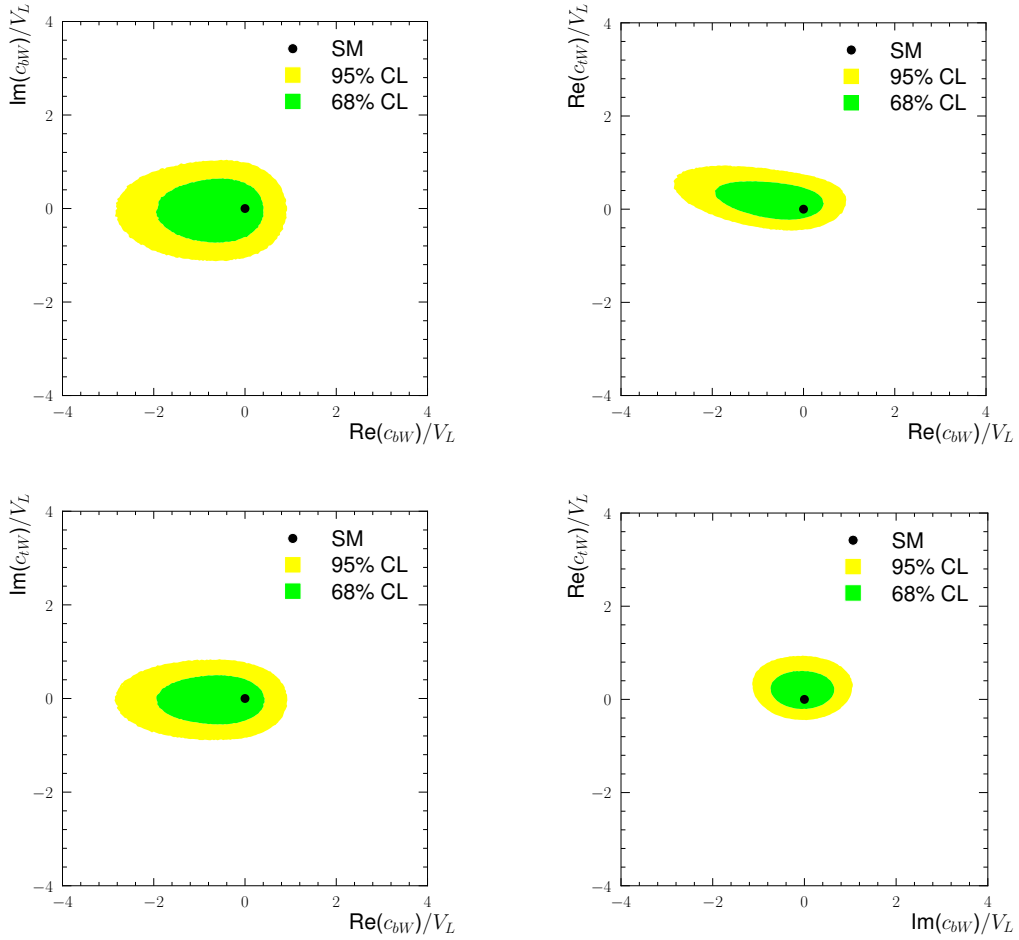

Figure 81: Two-dimensional marginalized 68% (green) and 95% (yellow) confidence regions of the EFT coefficients.

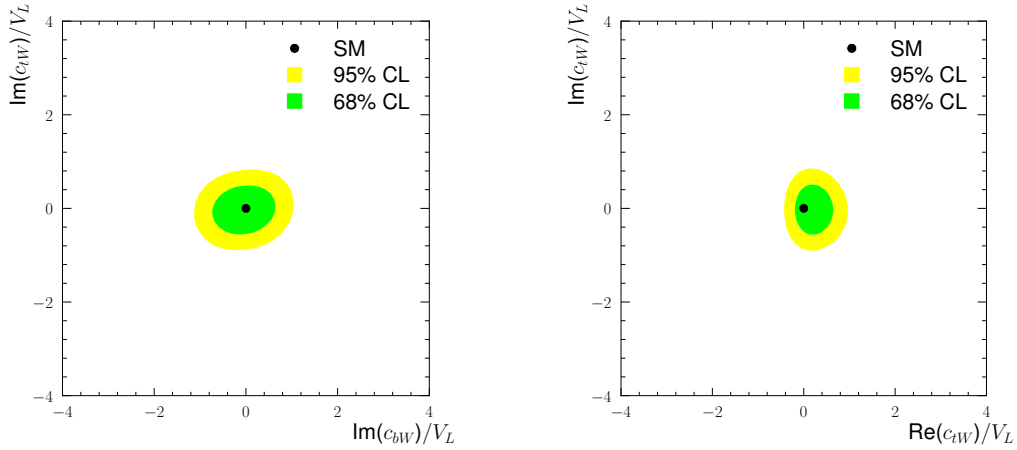

Figure 82: Two-dimensional marginalized 68% (green) and 95% (yellow) confidence regions of the EFT coefficients.

Appendix H

2D Probability Distributions Of The Combined Fit

This section shows all remaining two-dimensional marginalized probability distributions of the EFT coefficients. The distributions of the coefficients $c_{\varphi Q}^{(3)}$ and $c_{Qq}^{3,1}$ as well as $c_{\varphi tb}$ and $\mathrm{Re}\,(c_{bW})$ are shown in Figure 40 of Section 2.11.2.

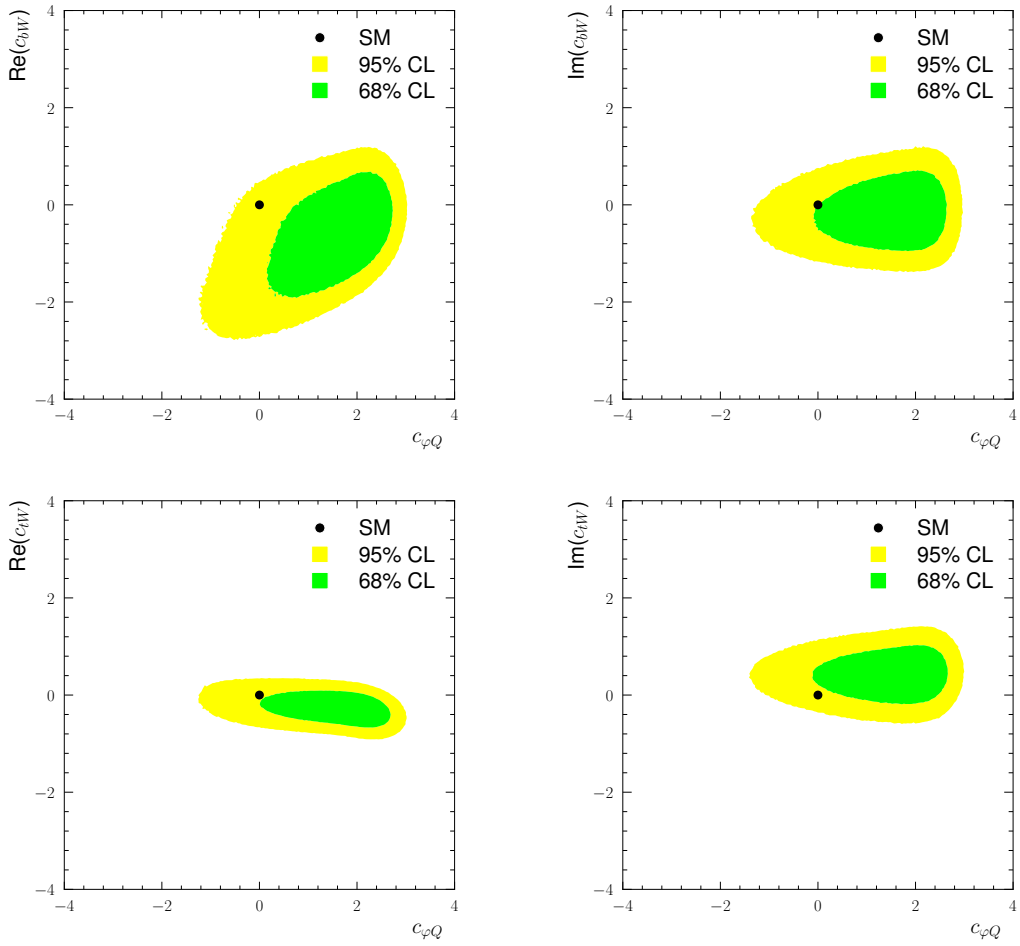

Figure 83: Two-dimensional marginalized 68% (green) and 95% (yellow) confidence regions of the EFT coefficients.

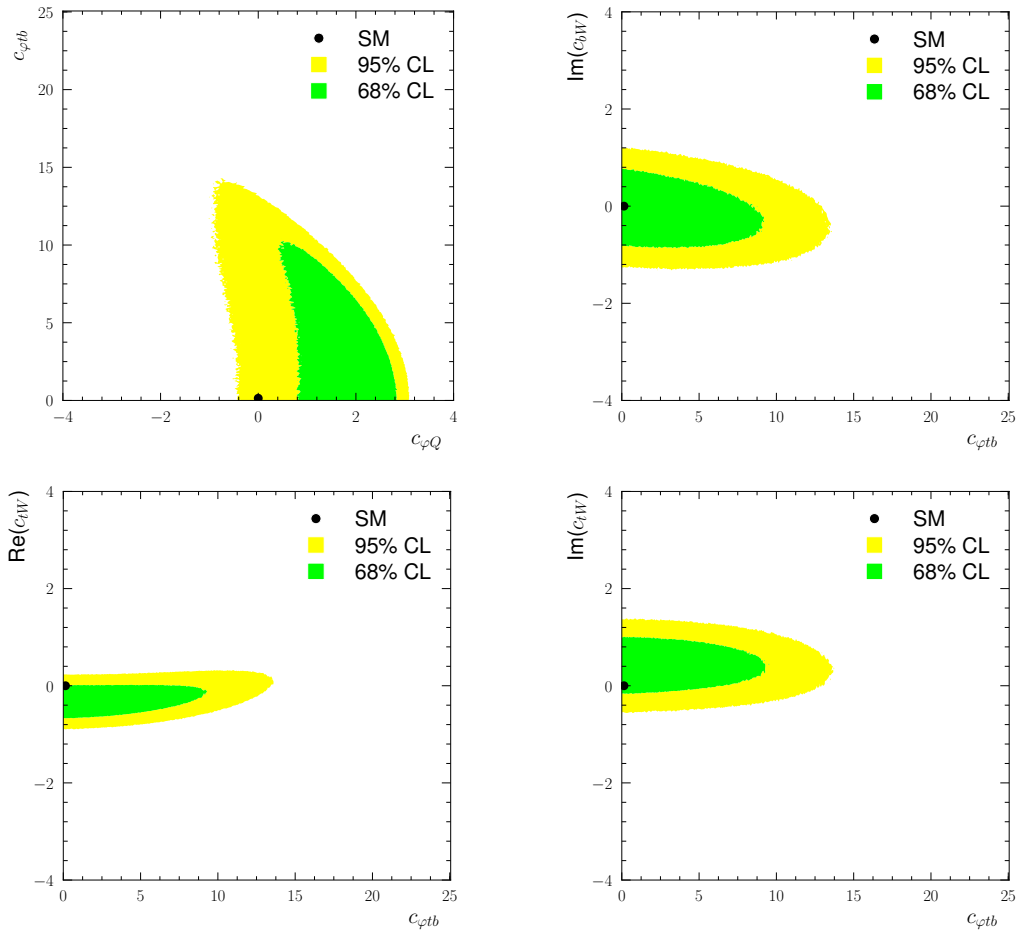

Figure 84: Two-dimensional marginalized 68% (green) and 95% (yellow) confidence regions of the EFT coefficients.

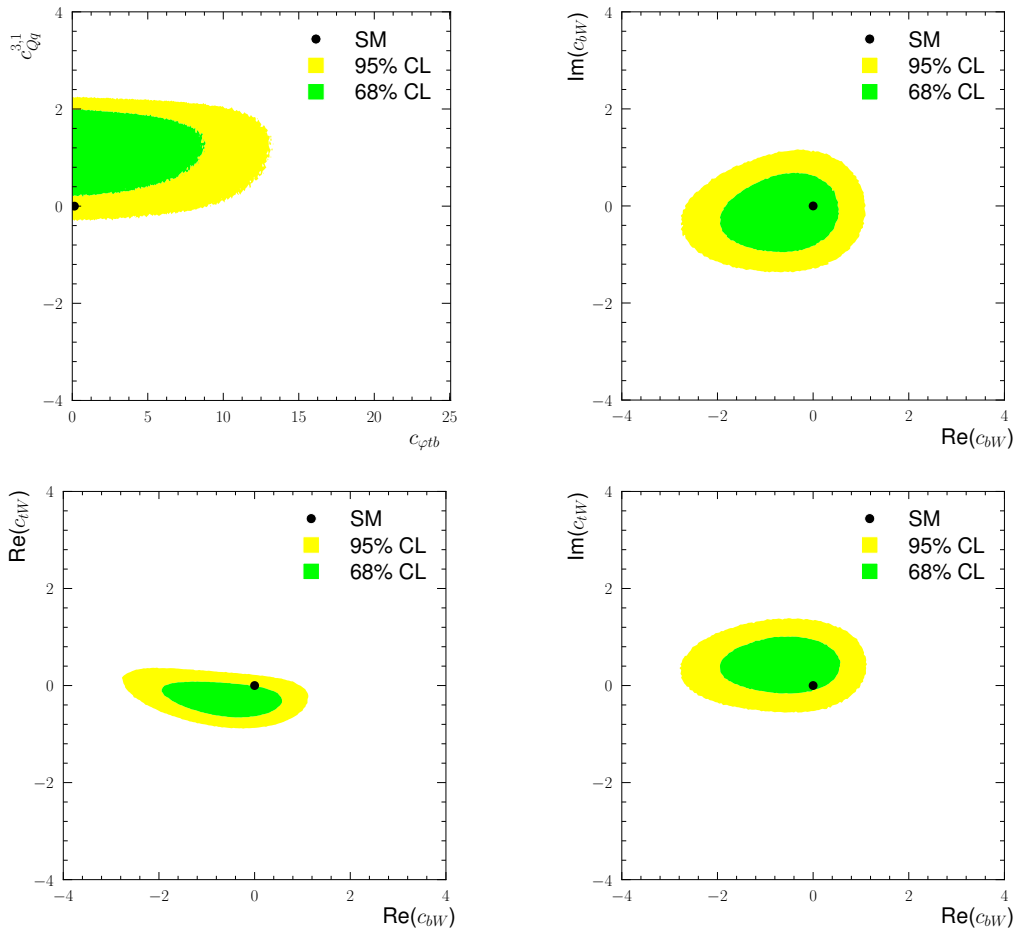

Figure 85: Two-dimensional marginalized 68% (green) and 95% (yellow) confidence regions of the EFT coefficients.

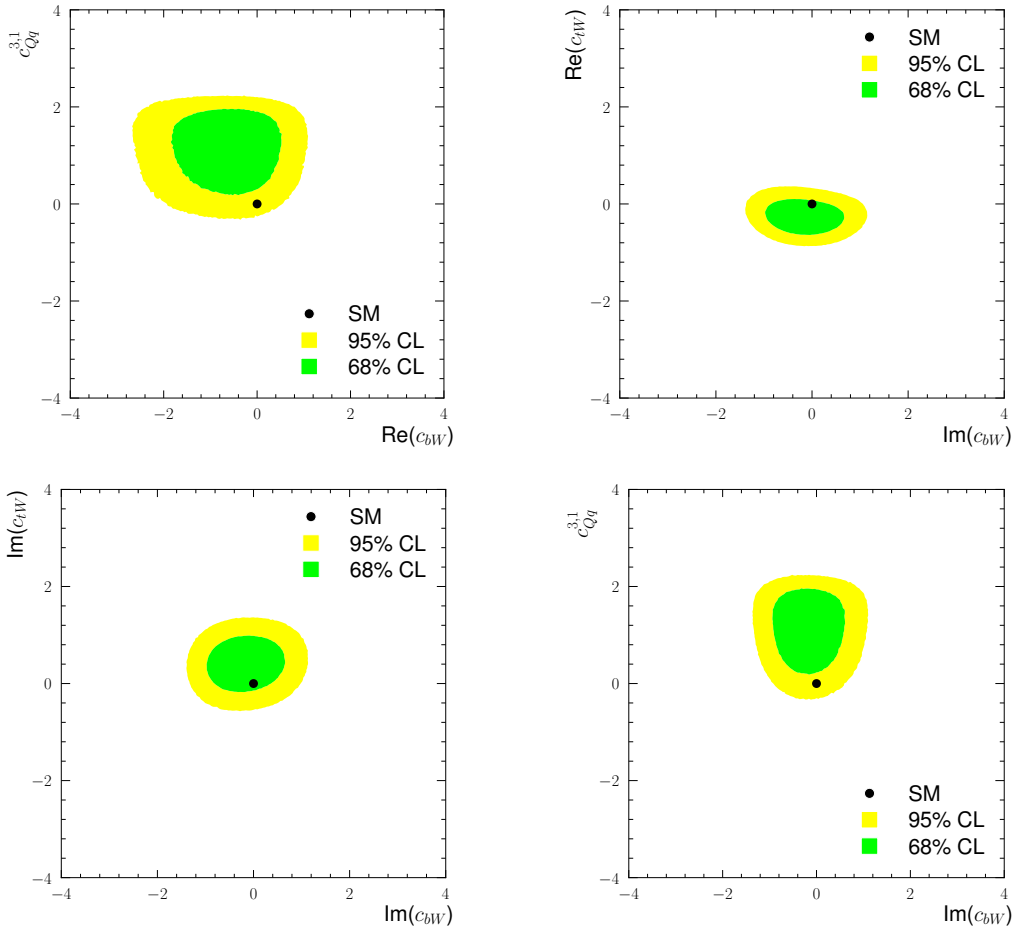

Figure 86: Two-dimensional marginalized 68% (green) and 95% (yellow) confidence regions of the EFT coefficients.

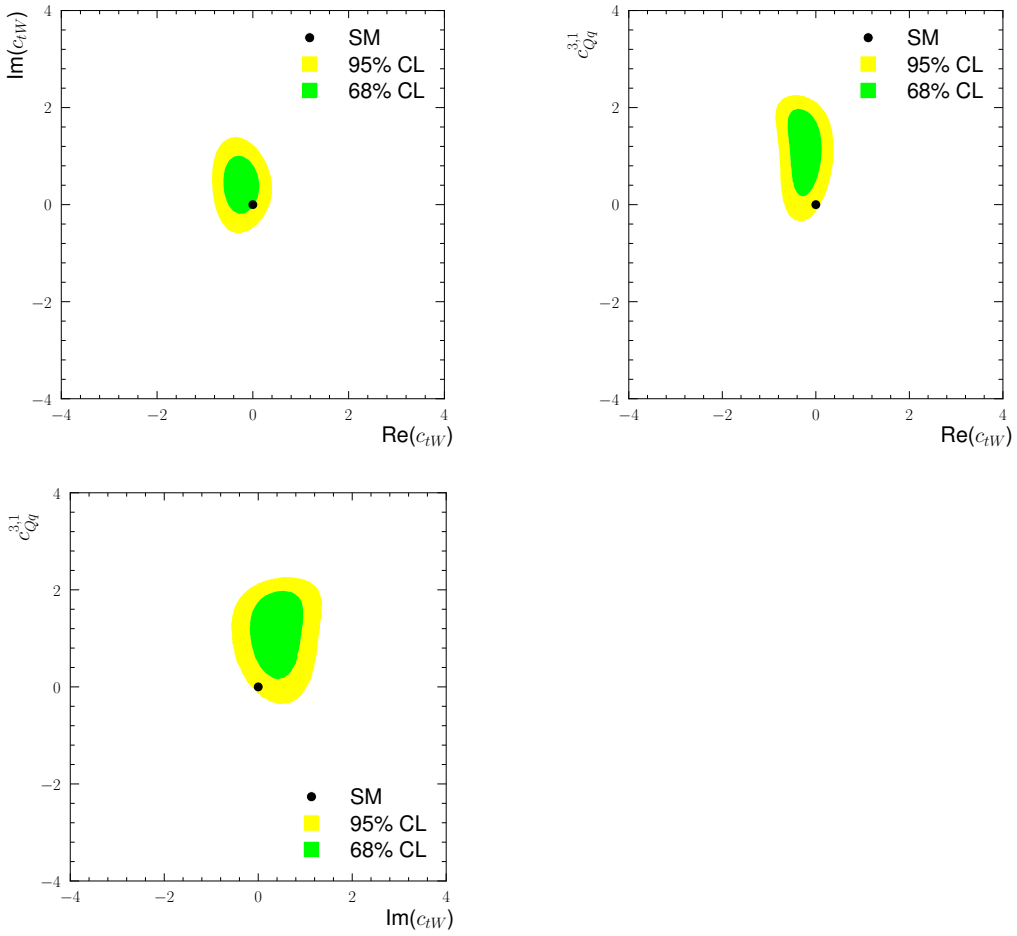

Figure 87: Two-dimensional marginalized 68% (green) and 95% (yellow) confidence regions of the EFT coefficients.

Appendix I

Systematic Uncertainties

This section gives a list of all systematic uncertainties that contribute to the correlations between the different measurements. Uncertainties that are only present in on of the measurement are not listed.

	F_0			F_L		
	up	down	sym.	up	down	sym.
BTAG b-tag	-0.001414	-0.001414	0.001414	-0.001207	0.001207	0.001207
BTAG c-tag	0.000856	-0.000856	0.000856	-0.000206	0.000206	0.000206
BTAG miss-tag	-0.000811	-0.000811	0.000811	0.000324	0.000324	0.000324
Diboson normalization	0.000000	0.000000	0.000000	0.000000	0.000000	0.000000
Electron energy resolution	0.000000	0.000000	0.000000	0.000000	0.000000	0.000000
Electron energy scale	0.000000	0.000000	0.000000	0.000000	0.000000	0.000000
Etmiss cell-out + soft jet resolution	0.000000	0.000000	0.000000	0.000000	0.000000	0.000000
Etmiss cell-out + soft jet scale	0.000000	0.000000	0.000000	0.000000	0.000000	0.000000
JER	-0.006103	-0.006103	0.006103	-0.002701	-0.002701	0.002701
JER Jet energy resolution	0.000000	0.000000	0.000000	0.000000	0.000000	0.000000
JES Jet vertex fraction	-0.003600	-0.001700	0.002650	0.001900	0.001300	0.001600
JES b-tagging	0.000000	0.000000	0.000000	0.000000	0.000000	0.000000
JES detector (1)	0.000000	0.000000	0.000000	0.000000	0.000000	0.000000
JES detector (2)	0.000000	0.000000	0.000000	0.000000	0.000000	0.000000
JES detector (3)	0.000000	0.000000	0.000000	0.000000	0.000000	0.000000
JES detector and modelling (1)	0.000000	0.000000	0.000000	0.000000	0.000000	0.000000
JES detector and modelling (2)	0.000000	0.000000	0.000000	0.000000	0.000000	0.000000
JES detector and modelling (3)	0.000000	0.000000	0.000000	0.000000	0.000000	0.000000
JES detector and modelling (4)	0.000000	0.000000	0.000000	0.000000	0.000000	0.000000
JES eta inter-calibr. (model. term)	0.000000	0.000000	0.000000	0.000000	0.000000	0.000000
JES eta inter-calibr. (stat. term)	-0.000700	-0.000700	0.000700	0.000100	0.000200	0.000150
JES flavour composition	-0.004200	0.001800	0.003000	0.001700	-0.001300	0.001500
JES flavour response	-0.002400	-0.000500	0.001450	0.001300	-0.000200	0.000750
JES modelling/theory (1)	-0.003000	0.001400	0.002200	0.001300	-0.000800	0.001050
JES modelling/theory (2)	0.000000	0.000000	0.000000	0.000000	0.000000	0.000000
JES modelling/theory (3)	0.000000	0.000000	0.000000	0.000000	0.000000	0.000000
JES modelling/theory (4)	0.000000	0.000000	0.000000	0.000000	0.000000	0.000000

Continued on next page

Table 29: Systematic uncertainties of the W helicity fractions F_0 and F_L.

	F_0			F_L		
	up	down	sym.	up	down	sym.
JES pile-up (mu)	0.000000	0.000000	0.000000	0.000000	0.000000	0.000000
JES pile-up (n-vertices)	0.000000	0.000000	0.000000	0.000000	0.000000	0.000000
JES pile-up (pT term)	0.000000	0.000000	0.000000	0.000000	0.000000	0.000000
JES pile-up (rho term)	-0.002100	0.002200	0.002150	0.000900	-0.001800	0.001350
JES punch through	0.000000	0.000000	0.000000	0.000000	0.000000	0.000000
JES single-particle	0.000000	0.000000	0.000000	0.000000	0.000000	0.000000
JES statistics (1)	-0.001500	0.000600	0.001050	0.000800	-0.000800	0.000800
JES statistics (2)	0.000000	0.000000	0.000000	0.000000	0.000000	0.000000
JES statistics (3)	0.000000	0.000000	0.000000	0.000000	0.000000	0.000000
JES statistics (4)	0.000000	0.000000	0.000000	0.000000	0.000000	0.000000
Jet reconstruction efficiency	0.000000	0.000000	0.000000	0.000000	0.000000	0.000000
Lepton ID SF	-0.002995	0.002995	0.002995	0.001916	-0.001916	0.001916
Lepton Reco SF	-0.000292	-0.000292	0.000292	0.000255	-0.000255	0.000255
Lepton TriggerSF	0.002604	-0.002604	0.002604	-0.001354	0.001354	0.001354
Luminosity	0.000000	0.000000	0.000000	0.000000	0.000000	0.000000
Muon momentum resolution (id)	0.000000	0.000000	0.000000	0.000000	0.000000	0.000000
Muon momentum scale	0.000000	0.000000	0.000000	0.000000	0.000000	0.000000
Muon momentum smearing res.	0.000000	0.000000	0.000000	0.000000	0.000000	0.000000
PDF	0.003300	-0.003300	0.003300	-0.004200	0.004200	0.004200
Possible polarization nonlinearity	0.000000	0.000000	0.000000	0.000000	0.000000	0.000000
Radiation	0.003300	-0.003300	0.003300	-0.005800	0.005800	0.005800
Template Statistics	0.009100	-0.009100	0.009100	-0.005600	0.005600	0.005600
Top Mass	0.001700	-0.001700	0.001700	-0.005000	0.005000	0.005000
Top-quark background norm.	0.000000	0.000000	0.000000	0.000000	0.000000	0.000000
W+heavy-jets flavour composition	0.000000	0.000000	0.000000	0.000000	0.000000	0.000000
W+jets norm. (overall SF)	0.000000	0.000000	0.000000	0.000000	0.000000	0.000000
W+jets shape modelling	0.000000	0.000000	0.000000	0.000000	0.000000	0.000000

Continued on next page

Table 29: Systematic uncertainties of the W helicity fractions F_0 and F_L.

	F_0			F_L		
	up	down	sym.	up	down	sym.
Z-jets normalization	0.000000	0.000000	0.000000	0.000000	0.000000	0.000000
t-channel NLO modelling	0.000000	0.000000	0.000000	0.000000	0.000000	0.000000
t-channel LO modelling	0.000000	0.000000	0.000000	0.000000	0.000000	0.000000
t-channel LO/NLO modelling	0.000000	0.000000	0.000000	0.000000	0.000000	0.000000
t-channel colour reconnection	0.000000	0.000000	0.000000	0.000000	0.000000	0.000000
t-channel hadronization	0.000000	0.000000	0.000000	0.000000	0.000000	0.000000
t-channel scale variation	0.000000	0.000000	0.000000	0.000000	0.000000	0.000000
t-channel top-quark finite width eff.	0.000000	0.000000	0.000000	0.000000	0.000000	0.000000
t-channel underlying event	0.000000	0.000000	0.000000	0.000000	0.000000	0.000000
tq NLO matching method	0.000000	0.000000	0.000000	0.000000	0.000000	0.000000
ttbar NLO modelling	0.002500	-0.002500	0.002500	-0.003200	0.003200	0.003200
ttbar hadronization	0.001900	-0.001900	0.001900	-0.001900	0.001900	0.001900
ttbar scale variation	0.000000	0.000000	0.000000	0.000000	0.000000	0.000000

Table 29: Systematic uncertainties of the W helicity fractions F_0 and F_L.

	$\sigma_{\text{fid}}(t)$			$\sigma_{\text{fid}}(\bar{t})$		
	up	down	sym.	up	down	sym.
BTAG b-tag	0.103502	-0.103502	0.103502	0.056828	-0.056828	0.056828
BTAG c-tag	-0.019560	0.019560	0.019560	-0.018246	0.018246	0.018246
BTAG miss-tag	0.029340	-0.029340	0.029340	0.036946	-0.036946	0.036946
Diboson normalization	0.000000	0.000000	0.000000	0.000000	0.000000	0.000000
Electron energy resolution	-0.019560	-0.019560	0.019560	-0.005770	-0.005770	0.005770
Electron energy scale	-0.029340	-0.029340	0.029340	-0.011540	-0.011540	0.011540
Etmiss cell-out + soft jet resolution	-0.009780	-0.009780	0.009780	-0.023080	-0.023080	0.023080
Etmiss cell-out + soft jet scale	-0.048900	0.048900	0.048900	-0.017310	0.017310	0.017310
JER	0.000000	0.000000	0.000000	0.000000	0.000000	0.000000
JER Jet energy resolution	-0.048900	-0.048900	0.048900	-0.005770	-0.005770	0.005770
JES Jet vertex fraction	-0.000000	0.000000	0.000000	-0.011540	0.011540	0.011540
JES b-tagging	0.009780	0.009780	0.009780	0.011540	0.011540	0.011540
JES detector (1)	-0.009780	0.009780	0.009780	-0.011540	0.011540	0.011540
JES detector (2)	-0.009780	0.009780	0.009780	-0.005770	0.005770	0.005770
JES detector (3)	-0.009780	0.009780	0.009780	-0.005770	0.005770	0.005770
JES detector and modelling (1)	-0.009780	0.009780	0.009780	-0.005770	0.005770	0.005770
JES detector and modelling (2)	0.009780	-0.009780	0.009780	0.011540	-0.011540	0.011540
JES detector and modelling (3)	-0.009780	0.009780	0.009780	-0.000000	0.000000	0.000000
JES detector and modelling (4)	0.009780	-0.009780	0.009780	-0.011540	-0.011540	0.011540
JES eta inter-calibration (modelling term)	-0.264060	0.264060	0.264060	-0.173100	0.173100	0.173100
JES eta inter-calibration (stat. term)	-0.009780	0.009780	0.009780	-0.005770	0.005770	0.005770
JES flavour composition	-0.000000	0.000000	0.000000	-0.005770	0.005770	0.005770
JES flavour response	-0.009780	-0.009780	0.009780	0.005770	-0.005770	0.005770
JES modelling/theory (1)	-0.127140	-0.127140	0.127140	-0.080780	-0.080780	0.080780
JES modelling/theory (2)	0.009780	-0.009780	0.009780	0.011540	-0.011540	0.011540
JES modelling/theory (3)	0.009780	-0.009780	0.009780	0.011540	-0.011540	0.011540
JES modelling/theory (4)	0.009780	0.009780	0.009780	0.005770	0.005770	0.005770

Continued on next page

Table 30: Systematic uncertainties of the fiducial cross sections $\sigma_{\text{fid}}(t)$ and $\sigma_{\text{fid}}(\bar{t})$.

	$\sigma_{\text{fid}}(t)$			$\sigma_{\text{fid}}(\bar{t})$		
	up	down	sym.	up	down	sym.
JES pile-up (mu)	0.009780	-0.009780	0.009780	0.005770	-0.005770	0.005770
JES pile-up (n-vertices)	0.009780	0.009780	0.009780	0.005770	0.005770	0.005770
JES pile-up (pT term)	0.019560	-0.019560	0.019560	0.005770	-0.005770	0.005770
JES pile-up (rho term)	-0.009780	0.009780	0.009780	-0.017310	-0.017310	0.017310
JES punch through	-0.009780	-0.009780	0.009780	-0.011540	-0.011540	0.011540
JES single-particle	-0.009780	0.009780	0.009780	-0.011540	0.011540	0.011540
JES statistics (1)	-0.009780	0.009780	0.009780	-0.011540	0.011540	0.011540
JES statistics (2)	0.009780	-0.009780	0.009780	0.005770	-0.005770	0.005770
JES statistics (3)	0.019560	-0.019560	0.019560	0.011540	-0.011540	0.011540
JES statistics (4)	-0.009780	0.009780	0.009780	-0.011540	0.011540	0.011540
Jet reconstruction efficiency	0.009780	0.009780	0.009780	0.005770	0.005770	0.005770
Lepton ID SF	-0.127140	-0.127140	0.127140	-0.080780	-0.080780	0.080780
Lepton Reco SF	-0.029340	-0.029340	0.029340	-0.005770	-0.005770	0.005770
Lepton TriggerSF	-0.136920	-0.136920	0.136920	-0.080780	-0.080780	0.080780
Luminosity	0.185820	-0.185820	0.185820	0.109630	-0.109630	0.109630
Muon momentum resolution (id)	-0.000000	-0.000000	0.000000	-0.011540	-0.011540	0.011540
Muon momentum scale	-0.009780	0.009780	0.009780	-0.005770	-0.005770	0.005770
Muon momentum smearing resolution	-0.009780	-0.009780	0.009780	-0.005770	-0.005770	0.005770
PDF	0.000000	0.000000	0.083560	0.000000	0.000000	0.084801
Possible polarization nonlinearity	0.000000	0.000000	0.000000	0.000000	0.000000	0.000000
Radiation	0.000000	0.000000	0.000000	0.000000	0.000000	0.000000
Template Statistics	0.000000	0.000000	0.000000	0.000000	0.000000	0.000000
Top Mass	0.000000	0.000000	0.000000	0.000000	0.000000	0.000000
Top-quark background norm.	0.000000	0.000000	0.000000	0.000000	0.000000	0.000000
W+heavy-jets flavour composition	0.000000	0.000000	0.000000	0.000000	0.000000	0.000000
W+jets norm.	0.000000	0.000000	0.000000	0.000000	0.000000	0.000000
W+jets shape modelling	0.000000	0.000000	0.000000	0.000000	0.000000	0.000000

Continued on next page

Table 30: Systematic uncertainties of the fiducial cross sections $\sigma_{\text{fid}}(t)$ and $\sigma_{\text{fid}}(\bar{t})$.

	$\sigma_{\text{fid}}(t)$			$\sigma_{\text{fid}}(\bar{t})$		
	up	down	sym.	up	down	sym.
Z-jets normalization	0.000000	0.000000	0.019560	0.000000	0.000000	0.017310
t-channel NLO modelling	0.000000	0.000000	0.000000	0.000000	0.000000	0.000000
t-channel LO modelling	0.000000	0.000000	0.000000	0.000000	0.000000	0.000000
t-channel LO/NLO modelling	0.000000	0.000000	0.000000	0.000000	0.000000	0.000000
t-channel colour reconnection	0.000000	0.000000	0.000000	0.000000	0.000000	0.000000
t-channel hadronization	-0.107580	-0.107580	0.107580	-0.046160	-0.046160	0.046160
t-channel scale variation	0.195600	-0.195600	0.195600	0.098090	-0.098090	0.098090
t-channel top-quark finite width effect	0.000000	0.000000	0.000000	0.000000	0.000000	0.000000
t-channel underlying event	0.000000	0.000000	0.000000	0.000000	0.000000	0.000000
tq NLO matching method	0.048900	0.048900	0.048900	0.017310	0.017310	0.017310
ttbar NLO modelling	-0.205380	-0.205380	0.205380	-0.248110	-0.248110	0.248110
ttbar hadronization	0.078240	0.078240	0.078240	0.000000	0.000000	0.144250
ttbar scale variation	0.009780	0.009780	0.009780	0.011540	0.011540	0.011540

Table 30: Systematic uncertainties of the fiducial cross sections $\sigma_{\text{fid}}(t)$ and $\sigma_{\text{fid}}(\bar{t})$.

	a_{010}			a_{020}		
	up	down	sym.	up	down	sym.
BTAG b-tag	-0.0003	0.0003	0.0003	-0.0001	0.0001	0.0001
BTAG c-tag	0.0008	-0.0009	0.0008	0.0004	-0.0004	0.0004
BTAG miss-tag	0.0000	0.0001	0.0001	0.0003	-0.0004	0.0003
Diboson normalization	-0.0001	0.0001	0.0001	0.0000	0.0000	0.0000
Electron energy resolution	-0.0024	-0.0028	0.0026	0.0024	0.0019	0.0021
Electron energy scale	0.0015	-0.0042	0.0031	0.0018	0.0003	0.0013
Etmiss cell-out + soft jet resolution	-0.0005	-0.0015	0.0011	-0.0001	0.0009	0.0007
Etmiss cell-out + soft jet scale	-0.0003	-0.0008	0.0006	0.0017	-0.0005	0.0013
JER	0.0000	0.0000	0.0000	0.0000	0.0000	0.0000
JER Jet energy resolution	-0.0043	-0.0043	0.0043	0.0082	0.0082	0.0082
JES Jet vertex fraction	0.0004	0.0011	0.0008	-0.0004	-0.0008	0.0006
JES b-tagging	-0.0010	0.0002	0.0007	-0.0013	0.0025	0.0020
JES detector (1)	-0.0004	0.0002	0.0003	-0.0008	0.0006	0.0007
JES detector (2)	0.0005	0.0000	0.0003	-0.0004	-0.0001	0.0003
JES detector (3)	0.0001	0.0000	0.0001	-0.0003	0.0001	0.0002
JES detector and modelling (1)	0.0001	0.0005	0.0004	-0.0008	0.0003	0.0006
JES detector and modelling (2)	-0.0005	0.0006	0.0005	-0.0001	-0.0005	0.0004
JES detector and modelling (3)	0.0000	0.0000	0.0000	0.0006	-0.0002	0.0005
JES detector and modelling (4)	0.0001	0.0000	0.0000	0.0000	0.0000	0.0000
JES eta inter-calibration (modelling term)	-0.0012	0.0020	0.0017	0.0029	-0.0032	0.0031
JES eta inter-calibration (stat. term)	0.0002	0.0001	0.0002	-0.0002	0.0001	0.0001
JES flavour composition	-0.0010	0.0016	0.0013	0.0034	-0.0019	0.0027
JES flavour response	0.0015	0.0003	0.0011	-0.0014	0.0011	0.0013
JES modelling/theory (1)	-0.0033	0.0024	0.0029	0.0022	0.0000	0.0015
JES modelling/theory (2)	-0.0001	0.0003	0.0002	0.0001	0.0000	0.0000
JES modelling/theory (3)	-0.0001	0.0005	0.0004	0.0006	-0.0006	0.0006
JES modelling/theory (4)	-0.0001	0.0003	0.0002	-0.0003	0.0000	0.0002

Continued on next page

Table 31: Systematic uncertainties of the angular coefficients a_{010} and a_{020}.

	a_{010}			a_{020}		
	up	down	sym.	up	down	sym.
JES pile-up (mu)	0.0011	-0.0014	0.0012	-0.0008	0.0006	0.0007
JES pile-up (n-vertices)	0.0001	0.0016	0.0011	0.0001	-0.0013	0.0009
JES pile-up (pT term)	0.0002	0.0002	0.0002	0.0003	0.0013	0.0009
JES pile-up (rho term)	-0.0010	0.0019	0.0015	0.0006	-0.0007	0.0006
JES punch through	0.0000	0.0000	0.0000	0.0000	0.0001	0.0001
JES single-particle	0.0000	0.0000	0.0000	0.0000	0.0000	0.0000
JES statistics (1)	0.0001	0.0015	0.0011	0.0009	-0.0013	0.0011
JES statistics (2)	0.0001	0.0001	0.0001	0.0001	0.0000	0.0001
JES statistics (3)	-0.0003	0.0004	0.0003	0.0009	-0.0006	0.0008
JES statistics (4)	-0.0001	0.0000	0.0001	-0.0004	0.0005	0.0004
Jet reconstruction efficiency	0.0001	0.0001	0.0001	0.0000	0.0000	0.0000
Lepton ID SF	-0.0001	0.0001	0.0001	0.0002	-0.0002	0.0002
Lepton Reco SF	0.0000	0.0000	0.0000	0.0001	-0.0001	0.0001
Lepton TriggerSF	-0.0004	0.0004	0.0004	0.0002	-0.0002	0.0002
Luminosity	0.0000	0.0000	0.0000	0.0000	0.0000	0.0000
Muon momentum resolution (id)	-0.0001	-0.0001	0.0001	-0.0002	-0.0002	0.0002
Muon momentum scale	0.0005	-0.0005	0.0005	-0.0002	0.0003	0.0002
Muon momentum smearing res.	0.0002	0.0002	0.0002	0.0004	0.0004	0.0004
PDF	0.0027	0.0027	0.0027	0.0023	0.0023	0.0023
Possible polarization nonlinearity	0.0000	0.0000	0.0000	0.0000	0.0000	0.0000
Radiation	0.0000	0.0000	0.0000	0.0000	0.0000	0.0000
Template Statistics	0.0000	0.0000	0.0000	0.0000	0.0000	0.0000
Top Mass	0.0000	0.0000	0.0000	0.0000	0.0000	0.0000
Top-quark background norm.	-0.0001	0.0001	0.0001	0.0000	0.0000	0.0000
W+heavy-jets flavour composition	-0.0017	0.0030	0.0024	-0.0012	0.0023	0.0018
W+jets norm.	0.0001	-0.0001	0.0001	0.0000	0.0000	0.0000
W+jets shape modelling	0.0016	0.0016	0.0016	-0.0010	-0.0010	0.0010

Continued on next page

Table 31: Systematic uncertainties of the angular coefficients a_{010} and a_{020}.

	a_{010}			a_{020}		
	up	down	sym.	up	down	sym.
Z-jets normalization	0.0006	-0.0006	0.0006	0.0008	-0.0008	0.0008
t-channel NLO modelling	-0.0026	-0.0026	0.0026	0.0045	0.0045	0.0045
t-channel LO model.	0.0013	0.0013	0.0013	-0.0042	-0.0042	0.0042
t-channel LO/NLO modelling	-0.0049	-0.0049	0.0049	0.0053	0.0053	0.0053
t-channel colour reconnection	-0.0018	-0.0018	0.0018	0.0003	0.0003	0.0003
t-channel hadronization	-0.0062	-0.0062	0.0062	-0.0002	-0.0002	0.0002
t-channel scale variation	0.0023	-0.0051	0.0039	0.0003	-0.0002	0.0003
t-channel top-quark finite width effect	0.0003	0.0003	0.0003	-0.0006	-0.0006	0.0006
t-channel underlying event	0.0010	0.0010	0.0010	-0.0014	-0.0014	0.0014
tq NLO matching method	0.0000	0.0000	0.0000	0.0000	0.0000	0.0000
ttbar NLO modelling	0.0018	0.0018	0.0018	-0.0020	-0.0020	0.0020
ttbar hadronization	-0.0003	-0.0003	0.0003	-0.0029	-0.0029	0.0029
ttbar scale variation	0.0010	-0.0019	0.0015	-0.0019	0.0023	0.0021

Table 31: Systematic uncertainties of the angular coefficients a_{010} and a_{020}.

	a_{100}			a_{110}		
	up	down	sym.	up	down	sym.
BTAG b-tag	0.0005	-0.0005	0.0005	-0.0002	0.0002	0.0002
BTAG c-tag	-0.0007	0.0008	0.0008	-0.0004	0.0005	0.0004
BTAG miss-tag	0.0000	0.0000	0.0000	0.0000	0.0000	0.0000
Diboson normalization	0.0000	0.0000	0.0000	0.0001	-0.0001	0.0001
Electron energy resolution	-0.0007	-0.0004	0.0006	0.0014	0.0014	0.0014
Electron energy scale	0.0007	-0.0024	0.0018	-0.0001	0.0019	0.0014
Etmiss cell-out + soft jet resolution	-0.0005	-0.0010	0.0008	0.0009	0.0013	0.0011
Etmiss cell-out + soft jet scale	-0.0006	-0.0002	0.0004	0.0008	-0.0003	0.0006
JER	0.0000	0.0000	0.0000	0.0000	0.0000	0.0000
JER Jet energy resolution	0.0009	0.0009	0.0009	0.0028	0.0028	0.0028
JES Jet vertex fraction	0.0003	0.0010	0.0007	-0.0006	-0.0014	0.0010
JES b-tagging	0.0006	-0.0018	0.0013	-0.0016	0.0031	0.0024
JES detector (1)	-0.0003	-0.0003	0.0003	-0.0004	-0.0002	0.0003
JES detector (2)	0.0002	-0.0001	0.0002	-0.0002	-0.0001	0.0002
JES detector (3)	0.0001	-0.0002	0.0002	-0.0001	0.0000	0.0000
JES detector and modelling (1)	-0.0003	-0.0004	0.0004	-0.0005	-0.0008	0.0006
JES detector and modelling (2)	-0.0002	-0.0004	0.0003	-0.0001	-0.0001	0.0001
JES detector and modelling (3)	-0.0003	-0.0002	0.0003	0.0002	-0.0001	0.0002
JES detector and modelling (4)	0.0001	-0.0001	0.0001	0.0000	0.0000	0.0000
JES eta inter-calibration (modelling term)	-0.0030	0.0028	0.0029	0.0059	-0.0073	0.0067
JES eta inter-calibration (stat. term)	-0.0009	-0.0002	0.0007	0.0003	-0.0012	0.0009
JES flavour composition	-0.0034	0.0024	0.0029	0.0039	-0.0047	0.0043
JES flavour response	0.0011	-0.0018	0.0015	-0.0040	0.0019	0.0031
JES modelling/theory (1)	-0.0036	0.0017	0.0028	0.0041	-0.0031	0.0037
JES modelling/theory (2)	-0.0003	0.0001	0.0002	-0.0002	0.0000	0.0001
JES modelling/theory (3)	-0.0005	0.0003	0.0004	0.0001	-0.0002	0.0002
JES modelling/theory (4)	-0.0001	0.0000	0.0001	-0.0001	-0.0001	0.0001

Continued on next page

Table 32: Systematic uncertainties of the angular coefficients a_{100} and a_{110}.

	a_{100}			a_{110}		
	up	down	sym.	up	down	sym.
JES pile-up (mu)	-0.0001	-0.0013	0.0009	-0.0024	0.0027	0.0025
JES pile-up (n-vertices)	0.0005	-0.0002	0.0004	-0.0001	-0.0014	0.0010
JES pile-up (pT term)	-0.0003	-0.0009	0.0007	-0.0005	0.0004	0.0005
JES pile-up (rho term)	-0.0017	0.0007	0.0013	0.0023	-0.0027	0.0025
JES punch through	-0.0001	-0.0001	0.0001	0.0000	0.0000	0.0000
JES single-particle	-0.0001	0.0000	0.0001	0.0000	0.0000	0.0000
JES statistics (1)	-0.0015	0.0006	0.0011	0.0009	-0.0024	0.0018
JES statistics (2)	-0.0001	-0.0001	0.0001	-0.0001	0.0000	0.0001
JES statistics (3)	-0.0008	0.0003	0.0006	0.0000	-0.0006	0.0004
JES statistics (4)	0.0000	-0.0003	0.0002	-0.0002	-0.0001	0.0002
Jet reconstruction efficiency	0.0001	0.0001	0.0001	-0.0002	-0.0002	0.0002
Lepton ID SF	-0.0001	0.0001	0.0001	0.0001	-0.0001	0.0001
Lepton Reco SF	0.0000	0.0000	0.0000	0.0000	0.0000	0.0000
Lepton TriggerSF	0.0001	-0.0001	0.0001	0.0001	-0.0001	0.0001
Luminosity	0.0000	0.0000	0.0000	0.0000	0.0000	0.0000
Muon momentum resolution (id)	-0.0001	-0.0001	0.0001	-0.0001	-0.0001	0.0001
Muon momentum scale	0.0002	-0.0005	0.0004	-0.0003	0.0005	0.0004
Muon momentum smearing resolution	-0.0005	-0.0005	0.0005	-0.0004	-0.0004	0.0004
PDF	0.0023	0.0023	0.0023	0.0025	0.0025	0.0025
Possible polarization nonlinearity	0.0008	0.0003	0.0006	0.0005	0.0002	0.0004
Radiation	0.0000	0.0000	0.0000	0.0000	0.0000	0.0000
Template Statistics	0.0000	0.0000	0.0000	0.0000	0.0000	0.0000
Top Mass	0.0000	0.0000	0.0000	0.0000	0.0000	0.0000
Top-quark background norm.	0.0000	0.0000	0.0000	0.0000	0.0000	0.0000
W+heavy-jets flavour composition	0.0019	-0.0036	0.0029	0.0010	-0.0019	0.0015
W+jets norm.	-0.0001	0.0001	0.0001	0.0001	-0.0001	0.0001
W+jets shape modelling	0.0042	0.0042	0.0042	-0.0014	-0.0014	0.0014

Continued on next page

Table 32: Systematic uncertainties of the angular coefficients a_{100} and a_{110}.

	a_{100}			a_{110}		
	up	down	sym.	up	down	sym.
Z-jets normalization	0.0001	-0.0001	0.0001	0.0006	-0.0006	0.0006
t-channel NLO modelling	-0.0055	-0.0055	0.0055	0.0000	0.0000	0.0000
t-channel LO modelling	0.0005	0.0005	0.0005	-0.0047	-0.0047	0.0047
t-channel LO/NLO modelling	-0.0035	-0.0035	0.0035	0.0004	0.0004	0.0004
t-channel colour reconnection	-0.0020	-0.0020	0.0020	0.0022	0.0022	0.0022
t-channel hadronization	-0.0025	-0.0025	0.0025	-0.0009	-0.0009	0.0009
t-channel scale variation	0.0050	-0.0066	0.0058	-0.0052	0.0055	0.0053
t-channel top-quark finite width effect	0.0001	0.0001	0.0001	-0.0007	-0.0007	0.0007
t-channel underlying event	0.0018	0.0018	0.0018	-0.0022	-0.0022	0.0022
tq NLO matching method	0.0000	0.0000	0.0000	0.0000	0.0000	0.0000
ttbar NLO modelling	0.0036	0.0036	0.0036	-0.0037	-0.0037	0.0037
ttbar hadronization	0.0023	0.0023	0.0023	-0.0029	-0.0029	0.0029
ttbar scale variation	-0.0002	-0.0008	0.0005	-0.0017	0.0022	0.0019

Table 32: Systematic uncertainties of the angular coefficients a_{100} and a_{110}.

	a_{120}		
	up	down	sym.
BTAG b-tag	-0.0001	0.0001	0.0001
BTAG c-tag	0.0012	-0.0014	0.0013
BTAG miss-tag	-0.0002	0.0002	0.0002
Diboson normalization	0.0000	0.0000	0.0000
Electron energy resolution	-0.0029	-0.0029	0.0029
Electron energy scale	-0.0021	-0.0014	0.0018
Etmiss cell-out + soft jet resolution	-0.0001	-0.0007	0.0005
Etmiss cell-out + soft jet scale	-0.0018	-0.0007	0.0014
JER	0.0000	0.0000	0.0000
JER Jet energy resolution	0.0010	0.0010	0.0010
JES Jet vertex fraction	0.0002	0.0005	0.0004
JES b-tagging	0.0004	-0.0007	0.0006
JES detector (1)	0.0003	-0.0010	0.0008
JES detector (2)	0.0004	-0.0007	0.0006
JES detector (3)	0.0001	-0.0001	0.0001
JES detector and modelling (1)	0.0010	-0.0006	0.0008
JES detector and modelling (2)	-0.0004	0.0007	0.0006
JES detector and modelling (3)	-0.0006	-0.0004	0.0005
JES detector and modelling (4)	-0.0001	-0.0001	0.0001
JES eta inter-calibration (modelling term)	-0.0013	0.0020	0.0017
JES eta inter-calibration (stat. term)	0.0006	-0.0003	0.0005
JES flavour composition	-0.0017	0.0021	0.0019
JES flavour response	0.0008	-0.0005	0.0007
JES modelling/theory (1)	-0.0028	0.0008	0.0020
JES modelling/theory (2)	-0.0006	0.0000	0.0004
JES modelling/theory (3)	-0.0007	-0.0002	0.0005
JES modelling/theory (4)	-0.0001	0.0000	0.0001

Continued on next page

Table 33: Systematic uncertainties of the angular coefficient a_{120}.

	a_{120}		
	up	down	sym.
JES pile-up (mu)	0.0018	-0.0007	0.0014
JES pile-up (n-vertices)	-0.0002	0.0013	0.0009
JES pile-up (pT term)	-0.0003	-0.0012	0.0009
JES pile-up (rho term)	-0.0004	0.0007	0.0006
JES punch through	0.0000	-0.0001	0.0001
JES single-particle	0.0000	0.0000	0.0000
JES statistics (1)	0.0004	0.0009	0.0007
JES statistics (2)	-0.0004	-0.0001	0.0003
JES statistics (3)	-0.0010	0.0001	0.0007
JES statistics (4)	0.0000	-0.0009	0.0006
Jet reconstruction efficiency	0.0000	0.0000	0.0000
Lepton ID SF	-0.0001	0.0001	0.0001
Lepton Reco SF	0.0000	0.0000	0.0000
Lepton TriggerSF	-0.0001	0.0001	0.0001
Luminosity	0.0000	0.0000	0.0000
Muon momentum resolution (id)	-0.0002	-0.0002	0.0002
Muon momentum scale	0.0002	-0.0002	0.0002
Muon momentum smearing resolution	-0.0007	-0.0007	0.0007
PDF	0.0029	0.0029	0.0029
Possible polarization nonlinearity	-0.0008	-0.0003	0.0006
Radiation	0.0000	0.0000	0.0000
Template Statistics	0.0000	0.0000	0.0000
Top Mass	0.0000	0.0000	0.0000
Top-quark background norm.	0.0000	0.0000	0.0000
W+heavy-jets flavour composition	-0.0025	0.0047	0.0037
W+jets norm.	-0.0001	0.0001	0.0001
W+jets shape modelling	0.0006	0.0006	0.0006

Continued on next page

Table 33: Systematic uncertainties of the angular coefficient a_{120}.

	a_{120}		
	up	down	sym.
Z-jets normalization	-0.0002	0.0002	0.0002
t-channel NLO modelling	-0.0012	-0.0012	0.0012
t-channel LO modelling	0.0029	0.0029	0.0029
t-channel LO/NLO modelling	-0.0030	-0.0030	0.0030
t-channel colour reconnection	-0.0014	-0.0014	0.0014
t-channel hadronization	-0.0044	-0.0044	0.0044
t-channel scale variation	0.0054	0.0003	0.0038
t-channel top-quark finite width effect	0.0000	0.0000	0.0000
t-channel underlying event	0.0033	0.0033	0.0033
tq NLO matching method	0.0000	0.0000	0.0000
ttbar NLO modelling	0.0014	0.0014	0.0014
ttbar hadronization	0.0015	0.0015	0.0015
ttbar scale variation	0.0047	-0.0021	0.0036

Table 33: Systematic uncertainties of the angular coefficient a_{120}.

	$\mathrm{Re}(a_{111})$			$\mathrm{Im}(a_{111})$		
	up	down	sym.	up	down	sym.
BTAG b-tag	0.0001	-0.0001	0.0001	0.0000	0.0000	0.0000
BTAG c-tag	0.0005	-0.0006	0.0006	-0.0001	0.0001	0.0001
BTAG miss-tag	0.0006	-0.0007	0.0007	0.0000	0.0000	0.0000
Diboson normalization	0.0001	-0.0001	0.0001	0.0000	0.0000	0.0000
Electron energy resolution	-0.0005	-0.0014	0.0011	0.0001	0.0000	0.0001
Electron energy scale	0.0027	-0.0036	0.0032	0.0003	-0.0002	0.0002
Etmiss cell-out + soft jet res.	0.0007	0.0001	0.0005	0.0001	0.0007	0.0005
Etmiss cell-out + soft jet scale	0.0000	-0.0002	0.0001	-0.0002	0.0002	0.0002
JER	0.0000	0.0000	0.0000	0.0000	0.0000	0.0000
JER Jet energy resolution	0.0003	0.0003	0.0003	-0.0006	-0.0006	0.0006
JES Jet vertex fraction	0.0006	-0.0002	0.0004	0.0001	-0.0003	0.0002
JES b-tagging	0.0014	-0.0015	0.0015	0.0000	0.0002	0.0001
JES detector (1)	-0.0004	0.0008	0.0006	0.0003	0.0003	0.0003
JES detector (2)	-0.0002	0.0002	0.0002	0.0002	0.0001	0.0001
JES detector (3)	-0.0003	0.0000	0.0002	0.0000	0.0000	0.0000
JES detector and modelling (1)	0.0002	0.0005	0.0004	0.0005	0.0002	0.0004
JES detector and modelling (2)	0.0000	0.0001	0.0001	0.0001	0.0006	0.0004
JES detector and modelling (3)	0.0001	-0.0003	0.0002	0.0000	0.0000	0.0000
JES detector and modelling (4)	0.0003	0.0000	0.0002	0.0000	0.0000	0.0000
JES eta inter-calibr. (mod. term)	-0.0062	0.0072	0.0067	0.0008	0.0000	0.0006
JES eta inter-calibr. (stat. term)	-0.0008	0.0010	0.0009	0.0006	0.0002	0.0004
JES flavour composition	-0.0042	0.0030	0.0036	0.0012	0.0001	0.0009
JES flavour response	0.0024	-0.0033	0.0029	0.0002	0.0009	0.0007
JES modelling/theory (1)	-0.0039	0.0029	0.0034	0.0013	0.0005	0.0010
JES modelling/theory (2)	-0.0001	0.0003	0.0002	-0.0001	0.0000	0.0000
JES modelling/theory (3)	0.0003	0.0001	0.0002	0.0001	0.0000	0.0001
JES modelling/theory (4)	-0.0003	0.0001	0.0002	0.0000	0.0000	0.0000

Continued on next page

Table 34: Systematic uncertainties of the angular coefficients $\mathrm{Re}(a_{111})$ and $\mathrm{Im}(a_{111})$.

	Re(a_{111})			Im(a_{111})		
	up	down	sym.	up	down	sym.
JES pile-up (mu)	0.0016	-0.0018	0.0017	0.0006	0.0004	0.0005
JES pile-up (n-vertices)	0.0002	-0.0007	0.0005	0.0001	0.0006	0.0004
JES pile-up (pT term)	-0.0004	0.0003	0.0004	0.0001	0.0004	0.0003
JES pile-up (rho term)	-0.0020	0.0024	0.0022	0.0008	-0.0001	0.0006
JES punch through	-0.0001	-0.0001	0.0001	0.0000	0.0000	0.0000
JES single-particle	0.0000	0.0000	0.0000	0.0000	0.0000	0.0000
JES statistics (1)	0.0000	0.0007	0.0005	0.0006	0.0001	0.0004
JES statistics (2)	0.0003	0.0000	0.0002	0.0000	0.0000	0.0000
JES statistics (3)	0.0003	-0.0002	0.0003	0.0001	0.0000	0.0001
JES statistics (4)	-0.0004	0.0003	0.0004	0.0000	0.0001	0.0001
Jet reconstruction efficiency	0.0001	0.0001	0.0001	0.0000	0.0000	0.0000
Lepton ID SF	-0.0001	0.0001	0.0001	0.0000	0.0000	0.0000
Lepton Reco SF	0.0000	0.0000	0.0000	0.0000	0.0000	0.0000
Lepton TriggerSF	-0.0003	0.0003	0.0003	0.0000	0.0000	0.0000
Luminosity	0.0000	0.0000	0.0000	0.0000	0.0000	0.0000
Muon momentum resolution (id)	0.0002	0.0002	0.0002	-0.0001	-0.0001	0.0001
Muon momentum scale	0.0004	-0.0005	0.0004	0.0000	-0.0001	0.0001
Muon momentum smearing res.	0.0001	0.0001	0.0001	-0.0002	-0.0002	0.0002
PDF	0.0028	0.0028	0.0028	0.0006	0.0006	0.0006
Possible polarization nonlinearity	-0.0012	-0.0005	0.0009	0.0000	0.0000	0.0000
Radiation	0.0000	0.0000	0.0000	0.0000	0.0000	0.0000
Template Statistics	0.0000	0.0000	0.0000	0.0000	0.0000	0.0000
Top Mass	0.0000	0.0000	0.0000	0.0000	0.0000	0.0000
Top-quark background norm.	0.0000	0.0000	0.0000	0.0000	0.0000	0.0000
W+heavy-jets flavour composition	-0.0014	0.0025	0.0020	0.0000	0.0000	0.0000
W+jets norm.	-0.0001	0.0001	0.0001	0.0000	0.0000	0.0000
W+jets shape modelling	0.0012	0.0012	0.0012	0.0000	0.0000	0.0000

Continued on next page

Table 34: Systematic uncertainties of the angular coefficients Re(a_{111}) and Im(a_{111}).

	Re(a_{111})			Im(a_{111})		
	up	down	sym.	up	down	sym.
Z-jets normalization	-0.0001	0.0001	0.0001	0.0001	-0.0001	0.0001
t-channel NLO modelling	-0.0027	-0.0027	0.0027	0.0007	0.0007	0.0007
t-channel LO modelling	0.0063	0.0063	0.0063	-0.0015	-0.0015	0.0015
t-channel LO/NLO modelling	-0.0027	-0.0027	0.0027	0.0001	0.0001	0.0001
t-channel colour reconnection	-0.0013	-0.0013	0.0013	0.0010	0.0010	0.0010
t-channel hadronization	-0.0018	-0.0018	0.0018	-0.0014	-0.0014	0.0014
t-channel scale variation	0.0017	-0.0076	0.0055	-0.0001	0.0011	0.0008
t-channel top-quark finite width eff.	0.0009	0.0009	0.0009	-0.0003	-0.0003	0.0003
t-channel underlying event	-0.0012	-0.0012	0.0012	-0.0002	-0.0002	0.0002
tq NLO matching method	0.0000	0.0000	0.0000	0.0000	0.0000	0.0000
ttbar NLO modelling	0.0022	0.0022	0.0022	0.0006	0.0006	0.0006
ttbar hadronization	0.0005	0.0005	0.0005	0.0007	0.0007	0.0007
ttbar scale variation	0.0003	-0.0006	0.0005	-0.0001	0.0002	0.0002

Table 34: Systematic uncertainties of the angular coefficients Re(a_{111}) and Im(a_{111}).

	Re(a_{121})			Im(a_{121})		
	up	down	sym.	up	down	sym.
BTAG b-tag	0.0003	-0.0003	0.0003	0.0001	-0.0001	0.0001
BTAG c-tag	-0.0010	0.0011	0.0011	-0.0002	0.0003	0.0002
BTAG miss-tag	-0.0006	0.0006	0.0006	0.0002	-0.0001	0.0002
Diboson normalization	0.0001	-0.0001	0.0001	0.0000	0.0000	0.0000
Electron energy resolution	0.0016	0.0017	0.0016	-0.0004	0.0000	0.0003
Electron energy scale	0.0008	0.0002	0.0006	-0.0001	-0.0003	0.0002
Etmiss cell-out + soft jet resolution	0.0016	0.0010	0.0013	-0.0003	0.0006	0.0005
Etmiss cell-out + soft jet scale	0.0008	-0.0008	0.0008	-0.0001	-0.0006	0.0004
JER	0.0000	0.0000	0.0000	0.0000	0.0000	0.0000
JER Jet energy resolution	-0.0027	-0.0027	0.0027	0.0023	0.0023	0.0023
JES Jet vertex fraction	-0.0005	0.0001	0.0003	0.0000	0.0003	0.0002
JES b-tagging	-0.0008	0.0010	0.0009	0.0002	0.0001	0.0002
JES detector (1)	-0.0010	0.0003	0.0007	0.0001	-0.0002	0.0002
JES detector (2)	-0.0002	-0.0003	0.0003	0.0002	-0.0002	0.0002
JES detector (3)	-0.0004	0.0001	0.0003	0.0001	0.0000	0.0001
JES detector and modelling (1)	-0.0012	-0.0001	0.0009	-0.0002	0.0000	0.0001
JES detector and modelling (2)	0.0003	-0.0009	0.0007	0.0000	0.0000	0.0000
JES detector and modelling (3)	0.0002	-0.0006	0.0005	-0.0001	0.0001	0.0001
JES detector and modelling (4)	-0.0004	0.0000	0.0003	0.0001	0.0001	0.0001
JES eta inter-calibration (modelling term)	-0.0004	-0.0011	0.0008	0.0000	0.0000	0.0000
JES eta inter-calibration (stat. term)	-0.0010	0.0001	0.0007	-0.0001	0.0000	0.0001
JES flavour composition	0.0006	-0.0002	0.0005	0.0005	0.0002	0.0004
JES flavour response	-0.0013	0.0001	0.0009	0.0006	-0.0005	0.0006
JES modelling/theory (1)	0.0018	0.0000	0.0013	0.0004	-0.0002	0.0003
JES modelling/theory (2)	-0.0001	-0.0005	0.0003	-0.0001	0.0001	0.0001
JES modelling/theory (3)	0.0008	-0.0012	0.0010	0.0000	0.0002	0.0001
JES modelling/theory (4)	-0.0001	0.0000	0.0001	0.0001	0.0000	0.0001

Continued on next page

Table 35: Systematic uncertainties of the angular coefficients Re(a_{121}) and Im(a_{121}).

	Re(a_{121})			Im(a_{121})		
	up	down	sym.	up	down	sym.
JES pile-up (mu)	-0.0006	0.0004	0.0005	-0.0002	0.0005	0.0004
JES pile-up (n-vertices)	0.0010	-0.0020	0.0015	0.0004	-0.0001	0.0003
JES pile-up (pT term)	-0.0005	-0.0010	0.0007	0.0002	-0.0001	0.0002
JES pile-up (rho term)	0.0004	-0.0005	0.0005	-0.0006	0.0003	0.0005
JES punch through	0.0000	0.0000	0.0000	0.0000	0.0000	0.0000
JES single-particle	0.0000	0.0000	0.0000	0.0000	0.0000	0.0000
JES statistics (1)	0.0002	-0.0012	0.0009	-0.0004	-0.0001	0.0003
JES statistics (2)	-0.0006	0.0000	0.0004	0.0001	0.0000	0.0001
JES statistics (3)	0.0005	-0.0011	0.0008	0.0000	0.0002	0.0001
JES statistics (4)	-0.0002	0.0000	0.0002	0.0001	-0.0001	0.0001
Jet reconstruction efficiency	-0.0001	-0.0001	0.0001	0.0000	0.0000	0.0000
Lepton ID SF	0.0003	-0.0003	0.0003	0.0000	0.0000	0.0000
Lepton Reco SF	0.0001	-0.0001	0.0001	0.0000	0.0000	0.0000
Lepton TriggerSF	0.0003	-0.0003	0.0003	0.0000	0.0000	0.0000
Luminosity	0.0000	0.0000	0.0000	0.0000	0.0000	0.0000
Muon momentum resolution (id)	-0.0001	-0.0001	0.0001	0.0000	0.0000	0.0000
Muon momentum scale	-0.0004	0.0004	0.0004	0.0001	0.0000	0.0001
Muon momentum smearing resolution	-0.0003	-0.0003	0.0003	0.0000	0.0000	0.0000
PDF	0.0034	0.0034	0.0034	0.0012	0.0012	0.0012
Possible polarization nonlinearity	0.0005	0.0002	0.0004	0.0000	0.0000	0.0000
Radiation	0.0000	0.0000	0.0000	0.0000	0.0000	0.0000
Template Statistics	0.0000	0.0000	0.0000	0.0000	0.0000	0.0000
Top Mass	0.0000	0.0000	0.0000	0.0000	0.0000	0.0000
Top-quark background norm.	0.0001	-0.0001	0.0001	0.0000	0.0000	0.0000
W+heavy-jets flavour composition	0.0029	-0.0054	0.0043	0.0007	-0.0013	0.0011
W+jets norm.	-0.0001	0.0001	0.0001	0.0000	0.0000	0.0000
W+jets shape modelling	-0.0018	-0.0018	0.0018	-0.0002	-0.0002	0.0002

Continued on next page

Table 35: Systematic uncertainties of the angular coefficients Re(a_{121}) and Im(a_{121}).

	Re(a_{121})			Im(a_{121})		
	up	down	sym.	up	down	sym.
Z-jets normalization	0.0002	-0.0002	0.0002	0.0000	0.0000	0.0000
t-channel NLO modelling	-0.0061	-0.0061	0.0061	-0.0024	-0.0024	0.0024
t-channel LO modelling	0.0017	0.0017	0.0017	-0.0009	-0.0009	0.0009
t-channel LO/NLO modelling	-0.0027	-0.0027	0.0027	-0.0008	-0.0008	0.0008
t-channel colour reconnection	0.0009	0.0009	0.0009	-0.0012	-0.0012	0.0012
t-channel hadronization	-0.0002	-0.0002	0.0002	-0.0002	-0.0002	0.0002
t-channel scale variation	-0.0020	0.0080	0.0059	0.0014	-0.0016	0.0015
t-channel top-quark finite width effect	0.0002	0.0002	0.0002	0.0000	0.0000	0.0000
t-channel underlying event	0.0034	0.0034	0.0034	0.0000	0.0000	0.0000
tq NLO matching method	0.0000	0.0000	0.0000	0.0000	0.0000	0.0000
ttbar NLO modelling	-0.0004	-0.0004	0.0004	-0.0010	-0.0010	0.0010
ttbar hadronization	0.0007	0.0007	0.0007	-0.0003	-0.0003	0.0003
ttbar scale variation	-0.0015	0.0015	0.0015	0.0000	0.0002	0.0001

Table 35: Systematic uncertainties of the angular coefficients Re(a_{121}) and Im(a_{121}).

Bibliography

[1] M. Aker et al. An improved upper limit on the neutrino mass from a direct kinematic method by KATRIN, 2019. arXiv: 1909.06048 [hep-ex].

[2] M. Tanabashi et al. Review of particle physics. *Phys. Rev. D*, 98:030001, Aug 2018.

[3] F. Englert and R. Brout. Broken Symmetry and the Mass of Gauge Vector Mesons. *Phys. Rev. Lett.*, 13:321–323, 1964.

[4] Peter W. Higgs. Broken symmetries, massless particles and gauge fields. *Phys. Lett.*, 12:132–133, 1964.

[5] Peter W. Higgs. Broken Symmetries and the Masses of Gauge Bosons. *Phys. Rev. Lett.*, 13:508–509, 1964. [,160(1964)].

[6] D. B. Chitwood et al. Improved measurement of the positive muon lifetime and determination of the Fermi constant. *Phys. Rev. Lett.*, 99:032001, 2007.

[7] ATLAS Collaboration. Observation of a new particle in the search for the Standard Model Higgs boson with the ATLAS detector at the LHC. *Phys. Lett. B*, 716:1, 2012.

[8] CMS Collaboration. Observation of a new boson at a mass of 125 GeV with the CMS experiment at the LHC. *Phys. Lett. B*, 716:30, 2012.

[9] ATLAS and CMS Collaborations. Combined Measurement of the Higgs Boson Mass in pp Collisions at $\sqrt{s} = 7$ and 8 TeV with the ATLAS and CMS Experiments. *Phys. Rev. Lett.*, 114:191803, 2015.

[10] Makoto Kobayashi and Toshihide Maskawa. CP Violation in the Renormalizable Theory of Weak Interaction. *Prog. Theor. Phys.*, 49:652–657, 1973.

[11] Richard D. Ball et al. Parton distributions from high-precision collider data. *Eur. Phys. J.*, C77(10):663, 2017.

[12] Fred L. Wilson. Fermi's theory of beta decay. *American Journal of Physics*, 36(12):1150–1160, 1968.

[13] K. G. Wilson and W. Zimmermann. Operator product expansions and composite field operators in the general framework of quantum field theory. *Commun. Math. Phys.*, 24:87–106, 1972.

[14] Steven Weinberg. Baryon and Lepton Nonconserving Processes. *Phys. Rev. Lett.*, 43:1566–1570, 1979.

[15] W. Buchmuller and D. Wyler. Effective Lagrangian Analysis of New Interactions and Flavor Conservation. *Nucl. Phys.*, B268:621–653, 1986.

[16] B. Grzadkowski, M. Iskrzynski, M. Misiak, and J. Rosiek. Dimension-Six Terms in the Standard Model Lagrangian. *JHEP*, 10:085, 2010.

[17] D. Barducci et al. Interpreting top-quark LHC measurements in the standard-model effective field theory, 2018. arXiv: 1802.07237 [hep-ph].

[18] J. A. Aguilar-Saavedra. Single top quark production at LHC with anomalous Wtb couplings. *Nucl. Phys.*, B804:160–192, 2008.

[19] J. A. Aguilar-Saavedra. A Minimal set of top anomalous couplings. *Nucl. Phys.*, B812:181–204, 2009.

[20] F. Abe et al. Observation of top quark production in $\bar{p}p$ collisions. *Phys. Rev. Lett.*, 74:2626–2631, 1995.

[21] S. Abachi et al. Observation of the top quark. *Phys. Rev. Lett.*, 74:2632–2637, 1995.

[22] Top Quark Mass Summary Plots. Technical Report ATL-PHYS-PUB-2019-020, CERN, Geneva, May 2019.

[23] ATLAS Collaboration. Direct top-quark decay width measurement in the $t\bar{t}$ lepton+jets channel at $\sqrt{s} = 8$ TeV with the ATLAS experiment. *Eur. Phys. J. C*, 78:129, 2018.

[24] Michal Czakon and Alexander Mitov. Top++: A Program for the Calculation of the Top-Pair Cross-Section at Hadron Colliders. *Comput. Phys. Commun.*, 185:2930, 2014.

[25] P. Kant, O. M. Kind, T. Kintscher, T. Lohse, T. Martini, S. Mlbitz, P. Rieck, and P. Uwer. HatHor for single top-quark production: Updated predictions and uncertainty estimates for single top-quark production in hadronic collisions. *Comput. Phys. Commun.*, 191:74–89, 2015.

[26] Georges Aad et al. Measurement of the $t\bar{t}$ production cross-section using $e\mu$ events with b-tagged jets in pp collisions at $\sqrt{s} = 7$ and 8 TeV with the ATLAS detector. *Eur. Phys. J.*, C74(10):3109, 2014. [Addendum: Eur. Phys. J.C76,no.11,642(2016)].

[27] Morad Aaboud et al. Measurement of the $t\bar{t}$ production cross-section using $e\mu$ events with b-tagged jets in pp collisions at $\sqrt{s}$=13 TeV with the ATLAS detector. *Phys. Lett.*, B761:136–157, 2016. [Erratum: Phys. Lett.B772,879(2017)].

[28] CMS Collaboration. Measurement of the $t\bar{t}$ production cross section in the $e\mu$ channel in proton–proton collisions at $\sqrt{s} = 7$ and 8 TeV. *JHEP*, 08:029, 2016.

[29] Albert M Sirunyan et al. Measurement of the $t\bar{t}$ production cross section, the top quark mass, and the strong coupling constant using dilepton events in pp collisions at $\sqrt{s} = 13$ TeV. *Eur. Phys. J.*, C79(5):368, 2019.

[30] Georges Aad et al. Comprehensive measurements of t-channel single top-quark production cross sections at $\sqrt{s} = 7$ TeV with the ATLAS detector. *Phys. Rev.*, D90(11):112006, 2014.

[31] ATLAS Collaboration. Fiducial, total and differential cross-section measurements of t-channel single top-quark production in pp collisions at 8 TeV using data collected by the ATLAS detector. *Eur. Phys. J. C*, 77:531, 2017.

[32] Morad Aaboud et al. Measurement of the inclusive cross-sections of single top-quark and top-antiquark t-channel production in pp collisions at $\sqrt{s} = 13$ TeV with the ATLAS detector. *JHEP*, 04:086, 2017.

[33] Serguei Chatrchyan et al. Measurement of the Single-Top-Quark t-Channel Cross Section in pp Collisions at $\sqrt{s} = 7$ TeV. *JHEP*, 12:035, 2012.

[34] Vardan Khachatryan et al. Measurement of the t-channel single-top-quark production cross section and of the $| V_{tb} |$ CKM matrix element in pp collisions at $\sqrt{s}$= 8 TeV. *JHEP*, 06:090, 2014.

[35] Albert M Sirunyan et al. Measurement of the single top quark and antiquark production cross sections in the t channel and their ratio in proton-proton collisions at $\sqrt{s} = 13$ TeV. 2018. arXiv: 1812.10514 [hep-ex].

[36] Georges Aad et al. Measurement of the production cross-section of a single top quark in association with a W boson at 8 TeV with the ATLAS experiment. *JHEP*, 01:064, 2016.

[37] Morad Aaboud et al. Measurement of the cross-section for producing a W boson in association with a single top quark in pp collisions at $\sqrt{s} = 13$ TeV with ATLAS. *JHEP*, 01:063, 2018.

[38] Serguei Chatrchyan et al. Observation of the associated production of a single top quark and a W boson in pp collisions at $\sqrt{s}$ =8 TeV. *Phys. Rev. Lett.*, 112(23):231802, 2014.

[39] Albert M Sirunyan et al. Measurement of the production cross section for single top quarks in association with W bosons in proton-proton collisions at $\sqrt{s} = 13$ TeV. *JHEP*, 10:117, 2018.

[40] Georges Aad et al. Evidence for single top-quark production in the s-channel in proton-proton collisions at $\sqrt{s}$ =8 TeV with the ATLAS detector using the Matrix Element Method. *Phys. Lett.*, B756:228–246, 2016.

[41] Vardan Khachatryan et al. Search for s channel single top quark production in pp collisions at $\sqrt{s} = 7$ and 8 TeV. *JHEP*, 09:027, 2016.

[42] Reinhard Schwienhorst, C. P. Yuan, Charles Mueller, and Qing-Hong Cao. Single top quark production and decay in the t-channel at next-to-leading order at the LHC. *Phys. Rev.*, D83:034019, 2011.

[43] ATLAS Collaboration. Probing the Wtb vertex structure in t-channel single-top-quark production and decay in pp collisions at $\sqrt{s} = 8$ TeV with the ATLAS detector. *JHEP*, 04:124, 2017.

[44] J. A. Aguilar-Saavedra and J. Bernabeu. W polarisation beyond helicity fractions in top quark decays. *Nucl. Phys.*, B840:349–378, 2010.

[45] Gordon L. Kane, G. A. Ladinsky, and C. P. Yuan. Using the Top Quark for Testing Standard Model Polarization and CP Predictions. *Phys. Rev.*, D45:124–141, 1992.

[46] Andrzej Czarnecki, Jurgen G. Korner, and Jan H. Piclum. Helicity fractions of W bosons from top quark decays at NNLO in QCD. *Phys. Rev.*, D81:111503, 2010.

[47] Joseph Boudreau, Carlos Escobar, James Mueller, Kevin Sapp, and Jun Su. Single top quark differential decay rate formulae including detector effects, 2013. arXiv: 1304.5639 [hep-ex].

[48] Joseph Boudreau, Carlos Escobar, James Mueller, and Jun Su. Deconvolving the detector in fourier space. *Journal of Physics: Conference Series*, 762:012041, oct 2016.

[49] CERN Service graphique. Overall view of the LHC. Vue d'ensemble du LHC. `https://cds.cern.ch/record/1708849`, Jun 2014. General Photo.

[50] ATLAS Collaboration. The ATLAS Experiment at the CERN Large Hadron Collider. *JINST*, 3:S08003, 2008.

[51] CMS Collaboration. The CMS experiment at the CERN LHC. *JINST*, 3:S08004, 2008.

[52] A. Augusto Alves, Jr. et al. The LHCb Detector at the LHC. *JINST*, 3:S08005, 2008.

[53] K. Aamodt et al. The ALICE experiment at the CERN LHC. *JINST*, 3:S08002, 2008.

[54] Esma Mobs. The cern accelerator complex. complexe des accélérateurs du cern. `https://cds.cern.ch/record/2197559`, July 2016. General Photo.

[55] Thomas Bayes. An essay towards solving a problem in the doctrine of chances. *Phil. Trans. Roy. Soc. Lond.*, 53:370–418, 1763.

[56] Johan Alwall, Michel Herquet, Fabio Maltoni, Olivier Mattelaer, and Tim Stelzer. MadGraph 5 : Going Beyond. *JHEP*, 06:128, 2011.

[57] J. Alwall, R. Frederix, S. Frixione, V. Hirschi, F. Maltoni, et al. The automated computation of tree-level and next-to-leading order differential cross sections, and their matching to parton shower simulations. *JHEP*, 07:079, 2014.

[58] Paolo Nason. A new method for combining NLO QCD with shower Monte Carlo algorithms. *JHEP*, 11:040, 2004.

[59] Stefano Frixione, Paolo Nason, and Carlo Oleari. Matching NLO QCD computations with Parton Shower simulations: the POWHEG method. *JHEP*, 11:070, 2007.

[60] Pierre Artoisenet, Rikkert Frederix, Olivier Mattelaer, and Robbert Rietkerk. Automatic spin-entangled decays of heavy resonances in Monte Carlo simulations. *JHEP*, 03:015, 2013.

[61] N. Davidson, G. Nanava, T. Przedzinski, E. Richter-Was, and Z. Was. Universal Interface of TAUOLA Technical and Physics Documentation. *Comput. Phys. Commun.*, 183:821–843, 2012.

[62] D. J. Lange. The EvtGen particle decay simulation package. *Nucl. Instrum. Meth. A*, 462:152, 2001.

[63] G. Corcella et al. HERWIG 6: an event generator for hadron emission reactions with interfering gluons (including supersymmetric processes). *JHEP*, 01:010, 2001.

[64] M. Bahr et al. Herwig++ Physics and Manual. *Eur. Phys. J. C*, 58:639, 2008.

[65] Johannes Bellm et al. Herwig 7.0/Herwig++ 3.0 release note. *Eur. Phys. J. C*, 76(4):196, 2016.

[66] Torbjörn Sjöstrand, Stefan Ask, Jesper R. Christiansen, Richard Corke, Nishita Desai, Philip Ilten, Stephen Mrenna, Stefan Prestel, Christine O. Ras-

mussen, and Peter Z. Skands. An Introduction to PYTHIA 8.2. *Comput. Phys. Commun.*, 191:159, 2015.

[67] ATLAS Collaboration. Measurement of the W boson polarisation in $t\bar{t}$ events from pp collisions at $\sqrt{s} = 8$ TeV in the lepton+jets channel with ATLAS. *Eur. Phys. J. C*, 77:264, 2017.

[68] ATLAS Collaboration. Erratum to: Measurement of the w boson polarisation in $t\bar{t}$ events from pp collisions at $\sqrt{s} = 8$ tev in the lepton + jets channel with atlas. *The European Physical Journal C*, 79(1):19, Jan 2019.

[69] ATLAS Collaboration. Analysis of the Wtb vertex from the measurement of triple-differential angular decay rates of single top quarks produced in the t-channel at $\sqrt{s} = 8$ TeV with the ATLAS detector. *JHEP*, 12:017, 2017.

[70] ATLAS Collaboration. Search for anomalous couplings in the Wtb vertex from the measurement of double differential angular decay rates of single top quarks produced in the t-channel with the ATLAS detector. *JHEP*, 04:023, 2016.

[71] J. A. Aguilar-Saavedra and S. Amor Dos Santos. New directions for top quark polarization in the t-channel process. *Phys. Rev.*, D89(11):114009, 2014.

[72] J. A. Aguilar-Saavedra, C. Degrande, and S. Khatibi. Single top polarisation as a window to new physics. *Phys. Lett.*, B769:498–502, 2017.

[73] Stefan Bimann, Johannes Erdmann, Cornelius Grunwald, Gudrun Hiller, and Kevin Krninger. Constraining top-quark couplings combining top-quark and $\boldsymbol{B}$ decay observables. 2019.

[74] Nathan P. Hartland, Fabio Maltoni, Emanuele R. Nocera, Juan Rojo, Emma Slade, Eleni Vryonidou, and Cen Zhang. A Monte Carlo global analysis of the Standard Model Effective Field Theory: the top quark sector. 2019.

[75] *ATLAS Computing: technical design report*. Technical Design Report ATLAS. CERN, Geneva, 2005.

[76] Hung-Liang Lai, Marco Guzzi, Joey Huston, Zhao Li, Pavel M. Nadolsky, Jon Pumplin, and C. P. Yuan. New parton distributions for collider physics. *Phys. Rev.*, D82:074024, 2010.

[77] Matt Dobbs and Jørgen Beck Hansen. The HepMC C++ Monte Carlo event record for High Energy Physics. Available via the following web-address: http://home.cern.ch/mdobbs/HepMC/. *Computer Physics Communications*, 134(1):41 – 46, 2001.

[78] A Buckley, T Eifert, M Elsing, D Gillberg, K Koeneke, A Krasznahorkay, E Moyse, M Nowak, S Snyder, and P van Gemmeren. Implementation of the ATLAS run 2 event data model. *Journal of Physics: Conference Series*, 664(7):072045, dec 2015.

[79] Nuno Castro, Johannes Erdmann, Cornelius Grunwald, Kevin Krninger, and Nils-Arne Rosien. EFTfitter—A tool for interpreting measurements in the context of effective field theories. *Eur. Phys. J.*, C76(8):432, 2016.

[80] M. Fischer, S. Groote, J. G. Korner, and M. C. Mauser. Complete angular analysis of polarized top decay at O(α_s). *Phys. Rev.*, D65:054036, 2002.

[81] John M. Campbell, Rikkert Frederix, Fabio Maltoni, and Francesco Tramontano. Next-to-Leading-Order Predictions for t-Channel Single-Top Production at Hadron Colliders. *Phys. Rev. Lett.*, 102:182003, 2009.

[82] Merkt, Sebastian Andreas, Bianchi, Riccardo Maria, Boudreau, Joseph, Gessinger-Befurt, Paul, Moyse, Edward, Salzburger, Andreas, and Tsulaia, Vakhtang. Going standalone and platform-independent, an example from recent work on the atlas detector description and interactive data visualization. *EPJ Web Conf.*, 214:02035, 2019.

[83] Sebastian Andreas Merkt, Riccardo-Maria Bianchi, Joseph Boudreau, Paul Gessinger-Befurt, Edward Moyse, Andreas Salzburger, and Vakhtang Tsulaia. Going standalone and platform-independent, an example from recent work on the ATLAS Detector Description and interactive data visualization. `https://cds.cern.ch/record/2628407`, Jul 2018. ATL-SOFT-SLIDE-2018-455.

[84] Carl D. Anderson. The positive electron. *Phys. Rev.*, 43:491–494, Mar 1933.

[85] Thomas Kittelmann, Vakhtang Tsulaia, Joseph Boudreau, and Edward Moyse. The virtual point 1 event display for the ATLAS experiment. *Journal of Physics: Conference Series*, 219(3):032012, Apr 2010.

[86] ATLAS Collaboration. The VP1 ATLAS 3D event display. `https://atlas-vp1.web.cern.ch/`. Accessed: 2019-10-24.

[87] J Boudreau and V Tsulaia. The GeoModel Toolkit for Detector Description. 2005.

[88] R. Brun and F. Rademakers. ROOT: An object oriented data analysis framework. *Nucl. Instrum. Meth.*, A389:81–86, 1997.

[89] Clhep. `http://proj-clhep.web.cern.ch/proj-clhep`. Accessed: 2019-10-24.

[90] Eigen. `eigen.tuxfamily.org/index.php`. Accessed: 2019-10-24.

[91] Sqlite (self-contained database). `https://www.sqlite.org/index.html`. Accessed: 2019-10-24.

[92] Json (data-interchange format). `https://www.json.org`. Accessed: 2019-10-24.

[93] Coin3D toolkit. https://bitbucket.org/Coin3D/coin/wiki/Home. Accessed: 2019-10-24.

[94] The Qt Framework. https://www.qt.io. Accessed: 2019-10-24.

[95] AppImage. Linux apps that run anywhere. https://appimage.org. Accessed: 2019-10-24.

[96] Homebrew. https://brew.sh/. Accessed: 2019-10-24.